EXPERIMENTAL INVESTIGATION OF WATER ENTRY OF A SOLID OBJECT AND SAND PARTICLES

A thesis submitted to The Faculty of Graduate Studies In partial fulfillment

of the requirements for the degree of

Doctor of Philosophy In

Biotechnology

By

Mahsa Janati

Ph.D. Biotechnology

Supervisor

Dr. Amir Azimi

Lakehead University Thunder Bay, Ontario April 2023

Author's Declaration Page

I hereby declare that I am the sole author of this thesis document. This is a true copy of this document, including any required revisions as accepted by my supervisor.

Dedicated to

My father, Farhad Janati, who never saw this adventure, my husband, my mother, and my sister for all their support, encouragement, and unwavering love.

Abstract

This thesis presents the results of two different approaches to water entry; first, in Part I, the results of the experimental investigation of the water entry of a solid object, a thick disk in stagnant water, are presented. The shape of the resulting surface crown in different release conditions and disks with various geometries should be characterized. Moreover, the pinch-off time and depth of the underwater cavity for disks with different densities in different release conditions are extracted and results are compared in different conditions. Energy losses due to the impact are also obtained and the results for different release heights and various disk densities are presented. A parameter study reveals the dependence of the underwater cavity structure on the governing dimensionless groups. The results of annular disks are also illustrated to see how a central hole can affect the pinch-off characteristics. In addition, the effects of confinement on the characteristics of the crown, pinch-off time, and pinch-off depth are investigated and results are compared with the condition of removing wall effects. The wall effects highly reduced the radial and vertical velocity of the surrounding water. Less vorticity with asymmetrical distribution is observed in the surrounding water. Consequently, less swirling strength, and mean and turbulent kinetic energies are observed in tanks with smaller widths.

Second, in Part II of this thesis, the results of experimental investigation in water entry of solid particles, known as particle cloud, are presented. Different release conditions and aspect ratios are considered, and the results are compared to each other. The experiments are conducted with the releasing of sand particles from a single vertical nozzle and the results are compared with the releasing of the same mass from two adjacent nozzles. It was found that dividing the total release mass into two equal portions is helpful in enhancing the mixing, reducing the turbidity, and consequently decreasing mass loss in water environment. Moreover, different release distances between two nozzles are investigated and the results are compared with the single particle cloud. Additionally, oblique release conditions with single particle cloud and twin particle clouds with different release distances are investigated. The oblique release angle is 45° and sand particles are discharged through two oblique nozzles in front of each other to increase the mixing and reduce the mass loss in the water column. Finally, the results of oblique release and vertical release sand particles in both single and twin conditions are compared to each other, and the results are presented accordingly.

Acknowledgments

Firstly, I would like to sincerely thank my supervisor Dr. Amir Hossein Azimi for his endless guidance, patience, encouragement, and enthusiasm. This work would not have been completed without his support, motivation, and effort. I aspire to your thoughtfulness and admire your dedication, unparalleled work ethic, and passion. Thank you for trusting me and giving me the chance to be in your research group which has changed my life.

I would like to thank my committee members Dr. Baoqiang Liao, Dr. Eltayeb Mohammadelhassan, and Dr. Majid Mohammadian (external examiner) who kindly agreed to evaluate the quality of my research work and gave me valuable suggestions and advice.

Above all else, I would like to thank my husband Arash, to whom I express my deepest love and appreciation, my mother Fariba Jeldi, my sister Dr. Maryam Janati My late grandmother Fatemeh Heydari Sani, My aunts Farzaneh and Marzieh Jeldi for their continuous support and encouragement. I would like to thank my dear friends Sandy & Ken Traynor for their generous and continuous support.

Table of Contents

List of tables

List of Figures

Chapter 1

1. General Introduction

1.1   Problem definition

The water entry of a solid object in stagnant ambient water can be classified as the water entry of single solid object and water entry of a cluster of particles. Water entry of a solid object has many applications in naval industry, military, sports, and other various engineering fields. The water entry of a cluster of small particles in water is known as particle clouds and has many applications in marine bed capping, land reclamation and dredging activities. The present thesis covers both water entry classifications, in Part I, the water entry of a single disk in different release conditions is investigated (see Figure 1.1a), and Part II of the thesis focuses on the releasing of a group of small solid particles in water with different release conditions (see Figure 1.2b).
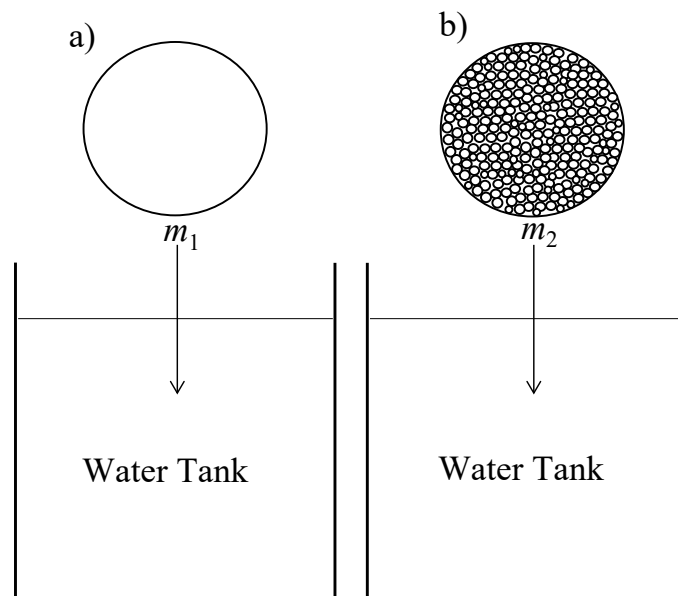
Figure 1.1. Schematic of water entry: a) a single object water entry; b) a group of small solid objects.

1.2   Water entry of a solid disk

Part I of the thesis investigates the water entry of cylindrical disks with different physical

1

characteristics and release conditions. The formation of underwater cavity and above water splash curtains are the particular focus of study in this part. The water entry problem has many applications in marine industry, sports, military, and various engineering fields. For over a century, the free-falling water entry has been the topic of scientific research studies. Worthington & Cole (1897, 1900) and Worthington (1908) initiated the investigation of water entry by using single-spark photography and produced fascinating images of splash and cavity formations. Mallock (1918) and Ramsauer & Dobke (1927) provided detailed description in the cavity shape. During World War II, the importance of water entry intensified due to its relevance to the water entry of missiles and the safety of underwater facilities. Extensive quantitative studies of water entry of spheres were performed using high-speed photography to study the effects of atmospheric pressure, density of the object, and surface properties on the splash and cavity formation (Richardson 1948; Gilbarg & Anderson 1948; May 1951, 1952). The geometry of disk, density ratio, release conditions such as release height, and wall effects can alter the pinch-off time, pinch-off depth, and the shape of the crown. The specific effects of such parameters are investigated and compared with the available research studies.

Chapter 2 of the thesis describes the experimental study of the water entry of thick solid disks and annular disks driven by the effect of gravity. The water entry, crown formation, and cavity dynamics of gravity-driven thick solid and annular disks are studied in three different release conditions. The effects of aspect ratio, geometry, and density of disks on crown formation, interface impact, seal development, and air entrainment are investigated. The crown dimensions are measured, and smaller crown geometries are found in annular disks. The disk's velocities in three different stages are measured. The velocity and vortex fields are extracted from the Particle Image Velocimetry (PIV) data and the results are shown in this chapter.

Chapter 3 describes the effects of impact energy on the crown formation and cavity dynamics of free-falling thick disks in stagnant water. To simulate the effects of impact energy on the dynamics of free-falling thick disks, four different release heights, h_r, and six different disk masses are considered. A threshold limit of $h_r = 4d_o$, where d_o is the disk diameter, is obtained to control different flow dynamics and motion of disk in water. Different patterns of cavity dynamics and crown characteristics are observed and reported during the impact and descending of solid disks. The evolution of crown characteristics such as crown shape, diameter, and height with time are

measured, and the pinch-off time and location of pinch-off are extracted from image analysis. The energy losses due to impact, crown formation, and pinch-off are calculated for the tests and results are reported.

Chapter 4 describes the wall effects on different characteristics of the subsequent phenomena of water entry. In this chapter three disks with different densities are released from four different heights in tanks with various cross sections. The crown formation, cavity dynamics, and the characteristics of the underwater cavity including pinch-off time and pinch-off depth are also measured and compared in different cases. Moreover, the position of the disk at the pinch-off time is obtained through image processing. The velocity field around the disk is also studied using the PIV measurements. Additionally, the vorticity behind the disk, swirling, average kinetic energy, and turbulent kinetic energy are obtained from the PIV data.

1.3   Water entry of particle clouds

In this part, the water entry of sand particles in stagnant water is investigated. Such phenomenon is called particle clouds evolution in the literature (Buhler and Papantoniou, 1991; Bush et al., 2003) Particle cloud has many applications in land reclamation and dredging activities (Azimi et al., 2011; Azimi et al., 2012a, 2012b; Manzouri and Azimi, 2019a, 2019b). Mixing of particles in the ambient water has several engineering applications, including wastewater disposal, construction of artificial islands, and mining industry. The understanding of particle dynamics and their controlling parameters are important for proper design, optimization, and monitoring of the dredging release processes.

In Chapter 5 the interaction and mixing of twin particle clouds in stagnant water are studied by a series of laboratory experiments. The importance of source separation distance and sand particle mass is investigated by introducing non-dimensional parameters. The frontal positions of twin particle clouds are compared with the corresponding single particle cloud frontal positions and a critical source separation distance is reported based on the maximum frontal velocity and minimum mass loss of twin particle clouds. The maximum frontal velocity of the critical twin particle cloud is found to be correlated with the depletion of the ambient entrainment in a region between the two clouds. In this chapter the width, velocity, and entrainment coefficient of twin particle clouds are also measured and compared in different release conditions.

Chapter 6 describes the evolution of single and twin oblique particle clouds in stagnant water and the effects of controlling parameters such as sand mass and nozzle spacing are studied. The time variations of particle cloud properties such as frontal position, horizontal and vertical centroids, cloud width, and frontal velocity are measured using the image analysis and Particle Image Velocimetry (PIV) techniques. The entrainment coefficients are extracted from the measurements and the results are compared with the literature. The effects of release angle and particle interactions are studied by comparing the time histories of maximum centerline velocities. The time history of the ratio of horizontal to vertical centroids in oblique particle clouds determined the potential location of sand particles and a practical model is developed to determine the size and location of particle clouds with time.

In Chapter 7, a summary of conclusions and suggestions for future studies are presented for both a single object and a cluster of solid particles water entry. Appendix A is a conference paper on the particle cloud water entry and Appendix B is a conference paper on the water entry of an annular disk.

Part I

Water entry of a single object (Disk)

Chapter 2

2. On the crown formation and cavity dynamics of free-falling thick disks

2.1   Introduction

The water entry of solid objects and subsequent physical phenomena such as crown formation, transient cavity, surface seal, and cavity pinch-off have been a well-known classical fluid dynamics problem and received considerable attention from the literature (Worthington & Cole, 1897 and 1900; Worthington, 1908; Gaudet, 1998; Bergmann et al., 2009; Aristoff & Bush 2009; Truscott et al., 2013; Mansoor et al., 2014; Marston et al., 2016; Sun et al., 2019; Zhou et al., 2021; and Rabbi et al., 2021). The phenomenon of solid entry in stagnant water has many applications in military, sports, ocean engineering, ship slamming, aerospace engineering, and naval-oriented studies (May, 1975; Kapsenberg, 2011; Abrate, 2013; Seddon & Moatamedi, 2006; Aristoff et al., 2010; Janati et al., 2022). The study of free-falling solid objects in stagnant water has significant safety importance in protecting underwater facilities from the impact. Despite the simple configurations, high-speed water entry is an unsteady and complex physical process through which the object instantly experiences a sudden change of ambient density and surface resistance. Many parameters such as geometry, density difference, impact velocity due to different release conditions of the falling object, and the ambient fluid properties control the formation of the transient cavity and crown characteristics.

Several studies have focused on the impact of free-falling spheres in stagnant water (Truscott and Techet, 2009; Marston et al., 2012; Tan et al., 2016). Duez et al. (2007) indicated that the surface treatment of spheres has significant effects on cavity formation. It was observed that a hydrophilic sphere does not generate a cavity until its impact velocity reaches a threshold and the value of which depends on the surface state. Aristoff et al. (2010) studied the water entry impact in decelerating spheres with various densities ranging from 0.20 g/cm^3 to 7.86 g/cm^3. It was found that the pinch-off depth, time, and total cavity depths have correlations with the sphere density. Linear relationships were proposed for variations of pinch-off characteristics with initial Froude

number of spheres, $Fr_i = V_o/(gd_o)^{1/2}$, where V_o is the impact velocity and d_o is the sphere diameter. However, such relationships became non-linear as the density of spheres decreased. It was reported that the pinch-off depth was strongly correlated with the sphere density whereas less dependency was found between pinch-off time and sphere density.

The water entry of solid objects has been tested in both guarded and unguarded release conditions (Mansoor et al., 2014). The crown formation occurs only in the unguarded release condition, where the disk falls freely through the air and impacts the water surface. Significant momentum transfer is resulted due to water impact, water surface splash, and crown development. The guarded water entry of spheres has been investigated by releasing spheres through a pipe and colliding with the water surface.

A cylindrical disk is classified as a thin or a thick disk based on the ratio of the disk diameter, d_o, to thickness, e, with a threshold of $\chi = d_o/e = 10$. The water entry of thin disks and their descent modes in water have been extensively investigated using both experimental and numerical methods (Willmarth et al., 1964; Field et al., 1997; Zhong et al., 2011; Auguste et al., 2013; Vincent et al., 2016; Bi et al., 2018; Xu et al., 2021). The boundary between stable and unstable oscillations of thin disks was determined based on a number of dimensionless parameters. Willmarth et al. (1964) found six controlling variables pertinent to the phenomenon which are the disk density, ρ_d, fluid density, ρ_f, fluid dynamic viscosity, μ, disk diameter, d_o, disk thickness, e, and the mean vertical velocity of the disk, V. Following the Buckingham theorem, three dimensionless parameters of Reynolds number, $Re = \rho_f V d_o/\mu = V d_o/\nu$, the dimensionless moment of inertia, $I^* = I_{disk}/\rho_f d_o^5 = \pi \rho_d e/64 \rho_f d_o$, and aspect ratio of the disk, $\chi = d_o/e$ were identified where I_{disk} is the moment of inertia of the disk.

A regime map was defined based on variations in the dimensionless moment of inertia, I^*, and the Reynolds number of the disk, Re (see Figure 2.1). Field et al. (1997) carried out a series of laboratory experiments to study the dynamics of free-falling disks in a glycerol mixture and reported four descending patterns steady, fluttering, chaotic, and tumbling. In addition, a chaotic transition area was defined between the fluttering and tumbling regimes. The data points in Figure 2.1 show the present tests and the dashed curve was suggested by Heisinger et al. (2014).
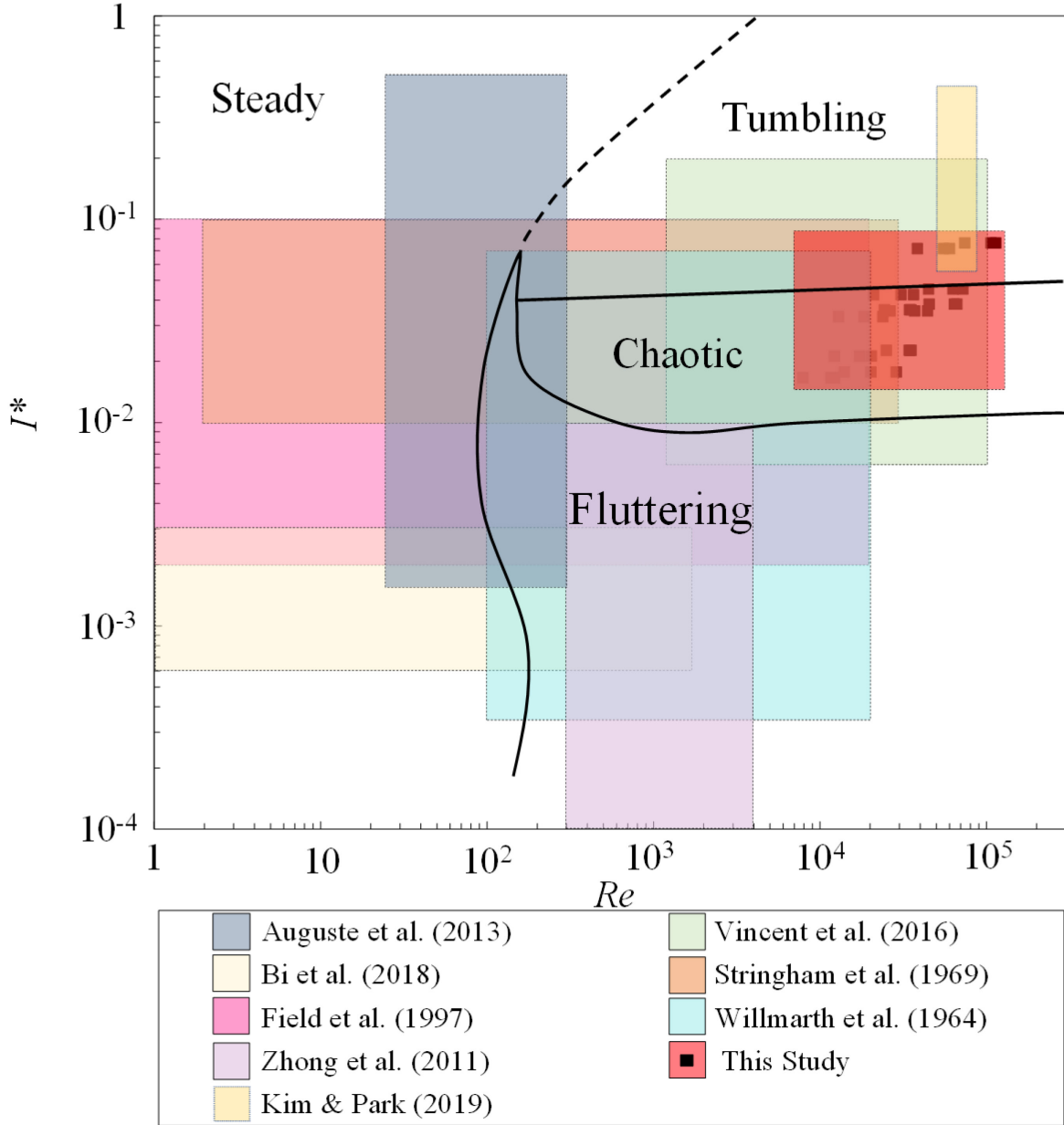
Figure 2.1. A regime plot showing the descend mode classifications of cylindrical disks into stagnant water. The bold solid line and curves define the regions of different disks' motion based on a dimensionless moment of inertia, I^*, and Reynolds number, Re. The falling modes were proposed by Field et al. (1997), and dashed curve by Heisinger et al. (2014).

The interaction of free-falling solid objects with water and cavity formation was investigated in disks with low impact velocity, V_o, ranging from 0.562 ms^{-1} to 3.11 ms^{-1}, and disk radius, r, ranging from 0.0127 m to 0.0307 m (Glasheen & McMahon, 1996). A linear correlation was

proposed between the square root of the disk's radius, $r^{1/2}$, and pinch-off time. It was found that the relative pinch-off depth, H_p/r, where H_p is the pinch-off depth and r is the radius of the disk, increases linearly with Froude number, Fr_o. Kim and Park (2019) studied the water entry of cylindrical objects with different aspect ratios and surface conditions. It was indicated that the transient cavity diminishes the drag force on the sinking body when it is fully encapsulated by the ambient. However, if air bubbles attach to the object after the pinch-off, they tend to detach irregularly and impose further drag force on the object. Therefore, the descending velocity decreases gradually due to energy dissipation to overcome the upward motion of the bubbles.

To the authors' knowledge, most of the available research studies in the literature focused on the free-falling of spheres. The investigation on the water entry of cylindrical disks is limited to the trajectory of thin disks and motor-driven disks in water (Aristoff and Bush, 2009; Bergmann et al., 2009; Bi et al., 2018). Despite the numerous resemblances in cylindrical falling objects to thick disks ($\chi = d_o/e < 10$), limited studies were carried out to investigate the impact and cavity formation of thick disks in stagnant water. In addition, the motion of free-falling thick annular disks, momentum transfer, and cavity formation is significantly different from the spherical, thin, and solid disks, which requires careful attention. This study explores cavity dynamics, crown formation, pinch-off development, and free-falling motion of thick solid and annular disks in both guarded and unguarded release conditions. The selected disks have rough edges and aspect ratios of $\chi = 1.5$ and 3. The effects of the dimensionless moment of inertia, I^* on the crown formation and cavity development induced by thick annular and solid disks are investigated by utilizing the Particle Image Velocimetry (PIV) technique to measure the velocity field and vortex structure around the falling disks.

2.2. Material and Methods

2.2.1 Experimental Setup

Laboratory experiments were conducted in the Multiphase Flow Research Laboratory (MFRL) at Lakehead University using a glass-walled tank with cross-section dimensions of 850 mm x 1650 mm and a depth of 800 mm (see Figure 2.2a). A schematic front view of the experimental setup, a sample image of Test No. 21, and the coordinate system are shown in Figure 2.2a. The experimental parameters such as the release height conditions, disk characteristics, impact

velocities, and aspect ratios are listed in Table 2.1. The impact Froude number, $Fr_o = V_o/(gd')^{1/2}$, where $d' = d_o - d_i$ is the equivalent diameter of the annular disk, d_o and d_i are the outer and inner diameters of the disk, respectively, and g is the gravitational acceleration. The median Reynolds numbers, $Re_m = Vd'/\upsilon$, where V is the mean downward velocity of the disk and υ is the kinematic viscosity of water, are listed in Table 2.1 as well.

Table 2.1. Experimental details and physical parameters of free-falling thick disks in stagnant water, $d_o = 76.2$ mm (3 in).

Test No.	h_{pipe}	h_{air}	d_i	e	M	ρ_d	V_o	χ	Fr_o	Re_m
	(mm)	(mm)	(mm)	(mm)	(g)	(kgm^{-3})	(ms^{-1})	(-)	(-)	(-)
1			0	25.4	125	1079	1.11	3	1.28	28812
2			0	25.4	160	1381	1.49	3	1.72	34372
3			0	25.4	270	2331	1.77	3	2.05	66463
4			38.1	25.4	94	1079	1.50	3	2.46	12260
5			38.1	25.4	120	1381	1.65	3	2.69	17316
6	300	0	38.1	25.4	202	2331	1.88	3	3.08	34510
7			0	50.8	250	1079	1.49	1.5	1.72	44301
8			0	50.8	320	1381	1.72	1.5	1.99	72152
9			0	50.8	540	2331	1.86	1.5	2.15	113630
10			38.1	50.8	188	1079	1.75	1.5	2.86	13876
11			38.1	50.8	240	1381	1.80	1.5	2.94	36511
12			38.1	50.8	404	2331	2.00	1.5	3.27	60054
13			0	25.4	125	1079	1.31	3	1.51	20255
14			0	25.4	160	1381	1.40	3	1.62	35317
15			0	25.4	270	2331	1.72	3	1.99	64208
16			38.1	25.4	94	1079	1.50	3	2.45	11660
17			38.1	25.4	120	1381	1.57	3	2.56	20352
18	200	100	38.1	25.4	202	2331	1.86	3	3.05	35143
19			0	50.8	250	1079	1.54	1.5	1.78	37049

20			0	50.8	320	1381	1.72	1.5	1.99	63120
21			0	50.8	540	2331	2.00	1.5	2.32	106557
22			38.1	50.8	188	1079	1.70	1.5	2.78	18452
23			38.1	50.8	240	1381	1.87	1.5	3.05	30650
24			38.1	50.8	404	2331	2.05	1.5	3.35	55417
25			0	25.4	125	1079	0.87	3	1.00	13994
26			0	25.4	160	1381	0.98	3	1.14	25079
27			0	25.4	270	2331	1.23	3	1.43	45386
28			38.1	25.4	94	1079	0.99	3	1.62	7909
29	100	200	38.1	25.4	120	1381	1.07	3	1.76	12208
30			38.1	25.4	202	2331	1.33	3	2.18	24416
31			0	50.8	250	1079	1.02	1.5	1.18	26360
32			0	50.8	320	1381	1.15	1.5	1.33	44975
33			0	50.8	540	2331	1.35	1.5	1.56	74157
34			38.1	50.8	188	1079	1.15	1.5	1.88	12951
35			38.1	50.8	240	1381	1.18	1.5	1.93	21018
36			38.1	50.8	404	2331	1.41	1.5	2.30	38512

The experimental tank was filled with tap water having a temperature of $T = 20 \pm 0.5$ °C, a density of $\rho_w = 998$ kgm^{-3}, and kinematic viscosity of $\upsilon = 1.02 \times 10^{-6}$ m^2/s. The water in the tank was at rest and maintained at a constant level with a depth of 650 mm in all experiments. Twelve disks with different densities, thicknesses, and cross-sections (i.e., full and annular shapes) were utilized in this study. The geometry configurations of the disks are illustrated in Figure 2.2b. The disks were made of compressed rubber and were considered to have homogenous densities, which were hydrophobized by treatment with a commercially available super hydrophobic agent, Glaco Mirror Coat' zero' (Soft99 Corp. Co., Ltd., Japan). The coating contains nanoparticles and organic reagents, resulting in a water contact angle of approximately 123°. The water contact angle was measured based on the proposed method by Truscott et al. (2013). The hydrophobic coatings were applied to each disk with an approximate thickness of 1 μm. As reported by Aristoff et al. (2010), such coatings did not appreciably affect the disk diameter or density. Three different densities of disks were selected as $\rho_d = 1,079$ kgm^{-3}, 1,381 kgm^{-3}, and 2,331 kgm^{-3} to study the water entry of

thick disks in the Tumbling, Chaotic, and the boundary between the two regimes (see Figure 2.1). The disks were solid, and flat, with a rounded rim and the side edge surface of the disks had roughness with an approximate root mean square roughness height of 1 ± 0.1 mm. The outside diameter of the disks was $d_o = 76.2$ mm and the centric hole diameter in the annular disks was $d_i = 38.1$ mm. Two disk thicknesses were selected in this study (i.e., $e = 25.4$ mm and 50.8 mm).
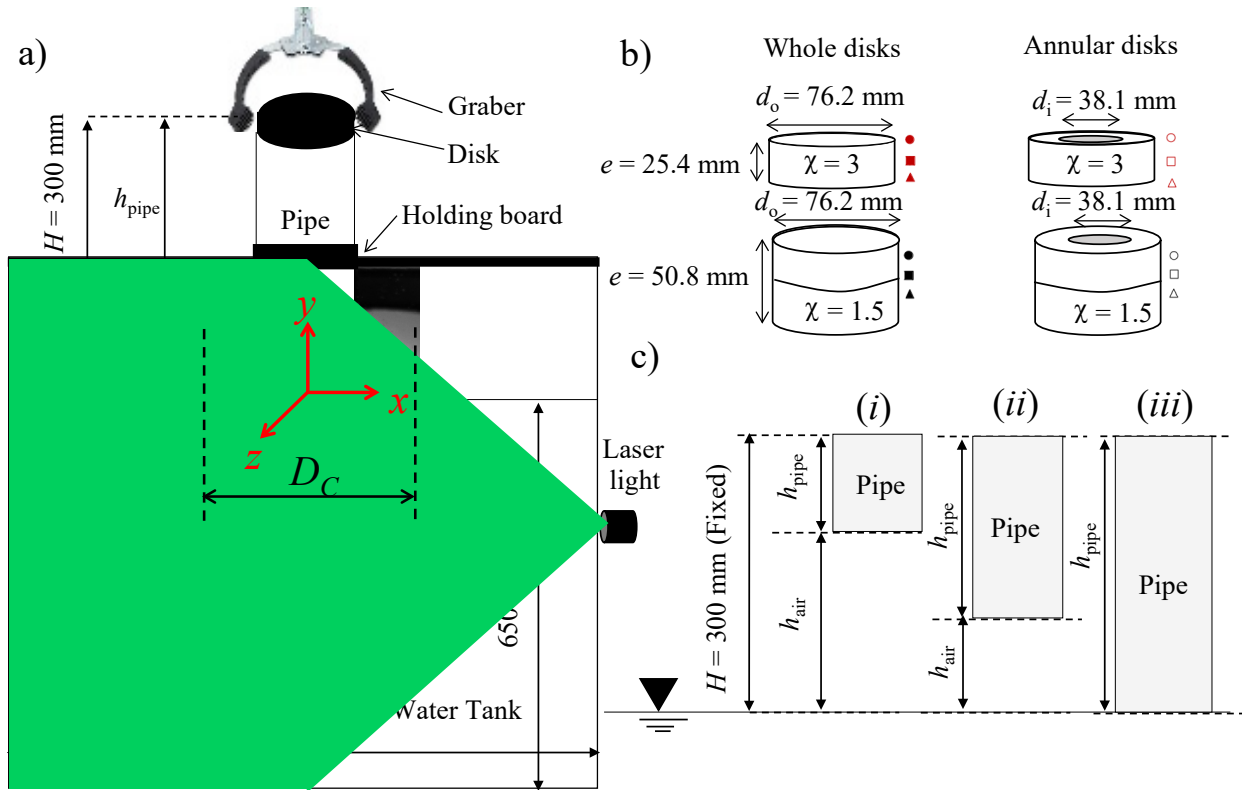
Figure 2.2. Schematic of the experimental set-up, coordinate system, and release condition: a) image of Test No. 21 at $t = 0.1$ s; $\chi = 1.5$, $\rho_d/\rho_w = 2.335$, $d_o = 76.2$ mm, $e = 50.8$ mm, $h_{pipe} = 200$ mm, $h_{air} = 100$ mm; b) schematic of cylindrical disks used in this study, symbols on the right-hand side of the disks refer to the symbols used on the plots; c) schematic of three different release conditions with a fixed total height of $H = 300$ mm: (*i*) partially guarded, disks were released through a 100 mm height pipe and 200 mm in air, (*ii*) partially guarded, disks were released through a 200 mm height pipe and 100 mm in air, (*iii*) fully guarded, disks were released through a 300 mm height pipe placed on the water surface and zero air height.

Disks were released from a fixed height of $H = 300$ mm, which is equivalent to four times of the disk diameter (see Figure 2.2c). Three different initial release conditions were considered for each

12

disk giving the total number of thirty-six tests (see Table 2.1). As shown in Figure 2.2c, in the first release condition (case *i*), disks were released through a uniformly lubricated pipe with $h_{pipe} = 100$ mm, which is 4 mm larger than the disk's diameter and is located 200 mm above the water surface. In the second release condition (case *ii*), disks were released through the same pipe with $h_{pipe} = 200$ mm and $h_{air} = 100$ mm above the water surface. The third release condition (case *iii*) is guarded by a 300 mm pipe that was precisely positioned on the water surface (i.e., $h_{pipe} = 300$ mm and $h_{air} = 0$). The releasing positions were centered such that all disks released and descended unconstrained, and the tank wall boundary did not affect the motion of disks. Each experiment was repeated three times to ensure the repeatability of tests and exhibited consistent cavity and crown formations over all trials. Error analysis was performed based on the analysis of the replicas and the uncertainty error was ± 0.2 mm in measurements of the disk's diameter, ± 0.5 mm in measuring the release height, and less than $\pm 3\%$ in all measured parameters. The impact velocity of each disk, V_o, was measured by high-speed imaging technique and the MatLab object detection algorithm (MatLab version R2018b, MathWorks, Natick, MA, US). The initial processing time for analyzing the water entry and impact is defined as when the disk fully enters the ambient water (May, 1975).

The upward splash and downward cavity were formed upon the impact of a disk with the water surface. The tank and falling disk were illuminated using two light sources (Woods L13, 1,000-W telescope work light, CA) from both sides of the glass tank. High-speed images with a frequency of 2500 fps and resolution of 1280 x 800 pixels were captured by a high-speed camera (Phantom, Miro Lab 110, New Jersey, Wayne, USA) and a camera lens of AF Nikkor 50 mm, f/1.4D (Nikon, Tokyo, Japan) was employed. A minimum of 10 minutes of relaxation time, which was obtained through a PIV analysis for the most agitated test, was taken between each experiment to eliminate the disk-water interactions and water fluctuations. The water surface level was rechecked during the relaxation time to maintain a consistent water level for the next experiment.

2.2.2   *Image Analysis and Data Mining*

The captured images were analyzed using the image processing toolbox of the MatLab software (version R2018b, MathWorks, Natick, MA, US). At first, the background sliding technique was implemented by subtracting the base image to remove local shadows. The threshold of the disk

was detected by implementing the thresholding techniques (i.e., boundary detection). Then, images were converted to binary images so that the critical parameters such as pinch-off depth and time, crown diameter, and frontal velocity of the disks were extracted. More details on image preparation and boundary detection algorithms can be found in the study of Janati and Azimi (2021a and b).

Data mining or knowledge analysis is a computational process with which meaningful patterns are extracted from a series of images or data. In the current study, data-mining techniques were utilized from the regime classifiers of the Weka software (Weka, Version 3.8.5). The Logistic Model Trees (LMT) classifiers are classification trees with logistic regression functions at the leaves. The classifiers in the Weka software perform regression algorithms and evaluate the precision of the proposed model (Witten and Frank, 2005). In this study, 24 data points were obtained from the images to determine the shape of the surface seal. Attributes in classifiers are categorized into nominal and numeric. Numeric attributes are variables such as impact velocity, and nominal attributes can be defined as different surface seal shapes such as Full Seal (FS), Partial Seal (PS), etc. The Weka software contains different classifiers such as Bayesian, Rules, Trees, Functions, etc. (Witten and Frank, 2005). In this study, all classifiers were tested and the model with the highest correctly classified instances was selected. The LMT classifier in this study showed the highest number of correctly classified cases with clear boundaries between different forms of surface seals.

2.2.3 *Particle Image Velocimetry (PIV)*

Velocity fields around free-falling disks were extracted from the time series of images and employed the time-resolved Stereo Particle Image Velocimetry (PIV) system. Time-resolved PIV is a technique used to capture and analyze the velocity field of fluid flows over time with high temporal resolution, which means that the measurements are taken at very short time intervals. This technique involves injecting small, light-reflecting particles into the fluid flow and illuminating them with a laser light sheet. A camera then captures the motion of the particles over a series of time intervals, allowing for the calculation of velocity vectors at each interval. By capturing data over time with a high temporal resolution, time-resolved PIV enables the study of dynamic flow phenomena, such as vortices, turbulence, and fluid-structure interactions, providing insight into the underlying mechanisms and kinetics of the process. In this study, the ambient water

was seeded with a 60 μm polyamide high-quality monodisperse tracer particles with a density of 1,030 kgm^{-3} to follow the motion of ambient fluid around the falling objects. The ambient water was fully mixed with seed particles to ensure a uniform distribution of seeding particles. A laser sheet with a thickness of 1 mm was launched from the side of the tank to illuminate the background fluid by creating a thin vertical plane of laser sheet through the symmetry axis of the cavity. A dual cavity Nd:YLF laser generator (DM20-527-DH/Stereo PIV, Ronkonkoma, NY, USA) was used to generate laser light with a wavelength of 527 nm for background illumination. The seeded images with tracer particles were captured by a high-speed camera (Phantom, Miro Lab 110, New Jersey, Wayne, USA) having a lens of AF Nikkor lens with a 50 mm focal length (f/1.4D, Nikon, Tokyo, Japan). The PIV Images were captured with a frequency of 500 fps, the exposure time was 5 μs, and the images had a resolution of 1280 x 800 pixels. The captured consecutive images were analyzed using a cross-correlation algorithm of the DaVis 10 software (DaVis 10, LaVision, GmbH, Göttingen, Germany).

Three interrogation window passes were considered as 48×48, 32×32, and 16×16 pixels with a 50% overlap for noise reduction. Such window-passing algorithms produce one velocity vector in every window of 16×16 pixels. A calibration plate that was predefined in the DaVis 10 software was implemented to convert pixels to millimeters with the Pinhole Mapping Function (PMF). The Vector Validation Algorithms (VVA) were used to remove the spurious vectors and post-processing analysis was applied to extract velocity vector fields. The position of the correlation peak can be measured with sub-pixel accuracy. In the PIV technique, the velocity field computation has a bias toward integer velocity values called the peak locking effect. The peak locking effect was monitored during PIV computations followed by Azimi et al. (2012a) and the computed velocity vectors were in the acceptable range (i.e., peak lock < 0.1) suggested by the LaVision manual.

2.3   Experimental Results

2.3.1   *Crown and cavity formation*

The geometrical characteristics of a crown, surface seal, and cavity formation on the wake of cylindrical disks are presented in this section. Experimental observations revealed that crown formation and pinch-off characteristics are linked together; however, they may result from

different hydrodynamic mechanisms. Figure 2.3 shows the effects of disk aspect ratio and density on the time evolution of crown and cavity. As can be seen in Figure 2.3, the impact frame was considered at $t/t_p = 0$. After the impact, the splash curtain raised and expanded to form a crown and then after reaching a certain depth, the cavity started to contract due to the underwater hydrostatic pressure. Then, the pinch-off occurs at t_p and the cavity is split into two upward and downward jets. The upward jet is known as the Worthington jet was formed due to the reaction of buoyancy and surface tension forces, and it accelerated to a considerable height above the water surface. Due to the effect of gravitational force, the crown returned to the water surface and collapsed. When the Worthington jet is formed, it has energy from the impacted disk to move upward, then after reaching a certain height it tends to return to the water surface and re-entering the water pool. Once it re-enters the water, again the static pressure forms around the jet and causes the second pinch-off. A vortex ring is formed by the downward jet at the top surface of the disk. It should be noted that the torus core of the vortex ring depends on the impact velocity generated by the density difference between the disk and water.

The consecutive high-resolution images of falling a gravity-driven thick disk with an aspect ratio of $\chi = 3$ (Test No. 13) and with the partial release condition are shown in Figure 2.3a. The timing in each image was normalized with the cavity pinch-off time, t_p, and the normalized time was tagged above each image. Experimental observations indicated that the surface closure depends on the impact velocity of the disk. In relatively high impact velocity (i.e., $V_o > 1.3$ ms^{-1}), the disk forms a cavity and crown, and the crown has closed afterward and forms a dome over the cavity. Such flow regime is known as the Full Seal (FS) regime. In relatively low impact velocity (i.e., $V_o \leq 1.3$ ms^{-1}), the crown has not fully sealed and formed a Partial Seal (PS) cavity. The mass, density, and impact velocity of the disk in Test No. 13 were $m = 125$ g, $\rho_d = 1,079$ kgm^{-3}, and $V_o = 1.31$ ms^{-1}, respectively. The vortex ring was dragged by the downward momentum of the disk and was divided into several spherical bubbles. The resulting bubbles moved upward due to the presence of buoyancy force and reached the water surface. After the upward jet reached its highest elevation, it returned to the water and created the second pinch-off. The second pinch-off interfered with the rising bubbles due to the vortex ring break-up, and such interaction dissipated the energy of the downward jet. A bubble column is formed on the wake of the disk after the jet interactions in the

16

mixing region. Finally, the surface water oscillation occurred through which all the energies that were transferred by the impact were dissipated.

The crown formation and cavity dynamics of a thick disk (i.e., Test No. 20, $\chi = 1.5$, $m = 320$ g, and $\rho_d/\rho_w = 1.384$) as it enters the water is illustrated in Figure 2.3b. The release condition is partially guarded with $h_{pipe} = 200$ mm and $h_{air} = 100$ mm. The time in all images was scaled with the time at which the pinch-off occurred (see Figure 2.3b, $t/t_p = 1$, $t_p = 0.1412$ s). The higher density of the disk in comparison to Test No. 13 increased the impact velocity to $V_o = 1.72$ ms^{-1} and consequently increased the acceleration of the disk. Higher acceleration directly affected the motion of the disk and produced a larger force at the impact.

Figure 2.3. Image sequence showing the significant consecutive phenomena formed by falling a gravity-driven thick disk, $d_o = 76.2$ mm, in stagnant water; a)Test No. 13; $\chi = 3$, $\rho_d/\rho_w = 1.08$, $d_i = 0$, $e = 25.4$ mm, $h_{pipe} = 200$ mm, $h_{air} = 100$ mm, and $t_p = 0.138$ s; b) Test No. 20; $\chi = 1.5$; $\rho_d/\rho_w = 1.384$, $d_i = 0$, $e = 50.8$ mm, $h_{pipe} = 200$ mm, and $h_{air} = 100$ mm, and $t_p = 0.1412$ s; c) Test No. 28; $\chi = 3$; $\rho_d/\rho_w = 1.08$, $d_i = 38.1$mm, $e = 25.4$ mm, $h_{pipe} = 100$ mm, and $h_{air} = 200$ mm, and $t_p = 0.1092$ s; d) Test No. 36; $\chi = 1.5$, $\rho_d/\rho_w = 2.335$, $d_i = 38.1$ mm, $e = 50.8$ mm, $h_{pipe} = 100$ mm, and $h_{air} = 200$ mm, and $t_p = 0.13$ s; Dimensionless times, t/t_p, are shown on top of each image.

18

As can be seen in Figure 2.3b, the droplets at the tip of the crown fell into the inner surface of the cavity, which formed ripples that spread over the surface of the cavity and disturbed the uniform sheet of cavity surface for $t/t_p \geq 0.652$. Figure 2.3c shows images of Test No. 28 for an annular disk with an aspect ratio of $\chi = 3$, density ratio of $\rho_d/\rho_w = 1.08$, impact velocity of $V_o = 1.65$ ms^{-1}, and mass of $m = 94$ g. As can be seen, a large bubble was detached from the disk and moved into the mixing region between the disk and water surface at $t/t_p = 1.117$ and 1.484, respectively. The large bubble moved downward because of the low-pressure zone in the wake of the disk and stayed in the middle of the mixing region for a short period. It was then stretched due to the upward buoyancy force and downward motion of water in the wake of the disk.

Due to the existence of a central jet in annular disks, the pinch-off, crown, and total descending times in annular disks were respectively 20%, 5%, and 10% shorter than that of the corresponding solid disk. Finally, the sequential images of water entry of a heavy annular disk (i.e., Test No. 36, with $\rho_d/\rho_w = 2.335$, $\chi = 1.5$, and $m = 404$ g) are illustrated in Figure 2.3d. The impact velocity of the heavy annular disk was $V_o = 1.41$ ms-1. The annular disk fell and generated a larger underwater cavity in comparison with the impact of lighter disks having a smaller impact velocity ($V_o = 1.15$ ms-1). In the heavy release of annular disks, the pinch-off depth moved upward and formed approximately in the middle of the total cavity depth. A dense column of microbubble streams was formed at the wake of the annular disk for $t/t_p \geq 2.455$.

2.3.2 *Water entry of disks with guarded release*

The surface crown can be fully blocked by the guarded release mechanism. The consecutive images of four experiments without a surface seal are illustrated in Figure 2.4. Four sample experiments were selected based on geometry (i.e., solid versus annular), density, and aspect ratio (i.e., $\chi = 1.5$ and 3), including Test No. 3, 5, 7, and 11. The water entry of a thick disk with an aspect ratio of $\chi = 3$, a density ratio of $\rho_d/\rho_w = 2.335$, and an impact velocity of $V_o = 1.77$ ms^{-1} (see Table 2.1, Test No. 3) is shown in Figure 2.4a. The disk in Figure 2.4a had the highest density among the other tests, which formed an engulfing cavity beneath the water surface. The cavity contraction occurred due to the formation of a low-pressure region inside the cavity and relatively high pressure of ambient water. The surface of cavity in Figure 2.4a was distorted, and surface ripples were formed, which made it difficult to precisely measure the pinch-off depth. As can be

seen at $t/t_p \geq 3.341$, the disk started to have a chaotic motion and rotate around its horizontal axis indicating less stability due to bubble detachment from the disk.

Figure 2.4. Time history images of water entry of thick disks, $d_o = 76.2$ mm, with fully guarded release condition, $h_{pipe} = 300$ mm, $h_{air} = 0$. The images show the outward splash, trajectory, deep seal, and bubble formation following the impact of a disk onto the water: a) Test No. 3, a thick disk without a central hole with $\chi = 3$, $\rho_d/\rho_w = 2.335$, $d_i = 0$, $e = 25.4$ mm, $t_p = 0.147$ s; b) Test No. 7, a thick disk without central hole with $\chi = 1.5$, $\rho_d/\rho_w = 1.08$, $d_i = 0$, $e = 25.4$ mm, $t_p = 0.108$ s, c) Test No. 5, a thick annular disk with $\chi = 3$, $\rho_d/\rho_w = 1.384$, $d_i = 38.1$ mm, $e = 25.4$ mm, $t_p = 0.075$ s,

d) Test No. 11, a thick annular disk with $\chi = 1.5$, $\rho_d/\rho_w = 1.384$, $d_i = 38.1$ mm, $e = 50.8$ mm, $t_p = 0.096$ s.

The cavity formation of a disk with a smaller aspect ratio and lower density (i.e., Test No. 7, $\chi = 1.5$, and $\rho_d/\rho_w = 1.08$) is shown in Figure 2.4b. The central hole in Test No. 5 ($\chi = 3$, and $\rho_d/\rho_w = 1.384$) eliminated the splash around the pipe and caused the cavity to pinch off immediately after entering the water at $t/t_p = 1$ (see Figure 2.4c).

The consecutive images of a relatively thick annular disk with an aspect ratio of $\chi = 1.5$ and density ratio of $\rho_d/\rho_w = 1.384$ (see Table 2.1, Test No. 11) is illustrated in Figure 2.4d. As can be seen in Figures 2.4c and 2.4d, in the annular disks, the pinch-off occurred very close to the water surface due to the elimination of surface seal and less air entrainment occurred due to the position of the pipe. The experimental observations indicated that the crown formation and development of mixing zone are affected by the central hole and release conditions. In the guarded release condition, the pinch-off phenomenon happened earlier in annular disks than that of solid disks. Moreover, the surface splash around the pipe did not form in annular disks since the compressed air moved through the central hole. In addition, the cavity behind the annular disk was smaller than the cavity at the rear of the solid disks. As the pipe is on the water surface in guarded release condition, less air entered the cavity and caused an early pinch-off.

2.3.3 Surface seal and crown characteristics

The images of surface seal formations and pinch-off of disks with different shapes and aspect ratios are shown in Figure 2.5. The shape of surface seals and pinch-off time in solid disks are classified into four different regimes. A Partial Seal (PS) refers to a case where the surface of the crown has a hole, and it is not fully closed (Figures 2.5a and 2.5b). A crown is called Full Seal (FS) if the crown above the water surface is fully sealed (Figure 2.5c). A Partial Seal with a central Jet (PSJ) is formed when an upward jet is pierced through the crown (see Figures 2.5d and 2.5e), and a Full-Seal with a central Jet (FSJ) is formed once an upward jet pierced the fully sealed crown (see Figure 2.5f). As shown in Figure 2.5g, the fully guarded release did not form a surface crown and this case was not included in the regime classification.

The Weka software (Witten and Frank, 2005) was used to correlate the initial release conditions and disk characteristics with the crown and surface seal formation. Accordingly, 24 data points were used for the boundary map and regime classification. Understanding the effects of governing parameters, such as the dimensionless moment of inertia and Froude number on the crown shapes is important for the prediction of disk descending velocity. A regime plot was developed based on the dimensionless moment of inertia, I^*, and impact Froude number, Fr_o, and the results are plotted in Figure 2.5h. A Logistic Model Tree (LMT) classifier from the Weka software was used for boundary visualization. As shown in Figure 2.5h, the Full Seal crown was formed in relatively high values of I^* (i.e., $I^* \geq 0.025$) and small impact Froude numbers (i.e., $Fr_o \leq 3$). In addition, the internal surface jet was formed as the impact Froude number became larger than 2.
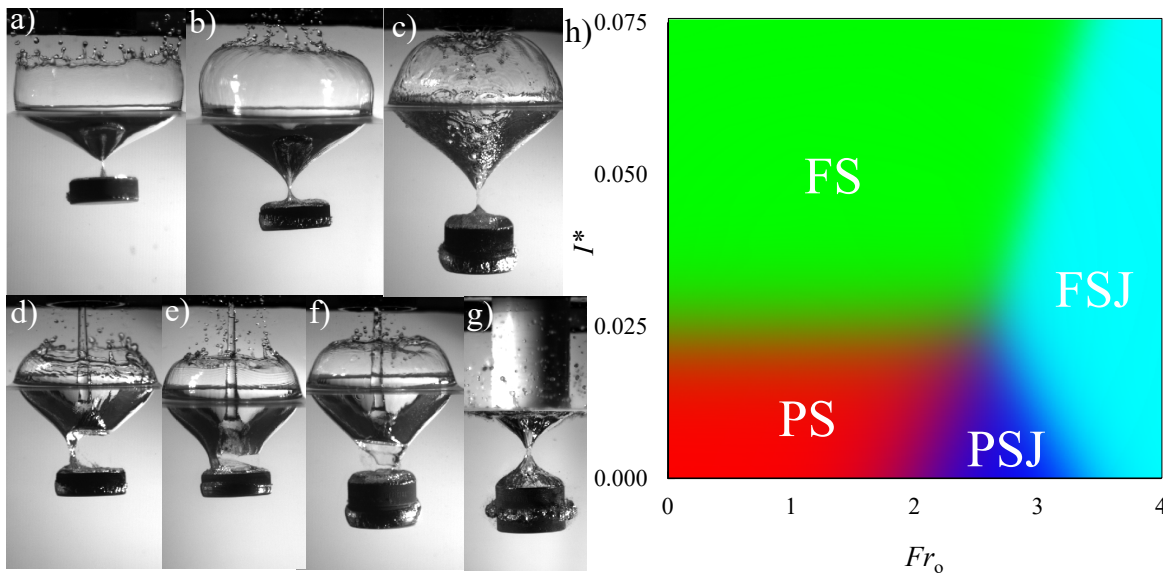
Figure 2.5. Classification of surface seal formation based on disk density and release condition: a) crown formation with a partial surface seal, PS, Test No. 13; b) crown formation of partial surface seal, PS, Test No. 14; c) full surface seal, FS, Test No. 20; d) partial surface seal with a central jet, PSJ, Test No. 17; e) partial surface seal with a central jet, PSJ, Test No. 28; f) full surface seal with a central jet, FSJ, Test No. 22; g) disk entry without a surface seal, Test No. 7; h) a boundary map showing the effects of Froude number, Fr_o, and dimensionless moment of inertia, I^*, on surface seal classifications. The Logistic Model Tree (LMT) classifier was used for boundary classification of the Weka software.

The size of the crown after the impact is important and can provide valuable information about the disk geometry, release condition, and energy losses due to the impact. The size of the crown, including the diameter and height of the crown, and the volume of cavity indicate the amount of water displaced from the surface. The mass displacement indicated the amount of work done by the impact and can be translated to the energy transfer from the disk and the stagnant ambient water. By increasing the impact velocity, more water underneath the disk is going to be displaced by the impact force and created a larger cavity and crown. Therefore, increasing the crown size because of higher impact velocity can be considered as higher energy transfer from disk to water which can be called energy as energy losses.

The correlation between the maximum diameter of surface crown at the pinch-off, D_C, as a function of disk density, ρ_d, is shown in Figure 2.6a. The maximum crown diameter was measured by employing the boundary detection technique of the MatLab software. Disks that traveled a greater distance inside the pipe than in the air (i.e., $h_{\text{pipe}} = 200$ mm $> h_{\text{air}} = 100$ mm) had approximately 40% larger crown diameter due to greater impact velocity as a result of less flow resistance. As can be seen from Figure 2.6a, the crown diameters in annular disks were between 10% and 20% smaller than the corresponding solid disks. This is due to the fact that less air entrainment occurred in disks with a central hole so less water was displaced to form a crown.

The experimental observations revealed that the crown size is correlated with the disk diameter and the impact velocity. Therefore, the diameter of the crown was scaled with the product of impact release height and disk diameter as $D_C/(h_o d_o)^{1/2}$. It should be mentioned that the impact release height, h_o, was obtained based on the calculated impact head as $h_o = V_o^2/2g$. The impact release height also incorporates the effect of the impact Froude number in the estimation of crown diameter. The correlations of normalized crown diameter, $D_C/(h_o d_o)^{1/2}$, with a dimensionless moment of inertia, I^* are shown in Figure 2.6b. The sample image in Figure 2.6b shows the crown formation in Test No. 30 at the pinch-off. As can be seen, annular disks with the same dimensionless moment of inertia generated relatively smaller crown sizes due to the formation of a central cavity jet (see Figures 2.5d and 2.5e).
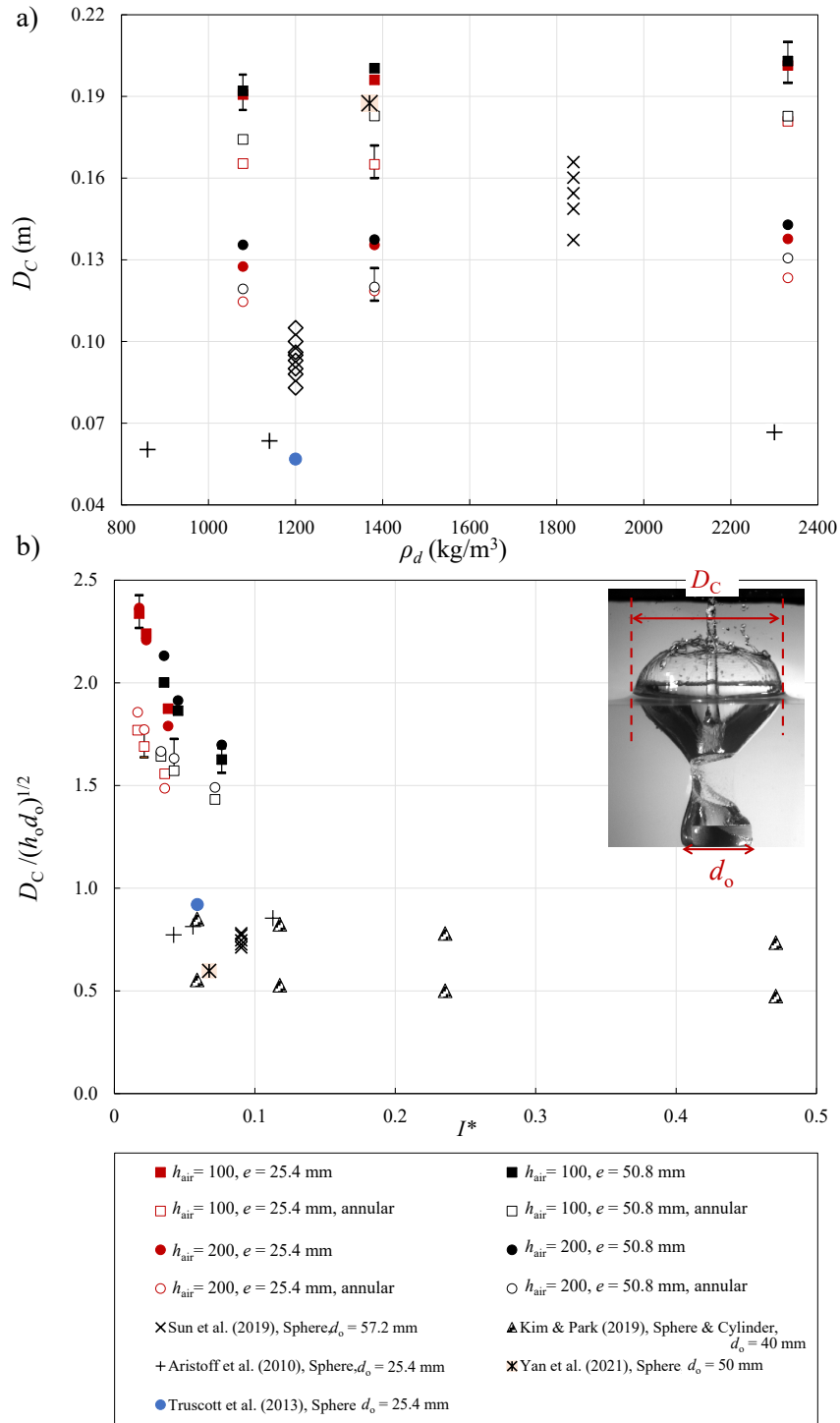
Figure 2.6. Variations of the surface crown diameter, D_C, with the density of disks, ρ_d, for partially guarded release conditions: a) variations of crown diameter, D_C, with the disk density; b) correlations of scaled crown diameter, $D_C/(h_o d_o)^{1/2}$, with the dimensionless moment of inertia, I^*. The sample image shows Test No. 30 at pinch-off, $\chi = 3$, $\rho_d/\rho_w = 2.34$.

The jet directed the splash curtains toward the center and caused smaller crown diameters. The scaled crown diameter in annular disks ranged between 1.45 and 1.85 whereas in solid disks, the normalized crown diameter ranged between 1.60 and 2.35. The results of other related studies were added to Figure 2.6 for comparison. The diamond symbols represent the study of Kim & Park (2019), which shows the crown becomes slightly smaller as the aspect ratio of the object reduced. The results of the dimensionless crown diameter of spheres were between 0.5 and 1, and by increasing the aspect ratio from χ = 1.5 to 3, the non-dimensional crown diameter increased accordingly.

2.3.4 Cavity characteristics at the pinch-off

The snapshot images at the time of pinch-off for an unguarded release condition of h_{air} = 100 mm, and h_{pipe} = 200 mm are illustrated in Figure 2.7. A noticeable difference was found at the pinch-off locations in disks with different densities. As can be seen in disks with ρ_d = 1,079 and 1,381 kgm^{-3}, pinch-off point attached to the top surface of the disk, whereas in the heaviest disk (ρ_d = 2,331 kgm^{-3}), the pinch-off point moved up approximately in the middle of the front of the disk and water surface. In comparison to lighter disks, the heaviest disks descend further down at the time of pinch-off. It was observed that the pinch-off height was moderately correlated with the disk density while the frontal position drastically increased by the density of the disk.

Figure 2.8 shows the effect of object geometry and release conditions on variations of pinch-off depth with impact Froude number. The results related to the previous studies in the literature were added to Figure 2.8 for comparison. Figure 2.8a shows that the pinch-off depth increased with increasing impact velocity and different increment rates were found between the guarded and partially guarded release conditions. As can be seen, all pinch-off depths of the current study related to the guarded release condition in the same Froude number, were smaller than the corresponding tests with partial guarded release conditions. Figure 2.8a shows that the pinch-off depths were also smaller in annular disks in comparison with the corresponding solid disks due to the formation of a central jet in annular disks. In other words, the central hole generates an upward cavity jet, which causes a pinch-off occurs earlier in comparison with the corresponding solid disks. Therefore, solid disks showed larger pinch-off depths with partially guarded release

conditions, which increased by increasing disk density and decreased with the aspect ratio of the disk.

$$\rho_d/\rho_w = 1.08, \quad \rho_d/\rho_w = 1.384, \quad \rho_d/\rho_w = 2.34$$
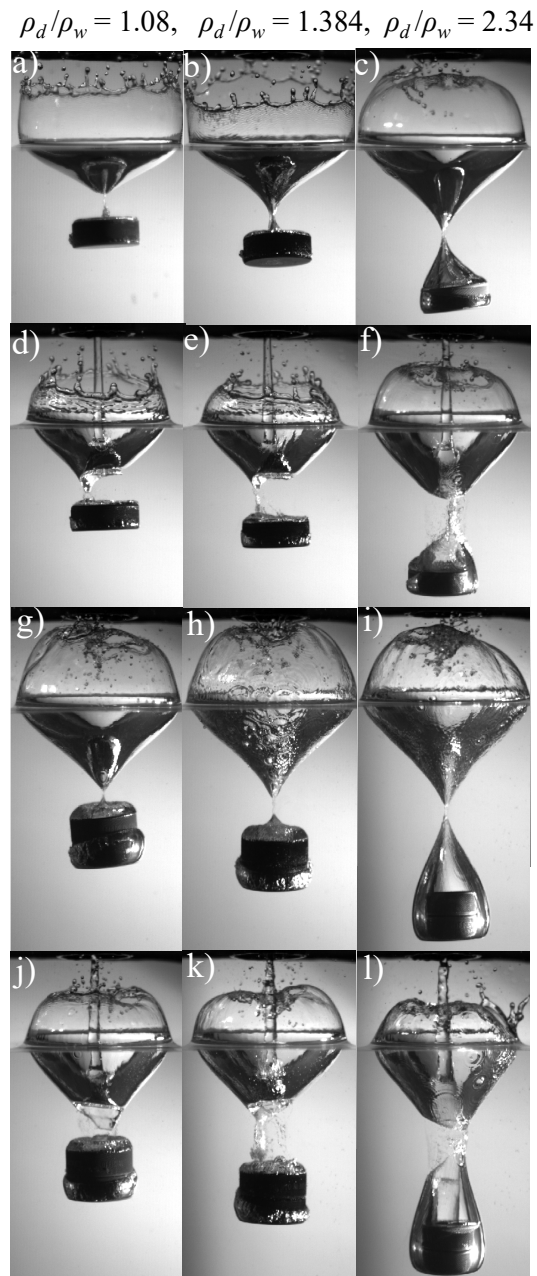
Figure 2.7. Images of the pinch-off (deep seal) for different disks and with partially guarded release condition, $h_{\text{pipe}} = 200$ mm and $h_{\text{air}} = 100$ mm: a) Test No. 13, $t_p = 0.138$ s; b) Test No. 14, $t_p = 0.138$ s; c) Test No. 15; $t_p = 0.142$ s; d) Test No. 16, $t_p = 0.115$ s; e) Test No. 17, $t_p = 0.118$ s; f) Test No. 18, $t_p = 0.126$ s; g) Test No. 19, $t_p = 0.137$ s; h) Test No. 20, $t_p = 0.141$ s; i) Test No.

21, $t_p = 0.147$ s; j) Test No. 22, $t_p = 0.119$ s; k) Test No. 23, $t_p = 0.128$ s; l) Test No. 24, $t_p = 0.130$ s.

In Figure 2.8b, pinch-off depths were normalized with the equivalent radius of the object, Hp/r', whether it's a sphere, disk, or droplet, and the results were plotted versus impact Froude number, Fr_o. The black solid line shows the proposed equation of Glasheen and McMahon (1996) for a force-driven disk (i.e., $Hp/r' = 2.297(V/(gr')^{1/2})$), which is located above all other measurements due to the existence of force. The red solid line illustrates the proposed theoretical model of Duclaux et al. (2007) for a sphere, and the dashed black line represents the theoretical study of Bergmann et al. (2008) for a motor-driven disk (i.e., $Hp/r' = 1.1(V/(gr')^{1/2})$ with a constant speed of $V = 5$ m/s. The solid red line and dashed red curve are the theoretical models by Duaclaux et al. (2007) for sphere, $Hp/r' = 1.6(V/(gr')^{1/2}$ and cylindrical object, $Hp/r' = (6.75(V^2/gr'))^{1/3}$, respectively.

As can be seen in Figure 2.8b, the solid disks results showed a good agreement with the theoretical model of Bergmann et al. (2008). However, the normalized pinch-off depth of disks with the guarded release conditions are approximately 20% smaller than the proposed model, and the annular disks showed higher values by 10% to 15%. The experimental, theoretical, and numerical results related to the previous studies are also added for comparison; Mansoor et al. (2014), Sphere $d_o = 20$ mm; Sun et al. (2019), Sphere $d_o = 57.2$ mm; Aristoff et al. (2010), Sphere $d_o = 25.4$ mm; Yan et al. (2021), Sphere $d_o = 50$ mm; Jalaal et al. (2019), Viscoplastic droplet with an equivalent diameter of $d_o = 3.2$ mm; Zhao et al. (2016), Numerical, Sphere $d_o = 25.4$ mm; Lee & Kim (2008), Sphere $d_o = 1.94$ mm; Speirs et al. (2018), multi-droplet water stream onto a pool of water, sphere droplets $d_o = 3.76$ mm; Kim & Park (2019), Sphere and Cylindrical objects with $d_o = 40$ mm. The experimental results of spheres from Zhao et al. (2016), Mansoor et al. (2014), Aristoff et al. (2010), Kim & Park (2019), Speirs et al. (2018), and Truscott et al. (2013) are mostly less than other theoretical studies depending on the properties of the object. The reason is due to the geometry of the disk, the cavity created by the disk is much larger than the cavity created by a sphere so the pinch-off occurs at a deeper point. In the study of Aristoff et al. (2010), they used spheres with various densities which also affected the pinch-off point as mentioned earlier.
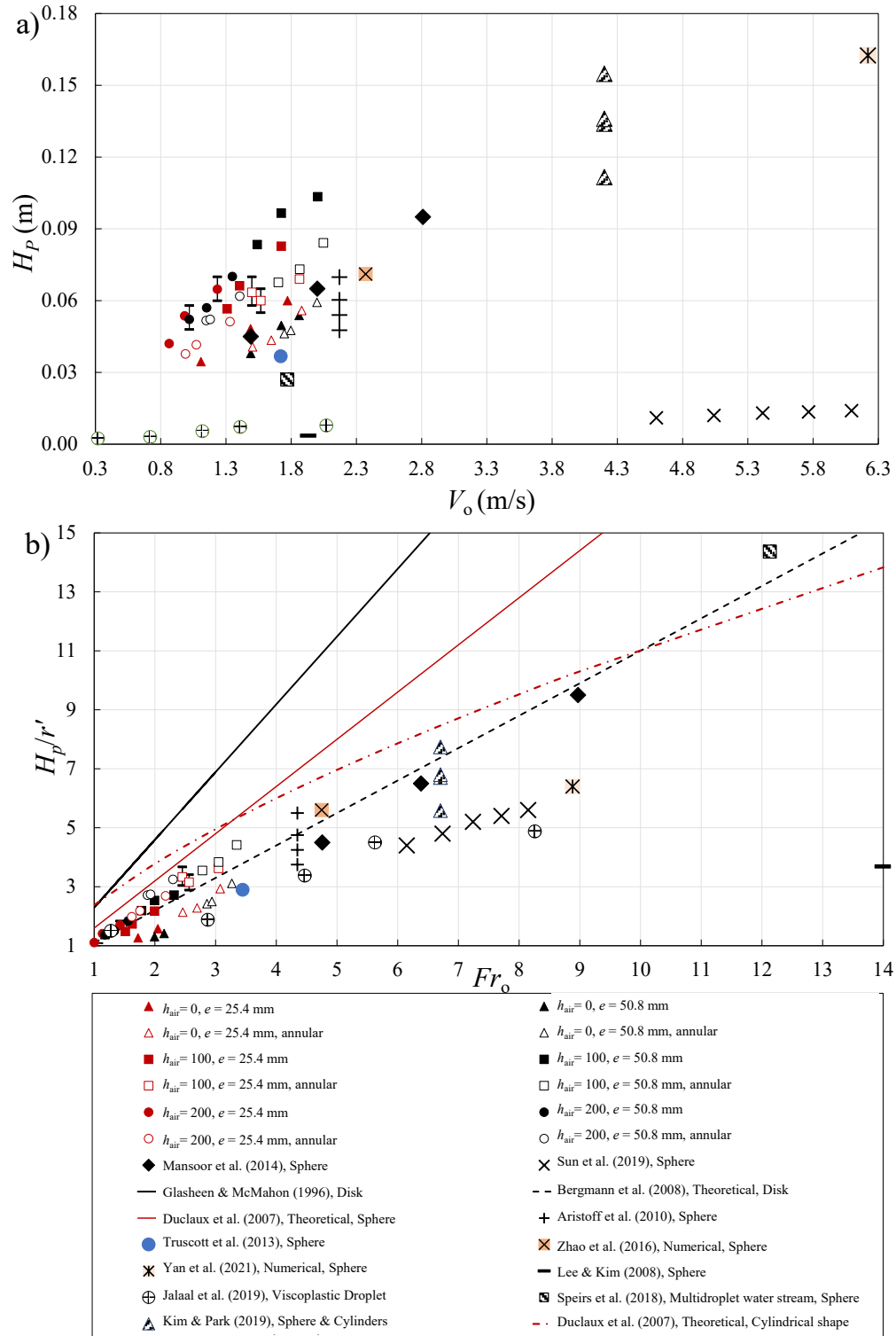
Figure 2.8. Variations of pinch-off depth, H_p, with the impact velocity, V_o, of the disks in different release conditions: a) correlations of pinch-off depth versus impact velocity; b) variations of pinch-off depth scaled with the equivalent disk radius, H_p/r', as a function of impact Froude number, Fr_o.

Solid curve represents data related to the proposed model by Glasheen & McMahon (1996) for a force-driven disk, $Hp/r' = 2.297(V/\sqrt{gr'})$, and dashed curve shows data related to the proposed model ($Hp/r' = 1.1(V/\sqrt{gr'})$) by Bergmann et al. (2008) for a disk entering water with a constant velocity. The solid red line and dashed red curve are the theoretical proposed model by Duaclaux et al. (2007) for sphere, $Hp/r' = 1.6(V/\sqrt{gr'})$, and cylindrical object, $Hp/r' = (6.75(V^2/gr'))^{1/3}$, respectively. Experimental, theoretical, and numerical results related to the previous studies are also added for comparison; Mansoor et al. (2014), Sphere $d_o = 20$ mm; Sun et al. (2019), Sphere $d_o = 57.2$ mm; Aristoff et al. (2010), Sphere $d_o = 25.4$ mm; Yan et al. (2021), Sphere $d_o = 50$ mm; Jalaal et al. (2019), Viscoplastic droplet with an equivalent diameter of $d_o = 3.2$ mm; Zhao et al. (2016), Numerical, Sphere $d_o = 25.4$ mm; Lee & Kim (2008), Sphere $d_o = 1.94$ mm; Speirs et al. (2018), multidroplet water stream onto a pool of water, sphere droplets $d_o = 3.76$ mm; Kim & Park (2019), Sphere and Cylindrical objects with $d_o = 40$ mm. Error bars are added to the results.

As was shown in Figure 2.7, the frontal positions of disks at pinch-off were highly dependent on the disk's density. The center of disk's frontal location at the pinch-off, H_d, was extracted for each test and the pinch-off depth were normalized by that and plotted against the disk's Froude number, Fr_o (see Figure 2.9). It can be seen that the results of theoretical studies are between 0.45 and 0.50, and the aspect ratio and density are also important in variations of data. For example, in the study of Kim & Park (2019), the cylinder with an aspect ratio of $\chi = 0.125$ has the value of $H_p/H_d = 0.95$, whereas this value for a sphere is approximately equal to 0.6. The normalized pinch-off depth in viscoplastic droplets (Jalaal et al., 2019) showed a good agreement with the theoretical models for $Fr_o \leq 3$. However, in higher values of impact Froude numbers the normalized pinch-off depth abruptly increased to approximately 0.85. The results of this study showed that H_p/H_d highly correlated with the aspect ratio, density, and release conditions.
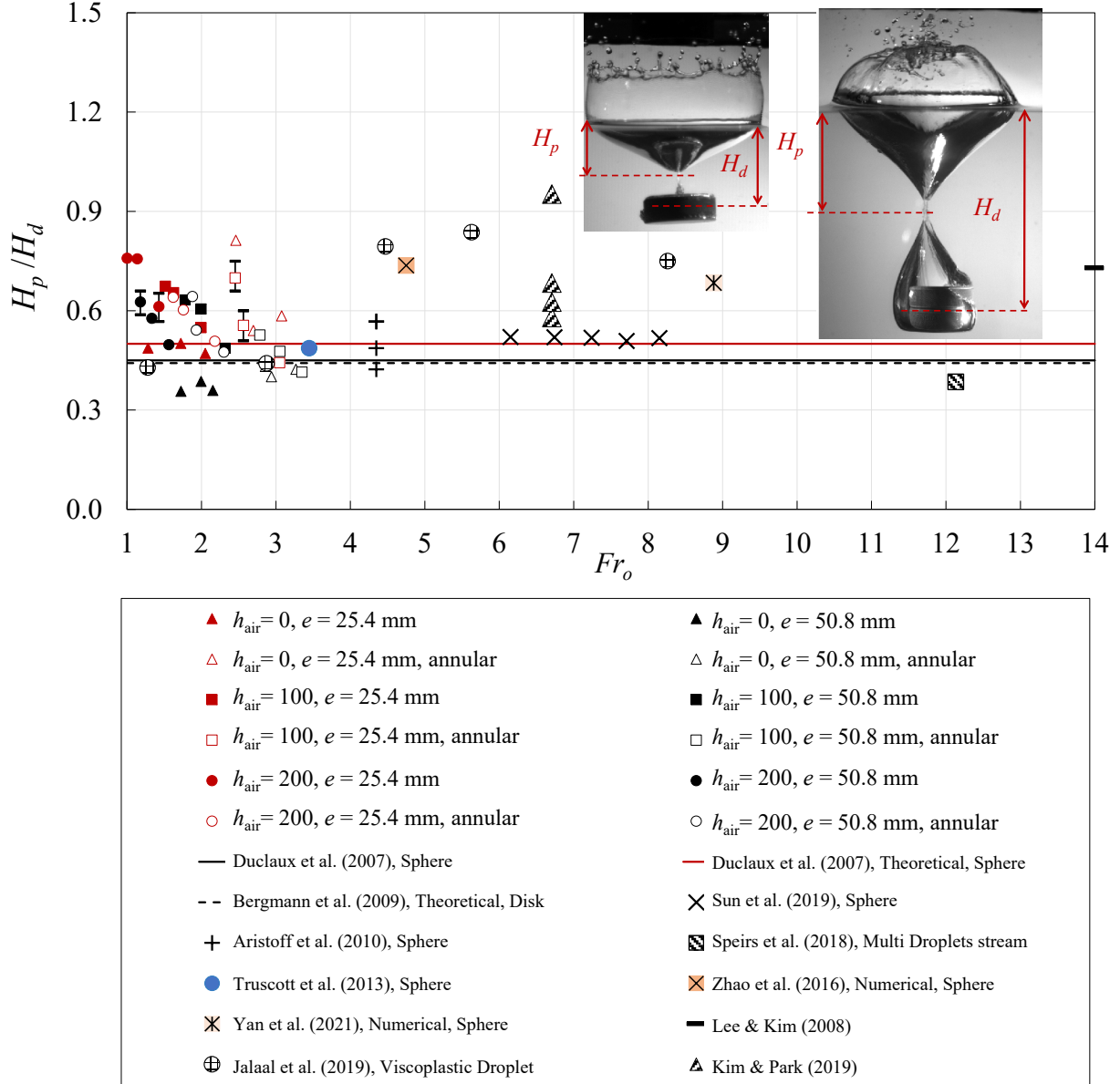
Figure 2.9. Variations of the pinch-off depth, H_P, of the disk to the central position of the disks at pinch-off times, H_d, with the Froude number, Fr_o. Results related to the previous theoretical and experimental studies (spheres, and disks) are also added for comparison. Error bars are added to the results.

The distance between pinch-off depth and the foremost frontal position is considered as the pinch-off thickness. The pinch-off thickness was measured in all tests and the results were scaled by the equivalent release height as $(H_f - H_P)/h'$. The equivalent release height, h', was calculated by considering two coefficients during the guarded and unguarded motions as $h' = \varphi_1 h_{air} + \varphi_2 h_{pipe}$.
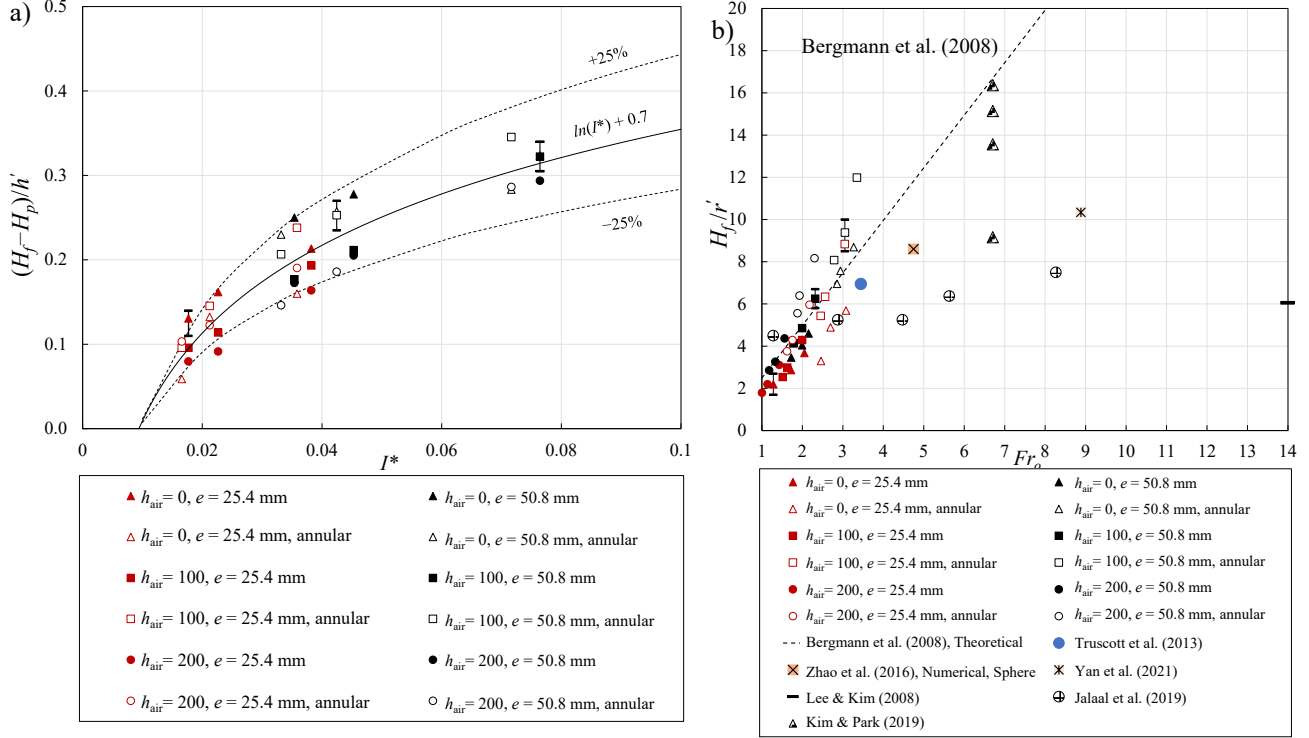
Figure 2.10. a) Variations of the normalized distance of the frontal position of the disks and the pinch-off depth $(H_f - H_p)/h'$ as a function of the non-dimensional moment of inertia of disks, I^*. The solid curve represents the proposed model; b) Variations of frontal position of the disk at pinch-off time scaled by the equivalent disk radius. The solid line represents the theoretical model proposed by Bergmann et al. (2008), $H_f/r' = 2.49(V/\sqrt{gr'})$. Error bars are added to some of the results.

The two coefficients of φ_1 and φ_2 were extracted from the measurements as 0.35 and 1.25, respectively. The variations of the normalized distance between the pinch-off point and frontal position with the dimensionless moment of inertia are shown in Figure 2.10a. The effect of the release condition was considered in the scaling parameter, h'. The variations of normalized pinch-off thickness with I^* can be predicted by a natural logarithm based model ($R^2 = 0.82$) as:

$$(H_f - H_p)/h' = 0.147 \, ln(I^*) + 0.7 \tag{Eq 2.1}$$

The proposed formulation was plotted in Figure 2.10a, and the two dotted curves show the $\pm 25\%$ variations from the proposed model. It can be deduced that regardless of the disk geometry, the normalized pinch-off thickness, $(H_f - H_p)/h'$, increased non-linearly with increasing dimensionless

moment of inertia. The frontal position of the disk was also normalized by the equivalent radius and plotted versus the impact Froude number (see Figure 2.10b). The theoretical model proposed by Bergmann et al. (2008) was added for comparison which showed a good agreement with the experimental data. The results related to the previous studies including spheres and droplets were also added in Figure 2.10b which had fewer values than the studies related to the disk.

The pinch-off time in the entry of solid objects is an important factor for understanding the rate of momentum transfer and energy dissipation rate. The pinch-off time, t_p, for all experiments were extracted from images and the correlations of pinch-off time with impact velocity, V_o, were plotted in Figure 2.11a. The pinch-off time in tests with a guarded release condition was found to be uncorrelated with the impact velocity. On the other hand, the pinch-off times in partially guarded release conditions were very similar and almost independent of impact velocity.

In partially guarded release condition, the annular disks had a relatively shorter pinch-off time (i.e., $t_p \approx 0.12$ s) than the solid disks (i.e., $t_p \approx 0.14$ s). The pinch-off time was normalized by the disk's diameter and gravitational acceleration as $t_p/(d_o/g)^{1/2}$. The variations of dimensionless pinch-off time with impact Froude number are shown in Figure 2.11b, and the results related to previous studies were also added for comparison. As can be seen, most of data from present study were located between the theoretical model of Duclaux et al. (2007) and the proposed model of Glasheen & McMahon (1996). The normalized pinch-off time for the viscoplastic droplets is smaller than other studies due to the properties of the fluid.
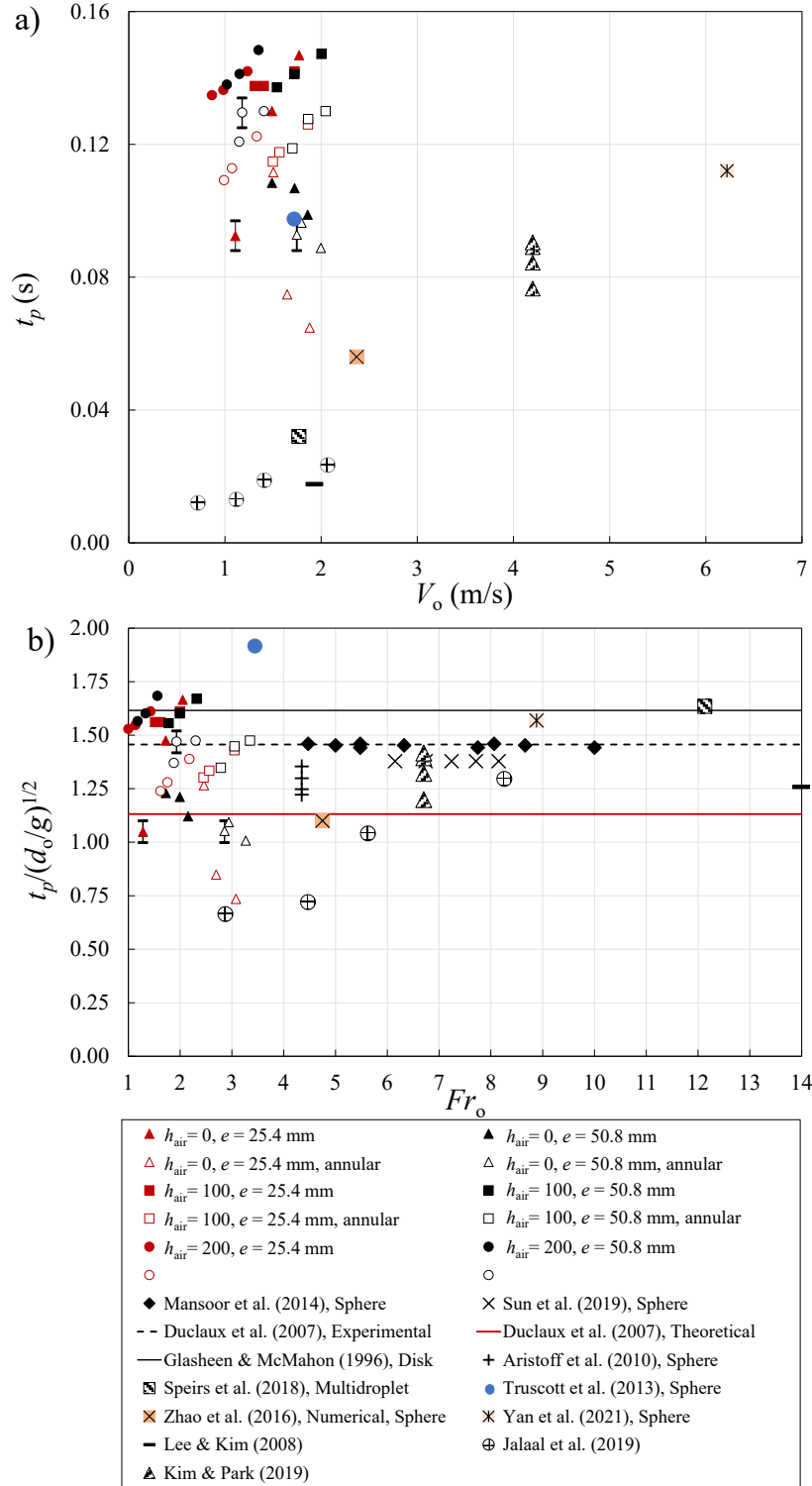
Figure 2.11. Effects of impact velocity, V_o, on variations of pinch-off time, t_p: a) raw data showing the correlation of pinch-off time with impact velocity; b) variations of dimensionless pinch-off time, $t_p/(d_o/g)^{1/2}$, with the impact Froude number, Fr_o. The solid curve represents the proposed

equation. Error bars are added to some of the results.

2.3.5   *Bubble dynamics*

During the water entry, a volume of air was dragged into the water by the disk. The volume and shape of air bubbles were found to be correlated with the disk geometry and release conditions. The deformation and detachment of bubbles from the disk after the pinch-off are illustrated in Figure 2.12. Spherical bubbles were formed at the beginning of the detachment stage. The Helmholtz instability forms an equatorial bulge in bubbles and changes the direction of acceleration (Birkhoff, 1975). Due to bubble acceleration and formation of Helmholtz instability, sphere bubbles were transformed into flattened sheets since they acquire a new asymptotic shape, known as a "spherical-cap bubble" (Davies and Taylor, 1950; Brennen, 1995) as shown in Figure 2.12.

The water entry and bubble formation in the wake of a disk are shown in Test No. 14 with an aspect ratio of $\chi = 3$ and Test No. 8 with an aspect ratio of $\chi = 1.5$ in Figures 2.12a and 2.12b, respectively. A relatively large bubble was detached from the vortex ring at $t = 211$ ms, it was deformed to a flattened bubble after 200 ms from detachment and reached the water surface at $t = 511$ ms after detachment. Two distinct bubbles were separated from the disk, and they rebounded and moved upward (Figure 2.12c). The detachment of bubbles from the vortex ring occurred at $t = 324$ ms and it was surrounded by sprays of microbubbles as illustrated in Figure 2.12d. Once a large bubble was detached from the disk, a jet ejected upward and inside the sphere bubble, which destabilized the bubble and transformed it into a horse saddle inflated bubble sheet. Figure 2.12 indicated that disks with a similar diameter, but a larger thickness (smaller aspect ratio) produced larger bubbles with a final deformation shape of a horse saddle whereas the medium-size bubbles deformed into spherical-cap bubbles. It was also observed that small bubbles were not able to form a flattened sheet, therefore, they just deformed into the ellipsoid while they rise to the water surface.
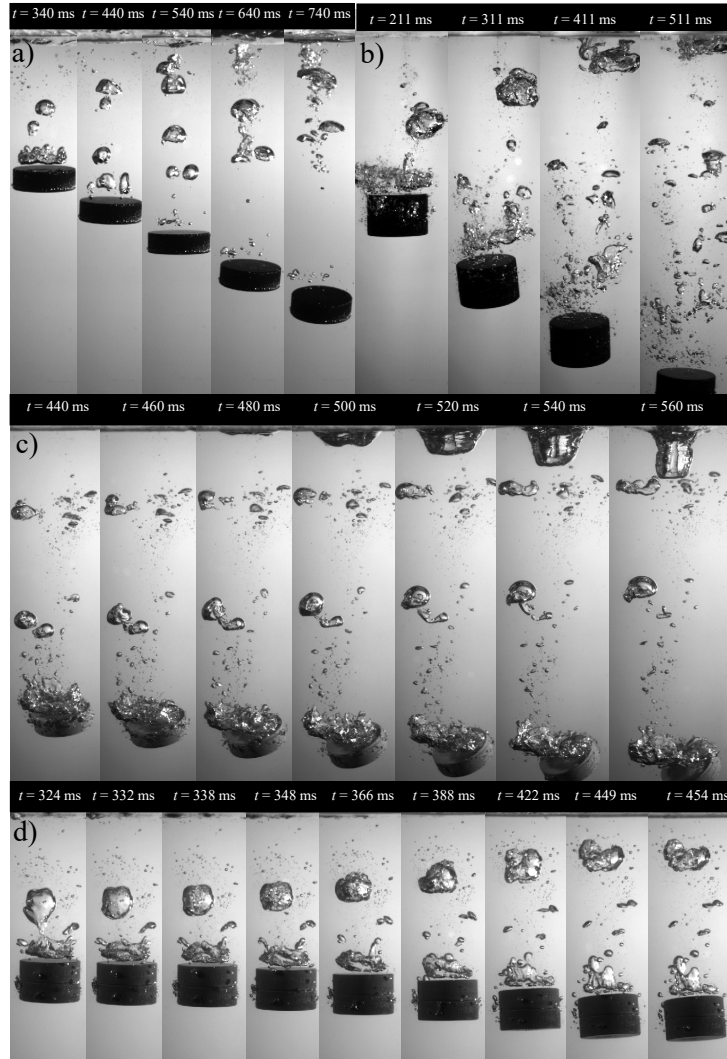
Figure 2.12. Time history images on bubble formation after pinch-off: a) sequence images of Test No. 14, $d_i = 0$, $e = 25.4$ mm, $\rho_d/\rho_w = 1.384$, $h_{pipe} = 200$ mm and $h_{air} = 100$ mm; b) sequence images of Test No. 8, $d_i = 0$, $e = 50.8$ mm, $\rho_d/\rho_w = 1.384$, $h_{pipe} = 300$ mm and $h_{air} = 0$; c) sequence images of Test No. 27, $d_i = 0$, $e = 25.4$ mm, $\rho_d/\rho_w = 2.34$, $h_{pipe} = 100$ mm and $h_{air} = 200$ mm; d) sequence images of Test No. 31, $d_i = 0$, $e = 50.8$ mm, $\rho_d/\rho_w = 1.08$, $h_{pipe} = 100$ mm and $h_{air} = 200$ mm.

2.3.6   Disk and ambient velocities

The vertical velocities of disks at three different stages during water entry were measured. The impact velocity, V_o, of the disk was measured during the impact with the water surface and until the disk was fully entered into the water.
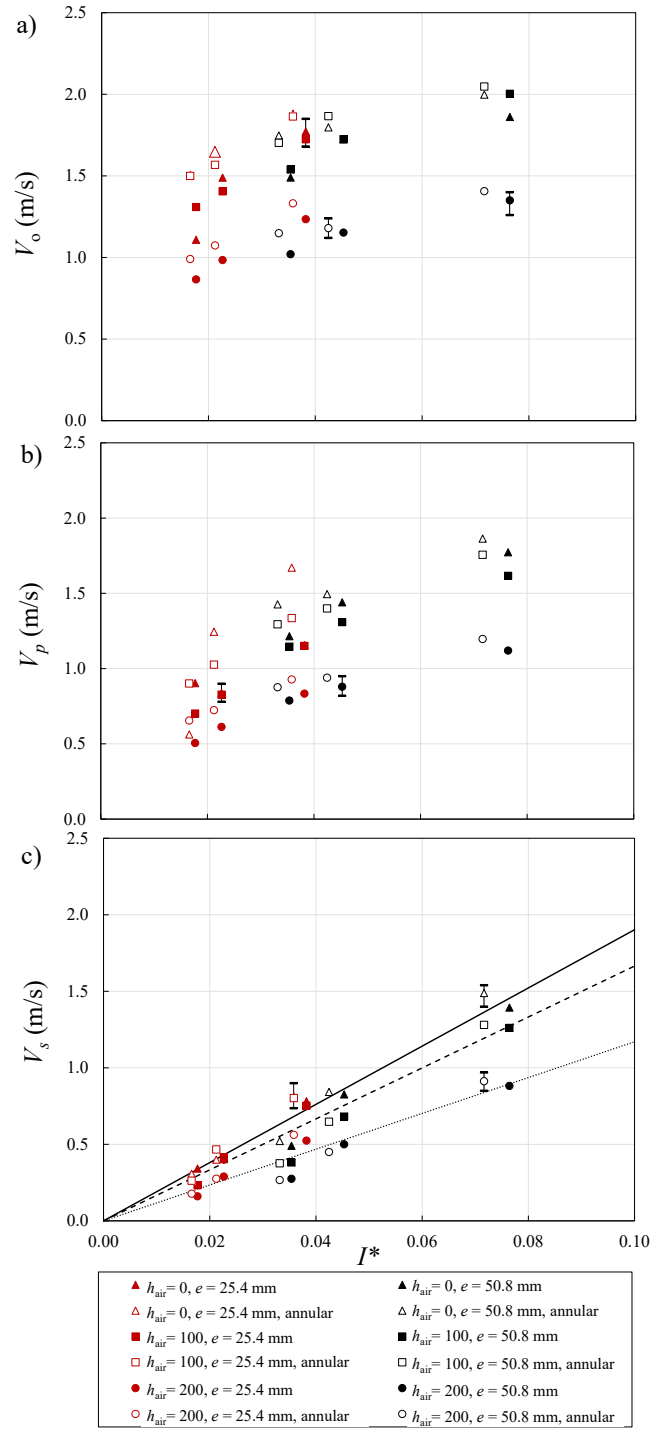
Figure 2.13. Variations of disk frontal velocities in different phases of motion with the dimensionless moment of inertia, I^*: a) variations of impact velocity, V_o, with I^*; b) correlations of pinch-off velocity, V_p, with I^*; c) variations of settling velocity, V_s, with I^*. The solid line, dashed line, and dotted line represent the proposed models for prediction of settling velocity for

guarded h_{air} = 0, unguarded with h_{air} =100 mm, and unguarded with h_{air} = 200 mm release conditions, respectively. Error bars are added to some points.

The variations of impact velocity with the dimensionless moment of inertia are shown in Figure 2.13a. The impact velocity increased by increasing I^* for both annular and solid disks and ranged between 0.86 ms^{-1} and 2.05 ms^{-1}. Figure 2.13b depicts the variations of disk's velocity at the pinch-off, V_P, indicating that pinch-off velocities were relatively smaller than impact velocities and ranged between 0.5 ms^{-1} and 1.86 ms^{-1}. The velocity of disks reduced after the pinch-off and approached the settling velocity of disk, V_s. Figure 2.13c shows the correlations of settling velocity, calculated after the pinch-off and at a point where the disk descended at a constant velocity, with I^* for both annular and solids disks with different release conditions. As can be seen, settling velocities increased linearly with I^* and ranged between 0.15 ms^{-1} to 1.5 ms^{-1}. The slopes of linear equations were 19.03, 16.65, and 11.70 for fully guarded h_{air} = 0, partially guarded release conditions with h_{air} =100 mm, and h_{air} = 200 mm, respectively. The coefficients of determination (R^2) for the proposed equations for h_{air} = 0, 100 mm, 200 mm were 0.99, 0.97, and 0.98, respectively.

The reduction in the acceleration of cylindrical disks due to water entry is directly correlated with the impact force and it is important to understand the effects of controlling parameters on variations of the impact force and momentum transfer during the impact. The acceleration reduction, a, was calculated between the time of disk entry and pinch-off and the results were normalized with the acceleration due to gravity, g. Figure 2.14 shows the effect of release height and disk aspect ratio on variations of normalized acceleration with the dimensionless moment of inertia, I^*. The high value of acceleration reduction, a, indicates less momentum transfer and the impact force becomes negligible when a/g approaches unity. On the other hand, the low values of a/g indicate that a great percentage of acceleration reduction caused the impact force. As can be seen in Figure 2.14, the acceleration reduction linearly decreased with I^* and the highest de-acceleration occurred in disks with the highest pipe release height. The correlation between normalized acceleration reduction and I^* for disks that are released from the water surface is shown by a solid line indicating more sensitivity with I^* and the proposed equation for this condition is expressed as $a/g = -9.6(I^*) + 1$ with $R^2 = 0.8$.
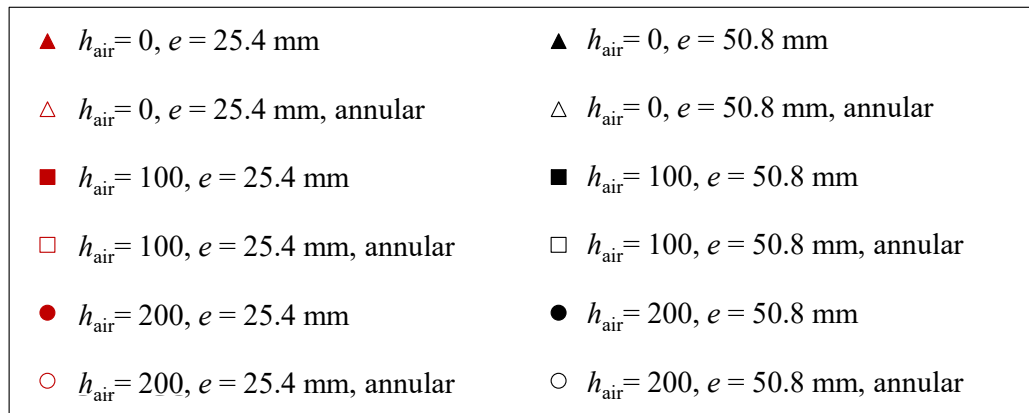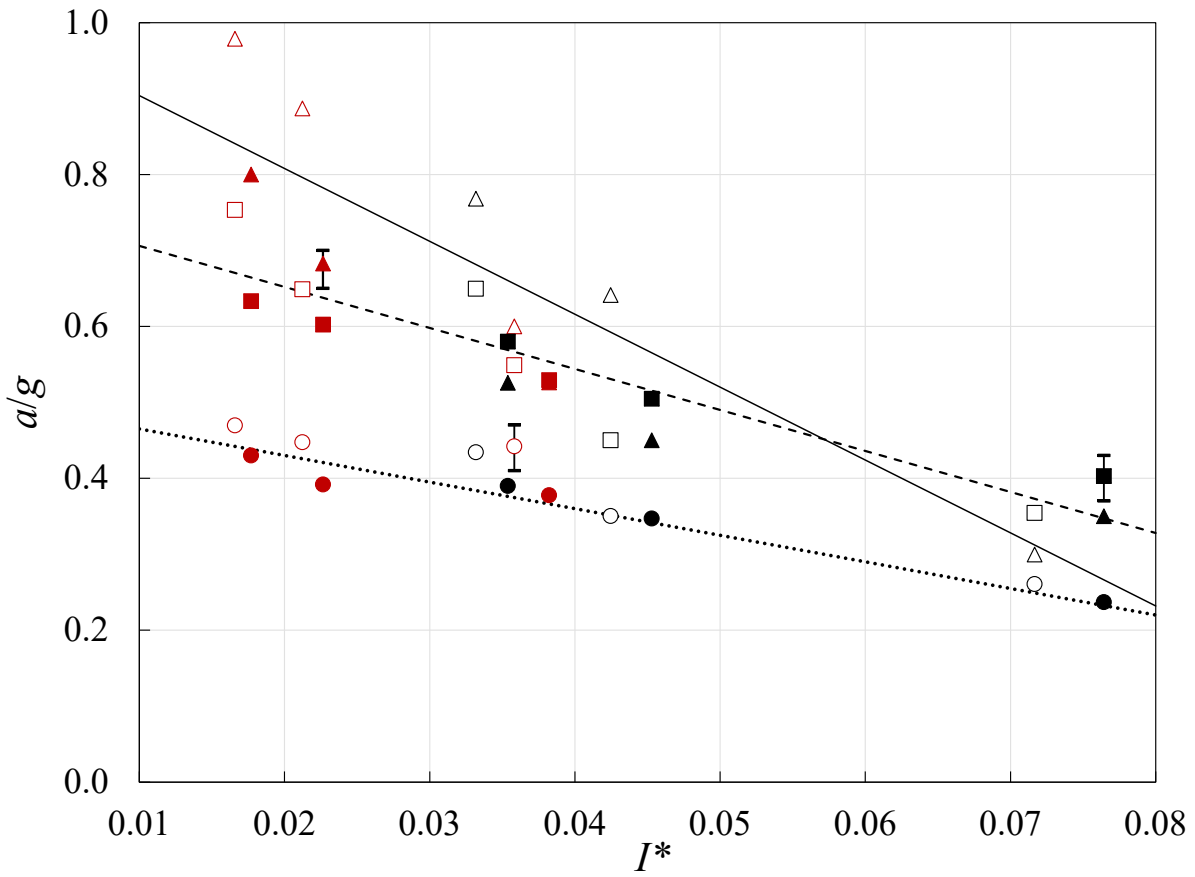
Figure 2.14. Variations of the non-dimensional acceleration reduction in free-falling disk, a/g, with the dimensionless moment of inertia, I^*. The solid line represents the results related to $h_{air} = 0$, the dashed line shows the results for $h_{air} = 100$ mm, and the dotted line represents the results related to $h_{air} = 200$ mm.

The release height increased the acceleration reduction and consequently the impact force and momentum transfer from the disk to the ambient water. However, the variations of I^* had less impact on variations of acceleration reduction and impact force. The proposed equations for correlation of a/g with I^* for the release heights of h_{air} = 100 mm and 200 mm are $a/g = -5.4(I^*) + 0.75$ with $R^2 = 0.83$ and $a/g = -3.5(I^*) + 0.5$ with $R^2 = 0.88$, respectively.

The instantaneous velocity fields around the disks were measured by utilizing the Particle Image Velocimetry (PIV) technique. The time-averaged radial velocity fields around solid and annular disks were extracted from the PIV data for Tests No. 1 to No. 6 and the results were shown in Figure 2.15. The contour plots of time-averaged radial velocity field for solid (left column) and annular (right column) disks in the fully guarded release condition, $\chi = 3$, $t = 1.5t_p$, and with different disk densities, representing the Chaotic, Tumbling and the boundary between the two regimes, are shown in Figure 2.15. The contour plots were obtained by averaging the 10 frames after and 10 frames before the selected time ($t = 1.5t_p$), which is equivalent to 0.04 s. The velocity fields were found very agitated at the pinch-off due to formation of jets and bubbles attaching the disk resulting in significant light reflections. Therefore, the time frames were selected after the pinch-off time and at $t = 1.5t_p$. The density differences in disks are graphically represented by grayscale so, light gray represents $\rho_d = 1,079$ kgm^{-3}, medium gray represents $\rho_d = 1,381$ kgm^{-3}, and dark gray represents $\rho_d = 2,331$ kgm^{-3}. The color in the legend shows the range of radial velocity between -0.5 ms^{-1} and 0.5 ms^{-1}.

The radial velocity field was found to be approximately axisymmetric around the disks. The water beneath the falling disk swept away during the downward motion of disks and the displaced water moved to the sides and formed a pair of vortices. The left column in Figure 2.15 shows the radial velocity field in solid disks. The intensity of radial motions was correlated with the density of disks and denser disks affected more ambient water. For example, the averaged radial velocity around the heaviest disk ($\rho_d = 2,331$ kgm^{-3}) was approximately two times the lightest disk with $\rho_d = 1,079$ kgm^{-3}. The right column in Figure 2.15 shows the radial velocity fields around annular disks with different densities. More eddies were generated in the wake of annular disks in comparison with the solid disks of the same density. Figure 2.15f shows a vortex pair next to the edges of central hole indicating the entrainment of ambient water through the hole. Furthermore, the intensity of

radial velocity at the wake of annular disk in Figure 2.15f was found to be smaller (i.e., $|u| \leq 0.2$) than the corresponding solid disk (i.e., $|u| \geq 0.5$, Figure 2.15c).
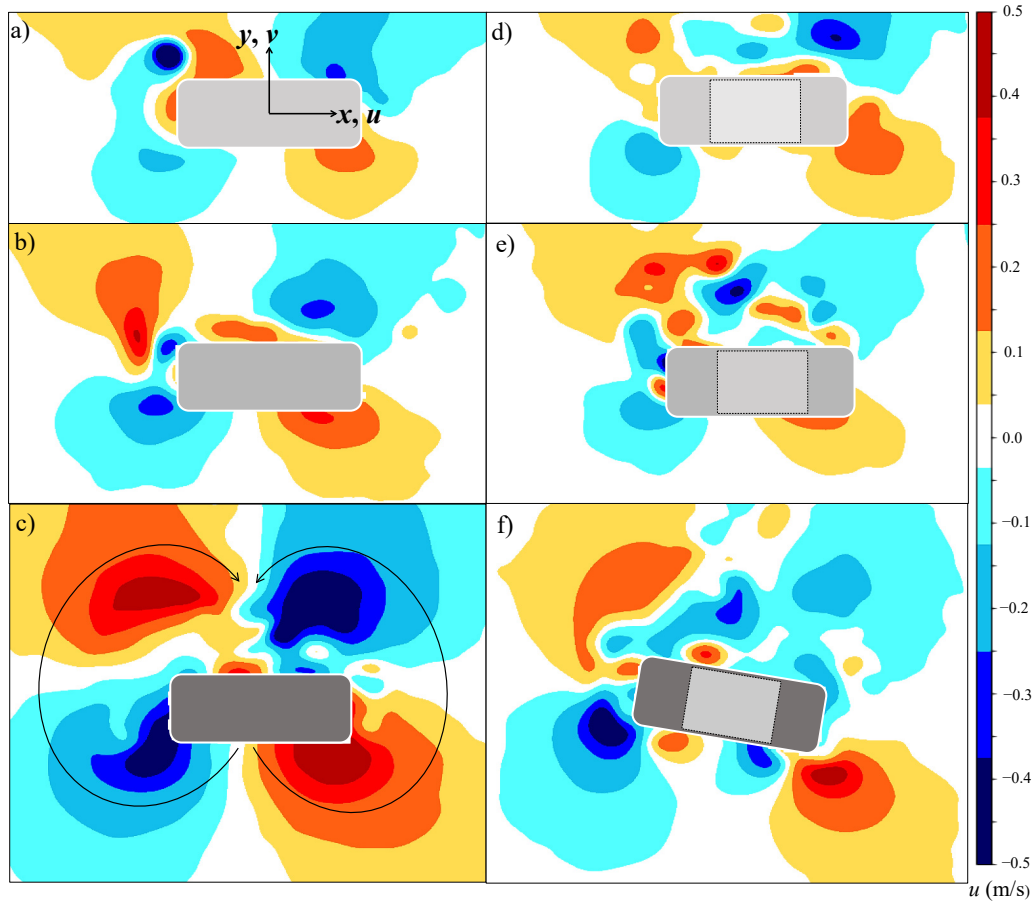
Figure 2.15. Effects of disk density and geometry on contour plots of radial velocity, u, in fully guarded release condition, $h_{pipe} = 300$ mm, $h_{air} = 0$: a) Test No. 1, $\rho_d = 1{,}079$ kg/m^3, $d_i = 0$, $d_o = 76.2$ mm; b) Test No. 2, $\rho_d = 1{,}381$ kg/m^3, $d_i = 0$, $d_o = 76.2$ mm; c) Test No. 3, $\rho_d = 2{,}331$ kg/m^3, $d_i = 0$, $d_o = 76.2$ mm; d) Test No. 4, $\rho_d = 1{,}079$ kg/m^3, annular disk, $d_i = 38.1$ m, $d_o = 76.2$ mm; e) Test No. 5, $\rho_d = 1{,}381$ kg/m^3, $d_i = 38.1$ mm, $d_o = 76.2$ mm; f) Test No. 6, $\rho_d = 2{,}331$ kg/m^3, $d_i = 38.1$ mm, $d_o = 76.2$ mm.

The contour plots of the vertical velocity field for the same tests and locations as described in Figure 2.15 for radial velocity variations are shown in Figure 2.16. The measured vertical velocity ranged between -1 ms^{-1} (downward motion) and 1 ms^{-1} (upward motion). As can be seen, the vertical velocity field increased with increasing the density of disks and the affected ambient water

was larger in solid disks. The averaged vertical velocities around the heaviest disk ($\rho_d = 2,331$ kgm^{-3}) were approximately four times the lightest disk with $\rho_d = 1,079$ kgm^{-3}.

As can be seen in Figure 2.16, the major area in vertical velocity fields moved downward and small areas had shown upward motion due to formation of shear flow and counter-clockwise vortices at the side of the disks. The PIV analysis also detected the presence of a central hole, which can be seen as a small upward velocity region in Figure 2.16f. A comparison between Figures 2.16c and 2.16f indicated that the peak downward velocity field did not form in annular disks and the velocity distribution pattern changed in annular disks.
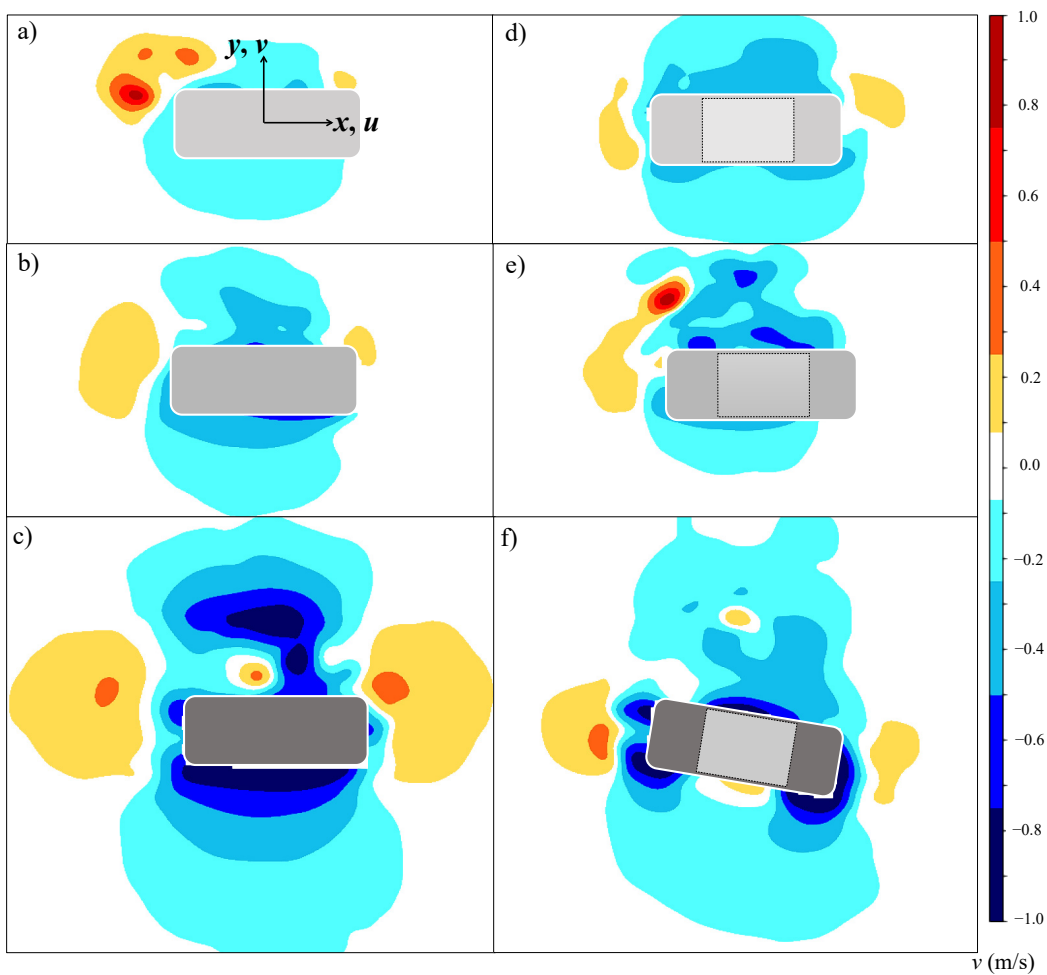
Figure 2.16. Effects of disk density and geometry on contour plots of axial velocity, v, in fully guarded release condition, $h_{pipe} = 300$ mm, $h_{air} = 0$: a) Test No. 1, $\rho_d = 1,079$ kg/m^3, $d_i = 0$, $d_o = 76.2$ mm; b) Test No. 2, $\rho_d = 1,381$ kg/m^3, $d_i = 0$, $d_o = 76.2$ mm; c) Test No. 3, $\rho_d = 2,331$ kg/m^3, $d_i = 0$, $d_o = 76.2$ mm; d) Test No. 4, $\rho_d = 1,079$ kg/m^3, $d_i = 38.1$ mm, $d_o = 76.2$ mm; e) Test No. 5, $\rho_d =$

1,381 kg/m³, d_i = 38.1 mm, d_o = 76.2 mm; f) Test No. 6, ρ_d = 2,331 kg/m³, d_i = 38.1 mm, d_o = 76.2 mm.

Vorticity strength around solid and annular disks was calculated from the radial and vertical velocity vectors and the contour plots of vorticity fields were prepared for Tests No. 1 to 6 (see Figure 2.17). The maximum clockwise and counter-clockwise vortex rotations were approximately 60 Hz. The vortex fields were approximately symmetrical and vortex strength increased with increasing disk density. A comparison between solid and annular disks indicates that more ambient water was affected by the vortex field around annular disks in comparison with the solid disks. Vortices in the wake of annular disks covered a larger area but the generated eddies were relatively smaller in annular disks.

Figure 2.17b shows an axisymmetric vortex structure that was created around the solid disk whereas periodic vortex shedding was formed at the wake of the annular disk with the same density (Figure 2.17e). The vortex structure around the heaviest solid disk is shown in Figure 2.17c. Two large counter-rotating vortices were formed which wrapped the disk with a thickness equal to half of the disk diameter. A pair of small vortices were observed at the wake of the disk, which may be the reason for bubble detachment at the top surface of the disk. Figure 2.17f shows the vortex field around the heaviest annular disk indicating that a vortex ring was formed at the edge of the disk and the hole. A train of vortex shedding was observed in the wake of the annular disk, which is compatible with the observations of Vincent et al. (2016) on the motion of annular thin disks. Moreover, the vortex circulations above the falling disks and the tilting in the annular disk in the tumbling regime are compatible with the results of Vincent et al. (2016). The maximum and minimum values of the vorticity were between −60 and 60 s⁻¹ which are similar to the results reported in the study of Vincent et al. (2016). The tilting in tumbling regime is a natural characteristic of the disk (as shown by Vincent et al. 2016) and the central hole increased the rotation of the disk as well. However, the rate of tilting of a disk (i.e., the angular velocity of the disk) was very small which makes the effect of angular velocity on the flow field negligible.
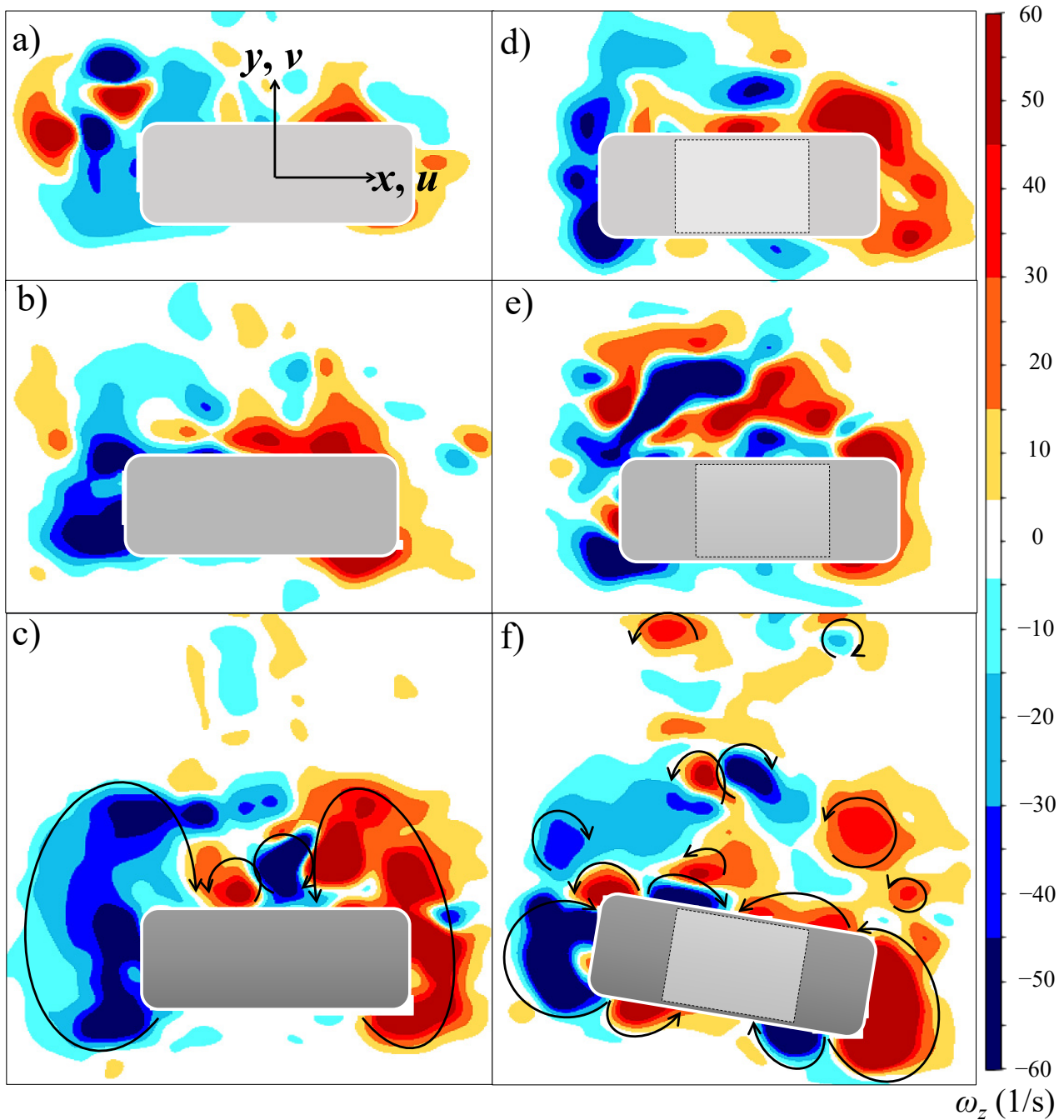
Figure 2.17. Effects of disk density and geometry on the instantaneous vorticity contours, $\omega_z =$ $(dv/dx - du/dy)$, in fully guarded release condition, $h_{pipe} = 300$ mm, $h_{air} = 0$: a) Test No. 1, $\rho_d =$ 1,079 kg/m^3, $d_i = 0$, $d_o = 76.2$ mm; b) Test No. 2, $\rho_d = 1,381$ kg/m^3, $d_i = 0$, $d_o = 76.2$ mm; c) Test No. 3, $\rho_d = 2,331$ kg/m^3, $d_i = 0$, $d_o = 76.2$ mm; d) Test No. 4, $\rho_d = 1,079$ kg/m^3, $d_i = 38.1$ mm, $d_o =$ 76.2 mm; e) Test No. 5, $\rho_d = 1,381$ kg/m^3, $d_i = 38.1$ mm, $d_o = 76.2$ mm; f) Test No. 6, $\rho_d = 2,331$ kg/m^3, $d_i = 38.1$ mm, $d_o = 76.2$ mm.

2.4.   Conclusions

The results of experimental investigation of free-falling thick disks and the subsequent phenomena for hydrophobic disks with different characteristics have been presented. Using a pipe for the guarded release mechanism, three release conditions including fully guarded and two partially guarded release conditions were designed. The ranges of dimensionless moment of inertia and Reynolds number in this study were identified along with the previous studies. The high-resolution sequential images were used to investigate the cavity dynamics and crown formation of cylindrical solid and annular disks. Moreover, the cavity and crown formations for solid and annular disks with different release conditions and aspect ratios were investigated in chaotic, tumbling and the boundary between chaotic and tumbling regimes. Important phenomena including pinch-off depth and time, and frontal position of disks with different geometries were measured at the pinch-off and the pinch-off time and depth in annular disks were found to be shorter due to the formation of a central cavity jet.

The release conditions have shown significant differences in cavity development and variations in pinch-off time and depth. In the fully guarded release condition, water surface splash and crown were not formed and the pinch-off of the cavity occurred earlier than the tests with unguarded release conditions. The crown characteristics such as crown diameter, and shape were extracted from the measurements. The normalized crown diameter was found to be correlated with the dimensionless moment of inertia. The results indicated that the crown diameters in the annular disks were between 10% and 20% smaller than that of the crown diameters in solid disks. The surface seal in crown formation was classified into four distinct regimes named as Partial Seal (PS), Fully Seal (FS), Partial Seal with a central Jet (PSJ), and Fully Seal with a central Jet (FSJ). It was found that the crown seal regimes were correlated with the impact Froude number and dimensionless moment of inertia. The results were found to be sensitive to the disk entry regime (i.e., chaotic versus tumbling), aspect ratio, and the existence of a central hole.

The frontal positions of disks at the pinch-off were measured and the results were plotted for different disks entry regimes. It was found that reducing the aspect ratio by half doubled the frontal position of the disk. Moreover, the growth rate of normalized distance between the frontal position and pinch-off depth followed a natural logarithm correlation. The frontal position of the disk was

also normalized by the equivalent radius and the results were compared with the theoretical model proposed by Bergmann et al. (2008) indicating a good agreement with the experimental data.

The velocities of disks at three phases of free-falling named impact, pinch-off, and settling velocities were obtained in this study. The settling velocity of disks was found to be highly dependent on the release conditions. The settling velocity of disks in the guarded release condition ($h_{air} = 0$) was found to be the highest among the three releasing conditions. In the unguarded release conditions, the settling velocity was smaller in tests with $h_{air} = 200$ mm than in the tests with $h_{air} = 100$ mm since the free-falling in the air significantly dampened the velocity of disks. The radial and vertical velocity fields around solid and annular disks were measured and vortex structures at the wake of disks with different densities were extracted from the PIV data. It was found that the velocities and vorticity fields strengthened by increasing the disk's density. Also, the vortex shedding was more prominent in quantity in the wake of the annular disks in comparison to the solid disks, where large axisymmetric vortices were formed.

Chapter 3

3. Effects of impact energy on the crown formation and underwater cavity of free-falling thick disks

3.1. Introduction

The water entry of a solid object is a complex fluid dynamics problem and has many practical applications in the military, industry, sports, marine and aerospace engineering (May, 1975; Kapsenberg, 2011; Abrate, 2013; Seddon & Moatamedi, 2006; Aristoff et al., 2010; Janati et al., 2022, Janati & Azimi, 2023). The pioneering work of Worthington (1882; 1908) and Worthington and Cole (1897; 1900) elucidated the water entry process by the careful analysis of images taken from a solid sphere that was dropped into a stagnant water. The surface properties of spheres including hydrophilic and hydrophobic states were also found to be very important in cavity development. During the water entry, a free-falling solid object instantly experiences a sudden density change from gas to the surrounding liquid. A series of subsequent phenomena occur below and above the liquid surface which is influenced by a wide range of parameters including the object's geometry and density, surface roughness of the object, and the initial released energy.

The cavity dynamics of a solid sphere that occurs below the water surface have been extensively investigated under various conditions (Duclaux et al., 2007; Gekle et al., 2009a, b; Gaudet, 1998; Aristoff and Bush, 2009; Truscott and Techet, 2009; Truscott et al., 2012; Marston et al., 2012; Mansoor et al., 2014; Marston et al., 2016; Tan et al., 2016; Zhou et al., 2021; and Rabbi et al., 2021). Upon the insertion of a solid object into a stagnant water, a cavity is formed followed by crown formation, surface seal, and pinch-off phenomenon (Eshraghi et al., 2020). Eshraghi et al. (2020) experimentally investigated the splash formation by a solid sphere and investigated the interplay between gravity, cavity pressure difference, and surface tension to control the occurrence of surface seal. An analytical model was developed to describe the trajectory and splash curtain dynamics. To evaluate the effects of initial energy on cavity dynamics,

hydrophobic spheres with different densities of ρ_s/ρ_w ranged between 1.18 and 19.3, and a wide range of sphere diameters, d_o, ranged between 9.525 mm and 19.05 mm with impact velocities ranged from 2.0 m/s to 6.0 m/s were used. The cavity characteristics were found to be highly dependent on the initial energy and sphere's surface condition.

Most recently, crown and splash formations of solid spheres, which occur above the water surface, were considered by Sun et al. (2019) and Zhang et al. (2022). Sun et al. (2019) investigated the free fall of spheres into water at different release heights, which resulted in various initial and impact energies. The parameters related to the pinch-off of a cavity are the pinch-off depth and time. Variations of those parameters with different impact energy were extracted and the results were compared with spheres fall into water and passing through a layer of viscous fluid. It was found that the viscous layer substantially modifies the splash and cavity formation above the free water surface. The immiscible layer develops a double-layer splash structures while the splash crown is continuous for the well-studied corresponding case of water entry. Recent studies on the energy dissipation of sand particles passing through an immiscible layer and through viscous ambient were also shown comparable features to the water entry of solid spheres (Mohammadidinani et al., 2017; Azimi, 2019; Manzouri and Azimi, 2019; Janati et al., 2022).

An analytical model was developed to understand the mechanism of surface seal splash of a solid wedge that impacts a quiescent water (Wang et al., 2022). The effect of surface tension, drag and gravity forces, and aerodynamic pressure were assessed. It was found that the aerodynamic pressure plays a significant role in crown evolution. Jackson et al. (2011) studied the effect of impact energy on the crown evolution of solid spheres by implementing shadow photography technique. The results showed that, by accelerating a solid sphere, the pressure drop increased inside the crown and once the pressure drop surpassed a critical value, it caused the crown to seal or formed a dome over the cavity above the water surface. Mansoor et al. (2014) confirmed the early study of May (1951) and found that the crown and underwater cavity in solid spheres are linked to each other even though the crown and underwater cavity are formed by different mechanisms.

Despite numerous studies on water entry and splash formation by solid spheres, limited studies focused on the effects of initial energy on cavity dynamics, pinch-off, and crown formation of free-

falling disks. Previous studies (Willmarth et al., 1964; Field et al., 1997; Zhong et al., 2011; Vincent et al., 2016; Bi et al., 2018; Xu et al., 2021) mainly focused on prediction of landing location of a disk falling under the effect of gravity and aerodynamic forces. The dimensionless moment of inertia ($I^* = I_{disk}/\rho_f d_o^5 = \pi\rho_d e/64\rho_f d_o$), Reynolds number ($Re = \rho_f V d_o/\mu = V d_o/\nu$), and aspect ratio of the disk ($\chi = d_o/e$), where I_{disk} is the moment of inertia of the disk, ρ_d is the disk density, ρ_f is the fluid density, μ is the fluid dynamic viscosity, d_o is the disk diameter, e is the disk thickness, and V is the mean vertical velocity of the disk, have been used to study the effect of controlling parameters on variations of descending trajectory of thin disk. Auguste et al. (2013) studied the trajectory of free-falling thin disks and found that the disk aspect ratio is an important element in variations of descending path of the disks. Glasheen and McMahon (1996) investigated the vertical water entry of thin disks with low Froude number, $Fr = u^2/(gr)$ where u is the velocity of thin disk, r is the disk radius and g is the gravitational acceleration. The impact Froude number ranged from 1 to 80 and disk radius, r, ranged between 12.7 mm and 30.7 mm. A non-linear relationship was proposed between the pinch-off time and the disk's radius as $t_P = 0.729r^{0.5}$. Glasheen and McMahon (1996) developed a model to predict the normalized pinch-off depth, H_p, based on the disk Froude number as $H_p/r = 2.297 Fr_d$ where $Fr_d = u_{rms}/(gr)^{0.5}$ and u_{rms} is the average falling velocity of the disk.

Most research studies on the dynamics of falling objects focused on thin disks where the disk diameter is at least ten times the disk thickness (i.e., $\chi = d_o/e > 10$) whereas some falling objects in military, space engineering, and industry have smaller aspect ratios. To the author's knowledge, the cavity dynamics and crown formation by thick disks have not been thoroughly investigated and require more attention. The main objective of the present chapter is to perform a comprehensive study on cavity dynamics, crown formation, and pinch-off of thick disks and to evaluate the effect of impact energy on the descending motion and energy losses due to the impact. The impact energy was varied by changing the release height and mass of the disks. Different impact energies in free-falling thick disks can significantly alter the momentum transfer, energy dissipation, crown development, and cavity formation. The aspect ratio in thick disks may affect the motion of disks in stagnant water. As a result, two different aspect ratios of $\chi = 1.5$, and 3 were tested in this study. In addition, the present study explored the formation of above-water crown and underwater cavity for different impact energies, disk densities, and aspect ratios. The pinch-

off characteristics, disk velocity decay, and energy dissipation of disks were also extracted from measurements and empirical models were proposed for better prediction on the motion of thick disks in water.

The organization of this chapter is as follows: in Section 3.2, the experimental setup and the image analysis are described, and the obtained results are reported in Section 3.3, followed by the conclusion in Section 3.4.

3.2. Experimental Setup

Laboratory experiments were performed in the Multiphase Flow Research Laboratory (MFRL) at Lakehead University, Canada. A glass-walled tank was employed with cross-section dimensions of 850 mm x 1650 mm and a depth of 800 mm. In all tests, the experimental tank was filled with tap water and at a constant level with a depth of 650 mm. The water had a temperature of $T = 20 \pm 0.5$ °C, a density of $\rho_w = 998$ kgm^{-3}, and kinematic viscosity of $\upsilon = 1.02 \times 10^{-6}$ m^2/s. Two light sources (Woods L13, 1,000-W telescope work light, CA) were located beside the water tank to illuminate the background in the tank. A high-speed camera (Phantom, Miro Lab 110, New Jersey, Wayne, USA) with a camera lens of AF Nikkor 50 mm, f/1.4D (Nikon, Tokyo, Japan) was located in front of the tank to capture images of disks falling into quiescent water. High-speed images were captured with a resolution of 1280 x 800 pixels and a frequency of 2500 fps. At least a 10-minute relaxation time was allocated between the experiments to eliminate the disk-water interactions and water surface fluctuations. The water surface level was rechecked during the relaxation time to maintain a consistent water level.

Six solid, flat disks with different densities of $\rho_d = 1,080$ kgm^{-3}, 1,381 kgm^{-3}, and 2,331 kgm^{-3}, and aspect ratios of $\chi = 1.5, 3$, were tested in this study. Four release heights of $h_r = 200$ mm, 300 mm, 400 mm, and 500 mm were considered to study the effect of the impact energy of thick disks on cavity formation and crown development. The impact energy of disks, $E_i = {}^1\!/_2 m_d V_o^2$, where m_d is the disk's mass ranged between 125 g and 540 g and V_o is the impact velocity were normalized by the initial release energy of disks (i.e., $E_o = m_d g h_r$), and the values were listed in Table 3.1. To form the crown and splash in a controlled environment, a release mechanism was designed consisting of a partially pipe that was 4 mm larger than the disk's diameter and 200 mm above the water surface (i.e., $h_{air} = 200$ mm). The disks were made of compressed rubber with a homogenous

density and were treated with a commercially available super hydrophobic agent, Glaco Mirror Coat zero (Soft99 Corp. Co., Ltd., Japan) to hydrophobized the disks. The coating contains organic reagents and nanoparticles, resulting in a water contact angle of 123.05°.

Table 3.1. Experimental details and physical parameters of the free-falling thick disks in stagnant water. The diameter of disk diameter in all experiments was $d_o = 76.2$ mm (3 in).

Test No.	e (mm)	h_r (mm)	m (g)	ρ_d (kgm^{-3})	V_o (ms^{-1})	E_i/E_o	h_r/d_o	$\chi = d_o/e$	I^*	Fr_o
1	25.4	200	125	1080	0.66	0.112	2.62	3	0.0177	1.08
2	25.4	200	160	1381	0.89	0.201	2.62	3	0.0226	1.45
3	25.4	200	270	2331	1.13	0.325	2.62	3	0.0382	1.85
4	25.4	300	125	1080	0.81	0.111	3.94	3	0.0177	1.32
5	25.4	300	160	1381	0.95	0.154	3.94	3	0.0226	1.56
6	25.4	300	270	2331	1.21	0.248	3.94	3	0.0382	1.97
7	25.4	400	125	1080	1.30	0.216	5.25	3	0.0177	2.13
8	25.4	400	160	1381	1.55	0.304	5.25	3	0.0226	2.53
9	25.4	400	270	2331	1.86	0.440	5.25	3	0.0382	3.04
10	25.4	500	125	1080	1.47	0.219	6.56	3	0.0177	2.40
11	25.4	500	160	1381	1.61	0.263	6.56	3	0.0226	2.63
12	25.4	500	270	2331	2.02	0.417	6.56	3	0.0382	3.31
13	50.8	200	250	1080	0.89	0.204	2.62	1.5	0.0354	1.46
14	50.8	200	320	1381	1.03	0.268	2.62	1.5	0.0453	1.68
15	50.8	200	540	2331	1.19	0.362	2.62	1.5	0.0764	1.95
16	50.8	300	250	1080	1.03	0.179	3.94	1.5	0.0354	1.68
17	50.8	300	320	1381	1.14	0.221	3.94	1.5	0.0453	1.86
18	50.8	300	540	2331	1.50	0.380	3.94	1.5	0.0764	2.45
19	50.8	400	250	1080	1.71	0.371	5.25	1.5	0.0354	2.79
20	50.8	400	320	1381	1.80	0.411	5.25	1.5	0.0453	2.94
21	50.8	400	540	2331	2.13	0.579	5.25	1.5	0.0764	3.49
22	50.8	500	250	1080	1.87	0.355	6.56	1.5	0.0354	3.05
23	50.8	500	320	1381	2.05	0.428	6.56	1.5	0.0453	3.35
24	50.8	500	540	2331	2.37	0.571	6.56	1.5	0.0764	3.87

The diameter of all disks was $d_o = 76.2$ mm, and the disk thicknesses were $e = 25.4$ mm and 50.8 mm, providing the aspect ratios of $\chi = d_o/e = 3$ and 1.5, respectively. Overall, 24 tests were performed, and experimental parameters such as release height, disk density, impact velocity,

aspect ratio, impact Froude number, $Fr_o = V_o/(gr)^{1/2}$, and normalized energy, E_i/E_o, were listed in Table 3.1. Figure 3.1 shows a snapshot image of a free-falling cylinder in stagnant ambient water at $t = 76$ ms. The image shows the water entry and splash formation of a cylinder with an aspect ratio of $\chi = 3$, density ratio of $\rho_d/\rho_w = 2.335$, and dimensionless release height of $h_r/d_o = 6.56$ (Test No. 12.)
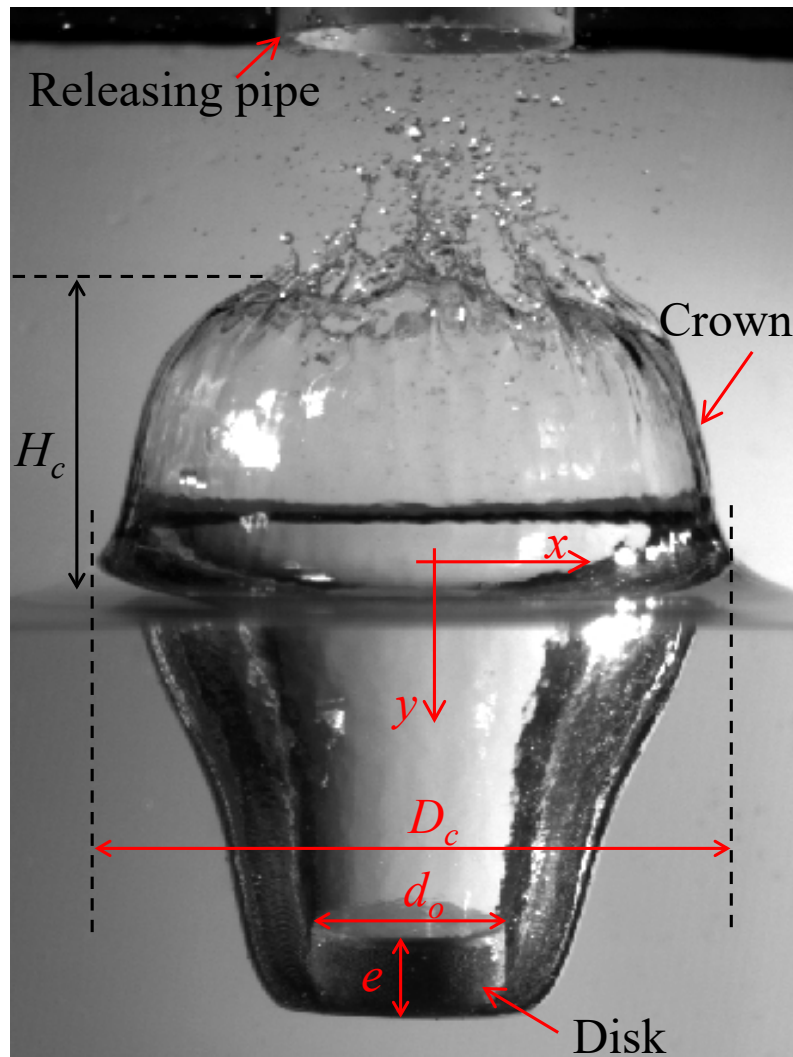
Figure 3.1. A snapshot image of free-falling disk entry in stagnant water for Test No. 12 and at $t = 76$ ms ($\chi = 3$, $\rho_d/\rho_w = 2.335$, $h_r/d_o = 6.56$).

The releasing mechanism was located at the center of the tank and all disks were released through a releasing pipe and freely entered the water. Experiments were repeated three times to ensure crown and cavity formations are consistent in all trials. The captured images were analyzed using

51

the image processing toolbox in MATLAB software (MATLAB version R2018b, MathWorks, Natick, MA, US). The results were extracted from high-speed images and were analyzed using the MATLAB based in-house program (Janati and Azimi 2021a, 2021b). The color contrast between the disk and the background image was high enough to be further eliminated during image analysis by implementing some post-processing techniques. The impact velocities were calculated based on the rate of disk penetration into water and started once the disk hit the water surface and until the disk was fully submerged in water.

3.3. Results and Discussions

3.3.1. Experimental observations

Experimental observations of crown dynamics and underwater cavity by free-falling thick disks with different impact energies and aspect ratios are shown in this section. The effect of impact kinetic energy, E_i, was studied by variations of disk mass (i.e., a combination of disk's density and volume) and release height. The images of crown and cavity formation of six cylindrical thick disks with a constant impact velocity induced from a release height of $h_r = 500$ mm (i.e., $h_r/d_o = 6.56$) and with different aspect ratios and densities are shown in Figure 3.2. All images were recorded at their pinch-off time. Each column in Figure 3.2 represents different disk densities, and each row shows disks with different aspect ratios. The geometrical characteristics of crown and cavity such as crown height, H_c, crown diameter, D_c, pinch-off depth, H_p, and frontal position, H_f, of disks are shown in Figure 3.2. As can be seen, the volume of the penetrated airflow increased with increasing impact velocity and air is drawn into the water in the wake of the disk. Therefore, the underwater cavity in disks with relatively higher impact energy, as a result of higher disk mass, formed a greater cavity than the lighter disks. As can be seen in Figure 3.2a, the disk with the lowest density, $\rho_d/\rho_w = 1.080$, and highest aspect ratio (i.e., $\chi = 3$), formed smooth and partially sealed crown. As the impact energy of disks increased, the crown was sealed, and the crown surface became rougher as micro ripples were formed on the crown surface. Moreover, more water droplets fell inside the cavity and cavity distortion occurred as the impact energy of disks increased. The crown wall was almost vertical in Figure 3.2a (i.e., Test No. 10, $\rho_d/\rho_w = 1.080$, $\chi =3$, $E_i/E_o = 0.219$), and it gradually curved as the disk impact energy increased (see Figures 3.2b and 3.2c). Moreover, the thickness of disks increased the mass and accordingly increased the

impact energy. It was observed that by increasing the thickness of disks, the slope of crown wall became more inclined towards the center of the crown due to high pressure drop inside the crown.
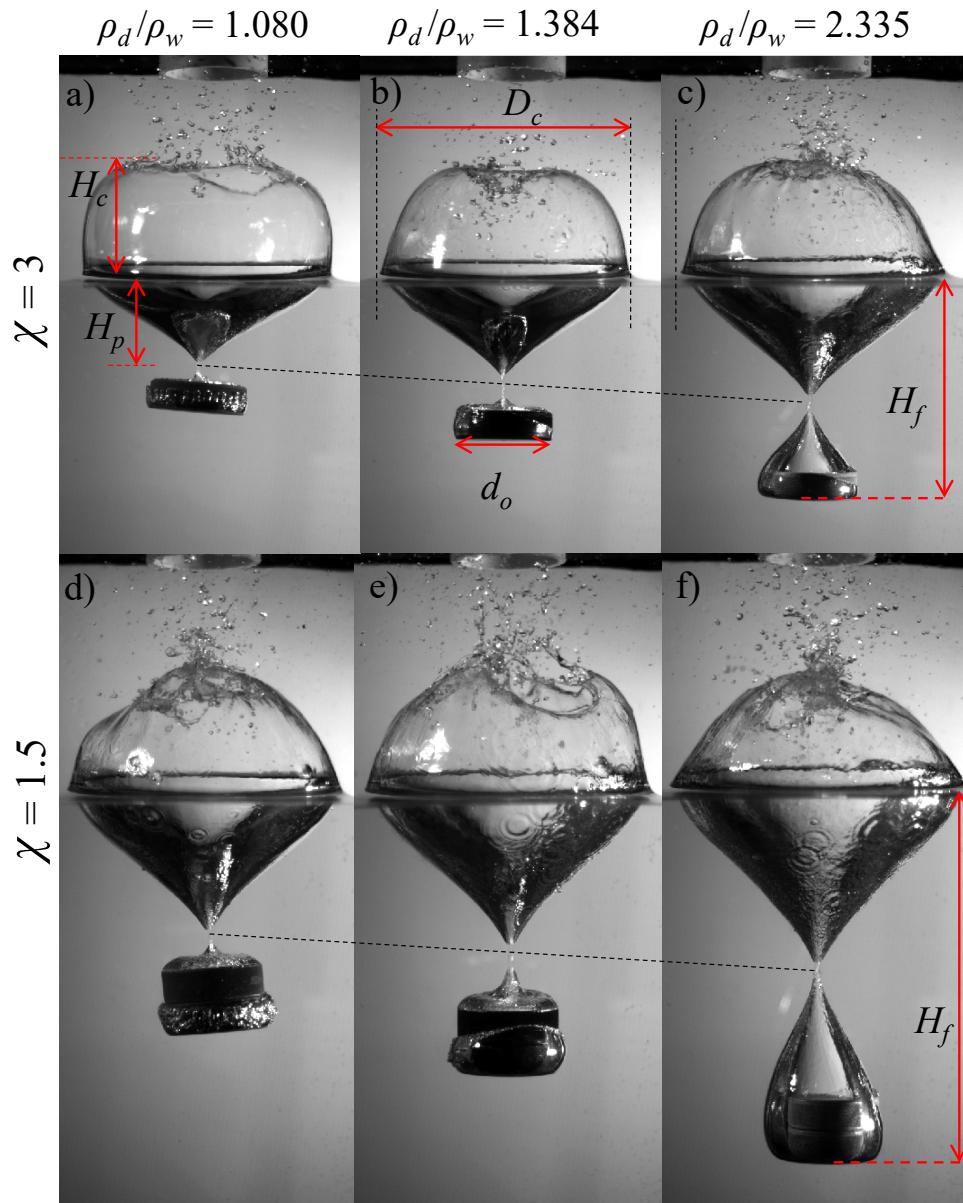
Figure 3.2. Effect of initial impact energy on the crown and cavity formations of free-falling thick disks. Disk density and mass varied and the release height was constant, $h_r/d_o = 6.56$: a) Test No. 10, $\chi = 3$, $\rho_d/\rho_w = 1.080$; b) Test No. 11, $\chi = 3$, $\rho_d/\rho_w = 1.384$; c) Test No. 12, $\chi = 3$, $\rho_d/\rho_w = 2.335$; d) Test No. 22, $\chi = 1.5$, $\rho_d/\rho_w = 1.080$; e) Test No. 23, $\chi = 1.5$, $\rho_d/\rho_w = 1.384$; f) Test No. 24, $\chi = 1.5$, $\rho_d/\rho_w = 2.335$. Images were taken at the pinch-off time.

A careful observation of snapshot images indicated that pinch-off depth, H_p, was marginally changed by disk impact energy whereas the frontal position of disks increased considerably. Such difference in the frontal position of submerged disks was detected and can be seen in Figures 3.2b and 3.2c. A conical air pocket was formed on the top of heaviest disk (see Figure 3.2c) whereas such conical air pocket did not form in relatively lighter disks. Formation of a conical air pocket in disks with the highest density of $\rho_d/\rho_w = 2.335$ was independent of the disk aspect ratio as it is shown in Figures 3.2c and 3.2f. The images in the first and second rows of Figure 3.2 show the effect of disk aspect ratio on crown and cavity formations. The mass of disks in the second-row images was double the first-row images and the additional mass (i.e., impact energy) dragged more air into the ambient water. The effect of disk density showed a marginal change in the location of pinch-off points; however, the additional mass by the second disk in tests with a lower aspect ratio increased the overall depth of the pinch-off.

As can be seen in Figures 3.2d to 3.2f, for tests with $\chi = 1.5$, the crown surface and underwater cavity became rougher than in tests with $\chi = 3$. The crown surface showed stronger perturbations and micro-waves were observed due to higher turbulence and falling water droplets inside the crown in tests with higher impact energy (i.e., heavier disk, $\chi = 1.5$). The edge of crown was curved inward due to gravity and sudden pressure reduction inside the crown. It is noteworthy to express that the conical cavity pocket attached to a disk with a density ratio of $\rho_d/\rho_w = 2.335$ is greater in $\chi = 1.5$ than in disks with $\chi = 3$. Those air pockets in Figures 3.2c and 3.2f enclosed the disk at the pinch-off without being ruptured whereas the presence of air bubbles around lighter disks indicated the initiation of air cavity rupture at the pinch-off.
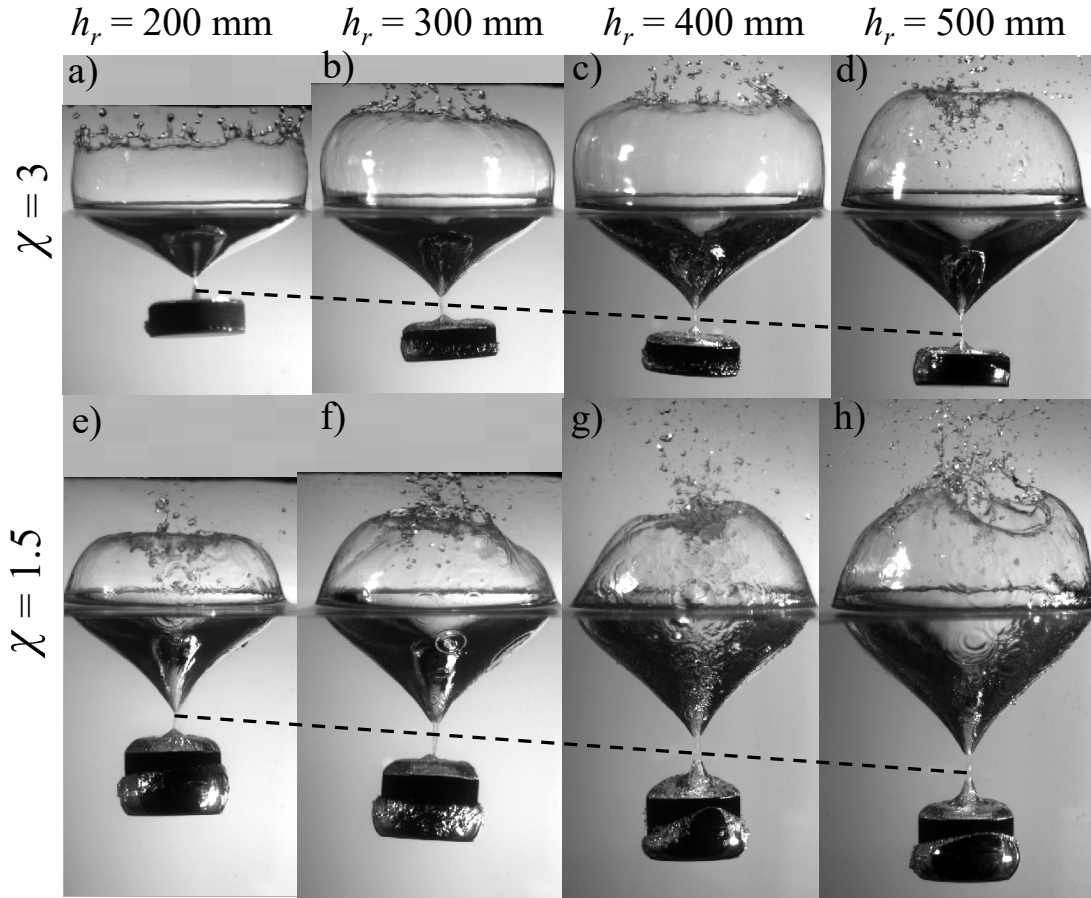
Figure 3.3. Effects of initial impact energy on the crown and cavity formations of free-falling thick disks. The release height and aspect ratio varied and disk density was constant, $\rho_d/\rho_w = 1.384$: a) Test No. 2, $\chi = 3$, $h_r/d_o = 2.62$; b) Test No. 5, $\chi = 3$, $h_r/d_o = 3.94$; c) Test No. 8, $\chi = 3$, $h_r/d_o = 5.25$; d) Test No. 11, $\chi = 3$, $h_r/d_o = 6.56$; e) Test No. 14, $\chi = 1.5$, $h_r/d_o = 2.62$; f) Test No. 17, $\chi = 1.5$, $h_r/d_o = 3.94$; g) Test No. 20, $\chi = 1.5$, $h_r/d_o = 5.25$; h) Test No. 23, $\chi = 1.5$, $h_r/d_o = 6.56$. Images were taken at the pinch-off time.

The effects of impact energy on crown and cavity formation were studied by comparing the snapshot images of free-falling disks at the pinch-off. The impact energy of disks in different tests was controlled by varying the mass of disks and release height. Figure 3.3 shows the snapshot images of free-falling disks at the pinch-off indicating the effects of release height and aspect ratio in disks with the same density ratio of $\rho_d/\rho_w = 1.384$. Each column in Figure 3.3 represents a particular release height, and each row shows a disk aspect ratio. As can be seen, the impact energy had significant effects on the crown shape and cavity evolution. In particular, the pinch-off depth,

H_p, and frontal position, H_f, varied with the impact energy. In disks with an aspect ratio of $\chi = 1.5$, the crown distortion was noticeable due to creation of vacuum pressure inside the cavity. As can be seen, the crown was deformed and developed a rough and asymmetric surface.

The crown shape in tests with a lower aspect ratio of $\chi = 1.5$ was fully sealed in most release heights except in Tests No. 13, 14, 16, and 17 having an impact energy less than 36% of the initial energy, E_o. The results indicated that the threshold value of impact energy to separate partial- from full-seal crowns is $E_i/E_o = 0.36$. Below the threshold impact energy ratio, the crown is partially sealed and above the threshold, it is fully sealed. Two cases of full-seal crown were observed for the aspect ratio of $\chi = 3$, which were belong to Tests No. 9, and 12, having impact energies of $E_i = 0.44E_o$ and $0.417E_o$, respectively. It is worth noting that both cases had impact energies more than the threshold impact energy of $E_i = 0.36E_o$. Experimental observations show that pressure drop within the crown increased with increasing the release height and decreasing with the disk's aspect ratio.

A sequence of snapshot images of free-falling thick disks entering into stagnant water is shown in Figure 3.4. The selected time series images show Test No. 7 with an aspect ratio of $\chi = 3$, density ratio of $\rho_d/\rho_w = 1.080$, normalized release height of $h_r/d_o = 5.25$, and impact energy of $E_i = 0.216E_o$. The time in each frame is tagged underneath each image, and the pinch-off time for this test occurred at $t_p = 134.4$ ms. The density of disk in Test No. 7 was close to the density of water and despite relatively high impact velocity, the crown was not fully sealed due to relatively small impact energy below the threshold impact energy of $E_i = 0.36E_o$. The consecutive images show a uniform and smooth crown surface with slight disturbances. The time reference (i.e., $t = 0$) in all experiments was defined when a disk hit the water surface and in Test No. 7 the entire disk submerged in water at $t = 0.4$ ms. The surface splash was formed, and the underwater cavity continuously expanded between $t = 0.4$ ms, and $t = 80.4$ ms. After the evolution phase, the edges of crown curved and turned inward to seal the top. The cavity volume continuously contracted near the top of the disk until the pinch-off occurred at $t_p = 134.4$ ms.

Two jets were formed and moved in opposite directions at the pinch-off. The upward jet is called "the Worthington jet" and it penetrated in the water and the downward jet pushed the disk further downstream. The cavity detached from the top of the disk and remained a number of micro bubbles

due to the sudden formation of vapor as a result of negative pressure (140.4 ms $\leq t \leq$ 440.4 ms). The Worthington jet contains enough energy to uplift the water around it. It then returned to the water and penetrated into the water and causing the second pinch-off at t_{p2} = 540.4 ms. The second pinch-off time was approximately four times the initial pinch-off in this test (i.e., t_{p2}/t_p = 4.02). The second pinch-off cavity is characterized by a hollow spherical shape. After separation from the water surface, the second pinch-off cavity collided with the upcoming bubbles and agitated a region of ambient water between the top of the disk and water surface (i.e., see images for 460.4 ms $\leq t \leq$ 960.4 ms). The final stage of evolution occurred for 1040.4 ms $\leq t \leq$ 1240.4 ms (7.74 < t/t_p < 9.23). At this stage, the disk descended freely while the remaining microbubbles approached the water surface.

It is interesting to study the effect of impact energy, by varying disk mass and release height, and aspect ratio on the water entry of thick disks. Our experimental observations indicated a completely different crown development and cavity formation for the tested aspect ratios. Figure 3.5 shows the time history of snapshot images of a cylindrical disk (i.e., Test No. 16, E_i = 0.179E_o) in stagnant water. The disk in Figure 3.5 had the same density and release height (i.e., ρ_d/ρ_w = 1.080 and h_r/d_o = 5.25) as Test No. 7, which was illustrated in Figure 3.4, and the impact energy was doubled due to increasing the thickness of the disk. The time duration from the onset of impact was tagged below each image and the pinch-off time occurred at t_p = 137.6 ms which was 3.2 ms longer than the same disk with half thickness (i.e., χ = 3).
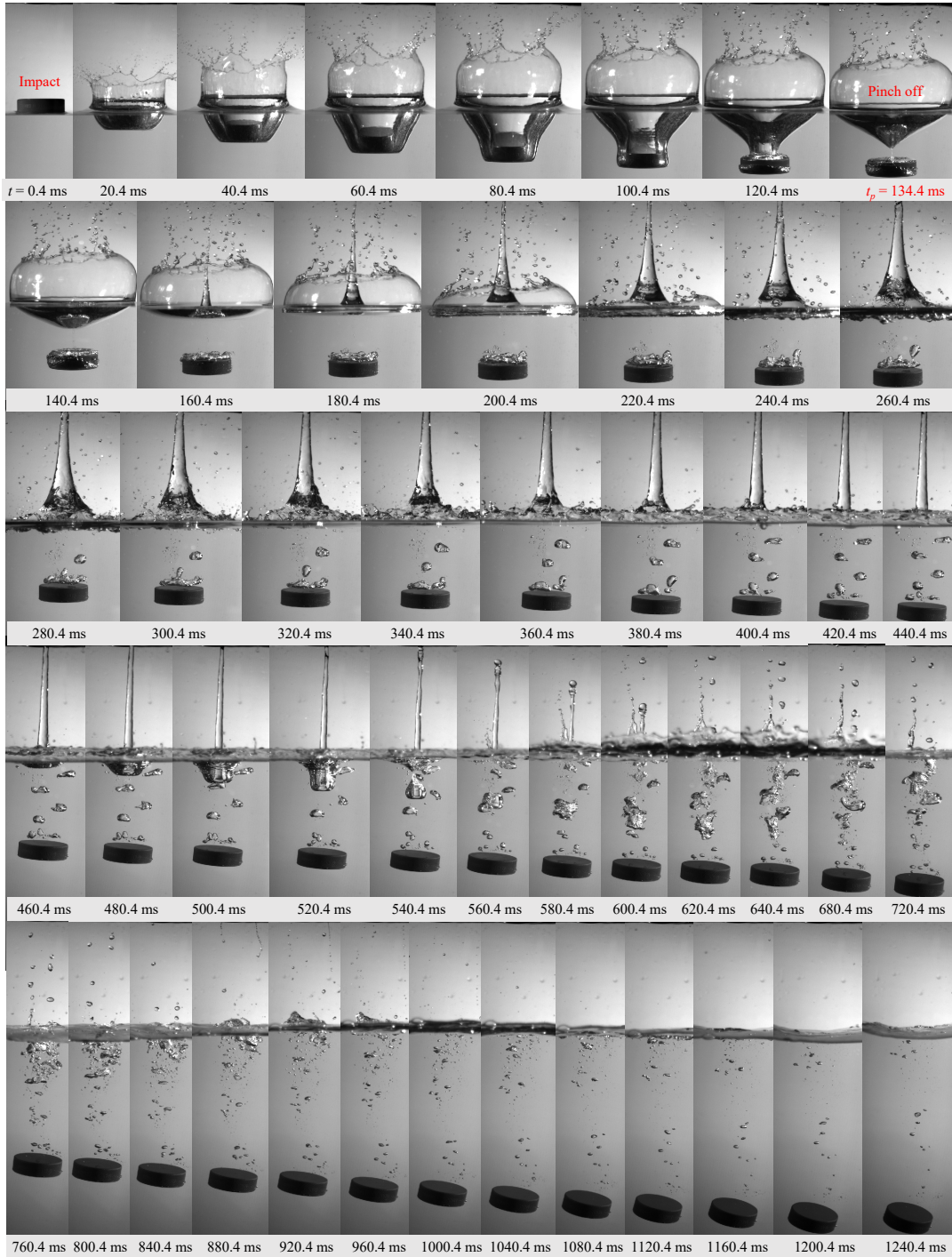
Figure 3.4. A sequence of snapshot images showing water-entry of a thick disk and cavity formation by falling a gravity-driven hydrophobic solid disk in stagnant water, Test No. 7; $\chi = 3$; $\rho_d/\rho_w = 1.080$, $h_r/d_o = 5.25$. The time is tagged under each frame, and the pinch-off time is $t_p = 134.4$ ms.

As can be seen in Figure 3.5, the crown was fully sealed at the pinch-off and the crown surface was asymmetric and distorted. The detached cavity volume after the pinch-off was larger in the thicker cylinder and it deformed from a spherical shape to a hyperbolic/paraboloid surface near the water surface. A comparison of both cases right after the impact at $t = 20.4$ ms, indicated that the rising splash curtain was proportional to the thickness of each disk; however, the splash curtain turned inward in the thicker and heavier disk (i.e., $\chi = 1.5$). The crown was fully sealed in the thicker and heavier disk (see Figure 3.5) and the underwater cavity stretched further down due to a higher pressure drop inside the crown. Therefore, the pinch-off depth became larger in thicker disks (i.e., $\chi = 1.5$) in comparison to the case with a larger aspect ratio of $\chi = 3$.

As it was shown in Figure 3.4, the crown was not fully sealed, and the inside surface of the cavity was exposed to atmospheric pressure. Therefore, the pinch-off occurred earlier and the pinch-off depth became smaller than in those cases with a full seal crown. As can be seen in Figure 3.5 (160.4 ms $\leq t \leq$ 220.4 ms; 1.165 $\leq t/t_p \leq$ 1.6), the upward Worthington jet destabilized the crown, ruptured the crown surface, and caused significant disturbances at the water surface. Considering the same disk with a higher aspect ratio and evolving at the same period, the Worthington jet did not interact with the crown as the crown in Figure 3.4 was not fully sealed. As a result, the partially closed crown was intact, and the crown surface remained smooth and without any micro ripples (see Figure 3.4). The higher momentum in disk with $\chi = 1.5$ dragged more air into water and more bubbles were detached from the disk after the pinch-off. The normalized settling time in both tests with aspect ratios of $\chi = 3$ and 1.5 were $t_s/t_p = 9.2$ and 6.4, respectively. This indicated that the overall settling time of the disk decreased by approximately 44% as the impact energy of the disk doubled.

It is important to correlate the impact velocity of cylindrical disks with their physical characteristics for further analysis of crown development and estimation of pinch-off. The impact velocity is used to calculate impact Froude number ($Fr_o = V_o/(gr)^{1/2}$) and dimensionless moment of inertia ($I^* = \pi\rho_d e/64\rho_f d_o$) which representing the physical characteristics of the disk. The correlation between dimensionless moment of inertia and impact Froude number can be used for prediction of impact velocity and other characteristic time and length scales associated with the falling cylindrical objects. The impact energy in each disk can be also calculated by knowing the mass and impact velocity of the disks.

Figure 3.5. A sequence of snapshot images showing the water-entry of a thick disk and cavity formation by falling a gravity-driven hydrophobic solid disk in stagnant water, Test No. 16; $\chi =$ 1.5; $\rho_d/\rho_w = 1.080$, $h_r/d_o = 5.25$. The time is tagged under each frame, and the pinch-off time $t_p =$ 137.6 ms.

Figure 3.6a shows the correlations between I^* and Fr_o for all tests in this study. As can be seen, the impact Froude number significantly increased as the release height went beyond four times of the disk diameter (i.e., $h_r = 4d_o$). As a result, two prediction models were proposed for relatively near and far release heights. The correlations between I^* and Fr_o indicated that the impact Froude number was correlated with the disks' mass. Two linear equations with the coefficients of determination of $R^2 = 0.88$ and 0.72 were proposed for near and far release heights as:

$$Fr_o = (11.7\chi - 2.7)\,I^* + (0.7 - 0.25\chi) \qquad \text{for } h_r/d_o \leq 4 \qquad \text{Eq. (3.1a)}$$

$$Fr_o = (16.5\chi - 6.6)\,I^* + (3.05 - 0.5\chi) \qquad \text{for } h_r/d_o > 4 \qquad \text{Eq. (3.1b)}$$
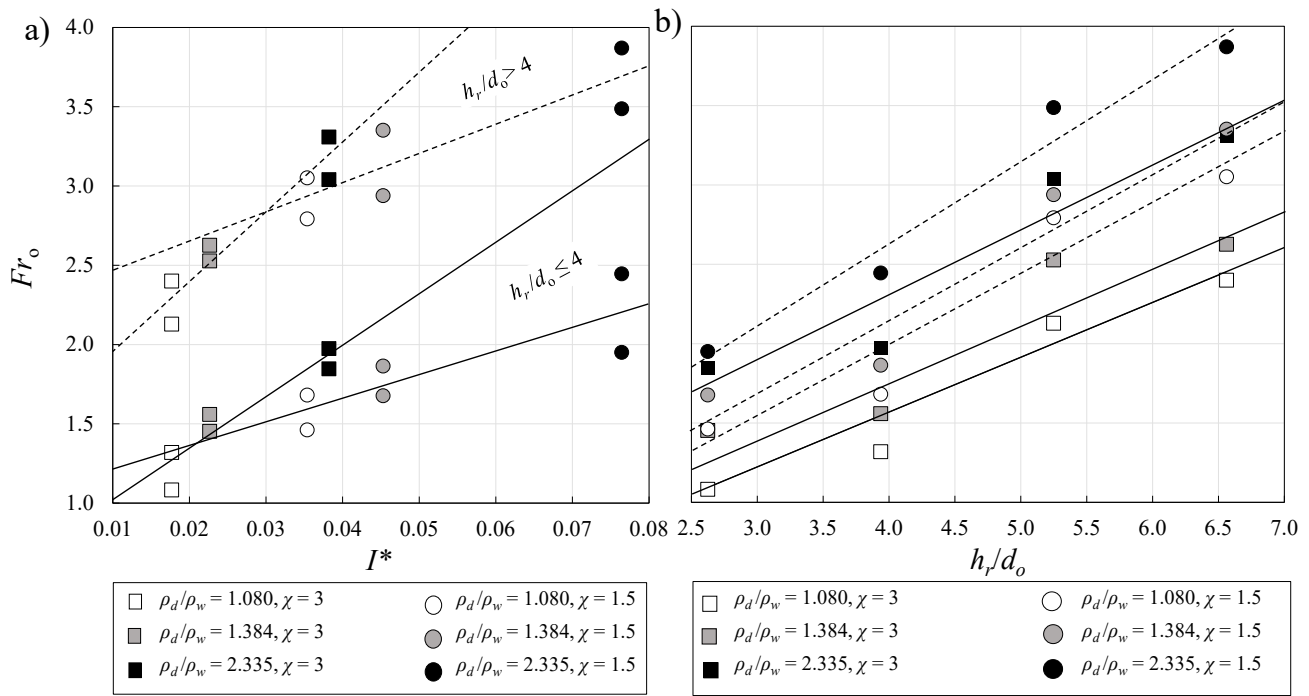
Figure 3.6. Variations of impact Froude number as a function of initial release condition and disk properties: a) correlations of Fr_o with the dimensionless moment of inertia; b) correlations of Fr_o with non-dimensional release height.

In the field, the impact Froude number can be predicted using the geometry and density of disks without measuring the impact velocity. Figure 3.6b shows the relationship between the impact Froude number and normalized release height. For a constant release height, the densest disk with $\chi = 1.5$ (i.e., the heaviest disk) had the maximum value of Froude number, and the lightest disk

61

with $\chi = 3$ had the lowest value of Froude number. Multi-regression analysis was developed to correlate the initial parameters with impact Froude number as:

$$Fr_o = (0.051\rho_d/\rho_w + 0.29) \, h_r/d_o + (0.38\rho_d/\rho_w - 0.23) \qquad \text{for } \chi = 3 \qquad \text{Eq. (3.2a)}$$

$$Fr_o = (0.056\rho_d/\rho_w + 0.38) \, h_r/d_o + (0.28\rho_d/\rho_w - 0.1) \qquad \text{for } \chi = 1.5 \qquad \text{Eq. (3.2b)}$$

In Figure 3.6b, the solid lines represent disks with $\chi = 3$ and dashed lines represent disks with $\chi = 1.5$. The coefficients of determination for Eq. (3.2a) and (3.2b) are $R^2 = 0.76$ and 0.98, respectively.

3.3.2. *Surface seal and crown characteristics at the pinch-off*

The crown geometry is affected by the impact energy of disk. The impact energy varies by variations in disk density, aspect ratio, and release height. In this study, the crown diameter at the pinch-off, D_c, was measured by the in-house MATLAB code. The crown diameter was normalized by the disk diameter and the variations of normalized crown diameter with impact Froude number are shown in Figure 3.7. The correlation between normalized crown diameter and impact Froude number was linear in both near and far release conditions and can be described as:

$$D_c/d_o = 0.28 Fr_o + (0.16 h_r/d_o + 0.78) \qquad \text{Eq. (3.3)}$$

The dashed lines in Figure 3.7 show ±5% variations from the proposed model. As can be seen in Figure 3.7, the normalized crown diameter increased dramatically in tests with far release conditions (i.e., $h_r/d_o > 4$). Therefore, release height is a determinative parameter in variations of crown diameter in comparison to density and aspect ratio of disks. The shape and diameter of the crown are completely altered at the threshold release height of $h_r/d_o = 4$. In order to understand the shape effect, the correlation of crown diameter with impact Froude number for solid spheres in water were extracted from the study of Sun et el. (2019) and included in Figure 3.7.
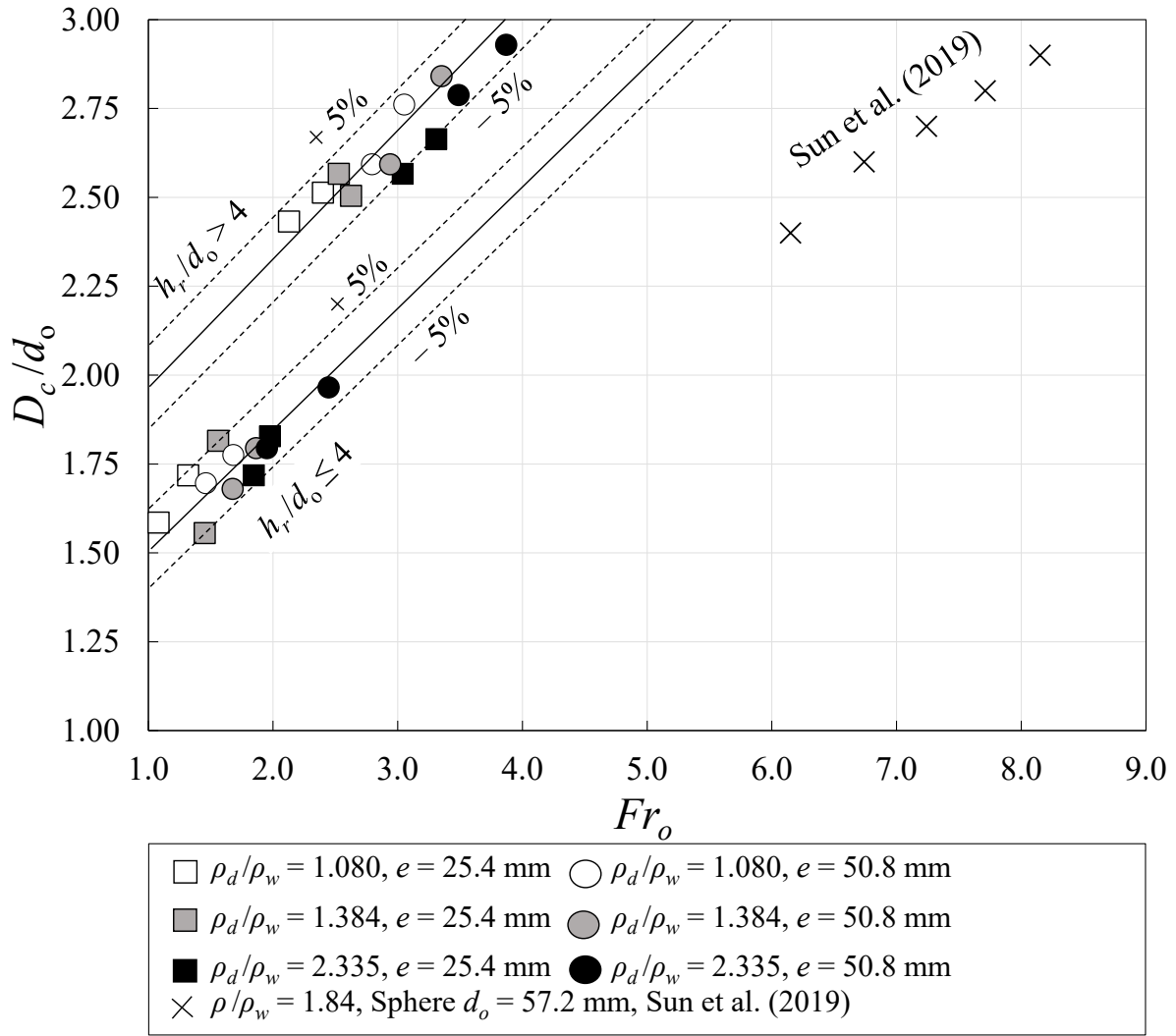
Figure 3.7. Variations of dimensionless crown diameter, D_c/d_o, with impact Froude number, Fr_o, for different release heights. The solid lines represent the proposed equation and the dashed lines show ±5% variations.

It was noticed that all release height ratios were greater than the threshold limit (i.e., $h_r/d_o > 4$) in the study of Sun et el. (2019), and impact Froude number ranged from 6.15 to 8.15. As can be seen in Figure 3.7, the correlation of normalized crown diameter with Fr_o in solid spheres was similar to disks released from the normalized height of $h_r/d_o > 4$, which ranges from $2.25 < D_c/d_o < 3$. Moreover, the linear correlation between impact Froude number and normalized crown diameter was similar in both sphere and disk. However, the normalized crown diameters in spheres with the

same impact Froude number were significantly lower than the corresponding disk which indicates the shape effect.
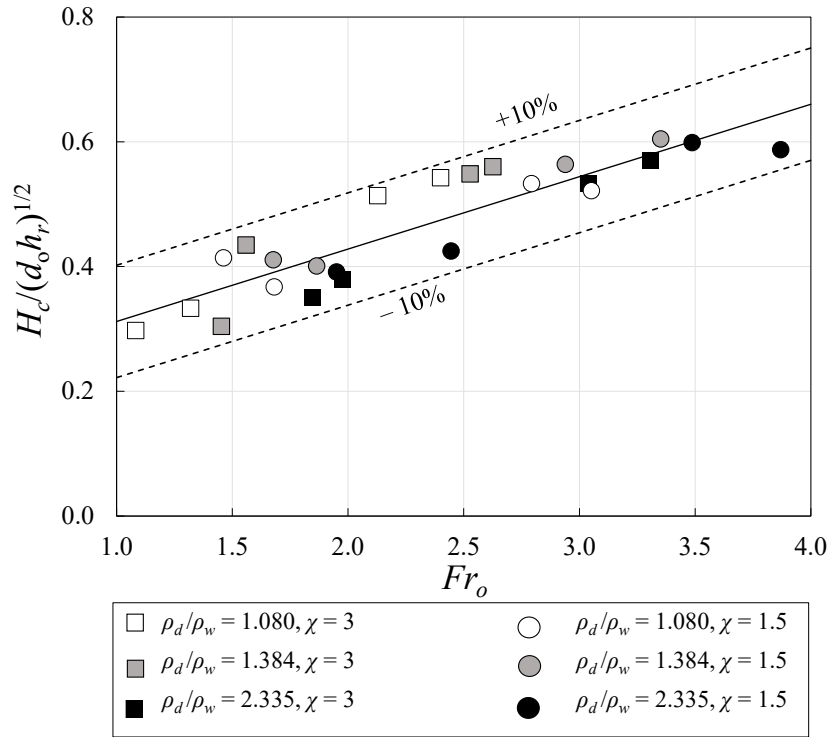
Figure 3.8. Variations of dimensionless crown height, $H_c/(d_oh_r)^{1/2}$, with impact Froude number, Fr_o, for different release heights. The solid line represents the linear correlation between normalized crown height and Fr_o and the dashed lines show ±10% variations.

The height of surface crown at the pinch-off was measured from the water surface and the results were normalized by the square root of release height and disks' diameter in form of $H_c/(d_oh_r)^{1/2}$. Figure 3.8 shows a linear correlation between normalized crown height and impact Froude number with a coefficient of determinations of $R^2 = 0.81$ as:

$$H_c/(d_oh_r)^{1/2} = 0.12 Fr_o + 0.2 \qquad \qquad \text{Eq. (3.4)}$$

The dashed lines in Figure 3.8 show ±10% variations from the proposed model.

The total duration of crown formation and its collapse is defined by the crown time, t_c, and it was measured in all experiments. The results were normalized by the square root of disk diameter and gravitational acceleration as $t_c/(d_o/g)^{1/2}$. Figure 3.9 shows the variations of normalized crown time

versus impact Froude number and a power-law model showed the best fit in the correlation of crown time with Fr_o as:

$$t_c/(d_o/g)^{1/2} = 2.16 Fr_o^{0.3} \qquad\qquad \text{Eq. (3.5)}$$
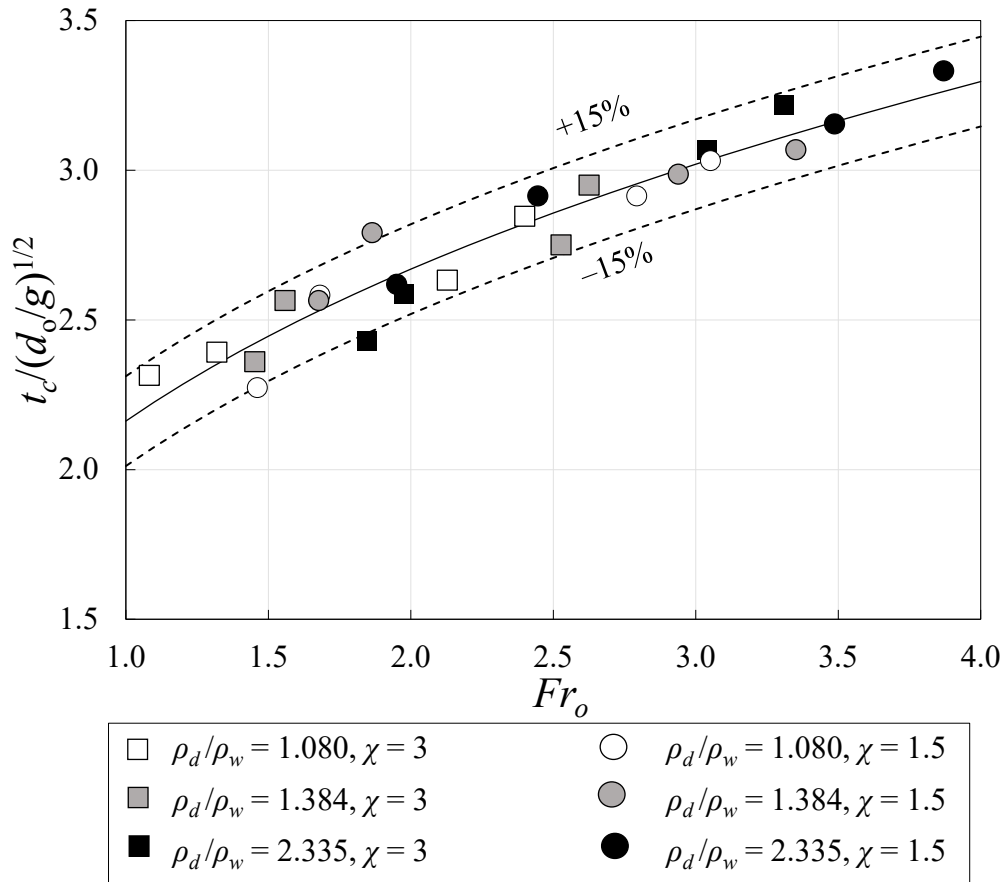
Figure 3.9. Variations of dimensionless crown time, $t_c/(d_o/g)^{1/2}$, as a function of impact Froude number, Fr_o, for disks with different initial impact energy. The solid curve represents the non-linear correlation between normalized crown time and Fr_o and the dashed curves show ±15% variations.

The coefficient of determinations of the above equation is $R^2 = 0.92$ and dashed curves in Figure 3.9 show ±15% variations from the proposed model. As can be seen in Figure 3.9, the crown time increased non-linearly with impact Froude number indicating that the crown time is also correlated with impact energy. The normalized crown time in this study varied between 2 and 3.5 times of characteristic time scale and it increased by increasing the release height as well.

3.3.3. Underwater cavity characteristics at pinch-off

The pinch-off is a prominent phenomenon during water entry of solid disks. Different characteristics of underwater cavity were measured at the pinch-off and the results are presented in this section. The pinch-off depth, H_p, in all experiments was measured and the results were normalized with the disk's diameter. Figure 3.10a shows the correlation between normalized pinch-off depth and impact Froude number for all experiments. The results showed that the location of pinch-off was directly affected by release height. A power-law model was proposed to predict the pinch-off depth based on impact Froude number as:

$$H_p/d_o = 0.45 Fr_o^{0.9}$$
Eq. (3.6)
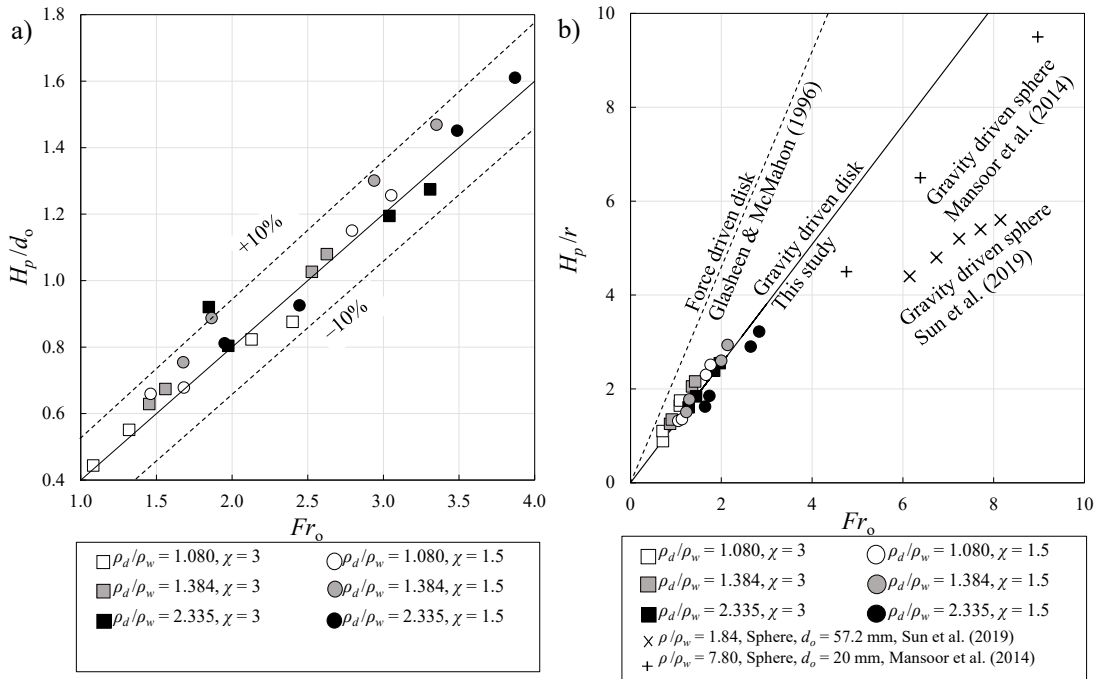
Figure 3.10. Variations of non-dimensional pinch-off depth with the initial impact and geometrical properties: a) correlations of H_p/d_o as a function of impact Froude number. The solid line represents the linear correlation between normalized pinch-off depth and Fr_o and the dashed lines show $\pm 10\%$ variations; b) correlations of H_p/r as a function of impact Froude number. The solid line represents the proposed model for gravity-driven disks, and the dashed line shows the proposed model of Glasheen and McMahon (1996) for modeling disks driven by a force transducer, r is the radius of the disk or spheres.

66

The power of impact Froude number in Eq. (3.6) indicates that the correlation between normalized pinch-off depth and impact Froude number is almost linear. The dashed curves in Figure 3.10a show ±10% variations from the proposed model. A comparison between the present results (i.e., gravity-driven) and the proposed equation of Glasheen and McMahon (1996) for prediction of pinch-off depth in disks driven by force transducer indicated that the addition of impact force increased the pinch-off depth (see Figure 3.10b). The results showed that dimensionless pinch-off depths in forced-driven disks had a linear relationship with the disk Froude number, $Fr = u_{rms}/(gr)^{1/2}$; however, the rate of change of normalized pinch-off depth was 55% smaller, in gravity-driven disks than the forced-driven disks.

The results for a gravity-driven sphere with various impact Froude numbers and a diameter of d_o = 57.2 mm from the study of Sun et al. (2019) were also included in Figure 3.10b for comparison. The density ratio of the solid sphere was ρ/ρ_w = 1.84, which is close to the density ratio of disks used in this study. Also, the diameter of the disk (d_o = 76.2 mm) is comparable to the diameter of spheres (d_o = 57.2 mm) used in the study by Sun et al. (2019). In addition, the data related to spheres with higher density ratio of ρ/ρ_w = 7.80, from the study of Mansoor et al. (2014), was added in Figure 3.10b. In comparison to Sun et al. (2019), spheres with a higher density ratio and smaller diameter had greater pinch-off depth. Based on the proposed model and the results obtained from the previous literature for spheres for a particularly high impact Froude number, the pinch-off depth in spheres is smaller than disks with the same Froude number which may be due to the formation of a boundary layer in solid spheres and flow separation in thick disks. However, in order to surely express these results, more data needed to compare the spheres and disks with similar densities and diameters.

The pinch-off time in each test was measured from the impact time till the time that the underwater cavity pinches off. The results were normalized with the disk's diameter and gravitational acceleration in form of $t_p/(d_o/g)^{1/2}$, and were plotted with the impact Froude number, Fr_o. Figure 3.11 shows that the normalized pinch-off time was classified based on the threshold release heights. It is inferred from the results that it took longer for disks with higher density to pinch-off than the lighter ones. Linear equations were proposed for prediction of pinch-off time for near and far release conditions as:

$$t_p/(d_o/g)^{1/2} = 0.13Fr_o + 1.36 \qquad \text{for } h_r/d_o \leq 4 \qquad\qquad\qquad \text{Eq. (3.7a)}$$

$$t_p/(d_o/g)^{1/2} = 0.13Fr_o + 1.20 \qquad \text{for } h_r/d_o > 4 \qquad\qquad\qquad \text{Eq. (3.7b)}$$

The coefficients of determination for the near and far release conditions were $R^2 = 0.73$ and 0.90, respectively. As can be seen, the pinch-off time increased with the disks' density below and above the threshold release height. Moreover, by increasing the disks' thickness the pinch-off time increased as well. The results for heavy solid spheres (i.e., $\rho/\rho_w = 7.80$) with different radius and impact Froude numbers from the study of Mansoor et al. (2014) were also added to Figure 3.11.

68
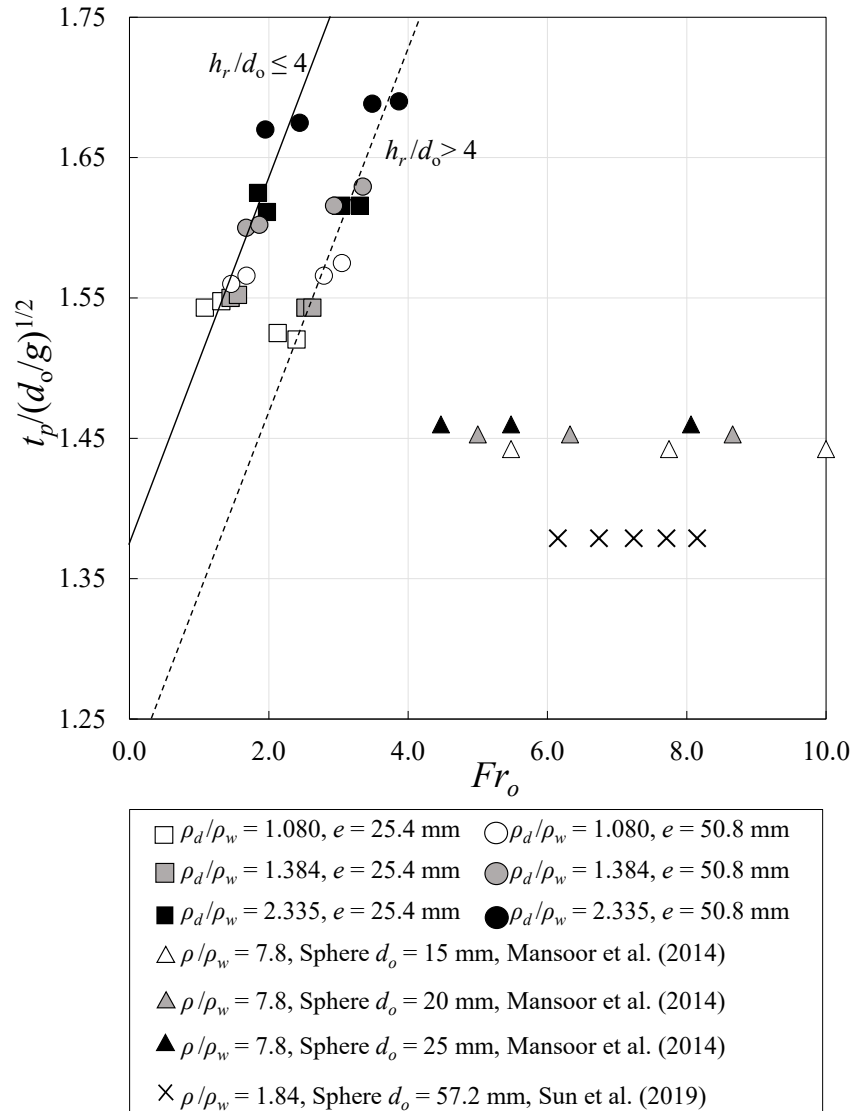
Figure 3.11. Variations of dimensionless pinch-off time, $t_p/(d_o/g)^{1/2}$, as a function of impact Froude number. The solid line and dashed line represent the linear correlation between normalized pinch-off time and Fr_o for $h_r/d_o \leq 4$ and $h_r/d_o > 4$ respectively.

As can be seen, the pinch-off time of spheres increased by increasing the relative sphere density which is compatible with the results of the disks' pinch-off time. As shown in Figure 3.11, the size of sphere was not a determinative factor in variations of pinch-off time. The dimensionless pinch-off time of spheres with radiuses of $r = 7.5$ mm, 10 mm, 12.5 mm was constant with approximately $t_p/(d_o/g)^{1/2} = 1.45$ for all cases in the study of Mansoor et al. (2014). The dimensionless pinch-off time of light spheres (i.e., $\rho/\rho_w = 1.84$) with a diameter of $d_o = 57.2$ mm, and impact Froude numbers ranging between $Fr_o = 6.15$ and 8.15 from the study of Sun et al. (2019) were also added to Figure 3.11 for comparison. The diameter of sphere in the study of Sun et al. (2019) was higher than Mansoor et al. (2014) while the density of sphere was smaller. This resulted in a relatively smaller pinch-off time in the lighter sphere despite having a larger diameter. As illustrated in Figure 3.11, the pinch-off time for disks and spheres with the same geometry and density remained almost the same. For example, the normalized pinch-off time in disks with a density ratio of $\rho_d/\rho_w = 2.335$ and aspect ratio of $\chi = 1.5$, is approximately $t_p/(d_o/g)^{1/2} = 1.68$ whereas the normalized pinch-off time for spheres with $\rho_d/\rho_w = 7.8$ and $d_o = 25$ mm was $t_p/(d_o/g)^{1/2} = 1.46$.

3.3.4. *Motion of thick disk in water*

A large amount of energy is dissipated by the impact once a solid object impacts the water surface. The energy losses due to the impact were calculated for all experiments with various initial energies, E_o. The normalized energy losses, $\Delta E/E_o$, are plotted versus the impact Froude number, Fr_o, Figure 3.12 shows that the normalized energy losses for each release height followed the same trend. As can be seen in Figure 3.12, disks with the smallest density (i.e., $\rho_d/\rho_w = 1.080$) and $\chi = 3$, had the maximum energy losses at the impact. Moreover, less energy was dissipated by the impact as release height and density of disk increased. At each release height, the normalized energy losses decreased by increasing impact Froude number. The minimum value of energy losses in all experiments and release heights was in the test with the highest mass (i.e., $\rho_d/\rho_w = 2.335$ and $\chi = 1.5$).
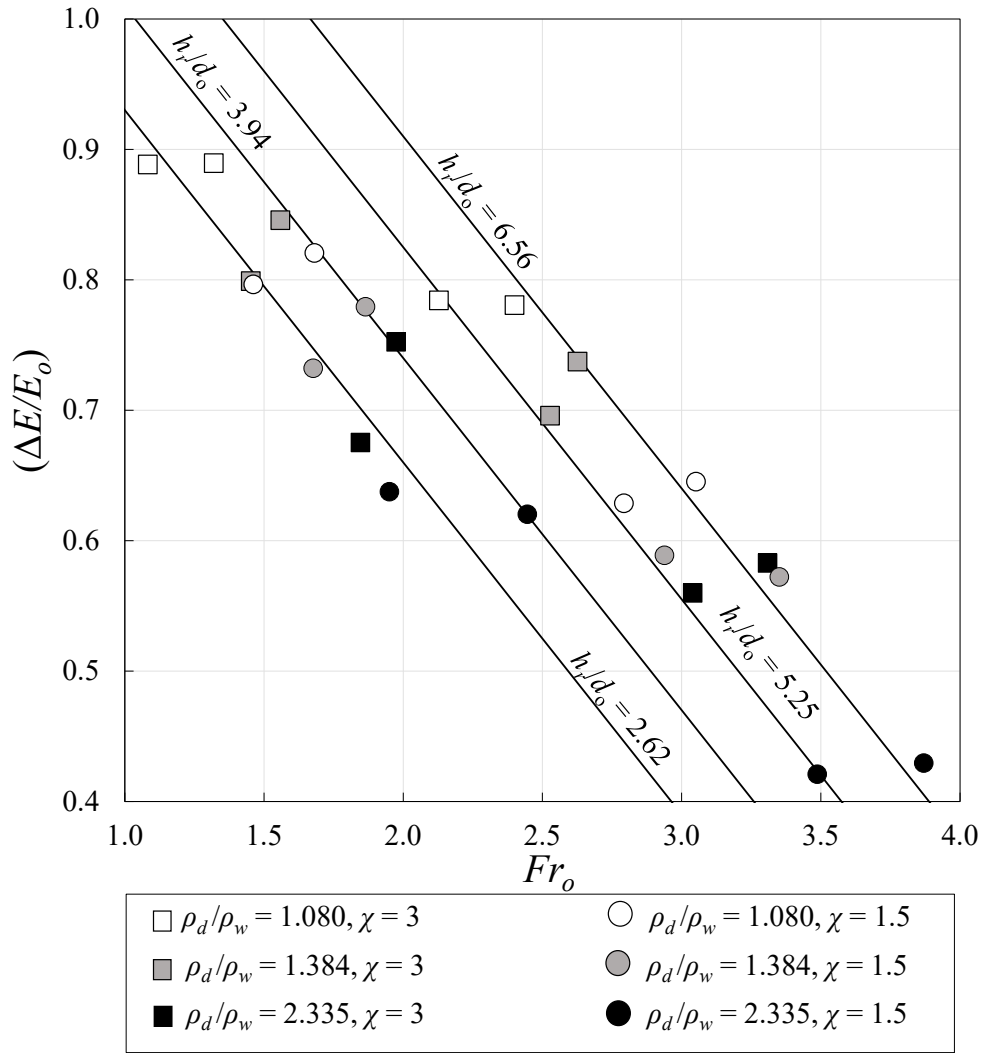
Figure 3.12. Correlations of normalized energy loss as a function of impact Froude number for different dimensionless release heights.

Figure 3.13 shows the variations of disk's frontal position versus non-dimensional time of the falling disks, t/T, where $T = (d_o/g)^{1/2}$ is the characteristic time scale. The subplots in Figure 3.13 show the frontal position of disks with an aspect ratio of $\chi = 1.5$, and 3, and with different release heights. As can be seen in Figure 3.13a, the variations of normalized frontal position with normalized time for $h_r/d_o = 2.62$, and 3.94 were compatible with each other. At the moment of impact until the depth equal to the disk diameter (i.e., $H_f/d_o = 1$), all disks had the same frontal positions. However, after the position of $H_f = d_o$, the effect of disk's mass on variations of frontal

position with time became effective. It was found that disks with higher densities, fell faster than disks with lower densities.
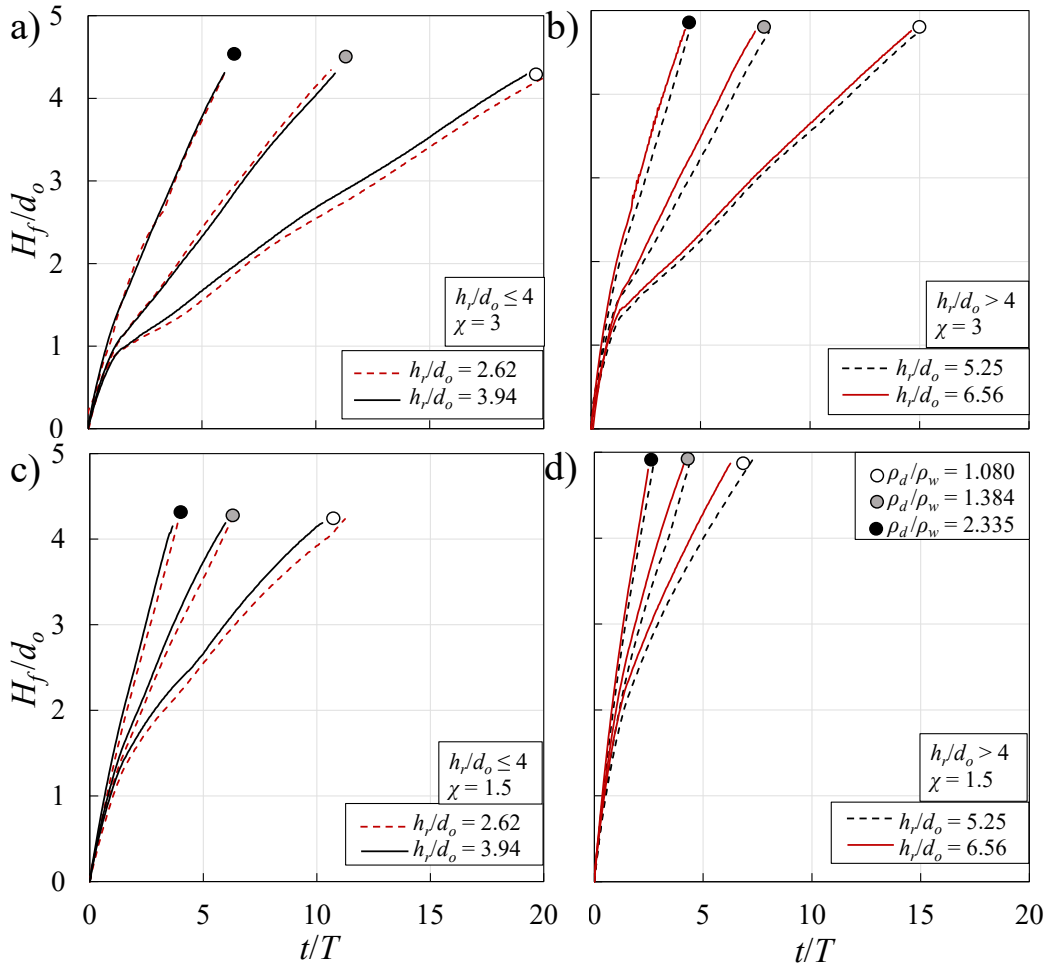
Figure 3.13. Variations of dimensionless frontal position, H_f/d_o, with non-dimensional time, t/T, for different disk thicknesses and release heights; a) $\chi = 3$, $h_r/d_o \leq 4$; b) $\chi = 3$, $h_r/d_o > 4$; c) $\chi = 1.5$, $h_r/d_o \leq 4$; d) $\chi = 1.5$, $h_r/d_o > 4$.

Figure 3.13a shows the trajectories of disks with near release height (i.e., $h_r/d_o \leq 4$). As can be seen, disks with a density ratio of $\rho_d/\rho_w = 1.080$, 1.384, and 2.335 reached the position of $H_f/d_o = 4$ at different normalized times of $t/T = 17.5$, 10, 5, respectively. Figure 3.13b shows the trajectories of disks with far release conditions (i.e., $h_r/d_o > 4$) and for disks with an aspect ratio of $\chi = 3$. A comparison between trajectories of disks in near and far release conditions indicated that far release condition reduced the duration of disks' descending time by approximately 70% of the total falling

time. For example, considering a constant point of $H_f/d_o = 4$, disks with a density ratio of $\rho_d/\rho_w =$ 1.080, 1.384, and 2.335 reached $H_f/d_o = 4$, at $t/T = 12.25, 7, 3.5$, respectively. Figures 3.13c and 13d show the trajectories of thick disks in both near and far release conditions, respectively. It can be seen that reducing the aspect ratio of disks by half (i.e., from $\chi = 3$ to 1.5), decreased the falling duration of disks by 50%.

The frontal velocity of gravity-driven falling disks was measured from the impact till the settling stage and the results were normalized by the disks' diameter and gravitational acceleration in form of $(gd_o)^{1/2}$. Figure 3.14 shows the variations of normalized frontal velocity of disks with normalized time, t/T, for different aspect ratios and release conditions. As can be seen in Figure 3.14, frontal velocities decayed with time and they were significantly altered by the near and far release conditions. As expected, disks with the highest density had the highest frontal velocities. The impact velocities in tests started from a maximum velocity during the water entry and decreased non-linearly until disks reached the bottom of water tank. As can be seen in Figure 3.14a, both normalized release heights of $h_r/d_o = 2.62, 3.94$ with an aspect ratio of $\chi = 3$, had similar trends, and the trajectory of velocities was classified based on the density of disks. Normalized impact velocities ranged between $1 < V/(gd_o)^{1/2} < 1.75$ and at the final settling phase the velocity of disks reduced to a new range of $0.25 < V/(gd_o)^{1/2} < 0.75$.

Figure 3.14b shows the trajectories of frontal velocity of disks with far release conditions (i.e., $h_r/d_o = 5.25, 6.56$) and an aspect ratio of $\chi = 3$. In these cases, the impact velocities were higher (i.e., $1.75 < V/(gd_o)^{1/2} < 2.5$) than those cases with near field release ($h_r/d_o \leq 4$). Settling velocities were approximately 40% more than settling velocities with the near field release. Figures 3.14c and 14d show the normalized velocity results for $\chi = 1.5$ and in both near ($h_r/d_o \leq 4$) and far field ($h_r/d_o > 4$) release conditions, respectively. In Figures 3.14c and 3.14d with $\chi = 1.5$, impact and settling velocities were greater than those disks with $\chi = 3$ and this may be due to higher mass of disk. A prediction model based on multi-regression analysis was proposed for estimation of disk velocity as:

$$V/(gd_o)^{1/2} = 0.3(t/T)^{0.62} \text{ for } \chi = 3 \ \& \ h_r/d_o \leq 4 \qquad \text{Eq. (3.8a)}$$

$$V/(gd_o)^{1/2} = 0.56(t/T)^{0.95} \qquad \text{for } \chi = 3 \ \& \ h_r/d_o > 4 \qquad \text{Eq. (3.8b)}$$

$$V/(gd_o)^{1/2} = 0.36(t/T)^{0.24} \qquad \text{for } \chi = 1.5 \ \& \ h_r/d_o \leq 4 \qquad\qquad \text{Eq. (3.8c)}$$

$$V/(gd_o)^{1/2} = 0.48(t/T)^{0.51} \qquad \text{for } \chi = 1.5 \ \& \ h_r/d_o > 4 \qquad\qquad \text{Eq. (3.8d)}$$

The average coefficient of determination was $R^2 = 0.98$.
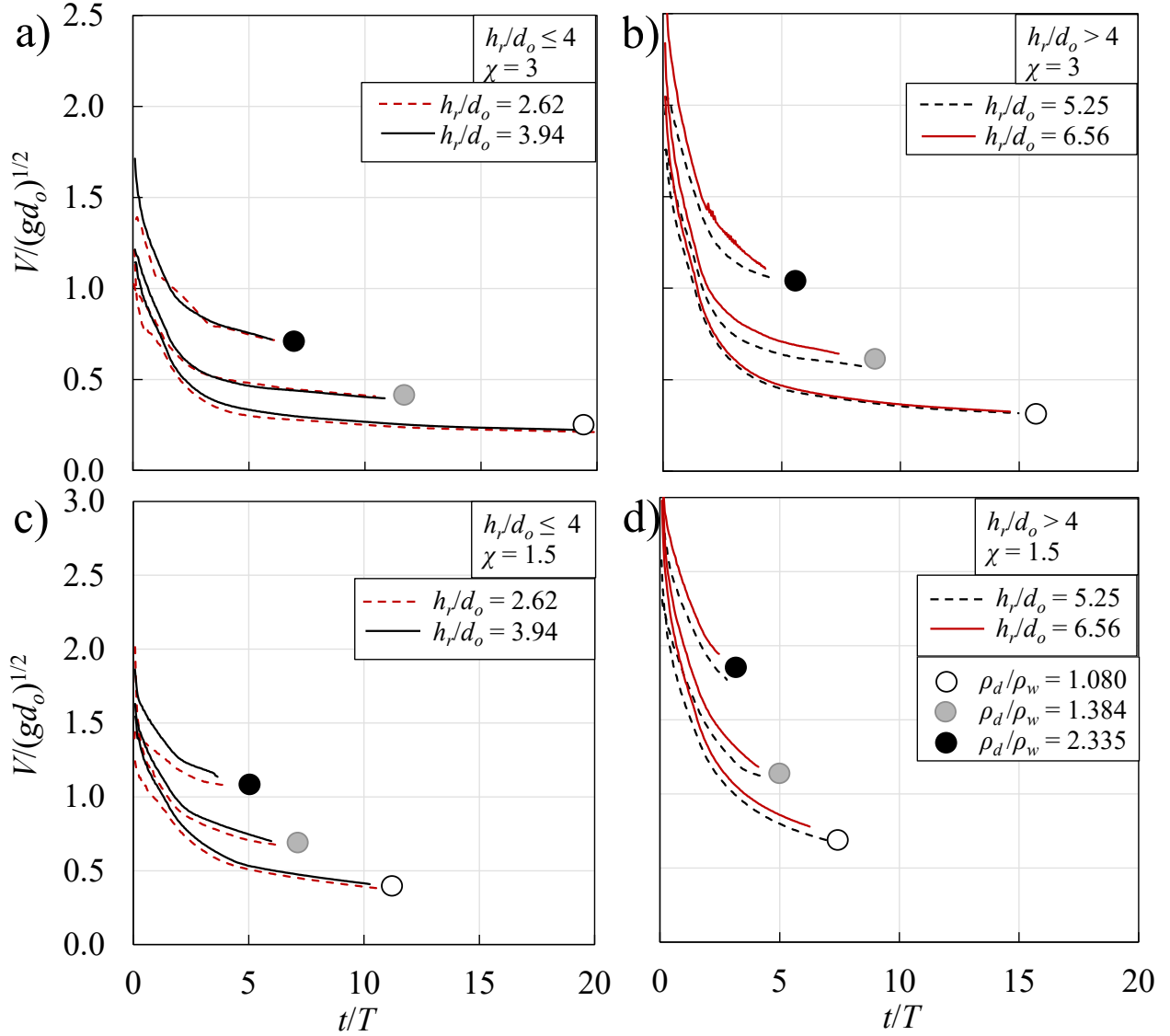
Figure 3.14. Variations of dimensionless velocity of disks, $V/(gd_o)^{1/2}$, with non-dimensional time, t/T, for different disk thicknesses and release heights: a) $\chi = 3$, $h_r/d_o \leq 4$; b) $\chi = 3$, $h_r/d_o > 4$; c) $\chi = 1.5$, $h_r/d_o \leq 4$; d) $\chi = 1.5$, $h_r/d_o > 4$.

3.4. Conclusions

The results of experimental investigations on the water entry of free-falling disks and the effects of impact energy on crown formation and cavity dynamics were presented in this study. Detailed observations of cavity formation and crown development have shown distinguished patterns with a threshold normalized release height of $h_r = 4d_o$ at which cavity and crown showed different behaviors in each regime. Effects of impact energy and aspect ratio were studied with constant release heights. The results indicated that the pinch-off depth in constant released height marginally increased with increasing disk's density.

As the thickness of disks increased, both cavity and crown surfaces were agitated and micro ripples were observed on the crown's wall. A conical air pocket was formed above the surface of disks at the pinch-off moment. Both underwater cavity and conical air pocket above the disk were larger in disks with smaller aspect ratio. The impact energies of disks were controlled by the release height and the results showed that the crown shape and seal type vary based on the disks'. The impact energy related to each release height was measured and it was found that the threshold impact energy to form fully sealed crown occurred when impact energy was equal to 36% of the initial energy (i.e., $E_i = 0.36E_o$). A threshold for impact energy was introduced as $E_i/E_o = 0.36$ to classify the seal type in crown formation, and it was observed that below the threshold value the crown is partially sealed. A correlation between the impact Froude number and dimensionless moment of inertia was proposed with which the impact Froude number can be predicted.

The crown geometry including crown diameter, and height in each experiment were measured and crown diameter was highly sensitive to the disks' impact energy in comparison to density or aspect ratio of disks. The results were compared with the water entry of solid spheres. It was found that in both disks and spheres, crown diameter increased by impact Froude number. To better understand the impact phenomenon, pinch-off depth and time were measured, and the results showed that the pinch-off time was classified based on the threshold release height. Disks with the same density and size pinched off at the same time. In both disks and spheres, pinch-off depth was affected by impact energy and normalized pinch-off depth increased by increasing impact Froude number. However, the rate of change of pinch-off depth with time was higher in disks than spheres.

Energy losses were estimated based on initial energy and impact energy of the disks at water surface. Release height and impact Froude number were the key controlling parameters. The results showed that disks with higher release heights have greater energy losses in comparison to disks released from a relatively smaller release height. It was also observed that thicker disks had less energy losses due to the impact. Moreover, the density of disks had an adverse correlation with energy losses. The variations of frontal position of disks with time was measured.

The variations of frontal positions with time in disks with the same aspect ratio and same release height were very similar. The initial energy of disk increased the descending velocity of disks. It was observed that the frontal velocity of disks drastically raised as release height went beyond the threshold. Also, in cases with the same release height, the aspect ratio was determinative of frontal velocity. By increasing the thickness of disks, the velocity of the disks became almost twice the case with a larger aspect ratio.

Chapter 4

4. Investigation of wall effect on the crown formation and underwater cavity of free-falling thick disks

4.1   Introduction

The motion of solid objects in water/viscous fluid is a fundamental problem amongst multiphase flow subjects. The water entry process involves a sequence of complex events that happen in less than a second. This problem has numerous applications in marine industry (Korobkin & Pukhnachov, 1988), military (Richardson, 1948; Gilbarg & Anderson, 1948; May 1951, 1952), dip-coating procedures (Burley, 1992), and aerospace structures (Seddon & Moatamedi, 2006). Accurate knowledge of water entry and fluid-solid interactions are required to understand and solve these problems. Worthington & Cole (1897, 1900) were the first researchers who considered the water impact dynamics and formation of air cavities using single-spark photography. During World War II, this topic caught more attention due to its military importance regarding the water entry of projectiles (Richardson, 1948; Gilbarg & Anderson, 1948; May, 1951, 1952). In recent years, by increasing the quality of high-speed cameras and developments of theoretical and numerical models, a better understanding of water entry and subsequent phenomena has been achieved (Field et al., 1997; Royer et al., 2008; Von Kann et al., 2010; Zhong et al., 2011, Lee et al., 2013; Bi et al., 2018; Janati & Azimi, 2022).

The closure mechanism of the cavity and its dependence on the atmospheric pressure were studied by Gilbarg and Anderson (1948). The most important factor in the development of the underwater cavity was found to be the surface seal. The experimental results showed that the early surface closure prevents further growth of the cavity while the deep closure results in long-closed cavities or bubble trails (Mirzaei et al., 2020). Birkhoff and Caywood (1949) studied water entry cavities and the surrounding flow fields using photographic technique and deduced that the cavity wall expands perpendicular to the cavity axis. Duclaux et al. (2007) studied the impact of a solid body in water and the collapse of the transient cavity upon the impact of a solid sphere in water both experimentally and theoretically. They proposed an analytical solution which describes the evolution of underwater cavity shape formed by a sphere. Based on their experimental results, the

pinch-off occurs at 0.45 of the sphere's position which is close to their theoretical prediction (i.e., $H_p/H = 0.5$).

The solid object spin and surface coating effects on the air cavity shape were indicated by Truscott and Techet (2009). Aristoff and Bush (2009), focused on the shape of air cavity and effects of gravity and surface tension forces on the cavity collapse. Four distinct regimes were classified to describe the interaction between solid sphere and water known as a surface seal, shallow seal, deep seal, and quasi-static regimes. Moreover, it was found that the hydrophilic surface properties of solid objects affect consecutive water entry and cavity formation. Yan et al. (2009) used a nonlinear mathematical formulation within an inviscid framework as well as numerical simulations of solid- liquid impact to describe the dynamics of the air cavity, and validate their results using experimental observations. Aristoff et al. (2010) determined the pinch-off depth and time of underwater cavity for the water-entry of low-density spheres.

Based on the existing literature, a disk can be categorized as a thin disk with an aspect ratio of $\chi = d_o/e > 10$, where d_o is the disk diameter and e is the disk thickness, or a thick disk with $\chi = d_o/e \leq 10$ (Auguste et al., 2013; Tchoufag et al., 2014; Fernandes et al., 2008). The trajectory of thin disks and their falling modes in water have been extensively studied in recent decades with different methods (Field et al., 1997; Zhong et al., 2011; Auguste et al., 2013; Heisinger et al., 2014). Willmarth et al. (1964) introduced three main dimensionless parameters that are essential in determining the falling pattern of a disk. The parameters are Reynolds number, $Re = \rho_f V d_o/\mu = V d_o/\nu$, the dimensionless moment of inertia, $I^* = I_{disk}/\rho_f d_o^5 = \pi \rho_d e/64\rho_f d_o$, and aspect ratio of the disk, $\chi = d_o/e$, where ρ_d is the disk density, ρ_f is the fluid density, μ is fluid dynamic viscosity, V is the mean vertical velocity of the disk, and I_{disk} is the moment of inertia of the disk. The borders between the different descending modes are defined based on the non-dimensional parameters (see Figure 2.1). Field et al. (1997) carried out a series of laboratory experiments to study the dynamics of free-falling disks in a glycerol mixture and reported four descending patterns steady, fluttering, chaotic, and tumbling. In addition, a chaotic transition area was defined between the fluttering and tumbling regimes. A regime map was defined based on variations in the dimensionless moment of inertia, I^*, and the Reynolds number of the disk, Re (see Figure 4.1).

Research studies on the water-entry topic have been focused on three main areas; *i*) the trajectory

of the solid object such as disks, coins, plates, cards, etc., *ii*) the impact force produced by the solid object at the initial phase of water entry, *iii*) investigation of transient cavity following the object during the water entry, as well as splash curtain formation and surface seal above the water surface. There are limited studies investigating the wall effect in the entry domain on the transient cavity and crown formation produced by the impact of solid objects onto liquids. For example, Royer et al. (2008) and Von Kann et al. (2010) have investigated this topic using sand as the impact medium. They managed to form an energetic jet shot out of the sand bed by decreasing depth of sand bed and reducing the container diameter. They also explored how the confinements change the resulting jet height and shape and the behavior of solid objects inside the bed. This phenomenon again is of importance to several military, industrial, biological and sports applications including the entry of ballistic missiles to a confined liquid space, slamming of boats and seaplane landings in slim canals, dip-coating operations in small fluid containers, creatures walking on confined water spaces and drag on swimmers and rowing oars in narrow channels (Mansoor et al., 2014). The focus of this study is the third case investigating of confinement effects on the transient cavity and splash formations produced by the impact of hydrophobic thick disks.
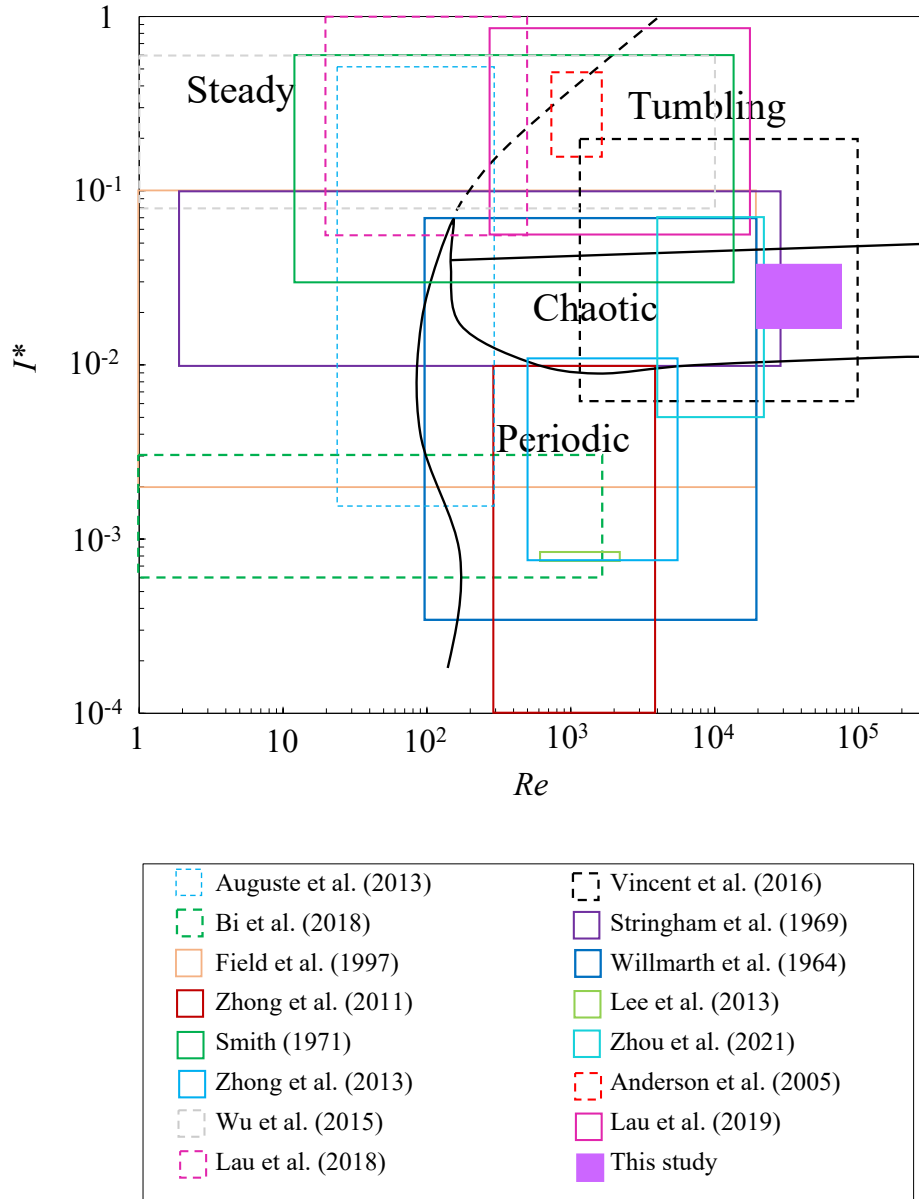
Figure 4.1. A regime plot showing the falling pattern of thick disks into stagnant water. The bold solid line and curves define the regions of different disks' motion based on dimensionless moment of inertia, I^*, and Reynolds number, Re. Falling mode based on Field et al. (1997), dashed curved by Heisinger et al. (2014).

4.2. Experimental Procedure

4.2.1. Experimental setup

A series of laboratory experiments were conducted in the Multiphase Flow Research Laboratory (MFRL) at Lakehead University, Canada. As can be seen in Figure 4.2, four glass-walled tanks were employed with cross-section dimensions of 850 mm x 1650 mm, 450 mm x 450 mm, 200 mm x 200 mm, and 150 mm x 150 mm a depth of 800 mm with a constant water level of 650 mm. The water temperature was $T = 20 \pm 0.5$ °C with a density of $\rho_w = 998$ kgm^{-3}, and kinematic viscosity of $\upsilon = 1.02 \times 10^{-6}$ m^2/s. For imaging purposes, two light sources (Woods L13, 1,000-W telescope work light, CA) were employed to illuminate the white background in the tank. A high-speed camera (Phantom, Miro Lab 110, New Jersey, Wayne, USA) with a camera lens of AF Nikkor 50 mm, f/1.4D (Nikon, Tokyo, Japan) was used in front of the tank to record the process of disks water entry. High-speed images were captured with a resolution of 1280 x 800 pixels and a frequency of 2500 fps. At least a 10-minute relaxation time, which was obtained through PIV measurements, was allocated between the experiments to eliminate the disk-water interactions and water surface fluctuations. Also, the water surface level was kept constant during all the experiments.
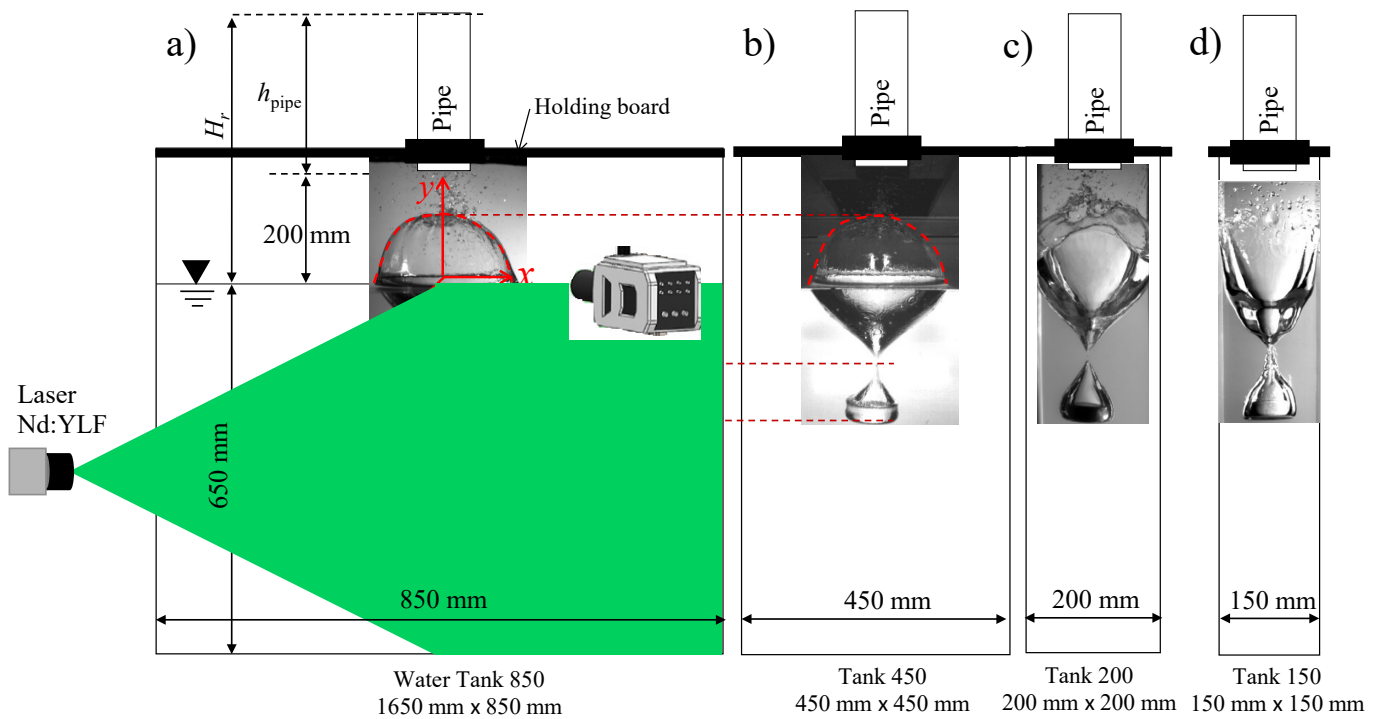
Figure 4.2. Schematic of the experimental setup and coordinate system at the pinch-off time, d_o = 76.2 mm, ρ_d/ρ_w = 2.335, χ = 3, h_{pipe} = 300 mm, h_r = 500 mm: a) pinch-off image of Test No. 12, Tank 1; b) pinch-off image of preliminary test, Tank 2; c) pinch-off image of Test No. 24, Tank 3; d) pinch-off image of Test No. 36.

Three disks with a diameter of d_o = 76.2 mm, and thickness of e = 25.4 mm, aspect ratios of χ = 3, and different densities were used in the tests. The disks had homogenous densities of ρ_d = 1,079 kgm^{-3}, 1,381 kgm^{-3}, and 2,331 kgm^{-3}, and they were released from four different release heights of h_r = 200 mm, 300 mm, 400 mm, and 500 mm in each tank. The disks were made of compressed rubber and were hydrophobized by a commercially available super hydrophobic agent, Glaco Mirror Coat zero (Soft99 Corp. Co., Ltd., Japan) resulting in a water contact angle of 123.05° (Janati & Azimi, 2023). As can be seen in Figure 4.2, at the beginning of the experiments, four water tanks were considered in order to see the wall effects on the crown and cavity formation. During the preliminary tests, it was found that the results from the largest tank, Tank 1650 mm x 850 mm, are similar to the results from the Tank 450 mm x 450 mm, with less than 2% differences. As a result, experimental results for the tank with 450 mm x 450 mm cross-section did not present here. For simplicity, The tanks with different cross sections of 1650 mm x 850 mm, 450 mm x 450 mm, 200 mm x 200 mm, and 150 mm x 150 mm are called Tanks 850, 450, 200, and 150, respectively. Regarding the similarity of the results in Tank 850 and Tank 450, the major parameters such as pinch-off depth, frontal depth at pinch-off, crown height and, shape are marked by dashed red lines in Figure 4.2a and Figure 4.2b to compare their results.

The release condition was partially guarded with h_{air} = 200 mm in the air before impacting the water surface (Janati & Azimi, 2023). Overall, 36 tests were performed in three main tanks including Tank 150, Tank 200, and Tank 850, and experimental parameters such as disk density, impact velocity, impact Froude number, $Fr_o = V_o/(gr)^{1/2}$, and release heights, h_r, were listed in Table 4.1. Figure 4.2 shows snapshot images of the same free-falling disks in stagnant ambient water at the Pinch-off. The image shows the water entry and splash formation of a disk with an aspect ratio of χ = 3, density ratio of ρ_d/ρ_w = 2.335, and release height of h_r = 500 in four different tanks. Each test was repeated three times to make sure the results were consistent in all experiments. Moreover, the disks were released into the center of the tanks and freely entered the water. The process was recorded by a high-speed camera (Phantom, Miro Lab 110, New Jersey,

Wayne, USA) with a camera lens of AF Nikkor 50 mm, f/1.4D (Nikon, Tokyo, Japan) and the results were analyzed using MATLAB software (MATLAB version R2018b, MathWorks, Natick, MA, US). The impact velocities were calculated based on the rate of disk penetration into water and started once the disk hit the water surface and until the disk was fully submerged in water.

Table 4.1. Experimental details and physical parameters of the free-falling thick disks in stagnant water in different tanks. The diameter of disk diameter in all experiments was $d_o = 76.2$ mm (3 in).

Test No.	Tank	h_r (mm)	m (g)	ρ_d (kgm^{-3})	V_o (ms^{-1})	Fr_o
1	150	200	125	1080	0.98	1.14
2	150	200	160	1381	1.05	1.21
3	150	200	270	2331	1.16	1.34
4	150	300	125	1080	1.09	1.26
5	150	300	160	1381	1.24	1.44
6	150	300	270	2331	1.53	1.77
7	150	400	125	1080	1.22	1.41
8	150	400	160	1381	1.34	1.55
9	150	400	270	2331	1.79	2.07
10	150	500	125	1080	1.42	1.64
11	150	500	160	1381	1.51	1.75
12	150	500	270	2331	1.93	2.23
13	200	200	125	1080	1.21	1.40
14	200	200	160	1381	1.29	1.49
15	200	200	270	2331	1.6	1.85
16	200	300	125	1080	1.32	1.53
17	200	300	160	1381	1.36	1.57
18	200	300	270	2331	1.73	2.01
19	200	400	125	1080	1.45	1.68
20	200	400	160	1381	1.51	1.75
21	200	400	270	2331	1.82	2.11
22	200	500	125	1080	1.61	1.86
23	200	500	160	1381	1.68	1.94
24	200	500	270	2331	2.06	2.38
25	850	200	125	1080	0.54	0.63
26	850	200	160	1381	0.89	1.03
27	850	200	270	2331	1.13	1.31
28	850	300	125	1080	0.81	0.93
29	850	300	160	1381	0.95	1.10

30	850	300	270	2331	1.45	1.68
31	850	400	125	1080	1.3	1.51
32	850	400	160	1381	1.55	1.79
33	850	400	270	2331	1.86	2.15
34	850	500	125	1080	1.47	1.70
35	850	500	160	1381	1.61	1.86
36	850	500	270	2331	2.02	2.34

The impact velocities were calculated based on the rate of disk penetration into water and started once the disk hit the water surface and until the disk was fully submerged in water.

4.2.2. *Particle Image Velocimetry (PIV)*

The velocity field following the free-falling disks were obtained in Tank 150 & Tank 850 using time-resolved Stereo Particle Image Velocimetry (PIV) system. The results then compared between the two aforementioned tank to see the effects of confinement. Water tanks were seeded with polyamide high-quality monodisperse tracer particles with size of 60 μm and density of 1,030 kgm^{-3} to follow the motion of surrounding water around the falling disks. Water was thoroughly mixed with seed particles and a relaxation time (10 minutes) was considered to remove any induced flow. A dual cavity Nd:YLF laser generator (DM20-527-DH/Stereo PIV, Ronkonkoma, NY, USA) was used to generate a laser sheet with a thickness of 1 mm for background illumination with a wavelength of 527 nm. The seeded images with tracer particles were captured by a high-speed camera (Phantom, Miro Lab 110, New Jersey, Wayne, USA) having a lens of AF Nikkor lens with a 50 mm focal length (f/1.4D, Nikon, Tokyo, Japan). The PIV Images were captured with a frequency of 500 fps, the exposure time was 5 μs, and images had a resolution of 1280 x 800 pixels. The captured consecutive images were analyzed using a cross-correlation algorithm of the DaVis 10 software (DaVis 10, LaVision, GmbH, Göttingen, Germany).

Three interrogation window passes were considered as 48×48, 32×32, and 16×16 pixels with a 50% overlap for noise reduction. The PIV system came with a calibration plate that was predefined in the DaVis 10 software to convert pixels to millimeters with the Pinhole Mapping Function (PMF). The Vector Validation Algorithms (VVA) were used to remove the spurious vectors and post-processing analysis was applied to extract velocity vector fields. It should be mentioned that

the contour plots were obtained by averaging 10 frames after and 10 frames before the selected time ($t = t_p$), which is equivalent to 0.04 s.

4.3.   Results and Discussions

4.3.1. Experimental observations

The results of free-falling thick disks with different densities and release heights impacting the water surface are presented in this section. Moreover, the effects of the confined medium on the crown formation, underwater cavity evolution, the frontal position of the disk at the pinch-off, pinch-off time, and pinch-off depth are shown by systematically increasing the cross sections of the water tank. At first, the sequence images related to three different experiments of the same disk, $d_o = 76.2$ mm, $\rho_d/\rho_w = 2.335$, and the same release height of $h_r = 500$ mm are illustrated in Figure 4.3. As can be seen in Figure 4.3, each row represents the results related to a particular tank size which is inversely proportional to the pinch-off time. For example, in Figure 4.3a which represents Tank 150, at the pinch-off (i.e., $t = 175$ ms), the crown is completely open and sticks to the wall of the tank, and it moves upward without any tendency to seal. The confinement causes surface undulations on the surface of the underwater cavity which is marked by dashed red lines. Moreover, the shape of the crown, cavity, and pinch-off is significantly altered by increasing the width of the water domain. As can be seen in Figures 4.3a to 4.3c, by increasing the cross-sectional dimensions of the water tank, the effect of the wall is reduced, and the crown is fully formed in Tank 850. Moreover, as illustrated in Figure 4.3, since it is the same disk in the three experiments, the cavity pinches off faster in larger tanks, (i.e., Tank 850) than in the smallest tank (i.e., Tank 150). At $t = 55$ ms, in Tank 850, the crown height is greater than Tank 200 and consequently Tank 150. After that at $t = 95$ ms, the crown is approximately sealed in Tank 850. In Tank 200, the crown is about to develop but, at the same time it moves down by the wall effect and the crown is fully open in Tank 150. No surface undulation is observed in Tank 200 and Tank 850.
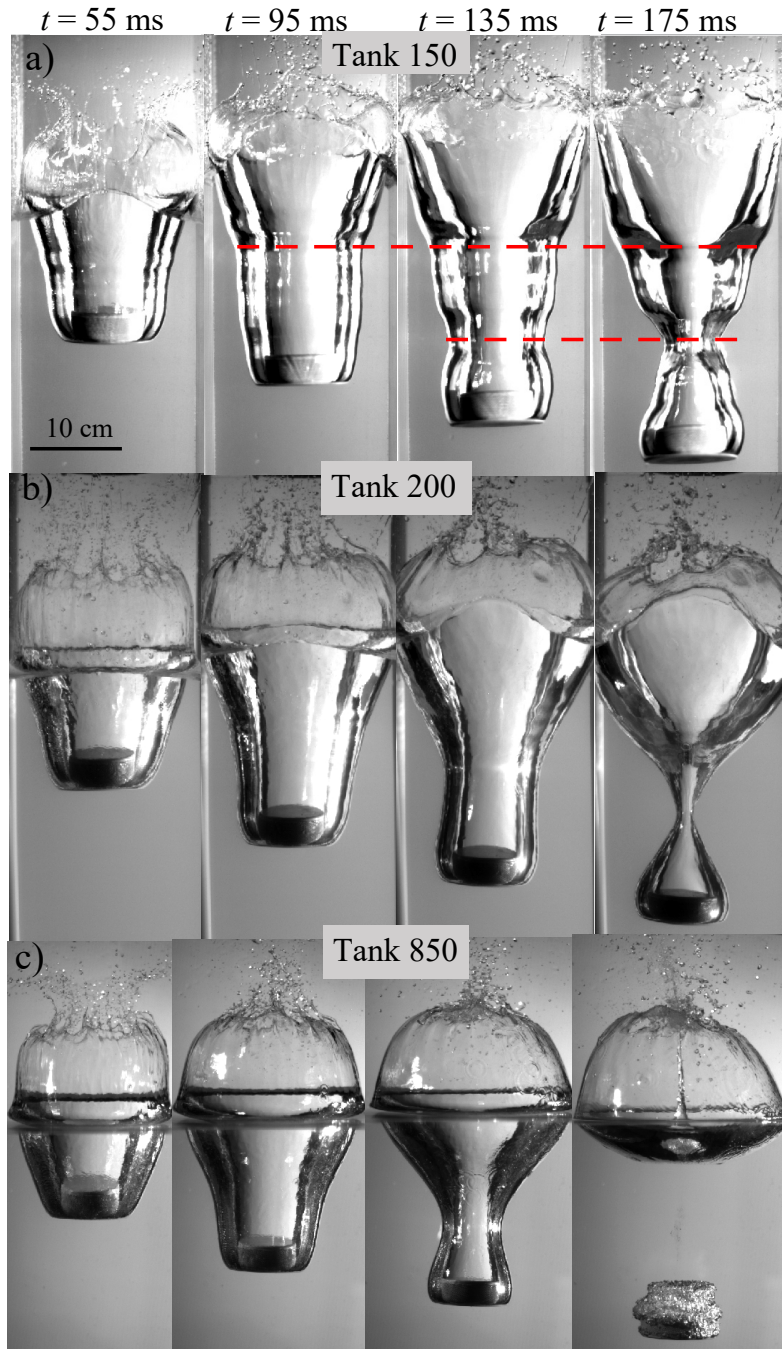
Figure 4.3. Image sequence showing the crown and cavity formation in different tank sizes by falling a gravity-driven thick disk, $d_o = 76.2$ mm, in stagnant water, $\chi = 3$, $\rho_d/\rho_w = 2.335$, $h_r = 500$ mm; a) Tank 150, Test No. 12, and $t_p = 197$ ms; b) Tank 200, Test No. 24, and $t_p = 176$ ms; c) Tank 850 mm, Test No. 36, and $t_p = 142$ ms.

In order to see the wall effects on the pinch-off time, the results related to the pinch-off time were extracted, non-dimensionalized, $t_p/(d_o/g)^{1/2}$, and illustrated versus Froude number Fr_o in Figure 4.4.
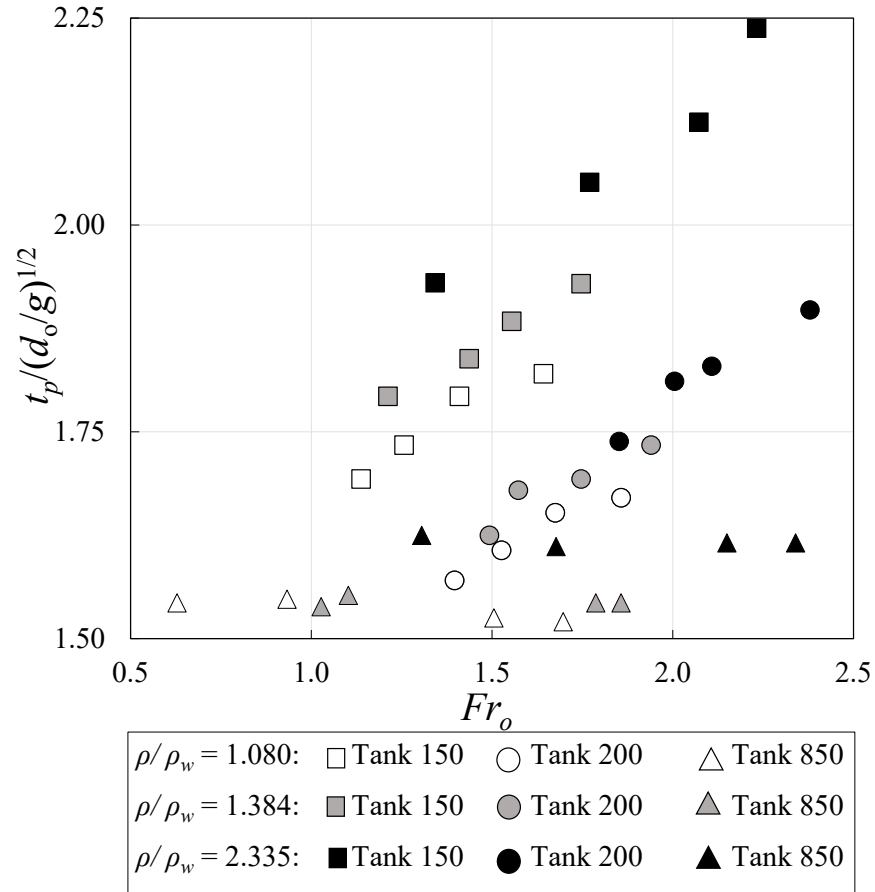
Figure 4.4. Effects of impact velocity, V_o, on variations of dimensionless pinch-off time, $t_p/(d_o/g)^{1/2}$, with the impact Froude number, Fr_o.

As can be seen in Figure 4.4, the dimensionless pinch-off time in Tank 850 is shown by the triangle symbols and they slightly fluctuate around $t_p/(d_o/g)^{1/2} = 1.6$. Decreasing the cross section of the water tank causes a delay in the pinch-off phenomena. As can be seen, the black square symbols represent the densest disk, $\rho_d/\rho_w = 2.335$ kgm^{-3}, in Tank 150. The pinch-off times of the cavity in Tank 150 are approximately 20 % greater than the ones in Tank 200 with black circle symbols. Moreover, by increasing the density of the disk, the pinch-off time increases as well. The densest disk, $\rho_d/\rho_w = 2.335$ kgm^{-3} in Tank 150 and Tank 200, has larger pinch-off times, approximately 20%, in comparison to the disks with a density ratio of $\rho_d/\rho_w = 1.080$ kgm^{-3}, and 1.384 kgm^{-3}.

Another parameter to investigate in this area for different tanks is the pinch-off depth. As can be seen in Figure 4.5, the pinch-off depth, H_p, in different experiments were measured from the water surface, non-dimensionalized by the radius of the disk, r, and plotted versus Froude numbers. It can be seen that in each water tank, the normalized pinch-off depth increases with the density of the disks; therefore, the densest disk has a greater pinch-off depth. Moreover, the results show that the pinch-off depths are proportional to the tank width. In Tank 850, the pinch-off depths are higher than the ones in smaller tanks. Overall, the pinch-off depth increases linearly with increasing the Froude number or release heights. For example, in Tank 850, once the Froude number increases from 0.63 to 1.7, the non-dimensional pinch-off depth is almost doubled.
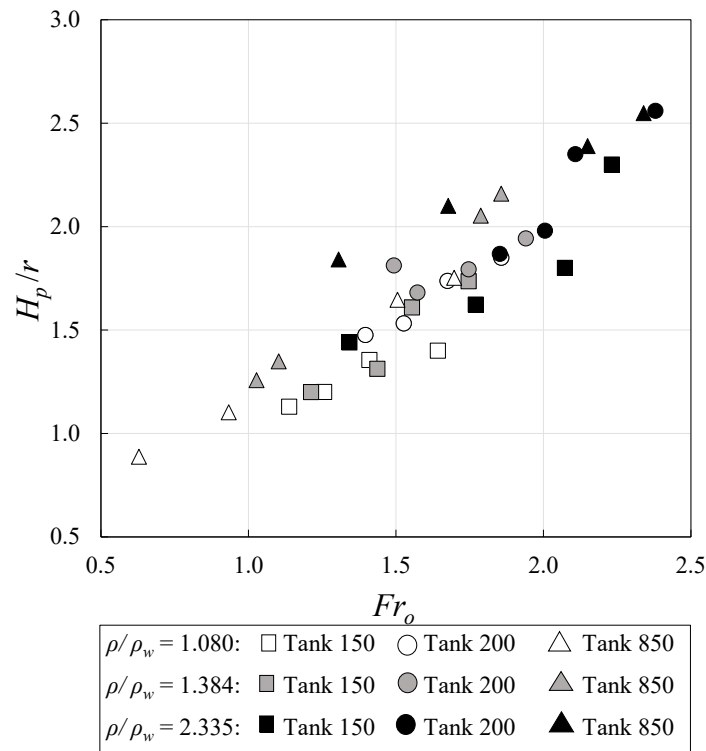
Figure 4.5. Variations of non-dimensionalized pinch-off depth with the impact Froude number in water tanks with different cross section dimensions.

The frontal positions of the disks in different water tanks were measured at the pinch-off time and the results were normalized by the disk's radius in Figure 4.6a. It can be seen that the frontal position of the disk is highly sensitive to the density of the disk. Disks with the density ratio of $\rho_d/\rho_w = 2.335$ kgm^{-3} have the largest frontal positions in the pinch-off time irrespective of the cross-section dimension of the tank. Moreover, in Figure 4.6b, the variations of the ratio of pinch-

off depth to the frontal position of the disks were plotted versus the Froude numbers.
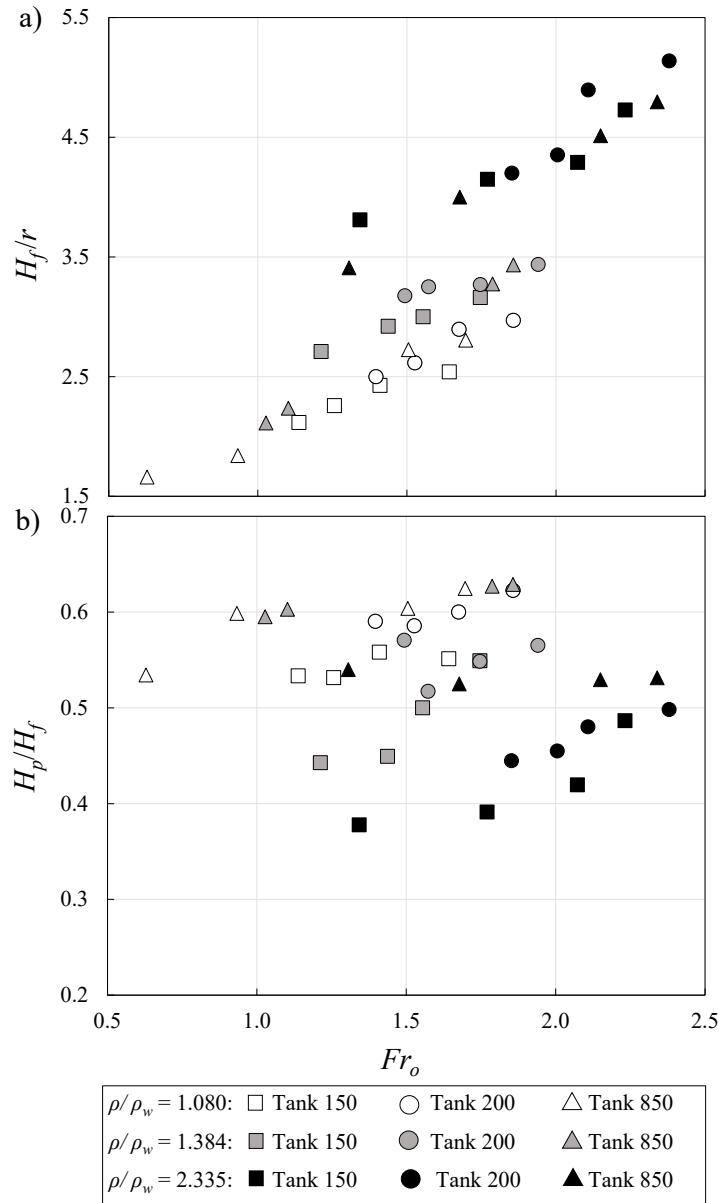
Figure 4.6. Variations of non-dimensionalized pinch-off depth with the impact Froude number in water tanks with different cross-section dimensions; a) non-dimensional pinch-off depth versus Froude number, b) Variations of ratio of pinch-off depth to frontal position of the disks with the Froude number.

The results show that the pinch-off depth, H_p, is approximately between 40% and 60% of the frontal position of the disks, H_p, based on the density of the disk and the wall effects. However, in

the large tank, Tank 850, the ratio of H_p/H_f, is approximately constant in the same density but different Froude numbers. In smaller tanks the ratio of H_p/H_f increases by increasing the Froude number. Moreover, the pinch-off depth of disk with a high density of ratio of $\rho_d/\rho_w = 2.335$ kgm^{-3} is approximately 50% of the frontal position of disk in the large tank, (i.e., Tank 850). In Tank 200, the pinch-off depth of disk with a density ratio of $\rho_d/\rho_w = 2.335$ kgm^{-3} starts from approximately 40% in lower Froude numbers and reaches 50% at the impact Froude number of $Fr_o = 2.3$.

4.3.2. PIV results

The PIV analysis of free-falling thick disks with different densities and release heights impacting water in two water tanks with different dimensions is presented in this section. The PIV results of radial and vertical velocity, vorticity, swirling strength, turbulent and average kinetic energies are extracted at the pinch-off. The results are related to pinch-off period, and it may include some fluctuations due to the agitated area due to the pinch-off.

At first, the results of radial velocity field, u, around a disk with $d_o = 76.2$ mm and the same release height of $h_r = 400$ mm are illustrated in Figure 4.7 in two small and large tanks at the vicinity of pinch-off. The color bar in the legend shows the range of radial velocity between -0.5 ms^{-1} and 0.5 ms^{-1}. As can be seen the right-hand column, Figures 4.7a, 4.7c, 4.7e, show the results of disks with three different densities in Tank 850 and left-hand column, Figures 4.7b, 4.7d, 4.7f, illustrate the results of the same three disks in Tank 150. The density of the disks is shown by the color of the disk. The light gray color represents the density ratio of $\rho_d/\rho_w = 1.080$ in the first row, dark gray shows $\rho_d/\rho_w = 1.384$ in the second row, and black color shows $\rho_d/\rho_w = 2.335$ in the third row of Figure 4.7.

In the confined tank, Tank 150, there is not enough cross-sectional space for radial velocities to move around. In contrast, in Tank 850, large area is affected by the moving disk with different densities. Moreover, the intensity of radial velocity is much higher in the larger tank compared to the small tank. The dark red and blue colors show the highest value of radial velocity of the surrounding water. It can be seen in Figure 4.7f, by increasing the density of the disk to $\rho_d/\rho_w = 2.335$, the rear affected area become narrower but drawn more vertically because of the greater velocity of the disk. Also, the radial velocity beneath the surface of the disk, particularly at the

bottom corner of the disk becomes affected with higher recorded radial velocity approximately greater than ± 0.35 ms^{-1}.
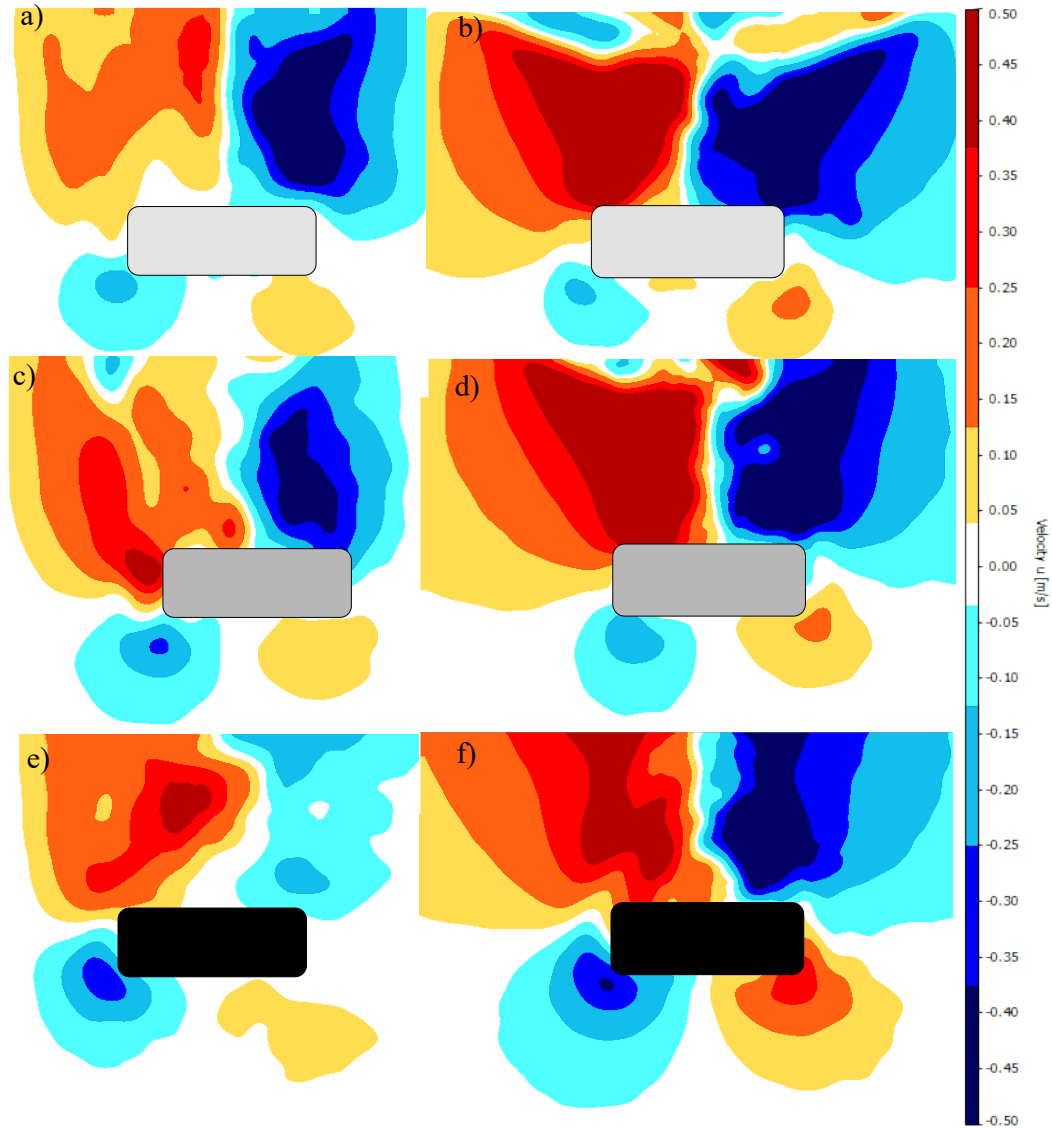
Figure 4.7. Effects of disk density and confinement on contour plots of radial velocity, u, in release height of, $h_r = 400$ mm: a) Test No. 7, $\rho_d/\rho_w = 1.080$; Tank 150, b) Test No. 31, $\rho_d/\rho_w = 1.080$; Tank 850, c) Test No. 8, $\rho_d/\rho_w = 1.384$, Tank 150; d) Test No. 32, $\rho_d/\rho_w = 1.384$, Tank 850; e) Test No. 9, $\rho_d/\rho_w = 2.335$, Tank 150, f) Test No. 33, $\rho_d/\rho_w = 2.335$, Tank 850.

The radial velocity field is more symmetrical in Tank 850 compared to Tank 150. Due to the sufficient space around the falling disk compared to the smaller tank the displaced water mass

beneath the falling disk can easily sweep away and forms a symmetrical velocity field. However, as illustrated in Figure 4.7a, in the small tank, Tank 150, the radial velocity field of the disk with a density of $\rho_d/\rho_w = 1.080$, is more symmetrical than the one around the densest disk in the same tank, Figure 4.7e. Since the disk has a lower velocity, and consequently lower Froude number, the surrounding water mass has enough time to move away and create a symmetrical field. The affected area of water (i.e., the lightest blue-colored area underneath the disk) for one side of the disk was calculated based on Figure 4.7 for all six cases and the areas were normalized by the projected area of the disk as a scaling factor. In Tank 150, the ratio of the blue-colored area underneath the disk to the projected area of the disk are 0.71, 0.89, and 1.09 for disks with the density of $\rho_d/\rho_w = 1.080$, 1.384, and by 2.335, respectively. Moreover, in Tank 850, the area ratios are 0.53, 0.83, and 1.92, respectively. The results showed that by increasing density of the disk, more volume of water was affected by the disk's motion. When the mass of the disk increases the force affected the mass is also increased; therefore, more water can be displaced due to the higher impact force. The affected volume of water due to insertion of disk can be also used to determine the coefficient of the added mass force.

Another parameter that can be examined here is the affected area based on the width of the tank. The measurements represent that the rate of change of the affected water area in the larger tank, (i.e., Tank 850) is much higher than the small tank (i.e., Tank 150). The reason is that the confinement limited the rate of change of affected area particularly in the denser disk (i.e., $\rho_d/\rho_w = $ 2.335); however, in disks with smaller densities (i.e., $\rho_d/\rho_w = 1.080$ and 1.384), because of the limited space, larger area is affected in depth underneath the disk. Moreover, there should be a threshold based on the tank width and disk density for the affected area below the disk since in Tank 150, disk with a density ratio of $\rho_d/\rho_w = 2.335$ affected less area in comparison to the large tank with the same disk (i.e., Tank 850 and $\rho_d/\rho_w = 2.335$).

The instantaneous vertical velocity field is measured by the PIV method for the same period -0.02 $t_p \leq t \leq 0.02t_p$ and $\Delta t = 0.04$ s and the results are shown in Figure 4.8. The color bar beside the figure shows the vertical velocity range between -0.5 ms^{-1} (downward) and 0.5 ms^{-1} (upward). Since the selected time frame is at the pinch-off time, $-0.02t_p \leq t \leq 0.02t_p$, the upper part of the underwater cavity pinches off already. As a result, in Figures 4.8b and 4.8d, a large reddish area with high intensity can be seen above the disk which shows the upward motion of water (i.e., $v \geq 0.35$ ms^{-}

[1]). However, due to the higher velocity of the densest disk, $\rho_d/\rho_w = 2.335$, in Figure 4.8f, the pinch-off time occurs faster, therefore, the upper part of cavity is removed already and the total momentum of the disk is downward with the magnitude of ($|v| \geq 0.35$ ms^{-1}).
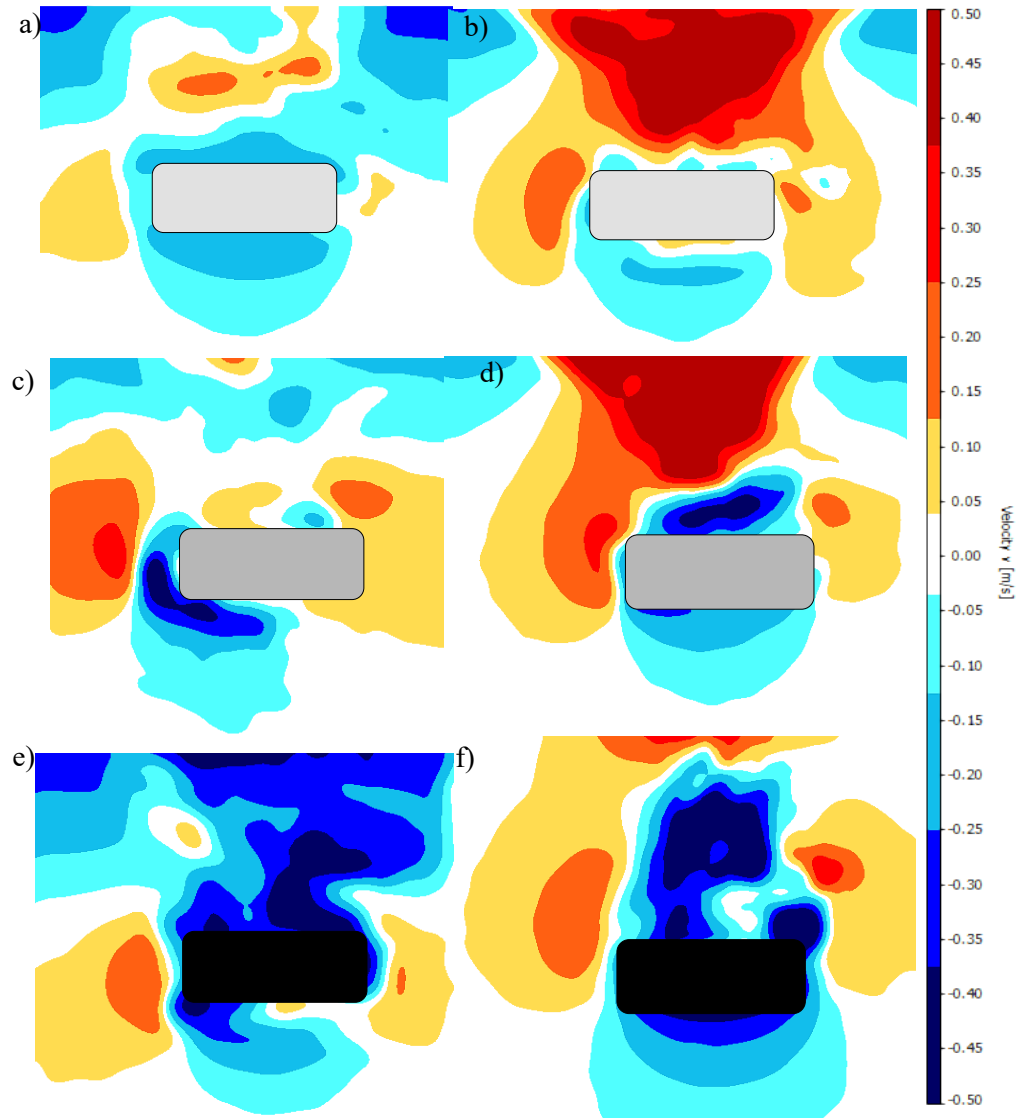
Figure 4.8. Effects of disk density and confinement on contour plots of Vertical velocity, v, in release height of, $h_r = 400$ mm: a) Test No. 7, $\rho_d/\rho_w = 1.080$; Tank 150, b) Test No. 31, $\rho_d/\rho_w = 1.080$; Tank 850, c) Test No. 8, $\rho_d/\rho_w = 1.384$, Tank 150; d) Test No. 32, $\rho_d/\rho_w = 1.384$, Tank 850; e) Test No. 9, $\rho_d/\rho_w = 2.335$, Tank 150, f) Test No. 33, $\rho_d/\rho_w = 2.335$, Tank 850.

On the other hand, in the confined condition (i.e., Tank 150), the velocity field in all three densities shows mostly downward motion beneath and rear of the disk with an upward motion of water on the lateral part that is close to the wall of the tank. In Figure 4.8a, the intensity of downward vertical and side upward velocities are low, i.e., $|v| \leq 0.1$ ms^{-1}, and small areas are affected by the upward velocity. In Figures 4.8c and 4.8e the intensity of the velocity field becomes larger by increasing the density of the disk and the lateral upward velocity areas are larger as well.
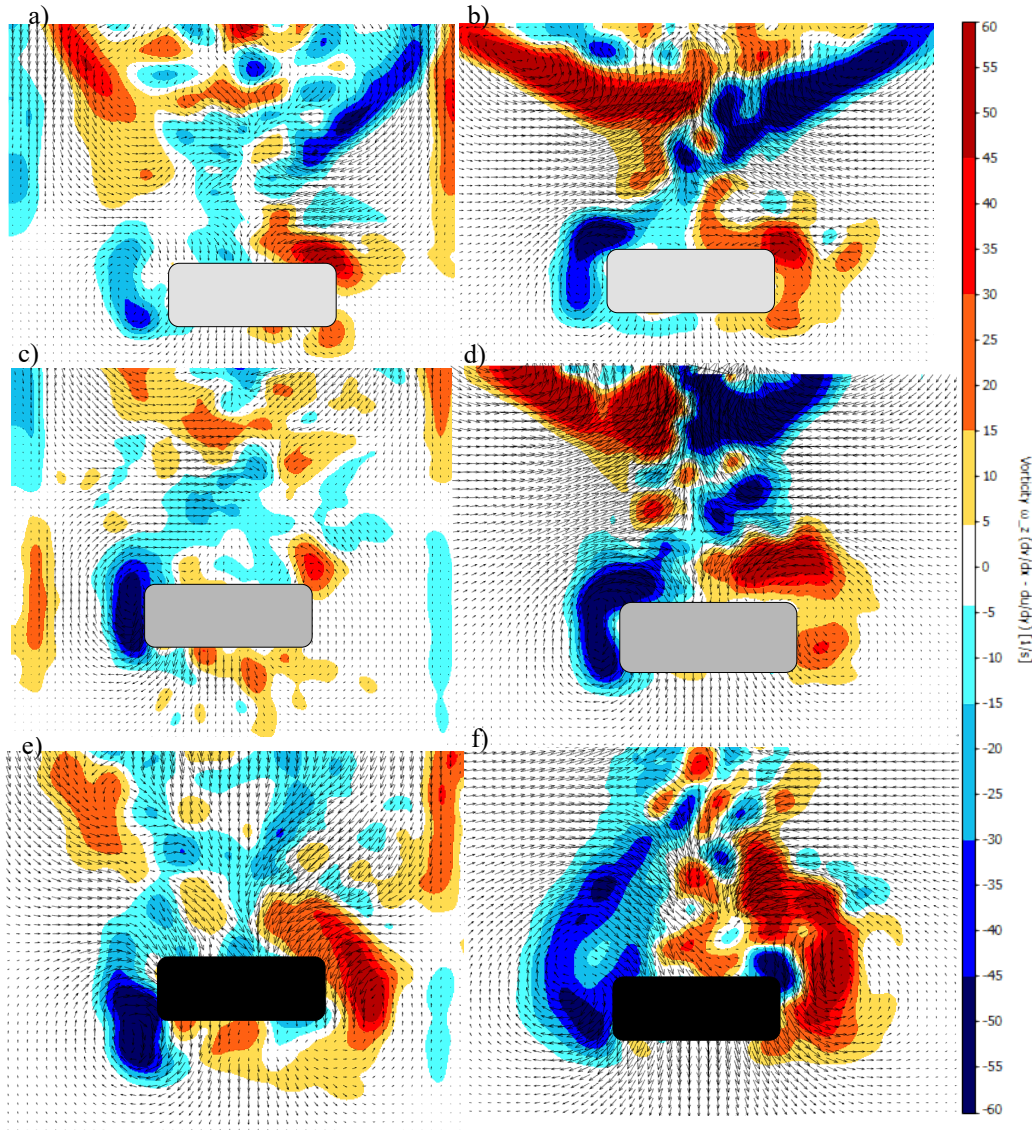
Figure 4.9. Effects of disk density and confinement on contour plots of vorticity, ω, in release height of, $h_r = 400$ mm: a) Test No. 7, $\rho_d/\rho_w = 1.080$; Tank 150, b) Test No. 31, $\rho_d/\rho_w = 1.080$; Tank 850, c) Test No. 8, $\rho_d/\rho_w = 1.384$, Tank 150; d) Test No. 32, $\rho_d/\rho_w = 1.384$, Tank 850; e) Test

No. 9, $\rho_d/\rho_w = 2.335$, Tank 150, f) Test No. 33, $\rho_d/\rho_w = 2.335$, Tank 850.

In Figure 4.9, the vorticity, ω, of the surrounding water was calculated from the PIV data based on the radial and vertical velocity vectors (i.e., $\omega = dv/dx\text{-}du/dy$). The color bar shows the maximum clockwise (i.e., 60 Hz) and counter-clockwise (i.e., −60 Hz) rotations beside the figure. In general, the vorticity fields around the disk in Tank 850 are symmetrical since they have sufficient lateral space to be formed and rotate around the disk. However, in Tank 150, the vorticity fields are not able to be formed due to the narrower space. Such narrowness can cause severe tilting for the disk in a confined space during the water entry process. Moreover, the wall effects can be seen in Figure 4.9a and 4.9c, which affected the vorticity formations and increased the energy loss. Therefore, the energy that is needed to form the symmetrical vortices is consumed on the friction between water and the tank's wall. Eventually, fewer vorticities with smaller values are generated for the same density and released height disks in different tank sizes. The vorticity values increase with the density of the disks in both confined and unconfined conditions. Moreover, in Figure 4.9f, $\rho_d/\rho_w = 2.335$, Tank 850, vorticity rings are larger than other cases and they included larger areas at the rear of the disk. The area ratio with the vorticity of $|\omega| \geq 45$ s^{-1} is doubled in Tank 850 compared to the same area in Tank 150. Therefore, the wall effects reduced both magnitude of vorticity and affected surrounding area in water.

Swirling strength is an effective vortex indicator in wall turbulence (Chen et al., 2018). In other words, the swirling strength shows the strength of the rotating vorticities. The swirling-strength (λ_{ci}) method was first proposed by Zhou et al., (1999) and later refined by Tomkins & Adrian (2003) used to extract vortex from background turbulence. In this chapter, the swirling strength of the vortices generated by the disk motion is calculated through PIV measurements and the results are shown in Figure 4.10. The swirling strength in a two-dimensional velocity field is calculated as:

$$\lambda_{ci} = \max\left(0, \frac{-\Delta}{4}\right) \qquad\qquad\qquad \text{Eq. (4.1)}$$

where Δ is calculated as below based on Zang et al. (2013):

$$\Delta = \left(\frac{\partial u}{\partial x} + \frac{\partial v}{\partial y}\right)^2 - 4\left(\frac{\partial u}{\partial x}\frac{\partial v}{\partial y} - \frac{\partial u}{\partial y}\frac{\partial v}{\partial x}\right) \qquad\qquad\qquad \text{Eq. (4.2)}$$

As can be seen, the swirling strengths are higher than $\lambda_{ci} \geq 0.002 \ \text{s}^{-2}$ around the edge of the disks which are more significant in the larger tank due the thoroughly formation of the vorticities.
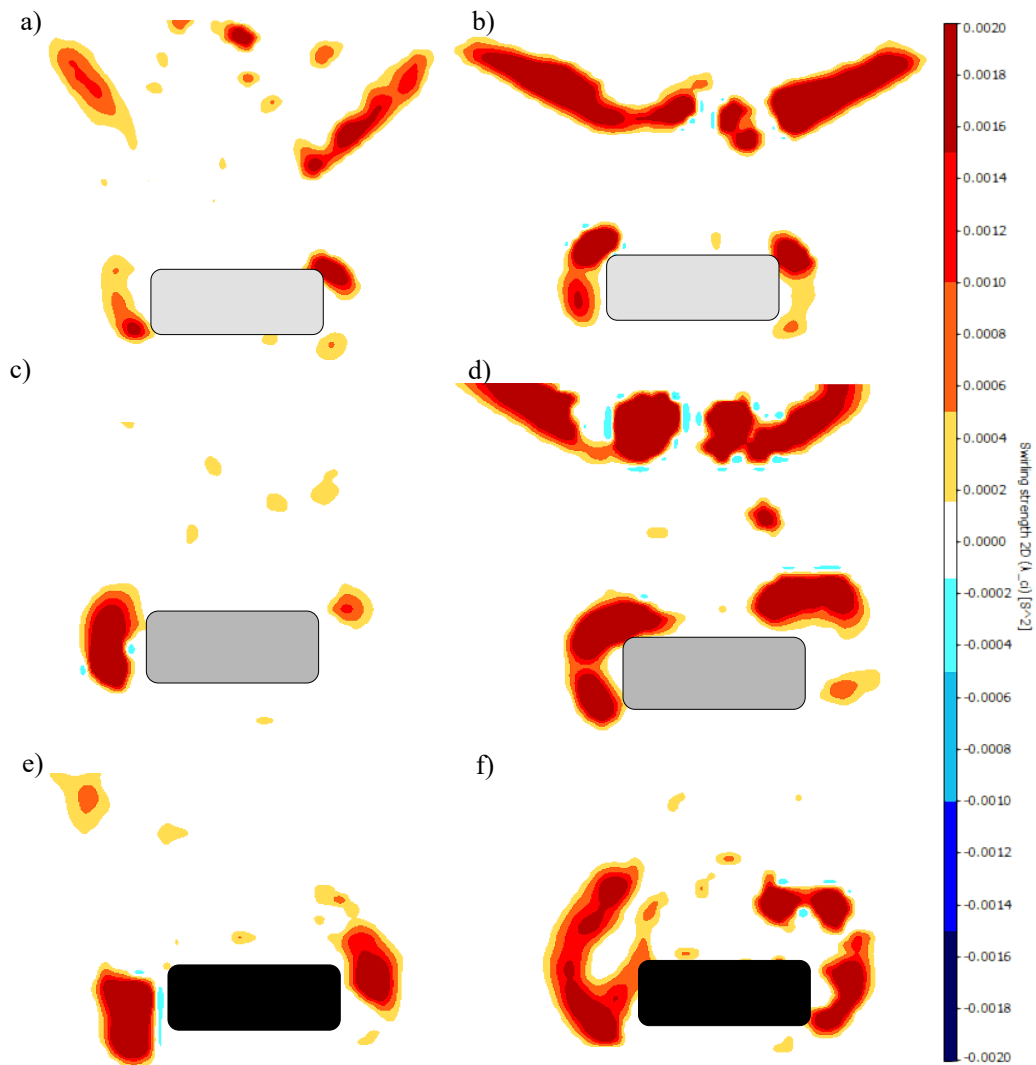
Figure 4.10. Effects of disk density and confinement on contour plots of swirling strength, in release height of, $h_r = 400$ mm: a) Test No. 7, $\rho_d/\rho_w = 1.080$; Tank 150, b) Test No. 31, $\rho_d/\rho_w = 1.080$; Tank 850, c) Test No. 8, $\rho_d/\rho_w = 1.384$, Tank 150; d) Test No. 32, $\rho_d/\rho_w = 1.384$, Tank 850; e) Test No. 9, $\rho_d/\rho_w = 2.335$, Tank 150, f) Test No. 33, $\rho_d/\rho_w = 2.335$, Tank 850.

Generally, in Tank 850, the intensity of the swirling strength is greater compared to the small tank in terms of both the values and strengths because there is enough space for them to be formed

without wall interactions. Moreover, the swirling strength is almost symmetrical in Tank 850. Since the vorticity structures were not fully formed in Tank 150, the swirling strengths were not significant accordingly. Additionally, the swirling strength can be seen in Tank 850, (see Figures 4.10b, 4.10d, and 4.10f), some areas by a distance from the disk, illustrates higher values which represent the after pinch-off upward jets close to the water surface level and this phenomenon is weak in Tank 150 since the vortices is not properly formed due to the wall effects.

The average kinetic energy of the disk was calculated from the PIV data and the results are shown in Figure 4.11 to compare the wall effects in Tank 150 and Tank 850. The average kinetic energy is proportional to the resultant velocity vector of both horizontal and vertical velocity components, u & v. In other words, the mean kinetic energy (MKE) is the average kinetic energy produced by the horizontal velocity, u, and vertical velocity, v. As can be seen in Figure 4.11, the average kinetic energy of the free-falling disk is symmetrical in Tank 850 and it is uniformly distributed at the rear of the disk. The magnitude of the average kinetic energy is mostly greater than 0.15 $(m/s)^2$ behind the falling disk in Tank 850, approximately 1.2 times projected area of the disk. However, in Tank 150, the maximum value for the average kinetic energy can be observed only in one side of the disk. For example, in Figure 4.11 a, at the right hand edge of the disk the average kinetic energy is greater than 0.15 for a small area, approximately 10% of the projected area of the disk in Tank 150. Moreover, the overall average kinetic energy behind the disk in Tank 150 is not symmetrical, whereas in Tank 850, the average kinetic energy distribution is completely symmetrical.

Additionally, for the densest disk with the density ratio of $\rho_d/\rho_w = 2.335$, in Tank 850, the area underneath the disk which is approximately 20% of the total affected area is symmetrically has the average kinetic energy with a range of 0.02 and 0.2 which is related to the density of the disk. However, for the same disk density in Tank 150, the affected area underneath the falling disk is only on the left hand side of the disk and approximately 7% of the total affected area. Overall, the average kinetic energy below the falling disk increases by increasing the density of the disk.
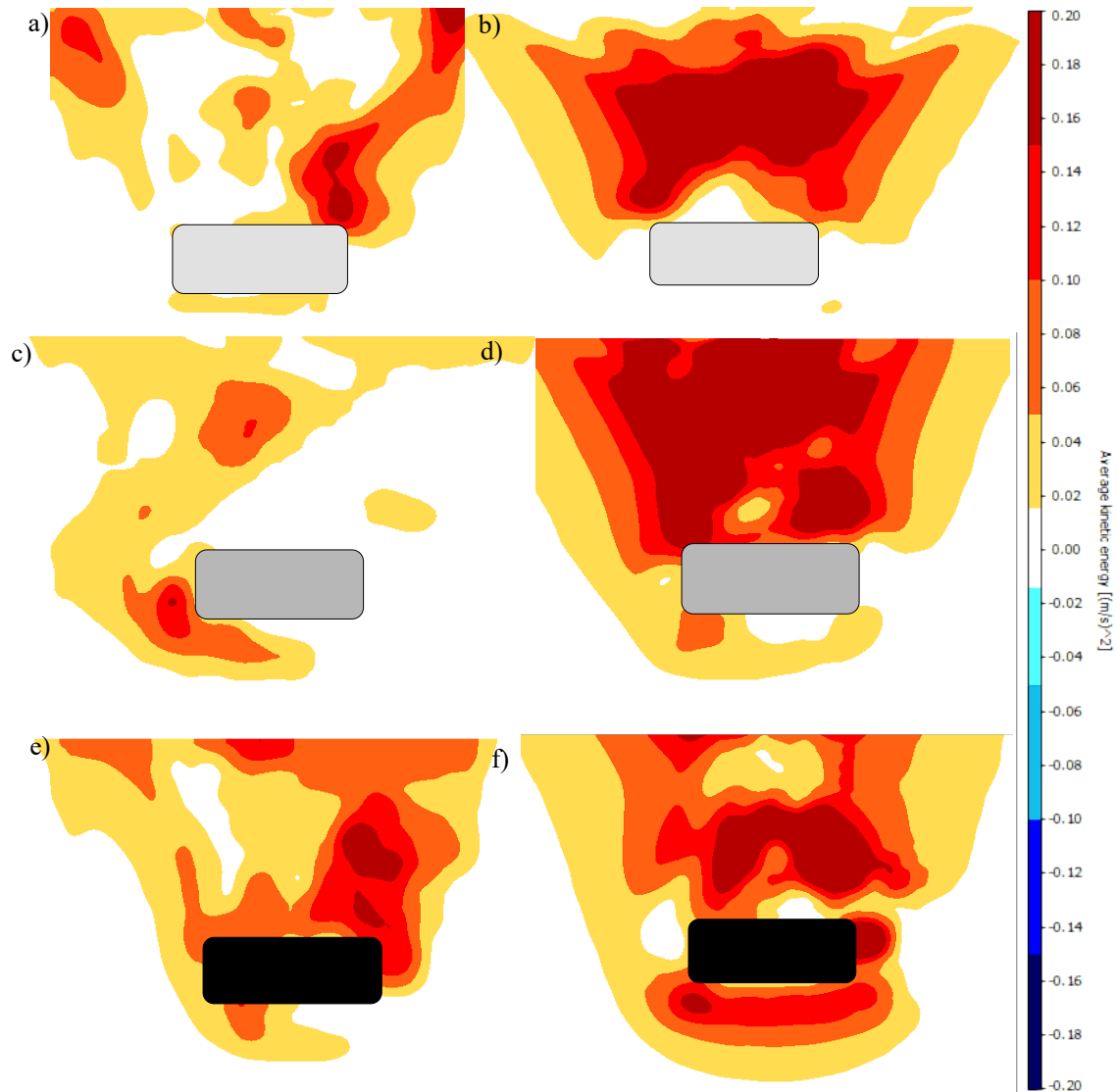
Figure 4.11. Effects of disk density and confinement on contour plots of average kinetic energy, in release height of, $h_r = 400$ mm: a) Test No. 7, $\rho_d/\rho_w = 1.080$; Tank 150, b) Test No. 31, $\rho_d/\rho_w = 1.080$; Tank 850, c) Test No. 8, $\rho_d/\rho_w = 1.384$, Tank 150; d) Test No. 32, $\rho_d/\rho_w = 1.384$, Tank 850; e) Test No. 9, $\rho_d/\rho_w = 2.335$, Tank 150, f) Test No. 33, $\rho_d/\rho_w = 2.335$, Tank 850.

In Figure 4.12, the results obtained from the PIV analysis of the free-falling disk are illustrated in two tanks. The turbulent kinetic energy (TKE) of the disk is the kinetic energy related to the fluctuation of the radial and axial velocities. The results showed that the velocity fluctuations are much higher in Tank 850 at the rear of the disk compared to Tank 150. For example, the TKE $\geq$ 0.15 (m/s)^2 that is shown by dark red covered almost the whole water column area at the rear of

the disk in Tank 850, whereas in Tank 150 this area reduced to approximately less than 5% of the rear water column. In Tank 150, the turbulent kinetic energy is less than 0.1 $(m/s)^2$ which indicates less velocity fluctuations due to confinement in the smaller tank. As can be seen in Figures 4.12a, 4.12c, 4.12e, in Tank 150, the maximum turbulent kinetic energy is more localized, however, in Tank 850, Figures 4.12b, 4.12d, 4.12f, a large area at the wake of disk has the maximum values of the turbulent kinetic energy.
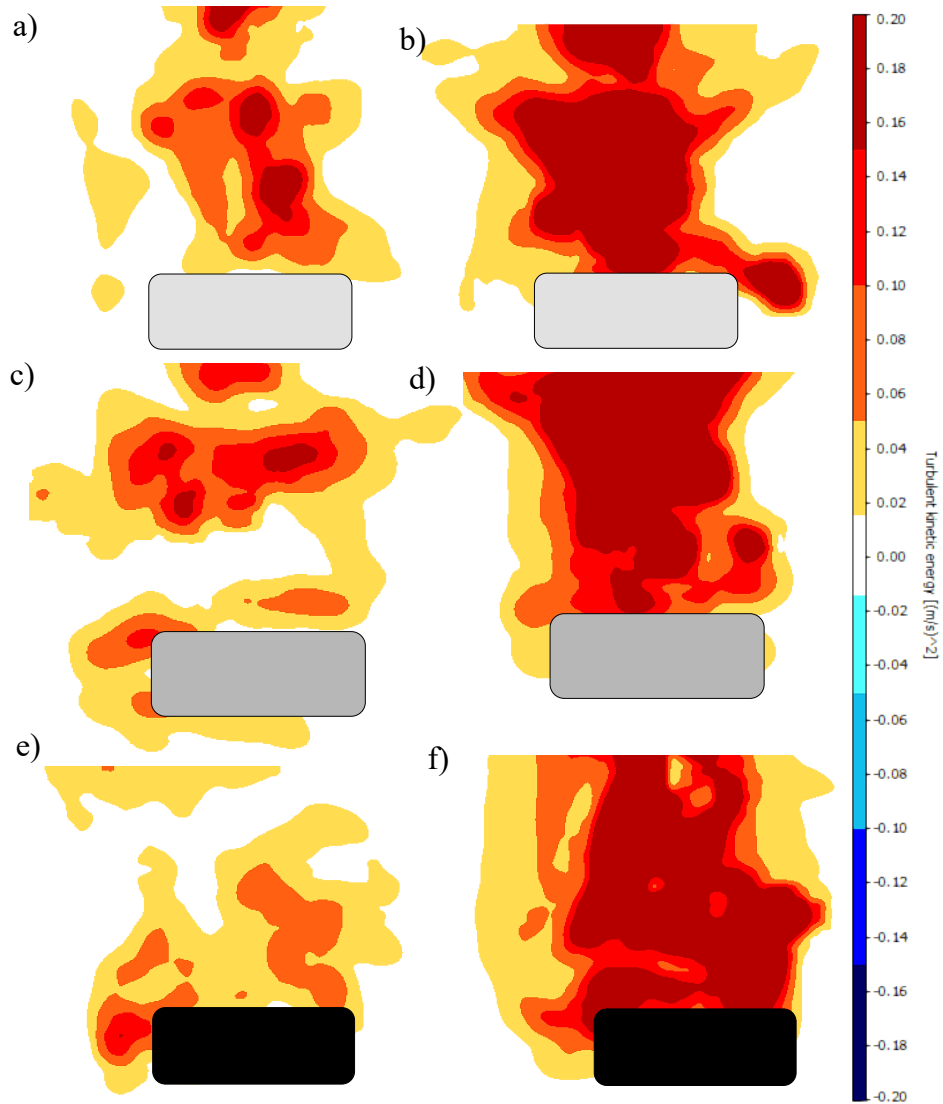
Figure 4.12. Effects of disk density and confinement on contour plots of Turbulent kinetic energy, in release height of, $h_r = 400$ mm: a) Test No. 7, $\rho_d/\rho_w = 1.080$; Tank 150, b) Test No. 31, $\rho_d/\rho_w = 1.080$; Tank 850, c) Test No. 8, $\rho_d/\rho_w = 1.384$, Tank 150; d) Test No. 32, $\rho_d/\rho_w = 1.384$, Tank 850;

e) Test No. 9, $\rho_d/\rho_w = 2.335$, Tank 150, f) Test No. 33, $\rho_d/\rho_w = 2.335$, Tank 850.

4.4.   Conclusions

The results of experimental investigations on the water entry of free-falling thick disks in tanks with different normalized tank width to disk diameter ratios of W/d_o of 1.97, 2.62, 5.90, and 11.15 were investigated in this chapter. Detailed observations of splash curtains and underwater cavity formation have shown noticeable differences between confined and unconfined media. The effects of release height and density of the disk were also studied in different tanks. The results indicated that in the confined tank (Tank 150), once the splash curtains formed, they stuck to the tank wall and moved up instead of being sealed. This process continued and consequently, surface undulations were formed on the surface of the underwater cavity. In the medium-sized tank (Tank 200), the crown is mostly formed, however it was partially sealed and in Tank 850 that was unconfined the crown was fully formed and fully sealed. Therefore, the crown and cavity formation were highly affected by the confinement effects.

The pinch-off time was also affected by the wall effects, in the largest tank (Tank 850), the pinch-off time was constant for a disk with the same density releasing from different release heights, approximately $t_p/(d_o/g)^{1/2} = 1.6$. However, by reducing the width dimension of the tank, it was found that the pinch-off time directly increased proportionally to the Froude number. Disks with greater density had higher pinch-off time. The results indicated that the pinch-off depths were directly increased by increasing the tank's width due to the removing of the wall effects . Moreover, the results showed that pinch-off depths became larger by increasing release heights and consequently increasing the Froude number. The results indicated that irrespective of the tank width, the frontal position of the disk at the pinch-off time was highly sensitive only to the density of the disk. By increasing the release height from 200 mm to 500 mm in Tank 850, the dimensionless pinch-off depth H_p/r is almost doubled from 0.88 to 1.75.

In this chapter, extensive PIV analyses were performed at pinch-off period and different characteristics of the flow field surrounding the free falling disks were obtained. The most significant results were found that in the confined tank, (i.e., Tank 150) the proper velocity and vorticity field were not able to be fully formed due to the small space between the disk and the tank's wall. The PIV results showed that in the wake of the disk in confined tank, Tank 150, the

velocity field is asymmetric and vortex structures were formed incompletely, while in Tank 850 due to the sufficient space around the disk, the velocity field is mostly symmetric. In terms of the affected area underneath the disk, by increasing the density of the disk from $\rho_d/\rho_w = 1.080$ to 1.384, and 2.335 the affected area of water underneath the disk is also increased. This increment is higher in Tank 850 in comparison to Tank 150, for example, in Tank 150 the ratio of affected area to the projected area of the disk are 0.71, 0.89 and 1.09 for and in Tank 850, the area ratios are 0.53, 0.83, and 1.92, respectively.

The vertical velocity field of the disk was obtained by PIV measurements, and it was found that the pinch-time in the densest disk occurred faster than other disks. Moreover, the local axial velocity of the surrounding water in Tank 150 and Tank 850 with densest disk are $|v| \geq 0.35$ ms^{-1}, however, the velocity field is symmetric in Tank 850 in comparison to Tank 150. The vorticity field is also thoroughly and symmetrically formed around the free-falling disks in Tank 850, whereas in Tank 150 the vorticity field is highly chaotic. In the smaller tank, i.e., Tank 150, because of the unbalanced vorticity, the disk experienced more tilting and instabilities while descending. The ratio of the area with the vorticity of $|\omega| \geq 45$ s^{-1} is almost twice in Tank 850 compared to the same area in Tank 150. Therefore, the confinement reduced both magnitude of vorticity and affected surrounding water area. Swirling strength was also obtained around the free-falling disks through PIV analysis. It was observed that the denser the disk, the higher the strength of swirling around the disk, and the wall effect reduces the swirling strength. Moreover, the magnitude of swirling strength around the edge of the disk is larger than $\lambda_{ci} \geq 0.002$ s^{-2} which showed more rotating flows around the free-falling disks.

Finally, the average and turbulent kinetic energy field for the surrounding water of free-falling disk were obtained by PIV measurements. The average kinetic energy in Tank 850 is uniformly distributed behind the falling disk which indicates the symmetrical distribution of vertical and radial velocity of the disk. The maximum value of the average kinetic energy, MKE ≥ 0.15, is concentrated in one side of the disk in Tank 150 and it covers only a small area which is approximately 10% of the projected area of the disk. The turbulent kinetic energy at the rear of the disk showed high velocity fluctuations in Tank 850 in comparison to Tank 150. The maximum TKE in Tank 150 is less than 10% of TKE in Tank 850 in all cases.

Part II

Water entry of a group of small solid objects

Chapter 5

5. Mixing of Twin Particle Clouds in Stagnant Water

5.1. Introduction and Literature Review

The ability to predict the dynamic behavior of the released sedimentary materials in aqueous environments is of significant environmental interest. During land reclamation and dredged material disposal, large amounts of sediments are discharged into the aquatic environments, which mix with the ambient and form sediment deposition (Bush et al., 2003; Zhao et al., 2014; Azimi et al., 2014 and 2015; Lai et al., 2018; Manzouri and Azimi, 2019a; Sharif and Azimi, 2020). Releasing dredging material into the ocean raises concerns about the feasibility of accurately predicting the motion of dredge material and precisely locating dredged materials in a targeted area to minimize sediment losses to the environment during disposal. In addition, if the waste disposal is contaminated, it is critical to predict the fate of both the solid waste and the fluid with which it interacts (Azimi et al., 2011; Bush et al., 2003; Lai et al., 2016a). The dredged material can be either instantaneously released into a quiescent ambient to form a particle cloud or continuously released to form slurry jets/plumes (Azimi et al., 2012a; Lai et al., 2016b; Moghadaripour et al., 2017a, 2017b). In other words, particle clouds are formed when a finite mass of particles is released through a nozzle or a pipe into quiescent ambient. The initial geometry and hydrodynamic conditions determine the motion of particles as sand/slurry jets or particle clouds. Moreover, the threshold of classification can be quantified by the initial parameters such as nozzles diameter, initial aspect ratio, and Stokes number (Moghadaripour et al., 2017b; Manzouri and Azimi, 2019b).

Mass of sand particles m and the initial release geometry such as nozzles diameter d_o and its angle to the fluid surface α play significant roles in vortex formation and dynamic motion of particle clouds. Sand mass can be represented by the length of occupied sand in a pipe with a diameter of d_o as $L_o = 4m/\pi d_o^2 c_o \rho_s$, where c_o is the initial sand volume fraction (i.e., $c_o = 0.6$ vol/vol) and ρ_s is

the sand density. The non-dimensional aspect ratio L_o/d_o was found to be one of the controlling factors to distinguish the motion of slurry jets and particle clouds.

Laboratory experiments indicated the importance of the cloud aspect ratio L_o/d_o on the motion of single-phase turbulent thermals (Bond and Johari, 2005), particle clouds in the ambient water (Lai et al., 2014; Moghadaripour et al., 2017b; Zhao et al., 2013) and through an immiscible interface (Mohammadidinani et al., 2017; Manzouri and Azimi, 2019b; Azimi, 2019).

Particle clouds have been conceptualized into three regimes known as the cloud formation process (Rahimipour and Wilkinson, 1992; Noh and Fernando, 1993). In the first phase, which is known as the initial acceleration or ballistic phase, particles are packed and descended as particle clouds with sharp fronts. The second phase (i.e., self-preserving or self-similar turbulent thermal) begins once the turbulence level in the ballistic phase increases due to the boundary shear and the momentum transfer. A strong vortex structure is formed through turbulent entrainment and particles are swept upward from the frontal region continuously by the vortex motion. The last phase is called a dispersive or a particle-settling phase within which sand particles have detached from the entrained fluid due to the buoyancy and uniformly descended at a slightly higher velocity than the settling velocity of the individual sand particles u_∞.

A depth where particles fall out of the thermal regime is called the fallout height or the boundary depth Z_b (Slack, 1963). Turner (1969) formulated the boundary depth by normalizing the cloud buoyancy $B_o/(z^2 u_\infty^2)$ where z is the distance from the nozzle to the cloud front and $B_o = g'V_o = g[(\rho_s-\rho_w)/\rho_w)](\pi d_o^2/4)L_o c_o$ where g' is known as the reduced gravity, g is the acceleration due to the gravity, V_o is the volume of sand particles, and ρ_w is the density of water. Bush et al., (2003) defined that the transition between thermal and swarm phases increases at the fallout height, which enhances with the mass of sand particles. Noh and Fernando (1993) reported that the threshold of the normalized cloud buoyancy of thermal is at $B_o/(z^2 u_\infty^2) = 0.1$. For $B_o/(z^2 u_\infty^2) \geq 0.1$, a particle cloud acts as a turbulent thermal, and for $B_o/(z^2 u_\infty^2) < 0.1$ particles settle down like a swarm of particles with a fall velocity of slightly higher than u_∞.

The growth rate of particle thermal can be quantified using the entrainment coefficient α_e as a ratio of entrainment velocity u_x to the centerline velocity u_z of particle clouds (Morton et al., 1956). To determine the entrainment capacity of the sand jet front, Azimi et al., (2012a) correlated the

average velocity of entrained water u_e with the particle cloud frontal velocity as $u_e = \alpha_e u_f$. For slurry jets, the entrainment capacity diminished by increasing particle concentration, it reached $0.50\alpha_e$ of single-phase water jets (Azimi et al., 2012a). An absolute entrainment coefficient α_o was introduced by normalizing the entrainment velocity with the initial sand jet velocity u_o. It was found that the absolute entrainment coefficient α_o of slurry jets was higher than single-phase water jets for $z/d_o < 80$. However, for $z/d_o \geq 80$, α_o depended on the nozzle size. Moghadaripour et al., (2017a) defined the entrained ambient flow into particle cloud (ΔQ_e) by introducing the rate of change of its volume with time as $\Delta Q_e = dV/dt$. Moreover, by dividing the entrained water flow rate by the particle cloud surface area A_s, the average velocity of entrained water u_e can be identified as $u_e = \Delta Q_e/A_s$.

The cloud number (N_C) was used in literature to study the motion of particle clouds in water and to characterize the conversion of thermal to settling regimes (Rahimipour and Wilkinson, 1992). Cloud number represents the ratio of particle settling velocity (u_∞) to the characteristic cloud velocity ($(B_o/\rho_w)^{1/2}/r$) as $N_C = u_\infty r(\rho_w/B_o)^{1/2}$ where r is the bulk radius of particle clouds. Particle clouds are in the thermal regime for $N_C < 1$ and in this regime, the cloud growth rate is a function of cloud number. For $N_C \geq 1$ (practically when N_C reaches 1.5), the growth rate of particle clouds becomes very small (Rahimipour and Wilkinson, 1992). Some experimental studies used the cloud number to investigate the motion of particle clouds in stagnant water (Lai et al., 2013, 2016a, b; Wang et al., 2015). Moghadaripour et al. (2017b) showed that the cloud number is the product of aspect ratio and particle size in the form of Stokes' number $St = [(\rho_s - \rho_w)d_{50}^2 u_o]/18\mu d_o$ where d_{50} is the mean particle size and μ is the dynamic viscosity of water. Wen and Nacamuli (1996) conducted flow visualization experiments and classified the motion of particle clouds into clump and cloud regimes based on the Rayleigh number defined as $Ra = (B_o/r_o^2)/u_z^2$ in which r_o is the initial equivalent radius of a sphere with the same total volume of particles and void spaces and it can be obtained as $r_o = [(3V_o)/(4(c_o)\pi)]^{1/3}$. The defined Rayleigh number is interchangeable with the cloud number N_C.

A trailing stem grows behind a cloud frontal head depending on the initial aspect ratio and particle size (Azimi et al., 2012a). In order to enhance the deposition mechanism of particle clouds and reduce environmental concerns, the trailing stem in particle clouds should be eliminated. This can be achieved by simultaneously releasing smaller sand masses from adjacent dredgers into the ambient water. The release of a pair or rows of single-phase water jets/plumes known as mutual

jet attractions resulted in a significant change in jet trajectories and energy dissipations (Lai and Lee, 2012). The jet mixing also leads to overlap of the passive scalar fields associated with the individual jets, resulting in merging characteristics that are drastically different from those of an independent free jet (Lai and Lee, 2012; Cenedese and Linden, 2014; Rooney, 2015 and 2016).

Despite the significance of releasing sedimentary material in numerous engineering and environmental practices, no comprehensive study has been devoted to the mixing and merging of a pair of particle clouds in homogenous ambient environments. The primary objective of this chapter is to investigate the particle dynamics of a twin particle cloud in stagnant and homogeneous ambient water. Similar to single particle clouds, dynamics of twin particle clouds are influenced by the initial aspect ratio, particle size, and the distance between the adjacent nozzles named as source separation distance (ε). Effects of the initial parameters on the cloud characteristics such as penetration length, cloud width, and frontal velocity were investigated in a pair of particle clouds with an initial mass of $m/2$, and the results were compared with a single particle cloud of mass m.

The sediment suspension duration in water has been used as a mixing indicator; therefore, obtaining the optimum distance between two adjacent clouds to minimize the sedimentation mixing time is of great interest. This can be helpful to design dredgers with two discharging pipes and is applicable to having two dredgers dumping dredged materials with a known source separation between two dredgers discharging pipes. A non-continuous releasing mechanism is suitable for the proposed setup. The total volume of the dredging material is divided into smaller volumes in the field and then released over time. The second objective of this chapter is to understand the effects of the initial aspect ratio L_o/d_o and the normalized source separation distance between two nozzles ε/d_o on the mixing capacity defined by entrainment coefficient α_e, and turbulence intensity defined as $u'_z/\overline{u_z}$. This chapter is organized as follows: in section 5.2, material and methods including experimental setup, image analysis, and particle image velocimetry techniques are described; in section 5.3, the experimental results on twin particle clouds are discussed and the effects of aspect ratio on particle cloud properties are investigated; finally, in section 5.4, the summary and conclusions of the mixing of twin particle clouds in stagnant water are presented.

5.2. Material and Methods

5.2.1. Experimental setup

Laboratory experiments were carried out in a rectangular glass-walled tank which measured 1.65 m long, 0.85 m wide, and 0.95 m high in the Multiphase Flow Research Laboratory (MFRL) at Lakehead University. The tank was filled with tap water with an ambient temperature of $20 \pm 2^\circ$ C ($\mu = 9.77 \times 10^{-4}$ kg/m.s) up to a constant water depth of 0.85 m. Sand particles with a density of 2564 kg/m^3 were selected and sand particle sizes were limited between sieve numbers #30 and #40 with a median sand size of $d_{50} = 0.507$ mm. The sand particles were carefully washed and dried before filling the pipes to avoid any impurities in sand particles. Figure 5.1 shows the schematic front view of the experimental setup and an example of twin particle cloud interactions. The process of releasing dry sand particles with different initial conditions was recorded by a high-speed camera with a capturing speed of 30 frames per second (Photron-FASTCAM, 1024PCI-100KC, Japan). Horizontal and vertical rulers were placed inside the tank for image calibration and correcting image distortions. The drop height of particles that resulted in the lowest percentage of mass in the trailing stem for L_o/d_o ranging from 9.7 to 38.8 was found to be at the water surface (Gensheimer et al., 2013). However, to eliminate bubble formation and to minimize air entrainment a short distance of approximately 5 mm was allocated between the nozzles and water surface (Azimi et al., 2012a; Moghadaripour et al., 2017a).

Two steel nozzles with the inner diameters of $d_o = 8$ mm were used in this study. The length of sand particles filled in each pipe (L_o) and the height of virtual origin (Z_v), indicating the imaginary released source of a merged cloud, are shown in Figure 5.1. It should be noted that the Stokes number for the current study is St = 0.55 indicating that the particles are classified as hydro-dynamically large particles in this field (Moghadaripour et al., 2017a).

The fluid with entrained particles was illuminated using two light sources (Woods L13, 1000-Watt Telescope Work Light, Canada) from both sides of the glass tank so that particles were visible for particle-tracking analysis. A total number of 28 experiments were conducted (see Table 5.1) to investigate the effects of aspect ratio (L_o/d_o) and a distance between two nozzles (ε) on the evolution of twin particle clouds with time. The cloud number values of this study ranged from

8.9x10^{-2} to 11.22x10^{-2} indicating that all experiments were within the cloud formation regime and not in the clump formation regime (Zhao et al., 2014).
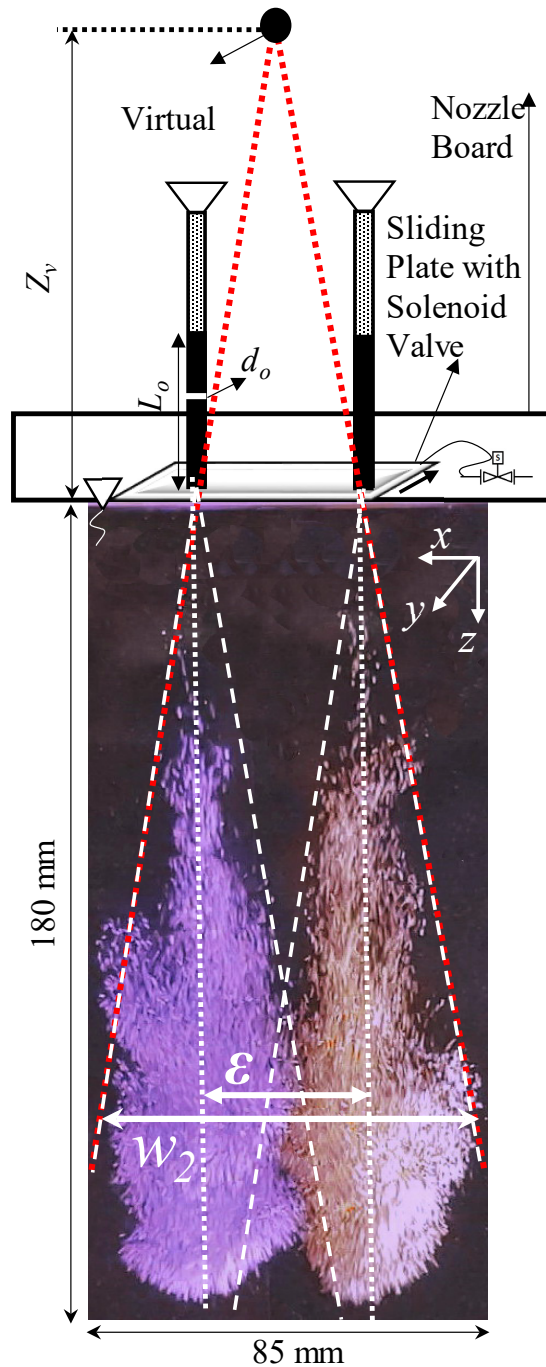
Figure 5.1. A schematic front view of the experimental setup, the coordinate system, and an example of twin particle cloud interactions for Test No. 3 (2x3 g, $\varepsilon = 40$ mm). Z_v indicates a vertical distance from the virtual origin to the water surface.

Different masses of dry sand particles (i.e., m = 6, 12, 18, and 24 g) were selected to form a wide range of L_o/d_o from 9.7 to 38.8 (see Figure 5.2). Based on the tank depth of z = 0.85 m in this study, no particle interactions were observed between the two adjacent particle clouds below the minimum aspect ratio of L_o/d_o = 9.7. The middle particle clouds were formed by increasing the sand mass with an increment of 6 grams (i.e., L_o/d_o = 19.4, 29.1). The non-dimensional aspect ratios and source separations provided flexibility to select the size of the pipes, carrying mass or type of equipment needed for dredging. It should be mentioned that the particle clouds behaved like sand jets beyond the maximum aspect ratio of L_o/d_o = 38.8.

As can be seen in Figure 5.2, particle clouds were fully formed in the existing water dept except in tests with L_o/d_o = 38.8 in which sand particles were entered continuously into the water. It should be noted that the formation of sand jets and particle clouds in water is scaled with the aspect ratio L_o/d_o and water depth z; therefore, a combination of these length scales determines the boundary between sand jets and particle clouds. A non-dimensional parameter in the form of $L_o/(zd_o)^{1/2}$ is introduced to incorporate the effect of water depth in formation of sand jets and particle clouds. Based on this study, particle clouds were found to form when $L_o/(zd_o)^{1/2} < 3.75$. However, future independent studies using different tank water depths are needed to ascertain the numerical value of 3.75.
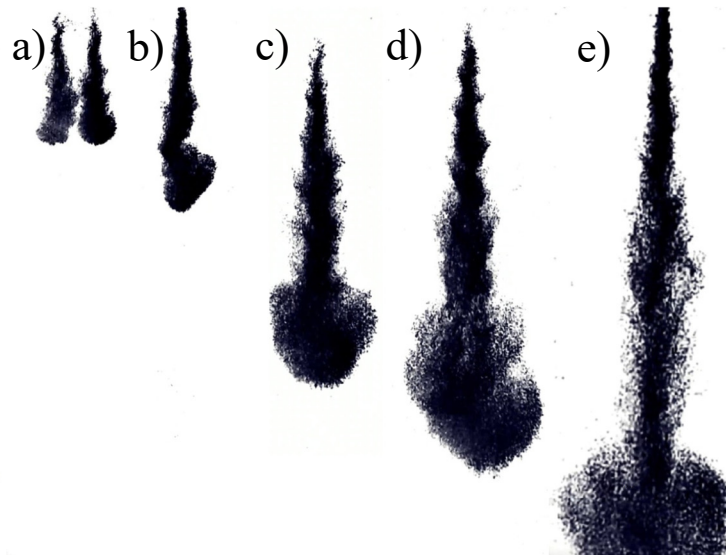
Figure 5.2. Raw images of particle clouds with different aspect ratios: (a) a twin-particle cloud, L_o/d_o = 9.7; (b) a single particle cloud, L_o/d_o = 9.7; (c) a single particle cloud, L_o/d_o = 19.4; d) a single

particle cloud, $L_o/d_o = 29.1$: e) a single particle cloud, $L_o/d_o = 38.8$.

For twin particle cloud tests, the mass of sand particles was equally divided by half and the motion of two adjacent particle clouds releasing from two pipes of different distances was studied. The benchmark tests for single particle clouds were labeled as (1xm g) and they had the same L_o/d_o as their corresponding twin clouds (2xm/2 g). To investigate the effects of source separation in particle clouds and to optimize the released distance, six nozzle separation distances (ε) ranging from 20 mm to 120 mm were selected corresponding to the non-dimensional separation distances of $\varepsilon/d_o = 2.5, 5, 7.5, 10, 12.5$ and 15. The $\varepsilon/d_o = 0$ represented the perfect alignment of two particle clouds by testing single particle clouds with a mass of m and the results were used for benchmark testing. Experiments were repeated three times to study the repeatability of measurements and to examine the uncertainty of experimental data. Variations of the frontal position z, cloud frontal width w, frontal velocity u_f, and the centerline vertical (u_z) and radial (u_x) velocities of particles at different evolution time frames were measured.

5.2.2. *Image analysis and data processing*

Image processing techniques were employed to extract data from recorded videos and images. The MATLAB image processing toolbox (Math Works, Inc., 2018) was customized to accurately detect the boundary of particle clouds and to detect the variations of frontal position and cloud width with time. The boundary detection and image thresholding techniques were employed from the background subtraction method of the PIVlab add on in MATLAB software to (i) differentiate particle clouds from background ambient, (ii) remove background noises, and (iii) find the boundary of the clouds (Thielicke and Stamhuis, 2014). Figure 5.3a shows the raw images of a particle cloud for Test No. 8.
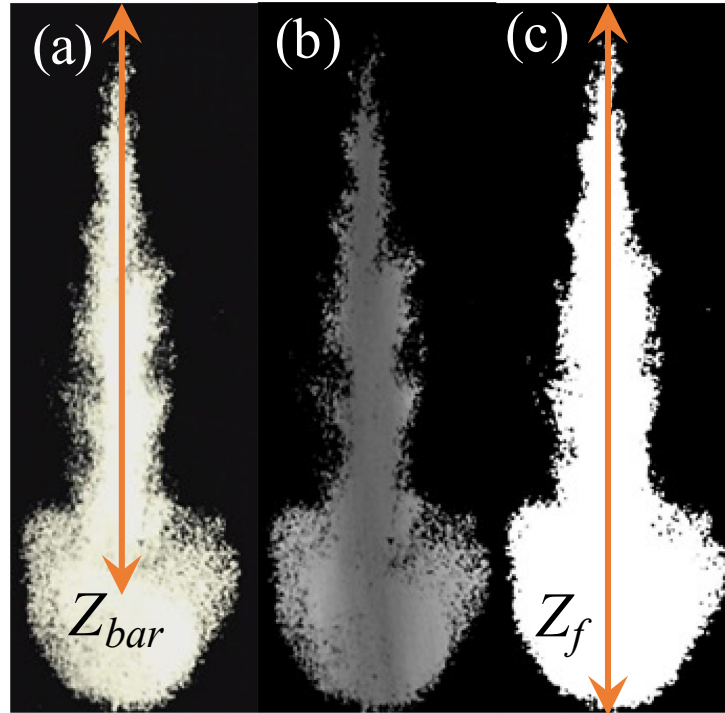
Figure 5.3. Raw and pre-processed images of particle clouds for Test No. 8 ($m = 12$ g, $L_o/d_o = 19.4$): (a) The original image of a particle cloud; (b) The pre-processed image with background subtraction using PIVlab; (c) The binarized image of a cloud which used for masking the cloud in PIV analysis. Z_{bar} is a vertical distance from water surface to the cloud's center of mass and Z_f is a vertical distance from the water surface to the front of the cloud.

The boundary of the cloud in raw images was detected by the background subtraction technique and the resulting image is shown in Figure 5.3b. Then, a mask was applied to the processed image to convert a grayscale into a binary image (see Figure 5.3c). The frontal position Z_f and the centroid of particle clouds Z_{bar} were determined by the image analyzing technique. The extracted cloud properties such as the maximum cloud width, frontal position, and velocities were extracted from the binary images. The binary data were converted to physical dimensions using a scaling image taken before each test.

A time-resolved Digital Particle Image Velocimetry Toolbox (PIVlab) was used to analyze the motion of particles in twin particle clouds. Using a region of interest (ROI) of 0.3 m vertically x 0.12 m horizontally and an image resolution of 2000 pixels by 1100 pixels, the diameter of sand particles in each image became comparable to approximately 1.85 times of a pixel. The motion of the particles in each consecutive image was used to calculate the velocity and direction of particles

in the surrounding fluid. The pre-processing filters known as CLAHE and Wiener2 de-noise were used to clarify and de-noise images before further analysis. The region of interest was split into a number of interrogation windows and the velocity vector calculation algorithm was repeated four times (i.e., 4-pass algorithm). In order to acquire high-resolution PIV data for measuring mean velocity and turbulence intensity, four interrogation windows with a systematically reducing size were selected. The interrogation started with a window size of 64 x 64 pixels with an overlap of 32 pixels (i.e., %50 overlap) in the first pass. The interrogation window was then reduced to 32 x 32 pixels with a 50% overlap in the second pass. The interrogation windows for the third and fourth passes were identical (16 x 16 pixels with 50% overlap). Finally, velocity data were extracted using a poly-line command in pixel values and it was converted to a physical unit of m/s with an accuracy of 0.00821 m/s for a pixel per frame.

5.3. Results and Discussion

5.3.1. Evolution of particle clouds

The fallout height formula for particle clouds based on the threshold value proposed by Noh and Fernando (1993) was rearranged to estimate the boundary depth as:

$$Z_b = \sqrt{\frac{g[(\rho_s - \rho_w)/\rho_w](\pi d_o^2/4)L_o}{0.1u_\infty^2}}$$

Eq. (5.1)

By extracting constant parameters, Eq. (5.1) was simplified as:

$$Z_b = \varphi_1 d_o^{3/2}(L_o/d_o)^{1/2}$$

Eq. (5.2)

where $\varphi_1 = [(\pi g(\rho_s - \rho_w)/(0.4\rho_w u_\infty^2)]^{1/2}$. The settling velocity of the particles in this study is approximately 0.075 m/s. Therefore, using $d_o = 0.008$ m, Eq. (5.2) simplifies to $Z_b \approx 0.105(L_o/d_o)^{1/2}$ and the boundary depths for $L_o/d_o = 9.7, 19.4, 29.1,$ and 38.8 in single particle clouds were 0.327 m, 0.462 m, 0.566 m, and 0.654 m, respectively (see Table 5.1).

The boundary depth is also correlated with the initial Reynolds number (Re) as:

$$Z_b = \phi_2 \, \text{Re} \, (L_o/d_o)^{1/2}$$

Eq. (5.3)

where $\varphi_2 = [(\pi c_o \mu^2 (\rho_s - \rho_w))/(0.4 \rho_w^3 u_\infty^2)]^{1/5}$ and $\mathrm{Re} = \rho_w u_o d_o/\mu$. The initial velocity of particle clouds is correlated with the nozzle diameter in the form of $u_o = c_1 (g d_o)^{1/2}$ where $c_1 = 0.68$ (Cai et al., 2010). Although the calculated boundary depths were similar for twin particle clouds with the adjacent nozzles, they were smaller than the calculated boundary depths for twin particle clouds releasing far from each other.

Table 5.1. Experimental details on the evolution of a pair of particle clouds in water with different hydrodynamic and non-dimensional parameters for $d_{50} = 0.507$ mm and $d_o = 8$ mm.

Test No.	Sand mass m	Nozzle spacing ε	L_o	r_o	Time scale T	V_o $(\times 10^3)$	B $(\times 10^{-5})$	N_c $(\times 10^{-2})$	L_o/d_o	Z_b
	(g)	(mm)	(mm)	(mm)	(s)	(mm^3)	(m^4/s^2)	(—)	(—)	(m)
1	1x6	0	77.6	11.60	1.38	3.90	6.01	11.22	9.70	0.33
2	2x3	20	77.6	11.60	1.38	3.90	6.01	11.22	9.70	0.33
3	2x3	40	77.6	11.60	1.38	3.90	6.01	11.22	9.70	0.33
4	2x3	60	77.6	11.60	1.38	3.90	6.01	11.22	9.70	0.33
5	2x3	80	77.6	11.60	1.38	3.90	6.01	11.22	9.70	0.33
6	2x3	100	77.6	11.60	1.38	3.90	6.01	11.22	9.70	0.33
7	2x3	120	77.6	11.60	1.38	3.90	6.01	11.22	9.70	0.33
8	1x12	0	155.2	14.60	1.95	7.80	12.02	9.99	19.40	0.33
9	2x6	20	155.2	14.60	1.95	7.80	12.02	9.99	19.40	0.46
10	2x6	40	155.2	14.60	1.95	7.80	12.02	9.99	19.40	0.46
11	2x6	60	155.2	14.60	1.95	7.80	12.02	9.99	19.40	0.46
12	2x6	80	155.2	14.60	1.95	7.80	12.02	9.99	19.40	0.46
13	2x6	100	155.2	14.60	1.95	7.80	12.02	9.99	19.40	0.46
14	2x6	120	155.2	14.60	1.95	7.80	12.02	9.99	19.40	0.46

15	1x18	0	232.8	16.70	2.39	11.70	18.03	9.33	29.10	0.57
16	2x9	20	232.8	16.70	2.39	11.70	18.03	9.33	29.10	0.57
17	2x9	40	232.8	16.70	2.39	11.70	18.03	9.33	29.10	0.57
18	2x9	60	232.8	16.70	2.39	11.70	18.03	9.33	29.10	0.57
19	2x9	80	232.8	16.70	2.39	11.70	18.03	9.33	29.10	0.57
20	2x9	100	232.8	16.70	2.39	11.70	18.03	9.33	29.10	0.57
21	2x9	120	232.8	16.70	2.39	11.70	18.03	9.33	29.10	0.57
22	1x24	0	310.4	18.40	2.76	15.60	24.04	8.90	38.80	0.65
23	2x12	20	310.4	18.40	2.76	15.60	24.04	8.90	38.80	0.65
24	2x12	40	310.4	18.40	2.76	15.60	24.04	8.90	38.80	0.65
25	2x12	60	310.4	18.40	2.76	15.60	24.04	8.90	38.80	0.65
26	2x12	80	310.4	18.40	2.76	15.60	24.04	8.90	38.80	0.65
27	2x12	100	310.4	18.40	2.76	15.60	24.04	8.90	38.80	0.65
28	2x12	120	310.4	18.40	2.76	15.60	24.04	8.90	38.80	0.65

Figure 5.4 shows the evolution and mixing process of a twin particle cloud with time and the separation of sand particles in the swarm phase for Test No. 2 (2 x 3 g, $\varepsilon/d_o = 2.5$ and $L_o/d_o = 9.7$). Here to differentiate between thermal and swarm regimes, the boundary depth for $B_o/(z^2 u_\infty^2) = 0.1$, which is the threshold value for the beginning of swarm regime (Noh and Fernando, 1993) was calculated. As shown in Figure 5.4, when a twin particle cloud released into water, each cloud behaved independently at first. Particle interactions were observed before merging and the interior sides of the particle clouds were mixed due to ambient entrainment. After mixing the interior boundaries, the twin cloud merged and mixed thoroughly and then descended as a single cloud with a virtual origin for $z/Z_b > 1$ (see Figure 5.4).

As illustrated in Figure 5.4, the boundary depth between thermal and swarm regime was $Z_b \approx 0.32$ m within which the parent cloud (i.e., the entrained fluid) washed colors out of the sand particles.

In the swarm phase, particles settled down with a similar velocity that was close to u_∞. It is noteworthy to mention that Eq. (5.2) works for single-particle cloud and twin particle clouds with small ε/d_o. For example, for a twin particle cloud with $\varepsilon/d_o = 2.5$ and $L_o/d_o = 9.7$, the extracted boundary depth from the experiment (Figure 5.4) was $Z_b \approx 0.32$ m that was very close to the boundary depth of a single-particle cloud ($Z_b = 0.327$ m) with the same aspect ratio which was calculated from Eq. (5.2).
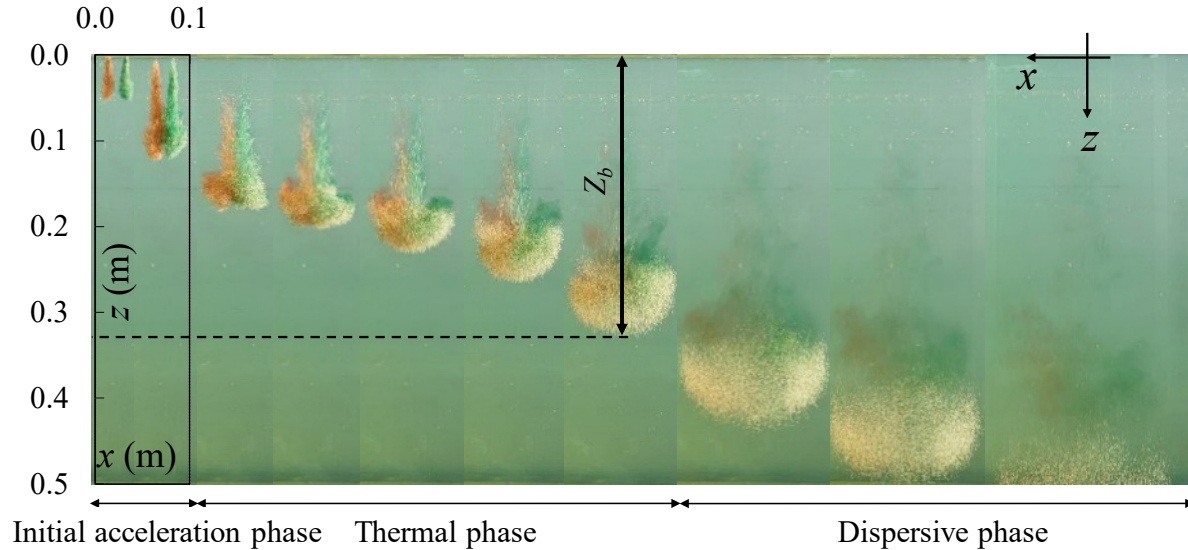
Figure 5.4. Consecutive images of a twin particle cloud evolution with time. The adjacent particle clouds and entrained ambient were photo illuminated for Test No. 2 (2**x**3 g, $\varepsilon = 20$ mm, $L_o/d_o = 9.7$, $Z_b \approx 0.32$ m).

5.3.2. *Penetration length*

The evolution of a twin particle cloud in stagnant water was characterized by its physical properties such as penetration length and growth rate. The evolution of a single (1x12 g) and a twin particle cloud (2x6 g) for $L_o/d_o = 19.4$ in different stages of motion and with different source separation distances ε/d_o of ranging from 2.5 to 15 are shown in Figure 5.5. As can be seen, when the two released particle clouds were very close to each other (i.e., $\varepsilon/d_o = 2.5$ and 5), the mixing occurred in the first phase and in particle clouds stems, which resulted in less ambient entrainment and detrainment. A smaller interaction between particles and the ambient fluid causes less energy loss and this resulted in a higher frontal velocity.
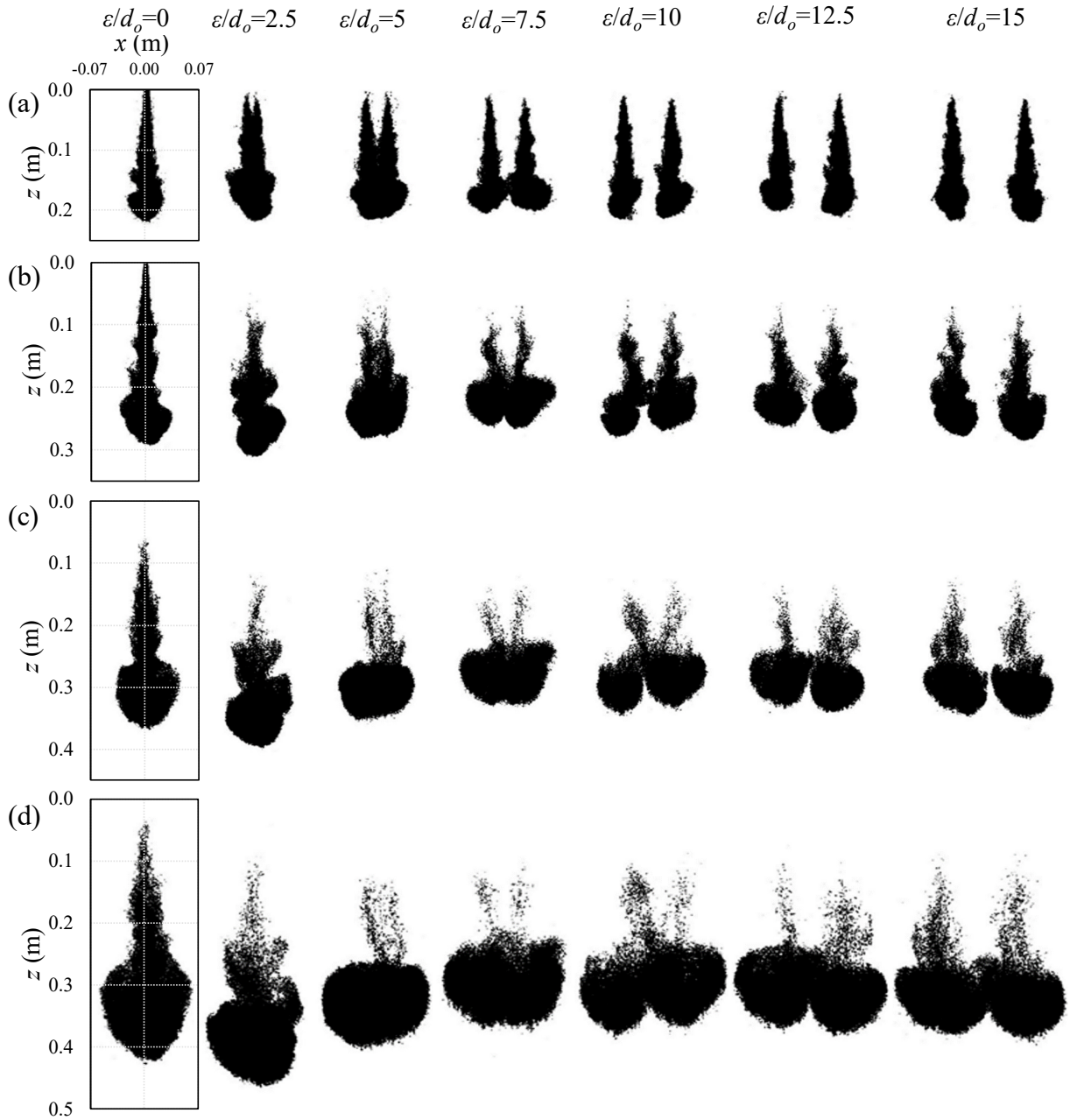
Figure 5.5. The evolution of a twin-cloud at different stages of motion and for different source separations for 1×12 g and 2×6 g ($L_o/d_o = 19.4$): (a) The initial acceleration phase, $t = 1$ s; (b) self-similar turbulent thermal phase, $t = 1.6$ s; (c) self-similar turbulent thermal phase, $t = 2.2$ s; (d) dispersive or particle-settling phase, $t = 2.667$ s.

As illustrated in Figure 5.5a, particle clouds were in approximately the same positions at $t = 1$ s. However, a twin particle cloud with $\varepsilon/d_o = 2.5$ penetrated more in the ambient by $z = 0.47$ m at $t = 2.667$ s in comparison with all other cases including the single particle cloud ($\varepsilon/d_o = 0$, $z = 0.42$ m)

(see Figure 5.5d). At $t = 2.2$ s, a twin cloud with $\varepsilon/d_o = 5$ had a similar penetration length of $z = 0.37$ m as the single particle cloud (see Figure 5.5c). However, when the normalized source separation distances became larger than $\varepsilon/d_o \geq 7.5$ particle clouds in a twin cloud acted independently and the swarm border height became similar to the half of the total mass (i.e., $Z_b = 0.327$ m for $L_o/d_o = 9.7$).

Figure 5.6 shows the variation of the cloud centroid thickness ($Z_f - Z_{bar}$) normalized with the frontal position Z_f with normalized time t/T where $T = [B_o^{1/2}/u_\infty^2]$ for both single and twin particle clouds with different aspect ratios L_o/d_o. As can be seen, the correlation of the centroid thickness with time was different for particle clouds with relatively high aspect ratios since they acted as a sand jet in this study and the payload size became comparable to the tank height (see Figure 5.6d). The normalized cloud centroid thickness ascended from the beginning of the tests and reached the maximum value at $t/T \approx 0.4$. Whereas in single particle clouds (shown by red symbols), the peak value occurred later than the twin clouds at around $t/T \approx 0.5$. Interestingly, at the beginning of the test, the normalized cloud centroid thickness of a single particle cloud was smaller than that of the twin particle clouds until $t/T \approx 0.5$. The peak values of ($Z_f - Z_{bar}$)/Z_f for all experiments were approximately between 0.35 and 0.39. After reaching the maximum thickness, which occurred at the maximum length of the cloud, it reduced due to the cloud length reduction and reached a plateau at the end of the tests. After the peak, the cloud centroid thickness of single clouds became larger than the twin particle clouds because the total length of the merged cloud after collision became smaller than the total length of the single cloud. It is noteworthy that the cloud length reduction happens after all sand particles enter the water. At the end of the first releasing phase, particle clouds reach their maximum length in both single and twin clouds, and the cloud lengths decrease due to expansion of the cloud front and fall of the trailing stem into the cloud frontal head.

For a relatively larger aspect ratio, the duration of maximum cloud centroid thickness was found to be longer. Figure 5.6d shows two peaks on variations of the normalized centroid thickness for a single cloud with 24 grams of sand particles. The first peak occurred at $t/T \approx 0.4$ and the second peak occurred at $t/T \approx 1.4$. For twin particle clouds, the trailing section merged with the frontal head due to the expansion of the cloud front. This is very advantageous since the trailing part of the cloud is removed by dividing the mass into twin clouds and consequently, the adverse effects of the mass loss in the marine ecosystem can be reduced accordingly.
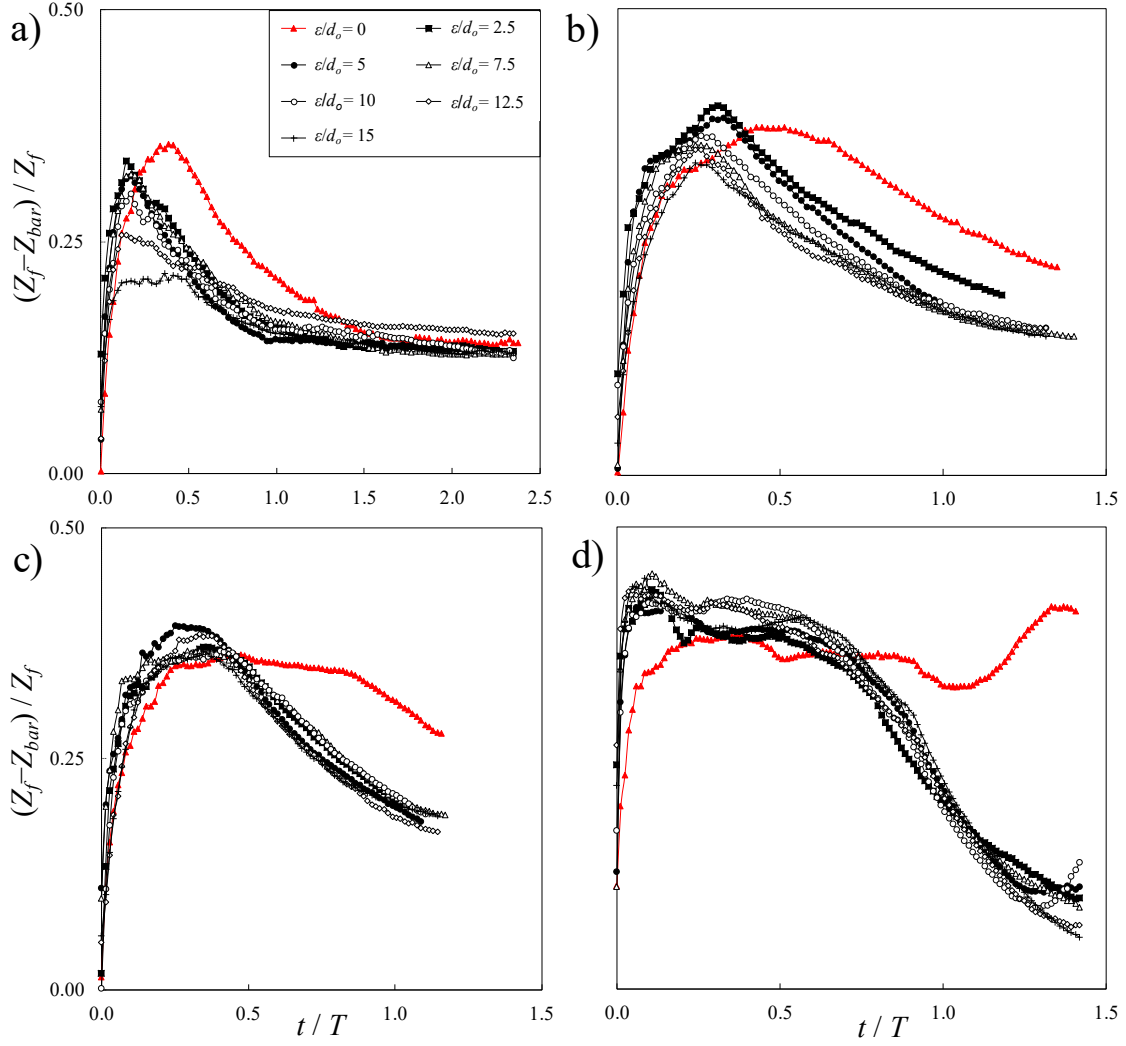
Figure 5.6. Variations of the normalized cloud centroid thickness with the non-dimensional time for single-coulds (red curves) and twin-clouds: (a) 2✕3 g versus 1✕6 g (L_o/d_o = 9.7); (b) 2✕6 g versus 1✕12 g (L_o/d_o = 19.4); (c) 2✕9 g versus 1✕18 g (L_o/d_o = 29.1); (d) 2✕12 g versus 1✕24 g (L_o/d_o = 38.8).

5.3.3. Cloud width

Figure 5.7 shows the variations of normalized effective width of twin particle clouds with normalized time for four aspect ratios ranging from L_o/d_o = 9.7 to 38.8 and normalized source spacing ε/d_o = 2.5 to 15. The time at which the frontal head of each cloud reached the boundary depth was obtained from the experimental data and it was found that the boundary depths occurred at $t/T \approx 1.4$. This normalized time was marked as a dotted red line in Figure 5.7 and showed the

117

boundary time between thermal and dispersive phases which can be used for environmental pollution management and in design processes of dredged material disposal.
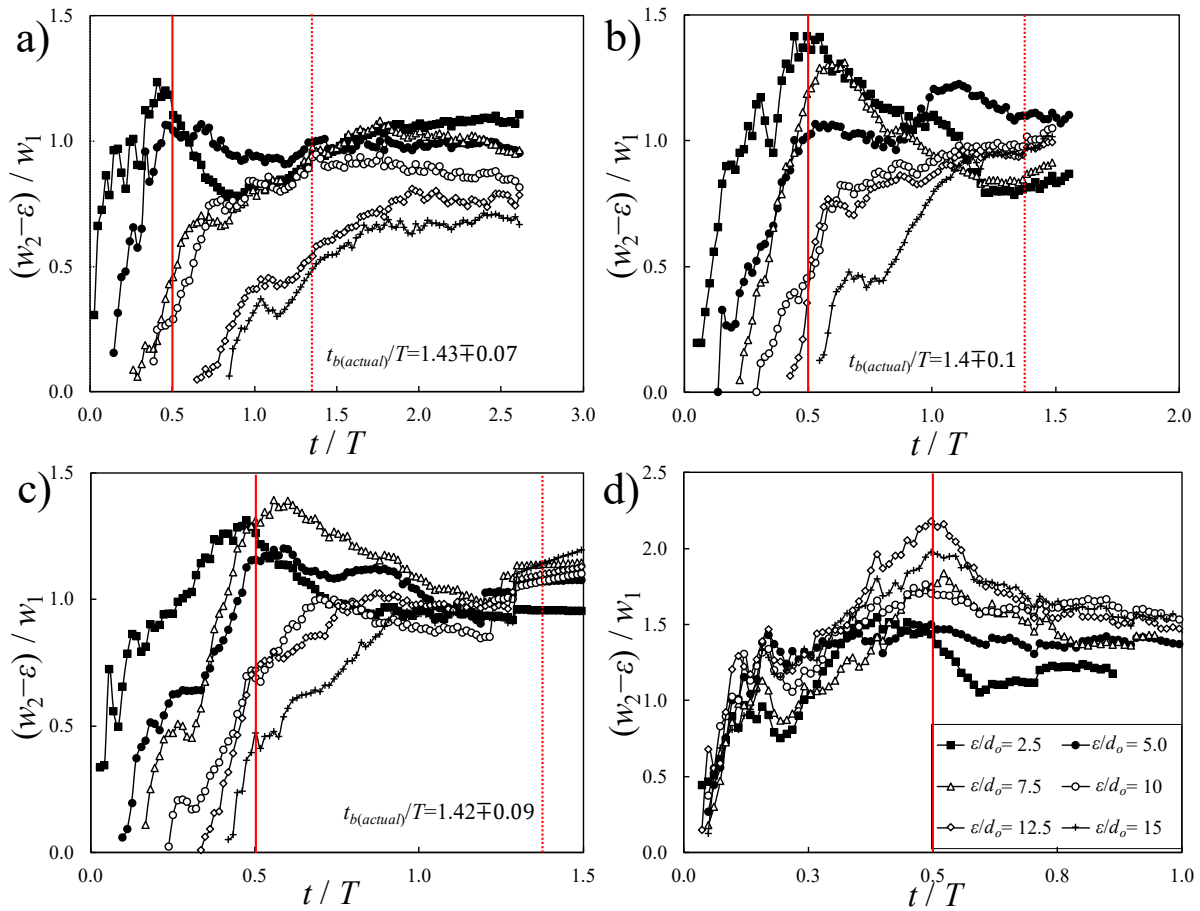
Figure 5.7. Variations of the effective cloud width for single-clouds and twin-clouds with the non-dimensional time: (a) 2x3 g versus 1x6 g ($L_o/d_o = 9.7$); (b) 2x6 g versus 1x12 g ($L_o/d_o = 19.4$); (c) 2x9 g versus 1x18 g ($L_o/d_o = 29.1$);(d) 2x12 g versus 1x24 g ($L_o/d_o = 38.8$). The red solid lines indicate the peak absolute width occurred at $t/T=0.5$ and the red dotted lines show the non-dimensional time that the curve started to be flatten.

The width of twin particle clouds was measured, and the effective cloud widths were calculated by subtracting the nozzle spacing ε from the cloud width and normalized with the width of a single cloud having the same aspect ratio. It was found that the cloud width expands linearly with time in the self-similar thermal phase (Bush et al., 2003). However, as can be seen in Figure 5.7a ($L_o/d_o = 9.7$), the normalized effective width drastically increased to approximately $(w_2-\varepsilon) = 1.25w_1$ when two particle clouds were released very close to each other for $\varepsilon/d_o =2.5$ and 5 and the ratio reduced

and became constant afterward. No peak was observed for twin clouds with larger nozzle spacing (i.e., $\varepsilon/d_o = 10$, 12.5 and 15), except for relatively large aspect ratios (Figure 5.7d). The results in Figure 5.7 indicated that the peak effective width of twin particle clouds increased by increasing aspect ratio and reached $(w_2-\varepsilon) = 2.2w_1$ for $L_o/d_o = 38.8$.

The peak normalized width was higher in closely released twin clouds than the other cases since particle interaction and mixing occurred from the beginning of sediment release until $t/T \approx 0.5$ and it fell down approaching $t/T = 1$. The red solid lines in Figure 5.7 show the time at which the maximum normalized effective cloud width occurred. For $t/T > 1$, the normalized cloud width slightly increased with time and reached the plateau approximately before $t/T = 1.5$. Similar peak values of normalized cloud width were found for ($\varepsilon/d_o = 2.5$, 5, and 7.5) as the cloud aspect ratio increased from 9.7 to 29.1 (see Figures 5.7a and 5.7c). When the distance between twin particle clouds increases, frontal heads spaced out, and less mixing occurred in their stems, but the frontal mixing still occurred. This can be seen in the correlation of normalized cloud width with time for $\varepsilon/d_o = 7.5$ and 10 in Figures 5.7b and 5.7c. In these tests, the maximum of the effective cloud width $((w_2-\varepsilon)/w_1)$ did not occur since the interactions were not strong enough to push frontal particles outward. Therefore, the effective cloud width $((w_2-\varepsilon)/w_1)$ gradually ascended with time and reached to a plateau between $(w_2-\varepsilon)/w_1 = 0.65$ and 1.05 for $L_o/d_o = 9.7$, between 0.8 and 1.1 for $L_o/d_o = 19.4$, and between 0.9 and 1.05 for $L_o/d_o = 29.1$. Furthermore, for large nozzle distances (i.e., $\varepsilon/d_o = 12.5$ and 15), particle clouds descended along, and their frontal heads touched each other. For a relatively higher aspect ratio, the maximum effective cloud width $((w_2-\varepsilon)/w_1)_{max}$ was observed at $t/T = 0.5$ in all source separations (see Figure 5.7d).

In order to study the effect of non-dimensional nozzle spacing ε/d_o on the growth rate and interaction of twin particle clouds, variations of the maximum non-dimensional cloud width $(w_2-\varepsilon)/w_1$ at $t/T = 0.5$ with ε/d_o were plotted for all ranges of aspect ratios and results were shown in Figure 5.8. The non-dimensional time of $t/T = 0.5$ was selected since at this time the normalized effective cloud widths $((w_2-\varepsilon)/w_1)$ reached their maximum values in most of the experiments (see Figure 5.7a-5.7d). The results showed that the maximum normalized cloud width for $L_o/d_o = 9.7$ and 19.4 occurred at $\varepsilon/d_o = 2.5$.
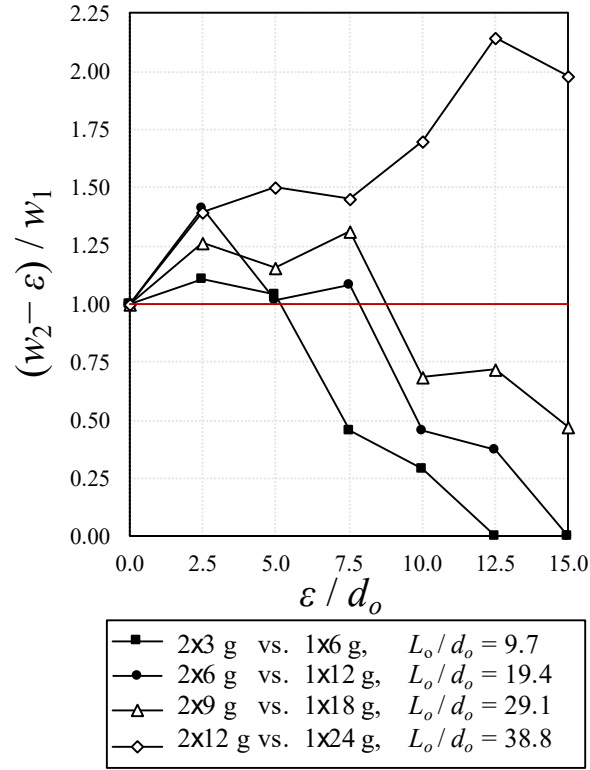
Figure 5.8. Effect of aspect ratio L_o/d_o on the variation of non-dimensional effective cloud width $(w_2–\varepsilon)$ at $t/T = 0.5$ with non-dimensional spacing between two nozzles ε/d_o. The horizontal solid line at $(w_2–\varepsilon)/w_1 = 1$ shows no cloud width effect.

The effective cloud width decreased for larger ε/d_o, which indicated that the effective cloud width of the twin clouds became smaller than the width of a single cloud. In addition, when the aspect ratio became larger (i.e., $L_o/d_o = 29.1$), the maximum effective width occurred in $\varepsilon/d_o = 7.5$ and the twin cloud followed the same pattern as the smaller aspect ratios. At a normalized distance of $\varepsilon/d_o = 15$, the twin cloud with $L_o/d_o = 29.1$ reached the maximum normalized width of $(w_2–\varepsilon)/w_1 = 0.5$ whereas this value for $L_o/d_o = 38.8$ was equal to 2. Moreover, for the largest aspect ratio, the maximum effective width $((w_2–\varepsilon)/w_1 = 2.15)$ occurred at $\varepsilon/d_o = 12.5$ and by increasing the source separations to $\varepsilon/d_o = 15$, the maximum effective width started to decrease and reached to two as illustrated in Figure 5.8.

Figure 5.9 shows the variations of the normalized swarm width $(w_{2\infty}–\varepsilon)/w_{1\infty}$ with normalized source distances ε/d_o. The results represented the final particle cloud shape in the settling stage. For small aspect ratio $L_o/d_o = 9.7$, the dimensionless width ratio was around unity for $\varepsilon/d_o = 0$, 2.5, 5, and 7.5, but it reduced to 0.7 for $\varepsilon/d_o = 15$. For such a high distance between two nozzles, the

clouds evolved far from each other and had weaker interactions with each other. Additionally, for medium aspect ratios ($L_o/d_o = 19.4$ and 29.1), the effective swarm width ratio became constant and oscillated around unity. However, for the high aspect ratio of $L_o/d_o = 38.8$, the single particle cloud acted as a sand jet and the single cloud width in the denominator became very small. In addition, for large source separations, the cloud width became larger than the single cloud width and as a result, the numerator of the ratio increased. Therefore, the normalized effective width escalated drastically from the unity at $\varepsilon/d_o = 5$, to approximately 1.5 at $\varepsilon/d_o = 10$ to 15. This indicated that the interactions between two adjacent clouds extended to the swarm regime and resulted in an effective cloud width up to 50% higher than the cloud width of a single particle cloud.
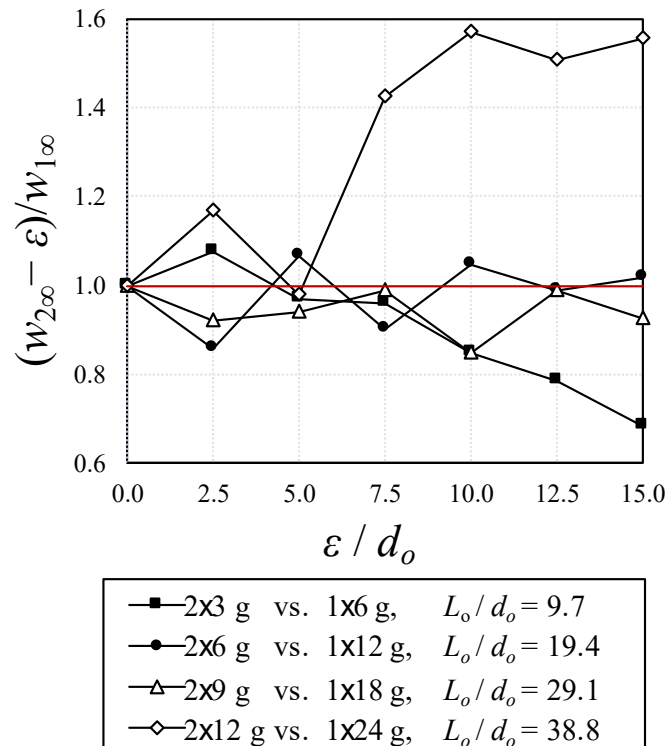
Figure 5.9. Effect of aspect ratio on the variation of non-dimensionall effective swarm width ($w_{2\infty}-\varepsilon$) at the settling stage ($t/T)_\infty$ with normalized spacing ε/d_o. The horizontal solid line at ($w_{2\infty}-\varepsilon)/w_{1\infty}$ = 1 shows no swarm width effect.

5.3.4. *Particle cloud velocity*

Figure 5.10 shows the variations of the frontal velocity of twin clouds u_f normalized with the settling velocity of individual particles u_∞ with the normalized vertical distance from the nozzle

for two cases of $L_o/d_o = 9.7$ and 19.4 (i.e., 2x3 g and 2x6 g). The frontal velocity data were obtained using the image processing technique (Math Works, Inc., 2018) and the results were compared with the proposed formulation of Moghadaripour et al. (2017b). Their proposed equation predicts the frontal velocity of particle clouds for $1.5 \leq L_o/d_o \leq 19.6$ as:

$$\frac{u_f}{u_\infty} = \varphi_3 \left[\frac{z}{d_o} \left(\frac{L_o}{d_o} \right)^\lambda \right]^\zeta$$

Eq. (5.4)

The value of the constant parameters was calculated based on particle size $d_{50} = 0.507$ mm and Stokes number St $= 0.55$. Thus, for large particle sizes the parameters of λ, φ_3, ζ were -0.4, 9.9, and -0.68, respectively (Moghadaripour et al., 2017b). In order to find the effects of source separation on variations of frontal velocity, the proposed equation for frontal velocity prediction of single particle cloud (solid curve) was multiplied by a factor to achieve the fit (dotted curve). The results indicated that the frontal velocity of a single particle cloud was 20% higher than a twin particle cloud in large source separations ($\varepsilon/d_o \geq 7.5$) with the aspect ratio of $L_o/d_o = 9.7$ and 10% higher for $L_o/d_o = 19.4$.

As can be seen in Figure 5.10, a discrepancy was found between the measured data and the best fit based on Moghadaripour prediction formula for $z/d_o < 20$ as the twin particle cloud did not merge completely from the beginning due to the source separation effect. A comparison between the calculated frontal velocity of twin clouds and the prediction curve of Moghadaripour et al. (2017b) indicated that the frontal head velocity in $L_o/d_o = 19.4$ was compatible with the Moghadaripour equation at $20 \leq z/d_o \leq 40$ (Figure 5.10d, 5.10e and 5.10f). After that, the frontal velocity became less than the prediction of Moghadaripour equation until $z/d_o = 60$ and became similar afterward. It can be seen that in both Moghadaripour equation and the measurements, the cloud frontal velocity tended to reach the particles settling velocity u_∞ when they further descend. The boundary height for $L_o/d_o = 9.7$ and 19.4 are $Z_b = 0.326$ m and 0.462 m indicating that the swarm regime began at $Z_b/d_o = 40.75$ and 57.75 and the corresponding frontal velocity was equal to 1.4 u_∞ similar to the value reported by Moghadaripour et al. (2017b).
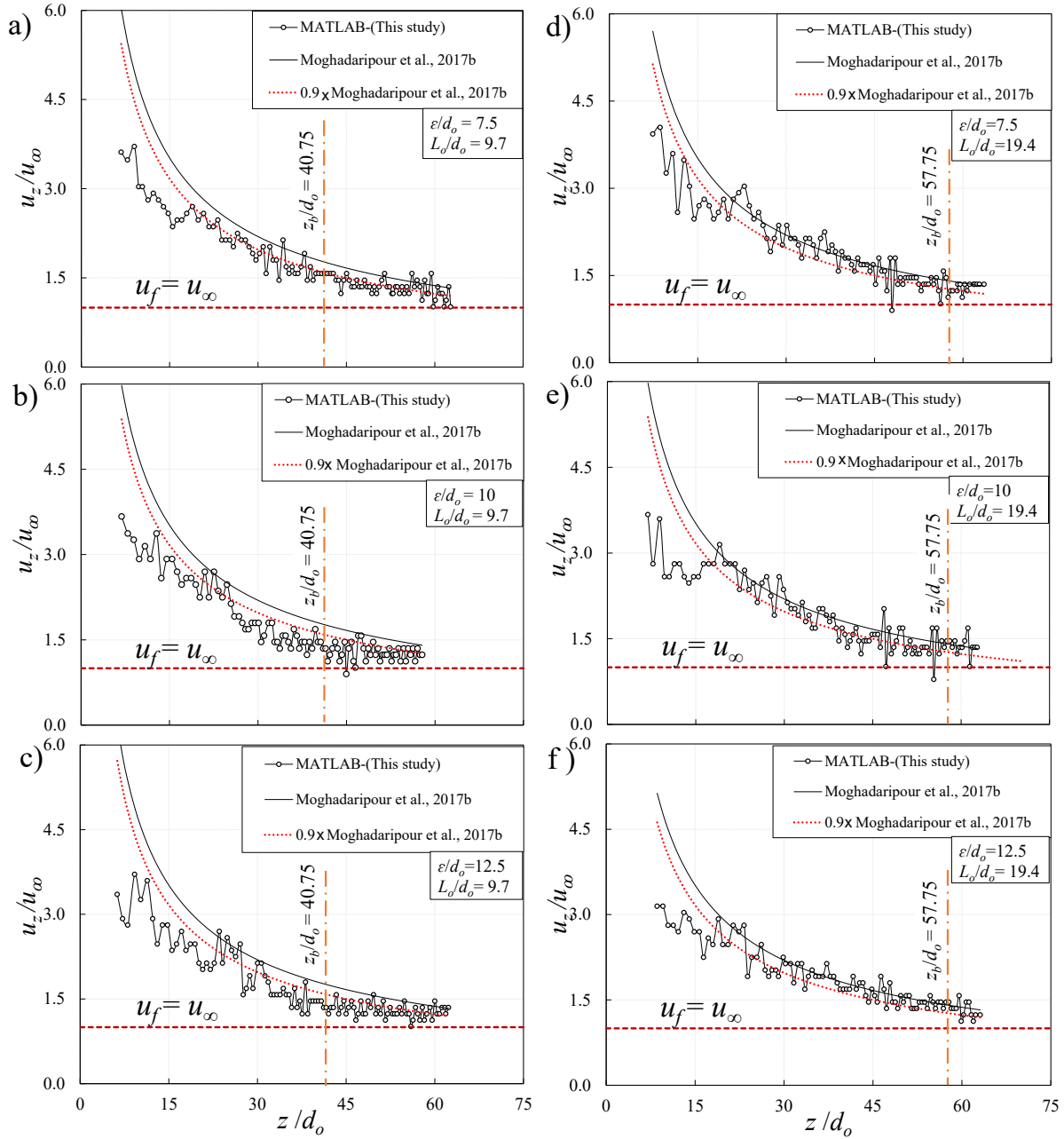
Figure 5.10. Variations of the normalized frontal velocity of a twin-cloud u_f/u_∞ with the normalized vertical depth z/d_o for (a) Test No. 4, 2✕3 g and $\varepsilon = 60$ mm; (b) Test No. 5, 2✕3 g and $\varepsilon = 80$ mm; (c) Test No.6, 2✕3 g and $\varepsilon = 100$ mm; (d) Test No. 11, 2✕6 g and $\varepsilon = 60$ mm; (e) Test No. 12, 2✕6 g and $\varepsilon = 80$ mm; (f) Test No. 13, 2✕6 g and $\varepsilon = 100$ mm, ($\varepsilon/d_o = 12.5$).

Effects of source separation on the cloud frontal velocity at different normalized times of $t/T = 0.5$, 1, 1.5, 2 and 2.5 for a twin particle cloud with the minimum aspect ratio (i.e., 2✕3 g, $L_o/d_o = 9.7$) are shown in Figure 5.11. As can be seen, when two particle clouds were close to each other (ε/d_o

123

= 2.5 and 5), the frontal velocities of the merged clouds were around 5% more than the corresponding single particle cloud in the first phase of releasing ($t/T = 0.5$). The frontal velocity of the twin cloud is higher than the single cloud particularly in $2.5 \leq \varepsilon/d_o \leq 10$. However, in the swarm phase (i.e., $t/T = 2.5$), the frontal velocity of the twin particle cloud and the single cloud reached their settling velocity, and the ratio in $\varepsilon/d_o = 2.5$ was slightly less than one. Here, the critical source separation distance was $(\varepsilon/d_o)_C = 2.5$ in which the frontal velocity of the twin cloud for $t/T \geq 1$ had the highest value (see Figure 5.5). It should be noted that as $T = [B_o^{1/2}/u_\infty^2]$ is considered to normalize the time, the buoyancy force is not balanced with the inertial force of sand particles for $t/T < 1$. Therefore, in $t/T = 0.5$, particle cloud is still in the first phase of formation and it is not fully discharged in the water. In this case, the maximum frontal velocity of the cloud occurred at $\varepsilon/d = 5$. Whereas for $t/T \geq 1$ the maximum frontal velocity of particle clouds occurred at $\varepsilon/d_o = 2.5$. In other source separations, the merging cloud has a frontal velocity somehow less than the single particle cloud frontal velocity of the same mass with a value ranging between 0.93 and 1.05.
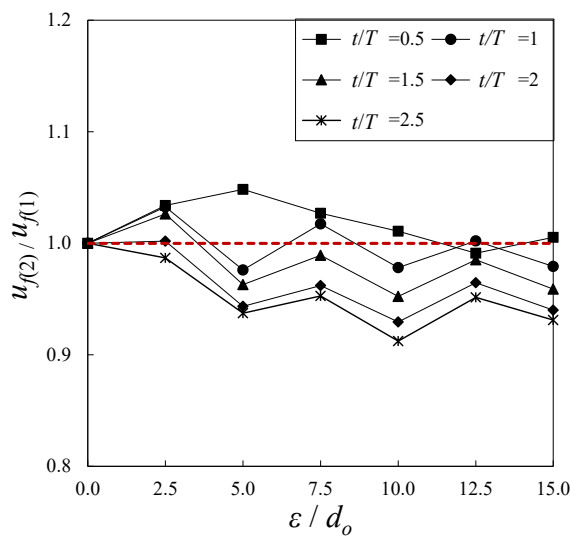
Figure 5.11. Effect of normalized nozzle spacing ε/d_o on the variation of the average frontal velocity ratio for the minimum aspect ratio ($L_o/d_o = 9.7$) at different non-dimensional time of $t/T = 0.5, 1, 1.5, 2$ and 2.5.
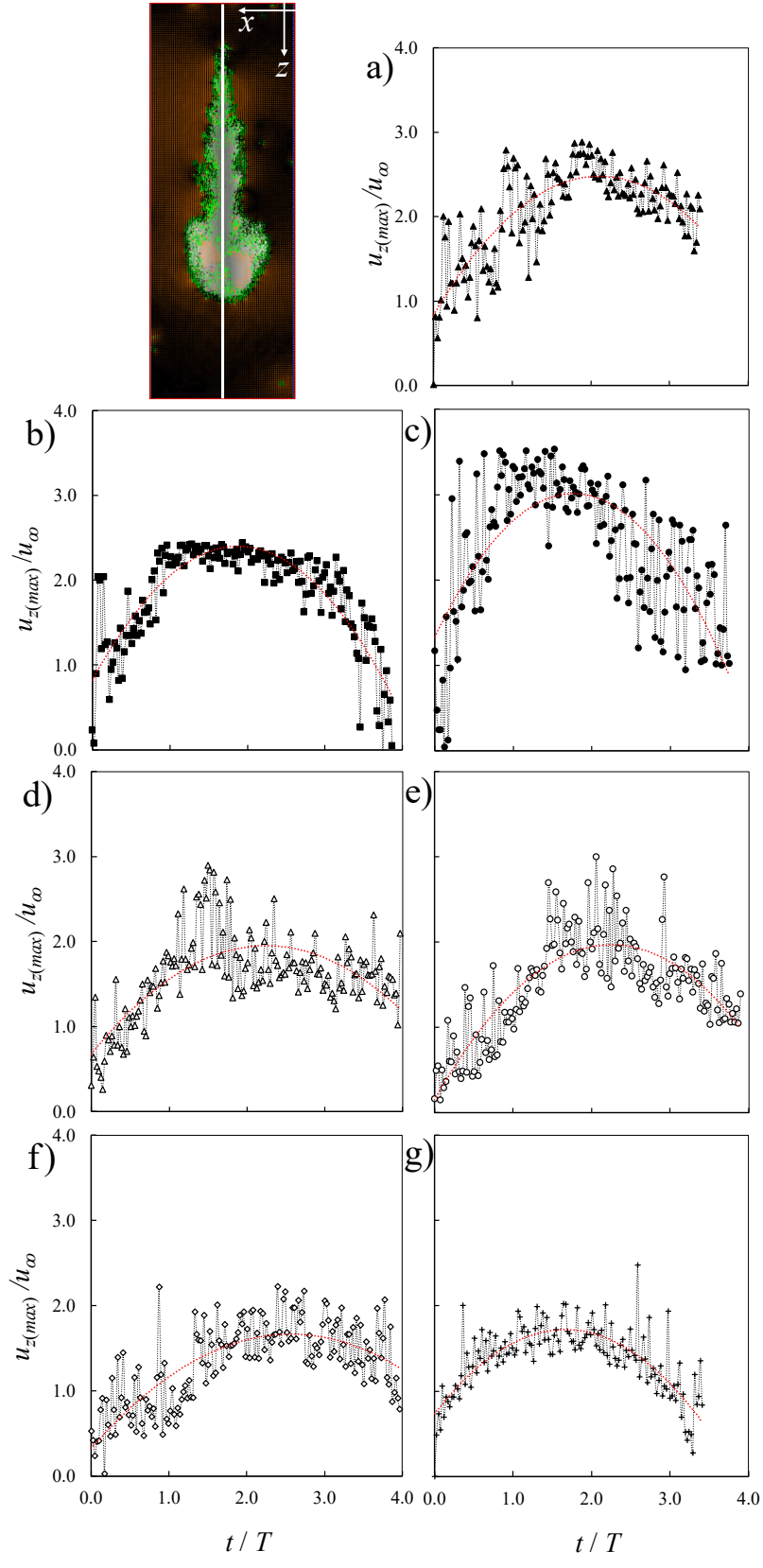
Figure 5.12. Variations of the non dimensional maximum centerline vertical velocity $u_{z(max)}/u_\infty$

125

with non dimensional time: (a) Test No. 8, 1x12g and $\varepsilon = 0$ mm, ($\varepsilon/d_o = 0$); (b)Test No. 9, 2x6 g and $\varepsilon = 20$ mm, ($\varepsilon/d_o = 2.5$); (c) Test No. 10, 2x6 g and $\varepsilon = 40$ mm, ($\varepsilon/d_o = 5$); (d) Test No. 11, 2x6 g and $\varepsilon = 60$ mm, ($\varepsilon/d_o = 7.5$); (e) Test No. 12, 2x6 g and $\varepsilon = 80$ mm, ($\varepsilon/d_o = 10$); (f) Test No. 13, 2x6 g and $\varepsilon = 100$ mm, ($\varepsilon/d_o = 12.5$); (g) Test No. 14, 2x6 g and $\varepsilon = 120$ mm, ($\varepsilon/d_o = 15$). The red dotted curves show the trend line of average $u_{z(max)}/u_\infty$.

The effects of source separation on variations of the maximum vertical velocity $u_{z(max)}$ on the cloud centerline with time were studied. Figure 5.12 shows the variation of normalized maximum vertical centerline velocity $u_{z(max)}/u_\infty$ with normalized time t/T for $L_o/d_o = 19.4$ and different nozzle spacing (i.e., Test No. 8 to 14). The vertical velocity profile in the cloud centerline (i.e., a fixed location) was extracted at each time step of 0.033 s. As can be seen in Figure 5.12, the maximum centerline vertical velocities continuously increased from zero and reached their maximum value of $u_{z(max)}/u_\infty$ at t/T between 1.5 and 2.5 depending on the source separations. The value of $u_{z(max)}/u_\infty$ decreased as the twin particle cloud entered the dispersive phase. Interestingly the maximum frontal velocity, which is related to the particle cloud overall velocity (see Figure 5.11), and the maximum centerline velocity, which is related to the individual particle velocity inside the clouds, did not occur at the same source separation distances. The maximum normalized centerline vertical velocity occurred at $\varepsilon/d_o = 5$ with a value of $u_{z(max)}/u_\infty = 3.5$ whereas the peak frontal velocity occurred at $\varepsilon/d_o = 2.5$. The trend lines were shown as red dotted curves in Figure 5.12. Figure 5.12 revealed that the twin clouds reached their maximum value earlier than the single particle clouds. The maximum normalized vertical velocity ($u_{z(max)}/u_\infty$) for a single particle cloud (see Figure 5.12a) occurred at $t/T = 1.88$ with a value of $u_{z(max)}/u_\infty = 2.88$ and for $\varepsilon/d_o = 5$, it occurred at $t/T = 1.5$. Moreover, mixing of particle clouds contributes to a quicker transition between both the initial acceleration and thermal phases and thermal and dispersive phases. Therefore, particle mixing in twin particle clouds resulted in a faster deposition. This phenomenon is beneficial for sediment loss prevention in restricted areas. As can be seen in Figure 5.12b, the maximum vertical velocity fluctuations inside the cloud were between $t/T = 1.2$ and 2.7 and they were less than other cases. However, as the clouds start to separate further, (see Figure 5.12c), the normalized maximum velocity fluctuations increased up to 30%. Local velocity fluctuations were observed in some tests (Figures 5.12c, 5.12d, and 5.12e) indicating the time that the adjacent clouds began to merge.

After merging, velocity fluctuations attenuated and reached the base turbulence intensity level with

an average value of approximately 12%. The base turbulence intensity level refers to the level of turbulence in a fluid flow in the absence of any perturbations or disturbances. It is a measure of the inherent turbulence of the flow and is often used as a reference point for comparison with the turbulence levels of disturbed flows. In other words, it represents the turbulence that would be present in the flow even in the absence of any external factors such as obstacles or boundary conditions. The base turbulence intensity level is typically quantified in terms of the root-mean-square (RMS) velocity fluctuations, which is a measure of the intensity of the turbulence fluctuations in the flow. As can be seen in Figures 5.12f and 5.12g, the centerline velocity of particles reduced to less than $2u_\infty$ as the source separation increased. Here, the source separation distance in which the highest individual velocity occurs can be defined once the twin cloud experienced the highest individual particle velocity at ($\varepsilon/d_o = 5$), and in this case, the maximum sand velocity reached slightly over $3u_\infty$.

Figure 5.13 shows the effects of aspect ratio L_o/d_o on variations of normalized maximum vertical velocity with non-dimensional time for single particle cloud and twin particle clouds with critical source separations of $\varepsilon/d_o = 2.5$ (i.e., at the location of peak frontal velocity) and 5 (i.e., at the location of peak centerline vertical velocity). The left column in Figure 5.13 (i.e., Figures 5.13a, 5.13d, and 5.13g) shows the effect of L_o/d_o in single particle clouds. As can be seen, the maximum values of the normalized vertical velocity delayed as L_o/d_o increased. A comparison of the figures in the left and middle columns of Figure 5.13 indicated the critical source separation (i.e., $\varepsilon/d_o = 2.5$) decreased the maximum vertical velocity similar to the cloud with $L_o/d_o = 9.7$ in Figure 5.13b. As can be seen in Figures 5.13b, 5.13e, and 5.13h, the maximum normalized vertical velocity ($u_{z(max)}/u_\infty$) was generally less than the corresponding single particle cloud and they reached their maximum value earlier than the single particle cloud.
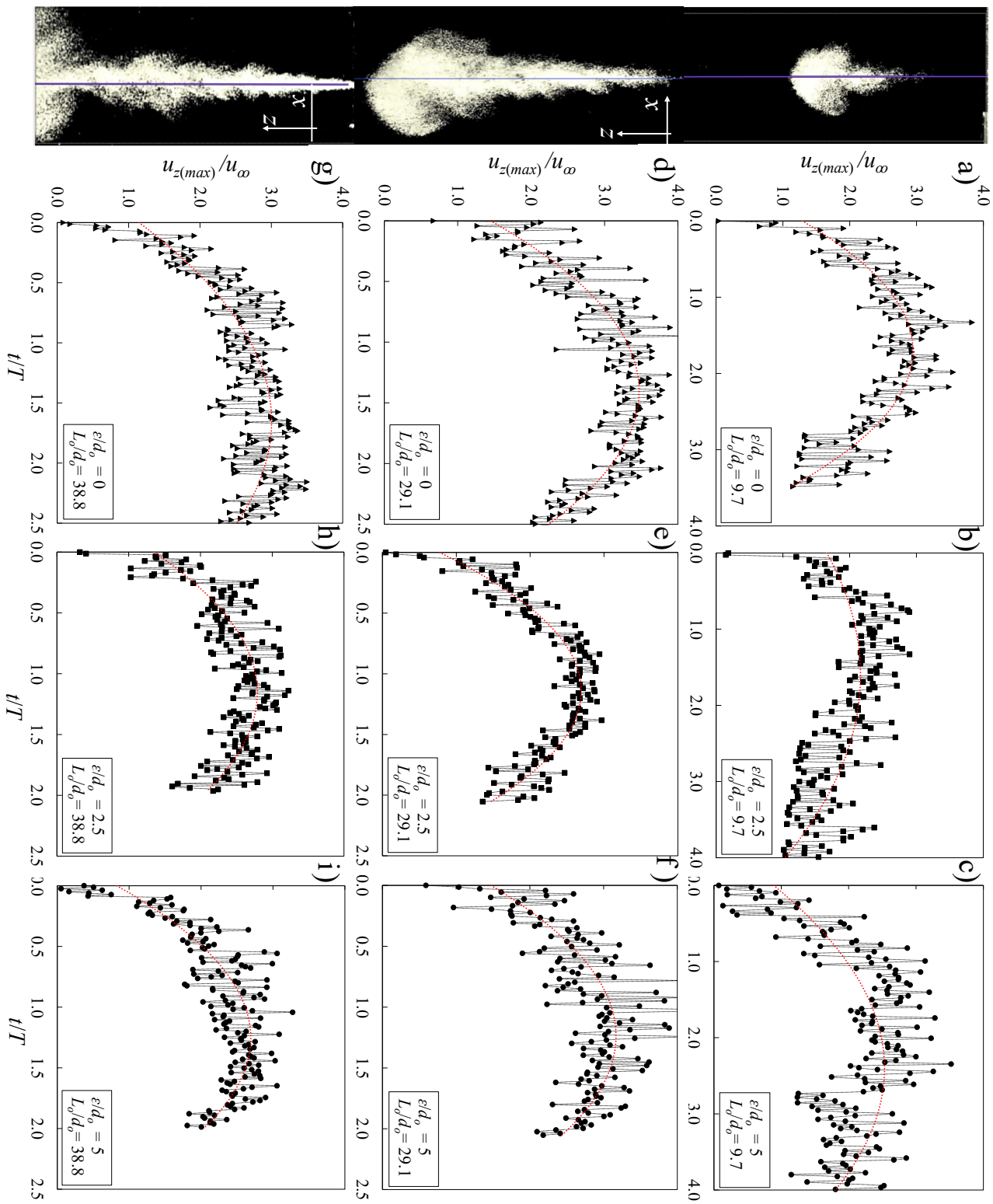
Figure 5.13: Variations of the non dimensional maximum centerline vertical velocity $u_{z(max)}/u_\infty$ with non dimensional time: (a) Test No. 1, 1x6 g and $\varepsilon = 0$ mm; (b) Test No. 2, 2x3 g and $\varepsilon = 20$ mm; (c) Test No.3, 2x3 g and $\varepsilon = 40$ mm; (d) Test No. 15, 1x18 g and $\varepsilon = 0$ mm; (e) Test No. 16, 2x9 g and $\varepsilon = 20$ mm; (f) Test No. 17, 2x9 g and $\varepsilon = 40$ mm; (g) Test No. 22, 1x24 g and $\varepsilon = 0$ mm; (h) Test No. 23, 2x12 g and $\varepsilon = 20$ mm; (i) Test No. 24, 2x12 g and $\varepsilon = 40$ mm. The red dotted curves show the trend lines of averaged $u_{z(max)}/u_\infty$.

Figure 5.14 shows the variations of normalized maximum positive and negative radial velocities ($u_{x(max)}/u_\infty$) with normalized effective time $(t - t_o)/T$, where t_o is the time that the particle cloud reaches the line *a-a* (see Figure 5.14a), for a single and twin particle clouds with an aspect ratio of $L_o/d_o = 19.4$ and different source separations. Section *a-a* in Figure 5.14 shows the location of peak cloud width in the stage of vortex formation (thermal phase) and it was smaller (i.e., $z = 0.35$ m) than the related boundary depth of $Z_b = 0.462$ m. Using this section line enabled us to capture the formation of vortices by the positive and negative radial velocities. Maximum positive and negative radial velocities existed inside the cloud because of the formation of vortex structures. The radial velocity data on line *a-a* was obtained from the PIVlab software for each time step and the maximum positive and negative velocities were extracted from each time frame. The highly symmetrical profiles of the particle's radial velocities indicate the accuracy of the releasing mechanism and the selected PIV algorithm. As can be seen in all cases, the magnitude of the horizontal velocities increased rapidly once the cloud frontal head started to pass section *a-a* and fluctuated in the frontal vortex region of the frontal head. A slight reduction of the radial velocity was observed after the frontal cloud head passed section *a-a* and radial velocities decreased quickly afterward and reached zero at the end. As can be seen in Figure 5.14a, the time duration of the single particle cloud to pass section *a-a* was about 30% higher than the twin particle clouds indicating that the trailing part of a single particle cloud remained longer in the water column (i.e., $(t - t_o)/T = 2.25$) than twin particle clouds with a non-dimensional time of $(t - t_o)/T \approx 1.75$. In single particle cloud, the maximum value of $u_{x(max)}$ was approximately $0.9u_\infty$ (Figure 5.14a) and the average value of $u_{x(max)}$ on line *a-a* was approximately $0.6u_\infty$. For twin particle clouds with other source separations, the average value of $u_{x(max)}$ in the aforementioned section was approximately $0.37u_\infty$. A comparison of radial and vertical centerline velocities indicated that both maximum and average vertical velocities were 3.25 times the radial velocities in the thermal phase in single particle clouds. In addition, the maximum and the average vertical and radial velocities were

correlated with the settling velocity of individual sand particle as: $u_{z(max)} = 2.88u_\infty$, $u_{x(max)} = 0.88u_\infty$ and $u_{z(avg.)} = 2.05u_\infty$, $u_{x(avg.)} = 0.63u_\infty$.
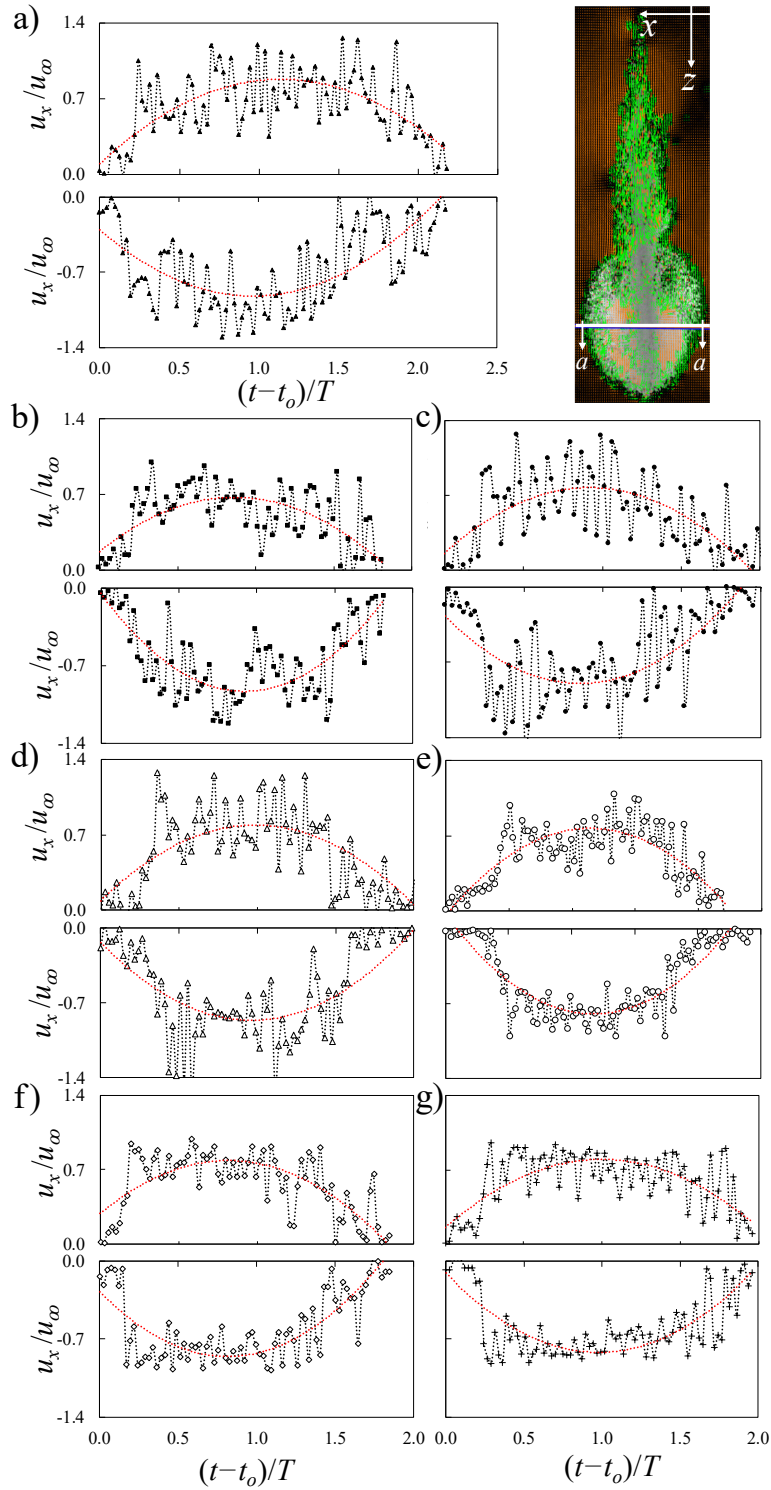
Figure 5.14. Variations of the normalized maximum positive and negative radial velocities

130

($u_{x(max)}/u_\infty$) in the fixed section of *a-a* with non-dimensional time $(t-t_o)/T$ for single and twin particle clouds; (a) Test No. 8 ($L_o/d_o = 19.4$), 1×12 g and $\varepsilon = 0$ mm, ($\varepsilon/d_o = 0$, $t_o = 2.22$ s); (b) Test No. 9, 2×6 g and $\varepsilon = 20$ mm, ($\varepsilon/d_o = 2.5$, $t_o = 2.03$ s); (c) Test No.10, 2×6 g and $\varepsilon = 40$ mm, ($\varepsilon/d_o = 5$, $t_o = 2.33$ s); (d) Test No. 11, 2×6 g and $\varepsilon = 60$ mm, ($\varepsilon/d_o = 7.5$, $t_o = 2.46$ s); (e) Test No. 12, 2×6 g and $\varepsilon = 80$ mm, ($\varepsilon/d_o = 10$, $t_o = 2.48$ s); (f) Test No. 13, 2×6 g and $\varepsilon = 100$ mm, ($\varepsilon/d_o = 12.5$, $t_o = 2.49$ s); (g) Test No. 14, 2×6 g and $\varepsilon = 120$ mm, ($\varepsilon/d_o = 15$, $t_o = 2.48$ s). The red dotted curves show the trend of average radial velocities.

The results show that the nozzle distances had a minor effect on the maximum radial velocities as the average values increased slightly by increasing nozzles distances from $0.32u_\infty$ for $\varepsilon/d_o = 2.5$ to $0.37u_\infty$ for $\varepsilon/d_o = 15$. However, as stated in Figure 5.12, the average values of u_z were $1.83u_\infty$ for $\varepsilon/d_o = 2.5$, then increased to $2.36u_\infty$ for $\varepsilon/d_o = 5$ and after that, it reduced to $1.087u_\infty$ for $\varepsilon/d_o = 15$. Therefore, the ratio of u_z to u_x decreased gradually by increasing nozzle distances from $\varepsilon/d_o = 5$ onward.

Figure 5.15 shows the effects of aspect ratio on variations of normalized maximum positive and negative radial velocities ($u_{x(max)}/u_\infty$) with normalized effective time $(t- t_o)/T$ for single particle cloud and twin particle clouds with critical source separations of $\varepsilon/d_o = 2.5$ (i.e., at the location of peak frontal velocity) and 5 (i.e., at the location of peak centerline vertical velocity). As can be seen in Figure 5.15, the passage time of the single particle clouds in all other aspect ratios was approximately 30% higher than the corresponding twin particle clouds. As the aspect ratio of twin particles increased, the number of sand particles became higher, and accordingly, the concentration inside the cloud became higher. The wake effects due to high sand concentration in single particle clouds resulted in relatively higher vertical and radial velocities. As can be seen in Figures 5.15a-5.15c, the radial velocity increased with increasing aspect ratio whereas in twin particle clouds the inter-particle collision canceled the aspect ratio effect.
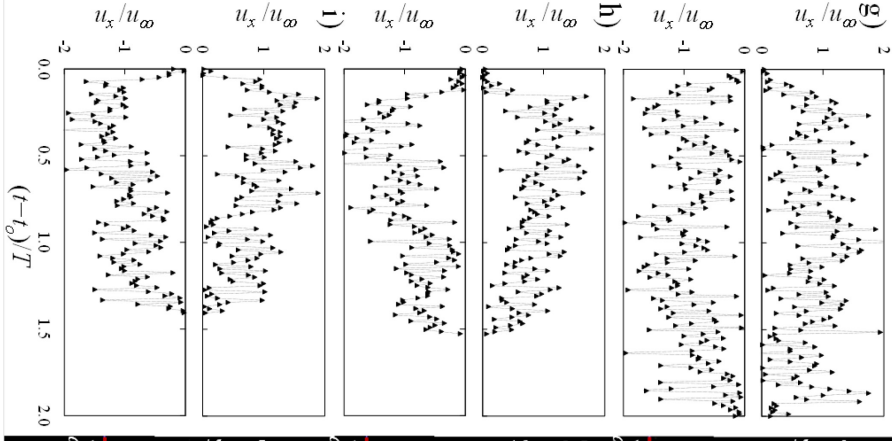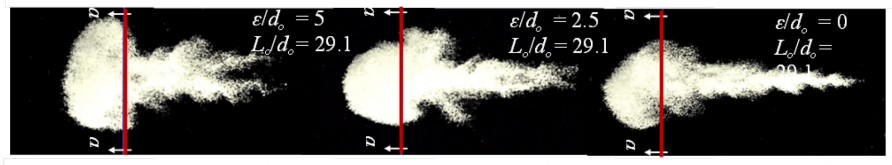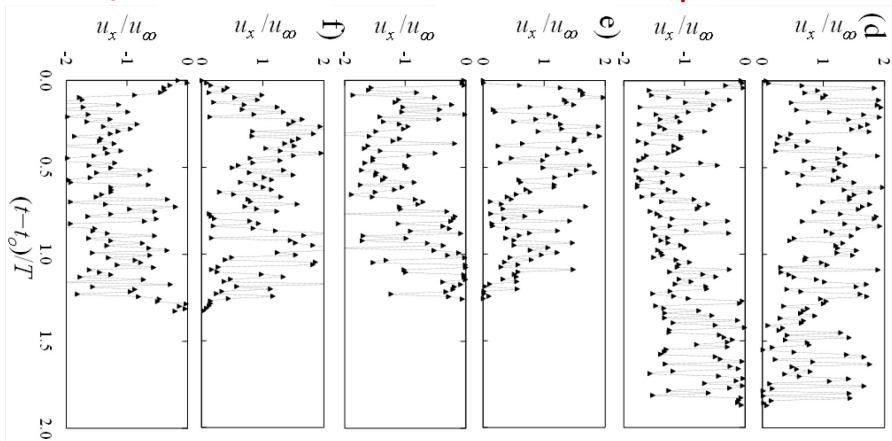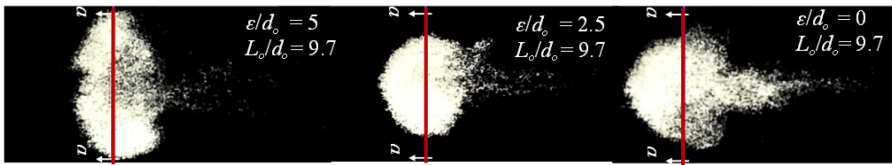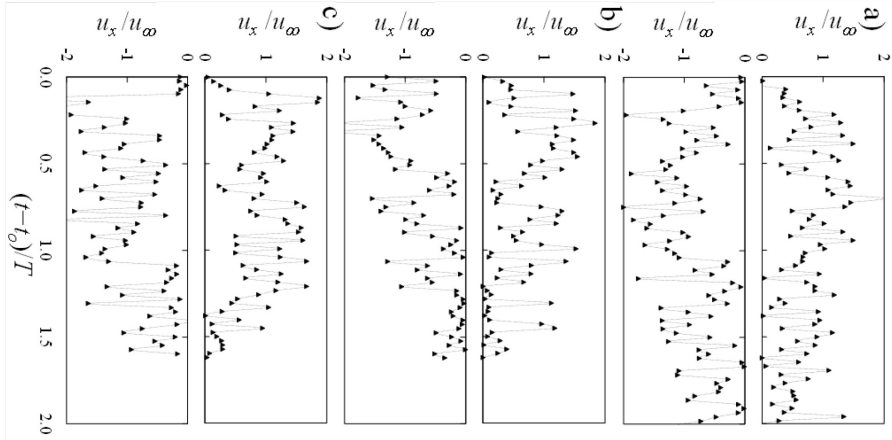
Figure 5.15: Variations of the normalized radial velocities ($u_{x(max)}/u_\infty$) on section *a-a* with non-dimensional time $(t-t_o)/T$ for single and twin particle clouds; (a) Test No. 1, 1x6 g and $\varepsilon = 0$ mm; (b) Test No. 2, 2x3 g and $\varepsilon = 20$ mm; (c) Test No.3, 2x3 g and $\varepsilon = 40$ mm; (d) Test No. 15, 1x18 g and $\varepsilon = 0$ mm; (e) Test No. 16, 2x9 g and $\varepsilon = 20$ mm; (f) Test No. 17, 2x9 g and $\varepsilon = 40$ mm; (g) Test No. 22, 1x24 g and $\varepsilon = 0$ mm; (h) Test No. 23, 2x12 g and $\varepsilon = 20$ mm; (i) Test No. 24, 2x12 g and $\varepsilon = 40$ mm. The red dotted curves show the trend lines of averaged $u_{x(max)}/u_\infty$.

5.3.5. *Ambient entrainment*

Considering the entrainment hypothesis introduced by Morton et al. (1956), the radial velocity component of the water phase u_x moving towards the particle cloud centerline is proportional to the average vertical cloud velocity u_z (i.e, $u_x \sim u_z$). Figure 5.16 shows the relationship between the entrainment coefficient and the aspect ratio of particle clouds using both experimental and numerical data from the literature. The entrainment coefficients of the particle clouds were calculated based on the numerical integration method described by Moghadaripour et al. (2017a) as the entrained flow rate at a certain time period was divided to the surface area and frontal velocity of the particle cloud. In this study, the boundary detection of surface area, cloud volume, and frontal velocity were performed by the Image Processing techniques and a MATLAB algorithm. Effects of source separation were shown as overbars in Figure 5.16 the upper limit of the over bars show the entrainment coefficient of twin particle clouds with large source spreading which are equivalent to $0.5(L_o/d_o)$. Whereas the lower bars indicate the entrainment coefficients of twin particle clouds with critical source separation values, which resulted in higher vertical velocity and less entrainment.

As can be seen in Figure 5.16 the entrainment coefficient diminished by increasing aspect ratio which represents higher sand mass and smaller nozzle size. The trailing part of the cloud has a greater descend velocity than the frontal head as the trailing part fell into the cloud head in the dispersive phase. As the cloud aspect ratio becomes larger, particle concentration inside the cloud enhances which results in a smaller entrainment coefficient. The entrainment coefficient in the study of Lai et al. (2013) (solid diamonds in Figure 5.16) was higher than in similar cases due to the presence of polydisperse particles in their research. The surface area and cloud volume became larger due to the spread of polydisperse particles. Consequently, the entrainment coefficient became greater than similar monodispersed particle clouds. An equation was proposed to estimate

133

the entrainment coefficient of particle clouds as:

$$\alpha_e = \frac{1}{5}\left(\frac{L_o}{d_o}\right)^{-1/4}$$

Eq. (5.5)

The proposed equation is applicable for $0.13 < L_o/d_o < 125$, the upper limit of $L_o/d_o = 125$ obtained from the study of Azimi et al. (2012b) with the entrainment coefficient of 0.06 for sand jets. For higher aspect ratios, Azimi et al. (2012b) recommended a constant entrainment coefficient of 0.06.
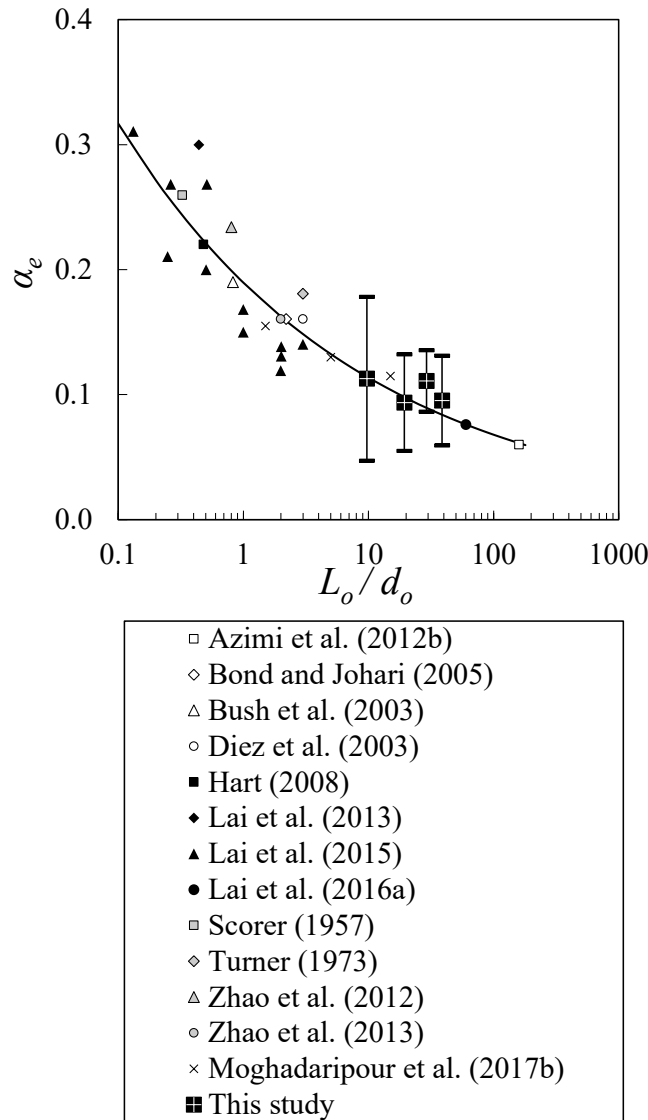
Figure 5.16. Effect of aspect ratio L_o/d_o on variations of entrainment coefficient α_e for sand jets and particle clouds.

5.3.6. Assessment of turbulence intensity

The turbulence intensity is defined as the ratio of velocity fluctuations to the mean flow velocity. Figure 5.17 shows the effect of source separation and aspect ratio on variations of sand turbulence intensity for single and twin particle clouds. All values of turbulence intensities were found to be less than other comparable studies (Azimi et al., 2012a; Sharif and Azimi, 2020) with a value of approximately 10% of the mean vertical velocity due to the cloud boundary interactions. For single source particle clouds (i.e., $\varepsilon/d_o = 0$), the turbulence intensity of sand particles was approximately 0.1 for $L_o/d_o = 9.7$ to 38.8 without a sudden jump.
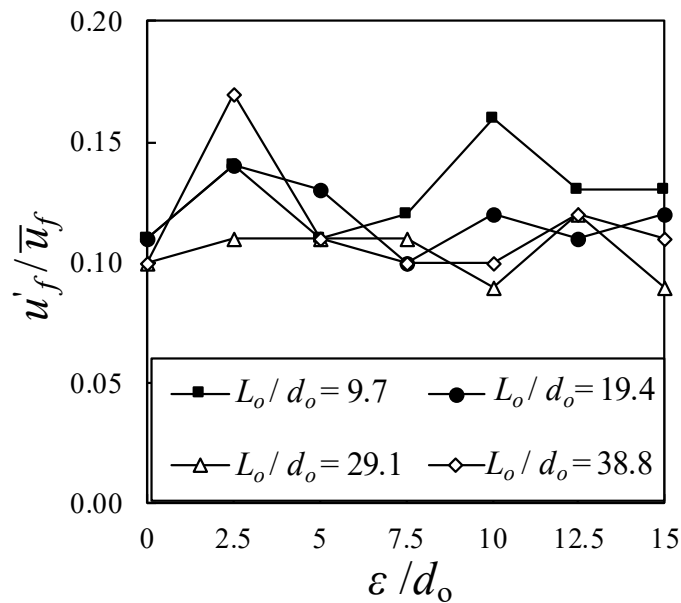
Figure 5.17. Effects of normalized nozzle spacing ε/d_o and aspect ratio L_o/d_o on the variations of sand turbulence intensity of twin-clouds.

5.3.7. Releasing method in field operation

In the proposed releasing model, the total volume of dredged material is divided into a number of smaller masses to optimize the mixing and reduce the spreading of suspended sediment in the form of turbidity. Moreover, the experimental results showed that the mixing is quite high when L_o/d_o is small. Therefore, if dredging materials are discharged consecutively and in small payload, instead of continuously releasing the total mass, the dredging process affects a smaller area of the ambient, which is beneficial for the water quality and decrease potential environmental pollution.

135

5.4.   Conclusions

The frontal velocity, cloud width, and cloud frontal position of the twin particle clouds with different aspect ratios and source separation distances were measured and the results were compared with the corresponding single-particle clouds. A normalized critical source separation distance $(\varepsilon/d_o)_C = 2.5$ was introduced when a twin particle cloud reached its maximum frontal velocity due to the smaller ambient entrainments and fewer interactions occurred between particles and the entrained water. As a result, in the critical distance ratio $(\varepsilon/d_o)_C$, the energy dissipations became smaller and frontal velocities became larger. In addition, releasing two particle clouds beside each other resulted in removing the trailing part, which may lead to less mass loss in the water environments.

The maximum normalized width of twin particle clouds indicated that the effective mixing and the optimum distance between clouds were enhanced by increasing the aspect ratio (L_o/d_o). It was found that in a small source separation ratio (i.e., $\varepsilon/d_o = 2.5$, 5, and 7.5), the normalized effective width drastically increased at first and reached the peak value and then it decreased and reached a plateau. The quasi-steady values of the normalized effective width increased by increasing the aspect ratio and no peak values were observed for the effective width of twin clouds of larger source separation distances (i.e., $\varepsilon/d_o = 10$, 12.5, and 15). It was observed that the swarm width of twin particle clouds oscillated around unity in small source separation ratios (i.e., $\varepsilon/d_o = 2.5$, 5, and 7.5) and small aspect ratios (i.e., $L_o/d_o = 9.7$). However, the swarm width decreased by 30% of the swarm width of the single particle cloud as ε/d_o increased. For medium aspect ratios (i.e., $L_o/d_o = 9.7$ and 19.4), the effective swarm width of twin particle clouds was similar to the single clouds and for high aspect ratio of $L_o/d_o = 38.8$, the swarm width increased by more than 1.5 times of the swarm width of the corresponding single particle cloud. In addition, the effective swarm width decreased with increasing the source separation ratio (ε/d_o). In larger nozzle distances, the swarm widths were on average 50% higher than the swarm width of single particle clouds.

The radial velocity data in the thermal phase showed that the time duration of a single particle cloud passing the vortex region was approximately 30% higher than the twin particle clouds. This indicated that the trailing part of a single particle cloud remains longer in the water than the twin particle clouds. In addition, the radial velocity of single particle clouds increased with increasing aspect ratio whereas in twin particle clouds the inter-particle collision canceled the aspect ratio

136

effect. The presence of a dense trailing part in the single particle clouds enhances the risk of mass loss during dredged material disposal. This is an environmental concern if particles remain in the water for a longer time. In addition, particles in the trailing part of the cloud tend to be swept away by the current and may be misplaced and deposited in other non-designated areas.

The maximum centerline velocity inside the cloud occurred at $\varepsilon/d_o = 5$ which dissipated the overall velocity of the cloud and resulted in a smaller frontal velocity in comparison with $\varepsilon/d_o = 2.5$. Moreover, more local velocity fluctuations were observed in smaller distance ratios (i.e., $\varepsilon/d_o = 5$, 7.5, and 10) than in larger distance ratios such as $\varepsilon/d_o = 12.5$ and 15. The local velocity fluctuations were not observed in critical distance ratio $(\varepsilon/d_o)_C = 2.5$ which resulted in less energy loss and high frontal velocity of the cloud. In addition, the maximum values of the normalized vertical velocity were delayed as L_o/d_o increase.

The entrainment coefficient constantly decreased by increasing the aspect ratio and an equation was proposed to estimate the entrainment coefficient of particle clouds as a function of aspect ratio. The turbulence intensity of particle clouds was assessed, and it was observed that in large aspect ratios, the velocity fluctuation was higher within closer distances from the nozzles. However, in small aspect ratios, the maximum velocity fluctuations occurred in larger distance ratios.

Finally, the results showed that dividing the total mass of releasing materials into two equal portions was highly beneficial for the aquatic environment. The positive effects were the velocity enhancement during the deposition process and the elimination of the trailing part in twin particle clouds which reduced mass loss that could negatively affect water ecosystems. The present study also has desirable implications that would be quite noticeable for engineers concerned with the design of systems that employ sand-jet and particle cloud concepts.

Chapter 6

6. On the Motion of Single and Twin Oblique Particle Clouds in Stagnant Water

6.1. Introduction and Literature Review

Many environmental engineering applications in dredging involve releasing sedimentary material into water environments such as lakes and oceans. These activities include excavation at the seabed, relocation of dredged materials, construction of artificial islands, and land reclamation (Zhao et al., 2012; Lai et al., 2013; Wang, 2014; Er et al., 2016). Moreover, partially treated wastewaters are discharged from submarine outfalls, and they often contain sediments and particulates; the settled near field sediments raise a concern about their impact on the environment and the benthic ecology (Chan et al., 2014). Dredging activities always alter the aquatic environment by improving the flow of water, removing degradable substances, and temporarily degrading water quality.

Once dredged materials are released into the ambient, a two-phase solid-liquid jet plume is formed. Based on the initial conditions, the jet plume can be formed either as a sand jet or as a particle cloud (Azimi et al. 2012a, b; Moghadaripour et al., 2017a, b). Sand jets are formed by a continuous discharge of sand particles whereas particle clouds are formed by releasing a finite amount of sand particles into stagnant water. Several experimental and numerical studies have been performed to study the evolution of sand jets and particle clouds in water (Bush et al., 2003; Azimi et al. 2011; Lai and Lee, 2012; Zhao et al., 2014; Lai et al., 2016a, b; Sharif and Azimi, 2020, 2021). To accurately deposit dredged materials into the targeted areas and prevent loss of sediments to the water bodies, which results in high turbidity and water quality degradation, a precise prediction of the size and trajectory of the resulting particle cloud is of great interest.

The motion of particle clouds is managed by adjusting the controlling parameters such as nozzle diameter, d_o, a mass of sand particles, m, initial releasing angle, α, the dynamic viscosity of the ambient fluid, μ, and median sand particle size, D_{50}. Recent experimental studies have shown the

effects of controlling parameters on the motion of particle clouds in stagnant water (Lai et al., 2018; Manzouri and Azimi, 2019a, b; Sharif and Azimi, 2020, 2021). Bond and Johari (2005) introduced a non-dimensional aspect ratio, L_o/d_o, to study the effect of initial geometry on the evolution of a single-phase buoyant thermal.

The mass of sand particles, m, can be parametrized by the length of the occupied sand particles in a nozzle with a diameter of d_o as $L_o = 4m/\pi d_o^2 c_o \rho_s$, where c_o is the initial sand volume fraction (i.e., $c_o = 0.6$ volume/volume) and ρ_s is the density of sand particles. Moghadaripour et al., (2017b) conducted a series of experiments to examine the effect of aspect ratio (i.e., L_o/d_o) on the motion of particle clouds. The aspect ratio ranged between 0.8 and 40.1 and it was found that L_o/d_o has a considerable effect on the cloud's width. The experimental study of particle clouds in a viscous fluid indicated that the width of particle clouds in viscous fluid increased with aspect ratio, although it did not exceed the growth rate of particle clouds in water (Azimi, 2019). The recent study on particle interactions in vertically released (i.e., $\alpha = 90°$) twin particle clouds with different distances from the adjacent nozzles and aspect ratios indicated that dividing the total mass of sand particles into two equal masses decreased the mass loss and turbidity and enhanced the mixing of particle cloud with water (Janati and Azimi, 2021).

Particle clouds experience three phases of motion that influence the spreading of particles in water (Rahimipour and Wilkinson, 1992). The initial acceleration phase starts from the onset of release until all sand particles enter the ambient water. The thermal phase begins when particles follow the frontal eddies, and the cloud front expands gradually. The frontal eddies are produced due to the formation of a shear layer around the cloud frontier because of the density difference between water and sand particles. The agitated particle thermal forms a vortex structure and expands symmetrically due to ambient entrainment. In a thermal regime, the cloud velocity decreases until all particles dissipate their kinetic energies and reach their settling terminal velocity. Then, the entrained fluid (i.e., parent cloud) falls behind the particles and the swarm phase initiates. The third phase is called the dispersive phase within which all particles descend with their settling velocity and the cloud expands at a very small rate (Rahimipour and Wilkinson, 1992). Noh and Fernando (1993) used normalized buoyancy, $B_o/(z^2 u_\infty^2)$, as a controlling parameter to quantitatively determine the boundary of thermal and swarm regimes in two-phase particle clouds. The buoyancy, B_o is equal to $g'V_o = g[(\rho_s - \rho_w)/\rho_w)](\pi d_o^2/4)L_o c_o$ where g' is the reduced gravity, g is the acceleration due to gravity, V_o is the volume of sand particles, ρ_w and ρ_s are the densities of water

and sand, respectively. It was found that particle clouds settle as a thermal for $B_o/(z^2u_\infty^2) > 0.1$ and for $B_o/(z^2u_\infty^2) \leq 0.1$, particles descend as a swarm with a settling velocity close to u_∞.

Azimi et al. (2012a) found that the velocity of the sand jet front (i.e., $L_o/d_o \rightarrow \infty$) is five times larger than the settling velocity of an individual particle of the same size. Moghadaripour et al. (2017b) proposed an equation to predict the frontal velocity of particle clouds and found a higher particle settling velocity at the beginning of the swarm regime than that of individual particles. They found that by increasing the aspect ratio, more particles followed behind the wakes of the frontier particles and, as a result, the frontal velocity of particle clouds increased with increasing aspect ratio, L_o/d_o. Bühler and Papantoniou (2001), defined a threshold value of $1.4u_\infty$ for cloud velocity, below that a particle cloud is considered in its swarm (i.e., dispersive) phase. Janati and Azimi (2021) investigated the effects of particle interactions by varying nozzle spacing and aspect ratio on vertically released twin particle clouds. It was found that mutual cloud attractions can cause significant changes in the merged cloud velocities. Moreover, in a very small distance between adjacent nozzles, the frontal velocity of twin particle clouds was higher than the frontal velocity of single particle clouds with the same aspect ratio.

Increasing the volume of particle cloud due to ambient entrainment is determined by the entrainment coefficient, α_e. The entrainment coefficient is defined as the ratio of entrained velocity to the centerline velocity of particle clouds (Morton et al., 1956). For single-phase jets, the entrainment coefficient is constant along the jet axis with a theoretical value of $\alpha_e = 0.13$ (Morton et al., 1956). Sharif and Azimi (2020) computed the entrainment coefficients of vertical particle clouds at different cross-sections. They found that the entrainment coefficient diminishes non-linearly as the inter-particle spacing increases in the transverse direction. In twin vertical particle clouds, the maximum cloud width occurred in the non-dimensional time scale of $t/T = 0.5$, where $T = [B_o^{1/2}/u_\infty^2]$ and the entrainment coefficient was found to be independent of the initial cloud condition and nozzle spacing (Janati and Azimi, 2021).

Observations of particle clouds indicate that a portion of sand particles forms a less concentrated tail behind the cloud which is between 2% and 20% of the initial mass (Ruggaber, 2000). This mass loss due to the trailing stem can be an environmental concern that may induce turbidity in water (Lai et al., 2018). To reduce the adverse effect of the trailing stem, the mass of dredge materials in each release can be reduced by simultaneously releasing a smaller mass from two

adjacent dredgers. In the field operation, the dredged materials are discharged at an angle with the water surface. The oblique release reduces the initial velocity of dredge materials and alters the path line of the resulted particle cloud.

In practice, sediment materials from river dredging are released either vertically downward or with an angle by employing a ramp or an oblique short pipe from the barges. In order to improve the mixing and spreading of sediments in a thin layer of dredge material into water body (i.e., lakes and oceans), it is possible to release sediments from two adjacent barges at a certain distance from each other. In Chapter 5, the efficiency of the release mechanism by two adjacent barges indicated that the cloud width in the swarm regime increased by 50% in comparison with a single particle cloud with double the mass (Janati and Azimi, 2021). The release angle, α, in twin particle clouds provides an additional tool for controlling the motion of particles in stagnant water and helps environmental engineers to reduce the footprints of the dredging process.

By altering nozzle distance and cloud's aspect ratio in twin particle clouds the final cloud width and the cloud frontal velocity were controlled which enabled engineers to mitigate the environmental concerns during the dredging process. In the present study, the dynamics of single and twin oblique particle clouds in stagnant water are investigated. The main characteristics of oblique particle clouds such as penetration length, particle contact time, clouds width, horizontal and vertical centroids, and frontal velocity were measured, and the entrainment capacity of the oblique twin particle clouds was extracted from measurements. The results of twin particle clouds with initial masses of $m/2$ are compared with a single oblique particle cloud with a mass of m to study particle-particle interactions in twin particle clouds. The simultaneous effects of the release angle, particle interactions by the varying distance between the adjacent nozzles (i.e., nozzle spacing, ε), and aspect ratio are studied as well.

6.2. Material and Methods

6.2.1. Experimental setup

A series of laboratory experiments were carried out in the Multiphase Flow Research Laboratory (MFRL) at Lakehead University to study particle dynamics of oblique single and twin particle clouds. A rectangular glass-walled tank with a dimension of 1.65 m x 0.85 m x 0.95 m was filled with tap water with an ambient temperature of $20 \pm 2°$ C (i.e., $\mu = 9.77 \times 10^{-4}$ kg/ms) to a constant water depth of 0.85 m. Two short pipes with an inner diameter of $d_o = 8$ mm, which were bent to $45°$ were mounted on the top of the tank (see Figure 6.1a). Sand particles with a density of 2564 kg/m^3 and a median sand size of $D_{50} = 0.507$ mm were used. Sand particles were passed through a series of sieves and sand particles between sieves #30 and #40 were only selected to improve the uniformity of sand particles. The sand particles were carefully washed and dried before filling the pipes to remove any impurities in sand particles. Each run was repeated three times to ensure the repeatability of individual runs and the average values with the lower and upper bounds were presented in the results section.

A high-speed camera (Photon-FASTCAM, 1024PCI-100KC, Japan) with a fixed sampling rate of 30 frames per second was located in front of the experimental set up to record the process of releasing dry sand particles with different initial conditions. Horizontal and vertical rulers were placed inside the tank for image calibration and to correct any image distortion. The release height of sand particles, which resulted in the lowest percentage of mass in the tailing part, for L_o/d_o ranging from 9.7 to 38.8 was found to be at the water surface (Gensheimer et al., 2013). To eliminate bubble formation and minimize air entrainment, a short distance of approximately 5 mm was allocated between the nozzles and the water surface (Azimi et al., 2012a; Moghadaripour et al., 2017a; Janati and Azimi, 2021). The mass flux of sand particles for oblique release ($d_o = 8$ mm, $\alpha = 45°$) was found to be constant and approximately equal to $\dot{m} = 4.7$ g/s for all aspect ratios. Figure 6.1a illustrates the schematic of the experimental setup, the adopted coordinate system, and the front view image of a twin oblique particle cloud. The twin particle clouds were marked with green and red colors for a better illustration of sand particles and parent clouds. Figure 6.1a shows that the two clouds released from nozzles with 45° angles collided with each other after a short distance from the nozzles. An image of a twin vertical particle cloud from the study of Janati and Azimi (2021) is shown in Figure 6.1b. The twin vertical particle clouds are used as benchmark

tests to study the effect of release angle in this study. The distance between two nozzles, ε, was subtracted from the measured cloud width, W, to attain the effective cloud width of twin vertical particle clouds, w_{2-V}. Similarly, the effective cloud width in twin oblique particle clouds is labeled as w_{2-O}.
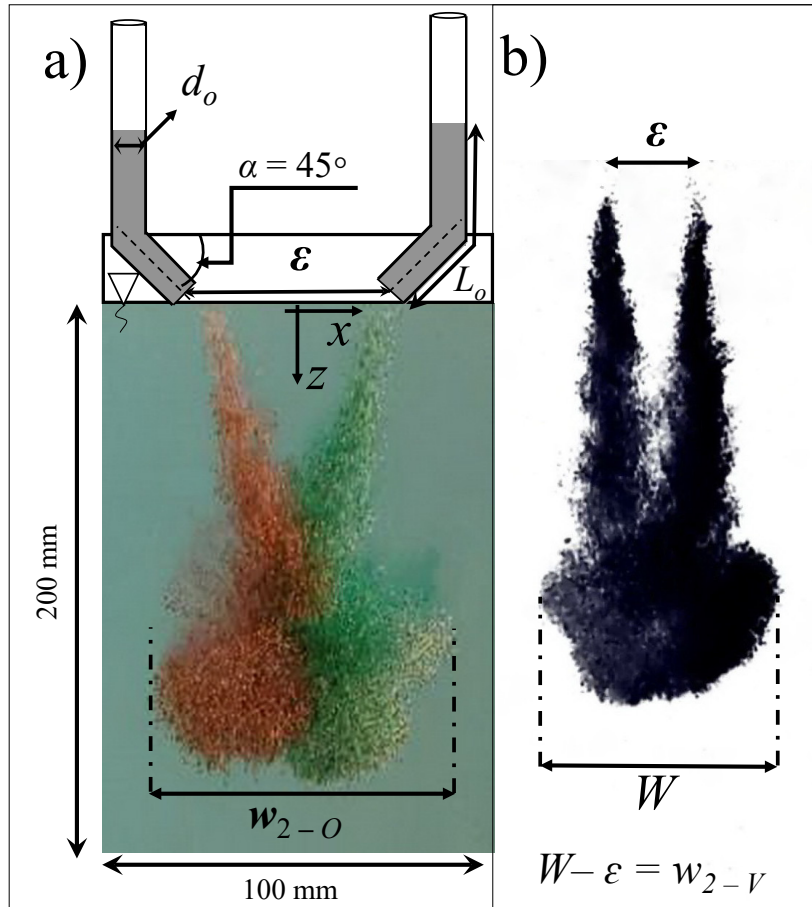
Figure 6.1. Front view images of twin particle clouds: a) schematic of the experimental setup, the photoluminescence image of an oblique twin particle cloud, and the coordinate system for Test No. 11 (2x6 grams, $\alpha = 45°$, $\varepsilon = 80$ mm); b) front view image of a vertically released twin particle cloud (2x6 grams, $\alpha = 90°$, $\varepsilon = 80$ mm) from the study of data Janati & Azimi, (2021), Chapter 5.

Different masses of dry sand particles (i.e., $m = 6, 12, 18,$ and 24 g) were selected to form single and twin oblique particle clouds with a relatively wide range of aspect ratios of $L_o/d_o = 9.7, 19.4,$ 29.1, and 38.8. For single oblique particle cloud tests, the total mass of sand particles was released from a 45-degree nozzle and for two oblique particle cloud tests, the total mass was first divided into two equal masses and then was released simultaneously from two adjacent pipes. The benchmark tests for single oblique particle clouds were labeled as (1 x m g) and they had the same

aspect ratio, L_o/d_o, as their corresponding twin oblique particle clouds (2 x $m/2$ g). Figure 6.2 shows the raw images of a single oblique particle cloud with different aspect ratios.

According to particle size classification based on Stokes number, $St = (\rho_s - \rho_w)D_{50}^2 u_o/18\mu d_o$, where u_o is the velocity of particles at the nozzle, particles are classified as hydrodynamically large particles for $S_t > 0.55$ (Moghadaripour et al., 2017a). It should be noted that $L_o/d_o = 9.7$ was selected as a minimum aspect ratio for twin oblique particle clouds since no particle interaction was observed below the selected minimum aspect ratio. The maximum aspect ratio of $L_o/d_o = 38.8$ was chosen since beyond this aspect ratio, the twin oblique particle clouds behave as sand jets and sand particles were continuously discharged into water. Janati and Azimi (2021) introduced a non-dimensional parameter, $L_o/(zd_o)^{1/2}$, which scales the motion of sand jets and particle clouds in the water. This parameter was introduced to incorporate the effect of water depth, z, and aspect ratio, L_o/d_o, on the motion of sand jets and particle clouds. The boundary between sand jets and particle clouds in this study occurred when $L_o/(zd_o)^{1/2} = 3.75$ and particle clouds were formed for $L_o/(zd_o)^{1/2} < 3.75$.

The fluid with entrained particles was illuminated using two light sources (Woods L13, 1000-Watt Telescope Work Light, Canada) from the sides of the glass tank. A total number of 26 experiments were conducted (see Table 6.1) to investigate the effects of aspect ratio, L_o/d_o, and source separations, ε/d_o, on the evolution of twin oblique particle clouds. The effects of nozzle spacing in twin oblique particle clouds and the most optimum nozzle distance were investigated with five nozzle spacings ranging from 40 mm to 120 mm which are corresponding to the non-dimensional separation distances of $\varepsilon/d_o = 5$, 7.5, 10, 12.5, and 15. The effects of release angle and interaction between each cloud were negligible for $\varepsilon < 40$ mm so, $\varepsilon = 40$ mm was used as the minimum distance between two nozzles. On the other hand, particle clouds did not have considerable interactions with each other and acted as single particle clouds for a distance larger than 120 mm.

Table 6.1. Experimental tests and non-dimensional parameters on oblique twin particle clouds with d_{50} = 0.507 mm, d_o = 8 mm, and release angle of α = 45º.

Test No.	Sand mass m	Nozzle releasing space ε	L_o	T	V_o (×10³)	B_o (×10⁻⁵)	L_o/d_o
	(g)	(mm)	(mm)	(s)	(mm³)	(m⁴/s²)	(−)
1	1x6	0	77.6	1.38	3.90	6.01	9.70
2	2x3	40	77.6	1.38	3.90	6.01	9.70
3	2x3	60	77.6	1.38	3.90	6.01	9.70
4	2x3	80	77.6	1.38	3.90	6.01	9.70
5	2x3	100	77.6	1.38	3.90	6.01	9.70
6	2x3	120	77.6	1.38	3.90	6.01	9.70
7	1x12	0	155.2	1.95	7.80	12.02	19.40
8	2x6	40	155.2	1.95	7.80	12.02	19.40
9	2x6	60	155.2	1.95	7.80	12.02	19.40
10	2x6	80	155.2	1.95	7.80	12.02	19.40
11	2x6	100	155.2	1.95	7.80	12.02	19.40
12	2x6	120	155.2	1.95	7.80	12.02	19.40
13	1x18	0	232.8	2.39	11.70	18.03	29.10
14	2x9	40	232.8	2.39	11.70	18.03	29.10
15	2x9	60	232.8	2.39	11.70	18.03	29.10
16	2x9	80	232.8	2.39	11.70	18.03	29.10

17	2x9	100	232.8	2.39	11.70	18.03	29.10
18	2x9	120	232.8	2.39	11.70	18.03	29.10
19	1x24	0	310.4	2.76	15.60	24.04	38.80
20	2x12	40	310.4	2.76	15.60	24.04	38.80
21	2x12	60	310.4	2.76	15.60	24.04	38.80
22	2x12	80	310.4	2.76	15.60	24.04	38.80
23	2x12	100	310.4	2.76	15.60	24.04	38.80
24	2x12	120	310.4	2.76	15.60	24.04	38.80

6.2.2. *Image analysis and data processing*

Image processing techniques in MATLAB image processing toolbox (Math Works, Inc., 2018) were employed to extract data from the time-history images. The boundary of the clouds was detected and the cloud's characteristics were obtained from image analysis and Particle Image Velocimetry (PIV). A Particle Image Velocimetry toolbox (PIVlab) from MATLAB software was implemented to obtain the velocity of individual particles in single and twin oblique particle clouds. The background subtraction method was employed to differentiate particle clouds from the background ambient. The background noises were removed and the boundary of the clouds was detected in each image. All images were converted to binary images and the cloud's physical properties such as cloud width, horizontal and vertical centroids, and frontal positions were extracted. More details about image preparation and image thresholding procedures can be found in Janati and Azimi (2021).

Depending on the width of merged cloud, the region of interest (ROI) was considered between approximately 165 mm and 200 mm in the horizontal direction and 465 mm in the vertical direction. The selection of the ROI represented the image resolution of approximately 2100 pixels (rows) by 900 (columns). It is noteworthy to mention that the median diameter of sand particles (i.e., D_{50} = 0.507 mm) is approximately 2.3 times the size of a pixel. The CLAHE and Wiener2

de-noise pre-processing filters were implied to de-noise the images for the PIV analysis. A 3-pass algorithm, in which the velocity calculation algorithm was repeated three times, was used in combination with three interrogation windows. The interrogation started with a window size of 64 x 64 pixels with an overlap of 32 pixels (i.e., 50% overlap). The interrogation window was then reduced to 32 x 32 pixels with 16 pixels overlap for the second and third passes. To extract velocity data, the poly-line command was used and pixel motions were converted to physical motions with a conversion rate of 0.00661 m/s for one-pixel movement per frame.

6.3. Results and Discussion

6.3.1. Evolution of single oblique particle clouds

Figure 6.2 shows the raw images of single oblique particle clouds with a wide range of aspect ratios between 4.85 and 38.8 at a time when all sand particles were discharged into water. As can be seen, the oblique discharge shifted the frontal head in a horizontal direction, which caused considerable variations in the size and velocity of the cloud's front (Moghadaripour et al. 2017b). The cloud frontal position, Z_f, (i.e., the cloud front distance from the nozzle), the horizontal, X_{bar}, and vertical, Z_{bar}, distances from the centroid of the cloud to the nozzle are marked in Figure 6.2. The images of particle clouds were converted to binary images and a MATLAB function was coded to calculate the centroids of the 2-Dimensional projection on x-z plane.
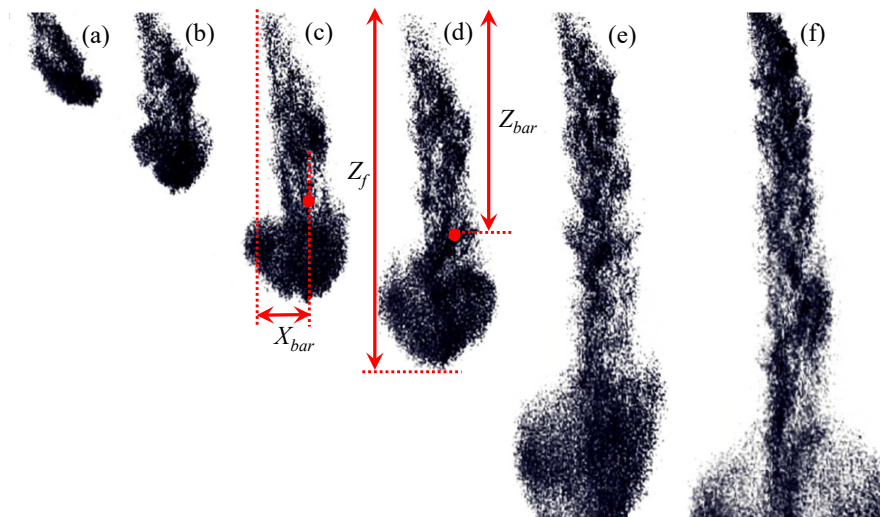
Figure 6.2: Raw images of single oblique particle clouds with a release angle of $\alpha = 45°$ and different aspect ratios at a time that all sand particles were discharged into water: a) $L_o/d_o = 4.85$; b) $L_o/d_o = 9.7$; c) $L_o/d_o = 14.55$; d) $L_o/d_o = 19.4$; e) $L_o/d_o = 29.1$; f) $L_o/d_o = 38.8$.

147

In order to understand the effect of aspect ratio on the overall motion of single oblique particle clouds in a systematic order, the variations of non-dimensional vertical centroid with time were plotted in Figure 6.3a. As can be seen, the vertical centroid of single oblique particle clouds increased linearly with time and aspect ratio. By employing multivariable regression analysis an empirical formulation was developed to predict the centroid of single oblique particle clouds in the vertical direction as:

$$\frac{Z_{bar}}{d_o} = \left(0.35(L_o/d_o)+10.7\right)\left(\frac{t}{T}\right)$$

Eq. (6.1)

The coefficient of determination of the proposed equation, R^2, is 0.9. The performance of the proposed model in the prediction of the vertical centroid for L_o/d_o = 4.85 and 38.8 are shown in Figure 6.3a.

Figure 6.3b shows the effect of aspect ratio on variations of the ratio of horizontal to vertical centroids of single oblique particle clouds with non-dimensional time t/T where $T = B_o^{1/2}/u_\infty^2$. The time variations of the centroid's ratio are important for managing dredging activities and estimation of the resulted sediment deposition. The overbars in data points indicate the uncertainty of measurements for L_o/d_o = 19.4 and similar uncertainty levels were found for other tests. It can be seen that at the beginning of the releasing process, the effect of aspect ratio on variations of X_{bar}/Z_{bar} is more pronounced than that the swarm regime. At t/T = 0.5, the non-dimensional centroid ratio of single oblique particle cloud for L_o/d_o = 9.7 is 0.27 whereas this ratio for an aspect ratio of L_o/d_o = 19.4 is 0.2. Such geometry differences reduce the gradual convergence of particles in twin oblique particle clouds during the collision of frontal heads. In a quasi-steady-state regime, where the frontal head descends vertically (i.e., $t/T \geq 1.5$), the ratio of horizontal to vertical centroids becomes time-independent with a value ranging from 0.06 to 0.12. It should be mentioned that the quasi-steady state regime is a concept used in fluid mechanics to describe a situation where the flow field has reached a state of relative equilibrium, such that the time rate of change of the flow parameters is much smaller than the characteristic time scales of the flow. In this regime, the flow can be considered to be steady in a statistical sense, even though there may be small fluctuations in the flow parameters due to turbulence or other sources of instability. The quasi-steady state regime is often used in the analysis of flows involving unsteady or time-varying phenomena, where the time scales of the flow are comparable to or shorter than the characteristic time scales of the flow physics. In these situations, the quasi-steady state assumption allows for

simplified modeling and analysis of the flow behavior, while still capturing the essential features of the dynamics. An empirical equation was proposed to predict X_{bar}/Z_{bar} by employing multivariable regression analysis with $R^2 = 0.9$ as:

$$\frac{X_{bar}}{Z_{bar}} = \left[0.3(L_o/d_o)^{-0.34} \right] (\frac{t}{T})^b \qquad \text{Eq. (6.2)}$$

where $b = -0.018(L_o/d_o)-0.45$ for $L_o/d_o \leq 20$ and -0.55 for $L_o/d_o > 20$. The proposed model for prediction of the centroid's ratio for $L_o/d_o = 4.85$ and 38.8 are shown in Figure 6.3b.
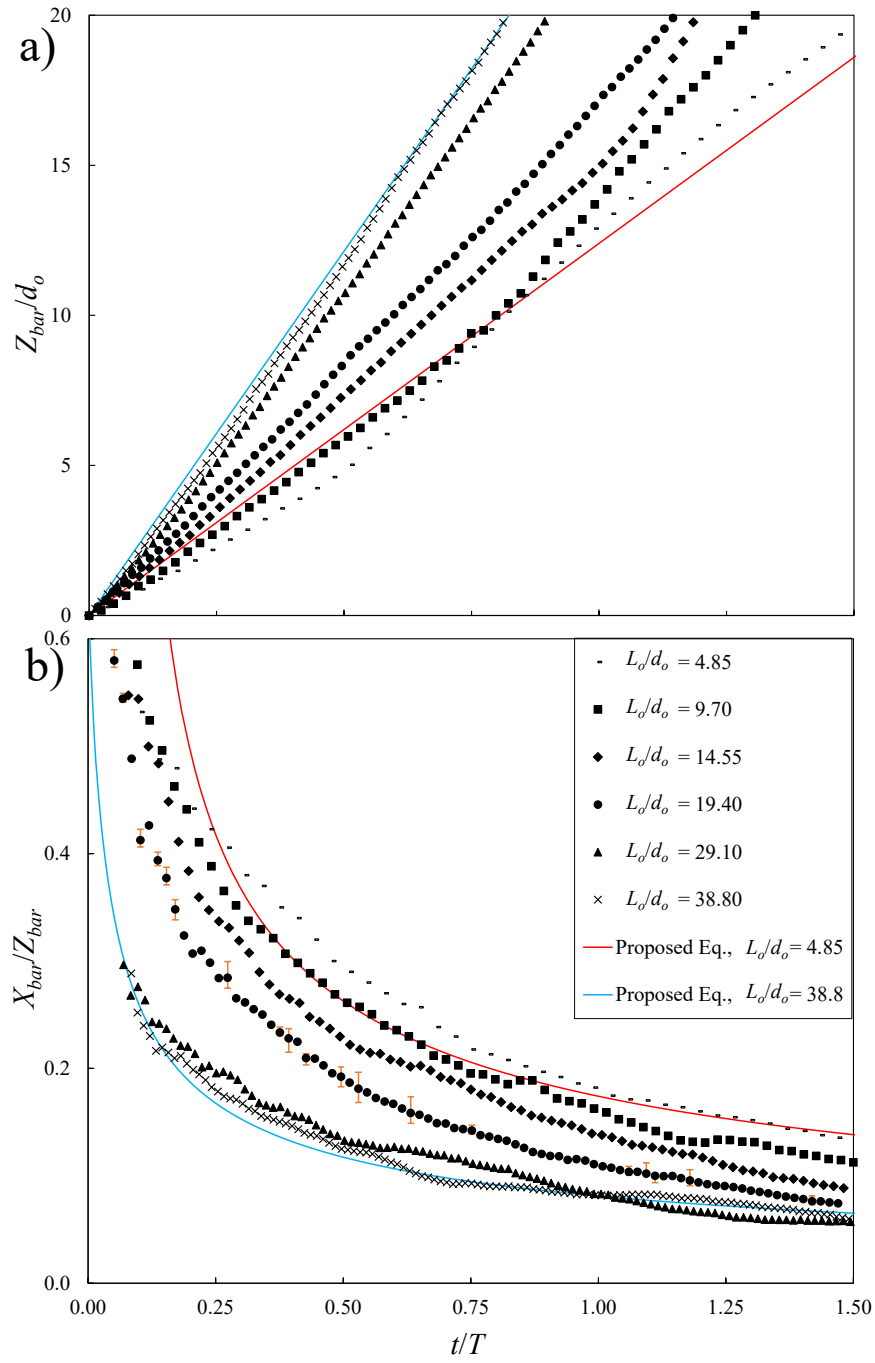
Figure 6.3. Effects of aspect ratio on the time evolution of oblique single particle clouds with a release angle of $\alpha = 45°$: a) variations of the vertical centroid of oblique single particle clouds (Z_{bar}) versus non-dimensional time, t/T; b) variations of the ratio of cloud's centroids, X_{bar}/Z_{bar}, with non-dimensional time, t/T.

Figure 6.4 illustrates the effects of aspect ratio, L_o/d_o, on the trajectory of single oblique particle clouds based on the position of the cloud's centroids, X_{bar} and Z_{bar}. The overbars in Figure 6.4 show the uncertainties of centroid measurements for L_o/d_o = 4.85 which were the maximum uncertainties amongst other particle cloud tests. It was found that particle clouds with smaller aspect ratios tend to move further in horizontal direction as they follow large vortices. The smaller advancement of particles in horizontal direction is due to the wake effect and breaking of large eddies by more particles in large aspect ratios. At the same vertical centroid position of Z_{bar}/d_o = 15, particle cloud with the smallest aspect ratio (i.e., L_o/d_o = 4.85) has a horizontal centroid position of X_{bar}/d_o = 2.5. Whereas for the largest aspect ratio (i.e., L_o/d_o = 38.8) the horizontal centroid position of the cloud decreased by 40% to X_{bar}/d_o = 1.55. Therefore, by increasing the aspect ratio, the tendency of particles to descend downward increases.

In order to predict the behavior of oblique particle clouds in stagnant ambient, the trajectory of oblique particle clouds can be obtained by implementing Eqs. (6.1) and (6.2). As can be seen in Figure 6.4, the modeled trajectory of oblique particle clouds for the largest and smallest aspect ratios was added, as red and blue curves, respectively. The proposed model shows a good agreement with the observed data in this study. As can be seen in Figure 6.4, the horizontal centroids in particle clouds with small aspect ratios are greater than the clouds with larger aspect ratios. Therefore, discharging small masses of dredged materials in water can affect a wider area. This result can be helpful in situations that a large area in water needs to be nourished or in construction of artificial islans where sedimentary materials should be disposed in a designated area.
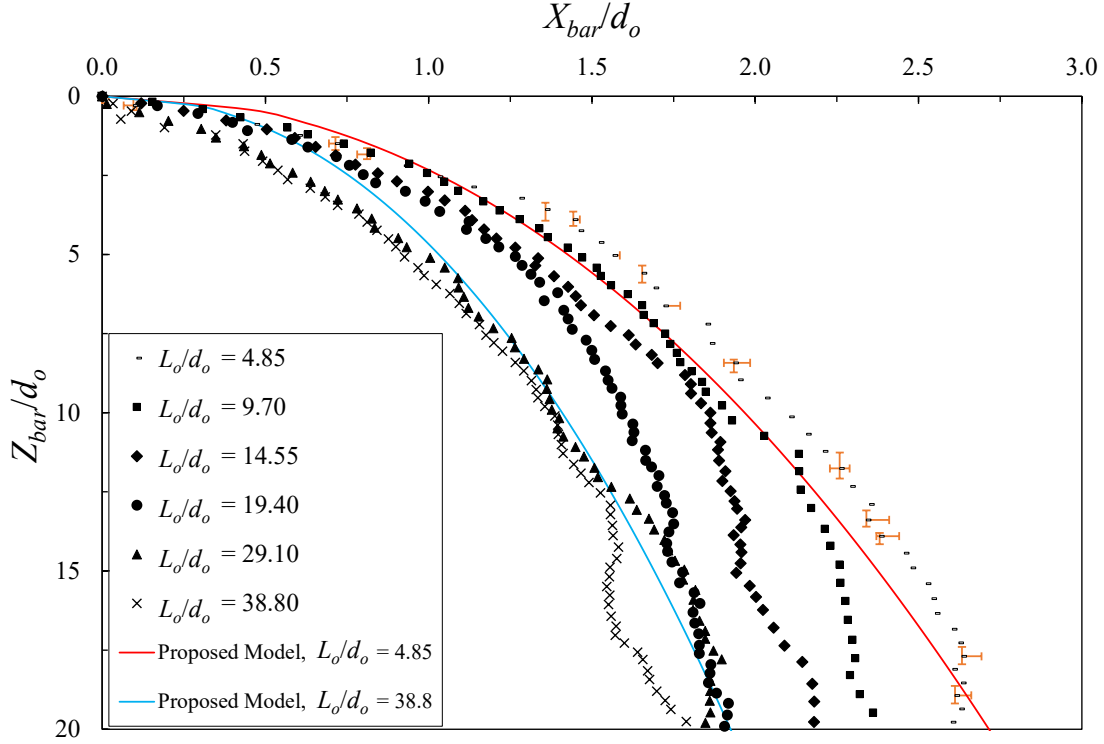
Figure 6.4. Effect of cloud aspect ratio, L_o/d_o, on the trajectory of single oblique particle clouds with a release angle of $\alpha = 45°$.

Variations of normalized cloud width, w/Z_f, with normalized time, t/T, for both vertical and oblique single particle clouds with different aspect ratios are shown in Figure 6.5. The solid symbols show the results of single vertical particle clouds, and the open symbols represent the results of single oblique particle clouds. The proposed equation for prediction of cloud width of single vertical particle clouds from the study of Moghadaripour et al., (2017b) was rearranged ($W/Z_f = \phi d_o(L_o/d_o)^{0.345}/3.57l(t/T)^{0.55-\zeta}$), where ϕ is 18.5, 6.5, and 6 for small, medium, or large particle size ranges, ζ is 0.6 for all ranges of particle size, and $l = (B_o^{1/2})/u_\infty$ and added in Figure 6.5a. This equation had a good agreement with the measurements of this study specifically from $t/T > 0.5$. As can be seen, the width of the cloud in single oblique particle clouds is larger than their corresponding vertical particle clouds with the same aspect ratios. Figure 6.5a also shows that the cloud's width in vertical clouds is independent of the aspect ratio, L_o/d_o, whereas the cloud's width in oblique particle clouds increased with increasing L_o/d_o. The sample images of oblique and vertical particle clouds ($L_o/d_o = 19.4$, $t/T = 0.93$) are shown in Figure 6.5a.

As can be seen, the width of the oblique particle cloud is larger than the frontal width of vertical clouds whereas the frontal position of the vertical cloud is larger than the oblique particle cloud.
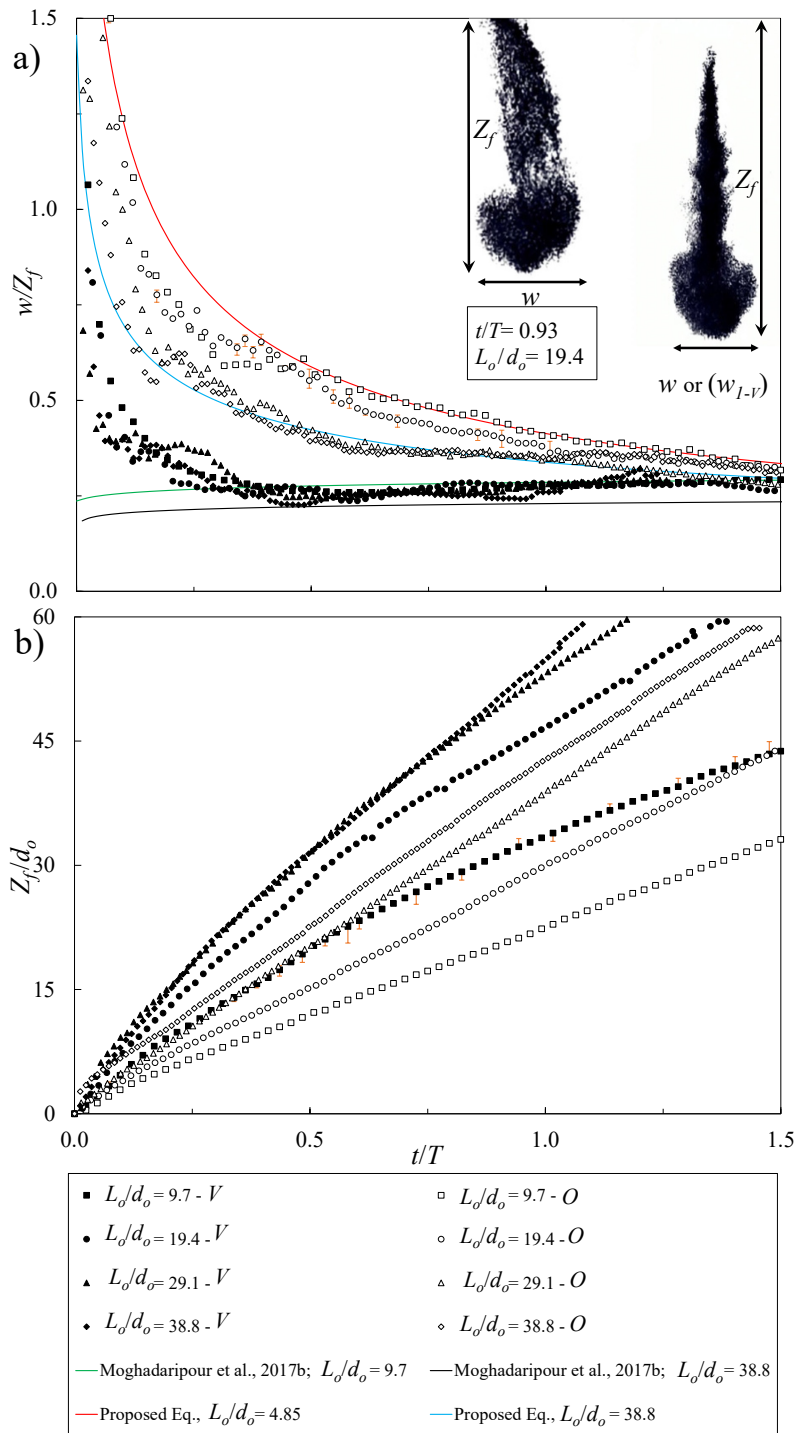
Figure 6.5. Time evolution of cloud front in single oblique and vertical particle clouds: a) variations of the normalized front width of the clouds with non-dimensional time (The image on

153

the left side is an oblique particle cloud with a release angle of $\alpha = 45°$ at $t/T = 0.93$ and $L_o/d_o = 19.4$ and the one on the right side is vertical particle cloud ($\alpha = 90°$) at $t/T = 0.93$ and $L_o/d_o = 19.4$); b) variations of the normalized frontal position of the clouds with non-dimensional time.

An empirical equation was proposed (i.e., $R^2 = 0.88$) to correlate the cloud width of oblique particle clouds time as:

$$\frac{w}{Z_f} = \left(-0.0024(L_o/d_o) + 0.4\right)\left(\frac{t}{T}\right)^{0.006(L_o/d_o)+0.56}$$ Eq. (6.3)

Since the frontal position, Z_f, of particle clouds increases during the cloud evolution, the variations of non-dimensional cloud's front, Z_f/d_o, with normalized time, t/T, for both vertical and oblique single particle clouds and with different aspect ratios is illustrated in Figure 6.5b. The correlation of normalized frontal position with time is required to calculate the variations of the cloud's width with time.

6.3.2. Effect of release angle on the evolution of twin oblique particle clouds

The effect of release angle in twin particle clouds is an important factor in the spread of particle clouds in ambient water. In order to isolate the effect of release angle, the results of oblique twin particle clouds are compared with the results of vertical twin particle clouds from the study of Janati and Azimi (2021). In order to study the effects of release angle on the evolution of twin particle clouds and defining the mixing efficiency over time, the effects of aspect ratio and nozzle spacing on variations of cloud width in twin oblique particle clouds with time were studied and the results were plotted in Figure 6.6a to 6.6d.

The cloud widths of twin oblique particle clouds were normalized with the corresponding cloud width of twin vertical particle clouds. The results revealed that the widths of twin oblique particle clouds were significantly larger than the cloud width of the corresponding twin vertical particle clouds, particularly at the beginning of the releasing process. The spreading of twin oblique particle clouds diminished at a certain non-dimensional time which was labeled as $(t/T)^*$. Due to particle collision in frontal heads of twin particle clouds and high turbulence level at the onset of release, the cloud width of twin oblique particle clouds was as high as six times the corresponding

154

twin vertical particle clouds. However, such mixing advantage decreased over time and the higher values of cloud width in oblique clouds were limited by the nozzle spacing for $t/T \geq (t/T)^*$.

The decay rate of normalized cloud width in twin particle clouds for $\varepsilon/d_o = 15$, which shows the most noticeable changes, was added in Figure 6.6 to determine the mixing efficiency of twin oblique particle clouds over time. As can be seen, the decay rate of normalized cloud width decreased with increasing aspect ratio until it reached the critical non-dimensional time, $(t/T)^*$. The critical mixing time are 1.5 for $L_o/d_o = 9.7$, $\varepsilon/d_o = 15$ and 0.47 for $L_o/d_o = 38.8$, which shows that $(t/T)^*$ decreased by increasing aspect ratio. In other words, by increasing aspect ratio the twin oblique clouds can interact and mix quicker than the condition where the aspect ratios are small. The critical mixing time in oblique particle clouds decreased by approximately 70% as the cloud aspect ratio increased from 9.7 to 38.8. The normalized time scale of $(t/T)^*$ indicates the instant at which the oblique release has more mixing efficiency over the vertical release in twin particle clouds and beyond $(t/T)^*$ the cloud width of twin particle cloud is independent of the release angle. As a result, it is important to accurately estimate the value of $(t/T)^*$ for design and management purposes. The results present that the proposed releasing model of sedimentary material in water can maximize the mixing, control the area in which the dredging material should be placed, and reduce the ambient turbidity.

Moreover, mixing time is an important parameter in the quality of water ecosystems as suspended sediments can cause some ecological problems. Therefore, by altering the aspect ratios and source separations in dredging activities, the mixing time can be optimized, which will be beneficial in the management and controlling of aquatic environmental pollution.
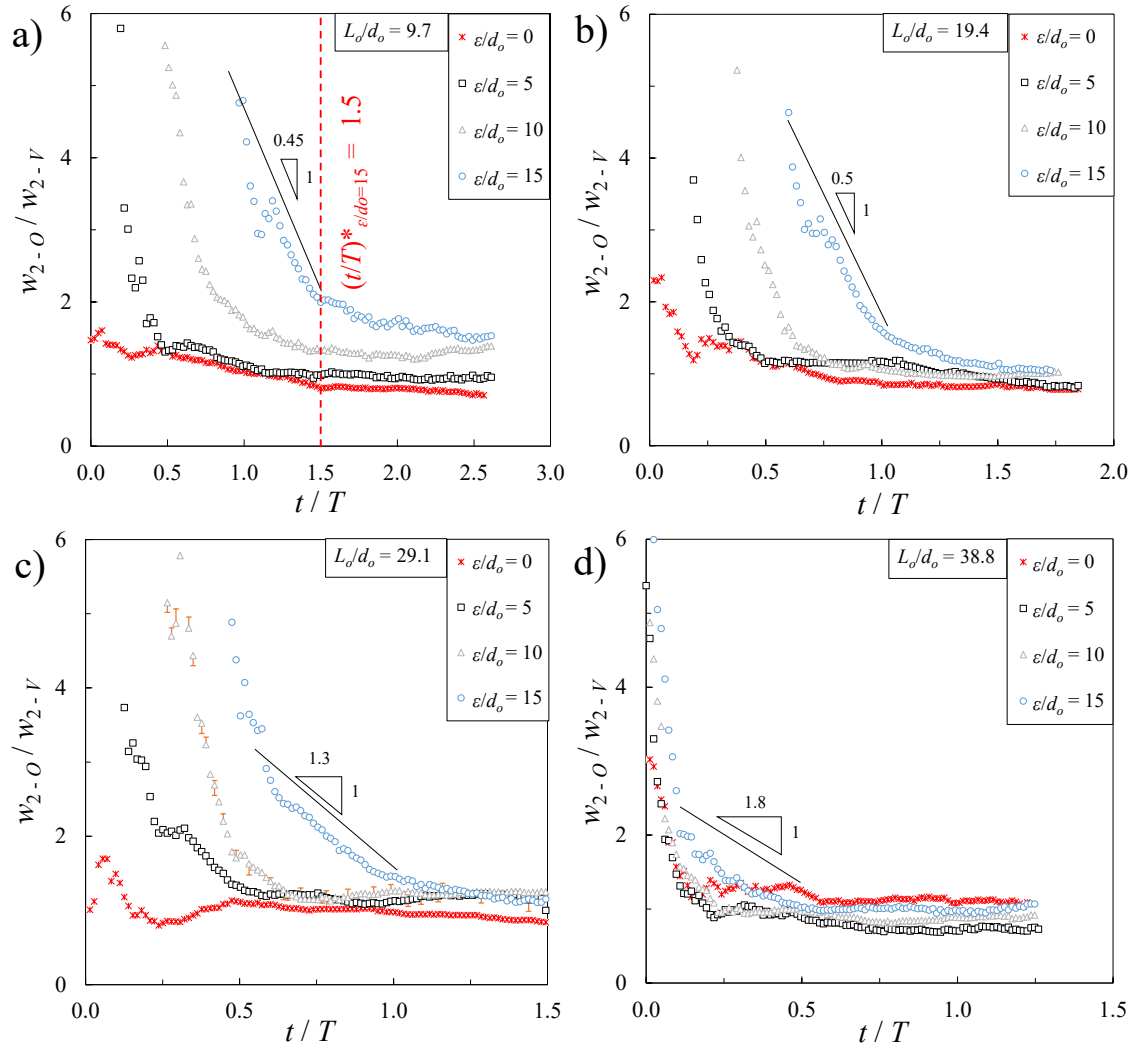
Figure 6.6. Effects of normalized nozzle spacing, ε/d_o, on variations of the total cloud width with time for twin particle clouds; a) 2x3 grams, $L_o/d_o = 9.7$; b) 2x6 grams, $L_o/d_o = 19.4$; c) 2x9 grams, $L_o/d_o = 29.1$; d) 2x12 grams, $L_o/d_o = 38.8$.

Figure 6.7 shows the correlations of non-dimensional mixing time, $(t/T)^*$, with aspect ratio and nozzle spacing. The overbars in Figure 6.7 indicate the uncertainty of measurements and similar uncertainty ranges were found for other tests in this study. The mixing time in twin oblique particle clouds with the smallest aspect ratio (i.e., $L_o/d_o = 9.7$) was longer due to the lower energy of sand particles. In contrast, by increasing the aspect ratio (i.e., $L_o/d_o = 38.8$, Figure 6.7d), the decay rate of normalized cloud width decreased and the results were independent of nozzle spacing. To obtain robust results for field operation and to have controls in dredging processes, an empirical formula

was developed to predict the mixing time, $(t/T)^*$, using a multivariable regression analysis with R^2 = 0.97 as:

$$\left(\frac{t}{T}\right)^* = \left(-0.002\left(\frac{L}{d_o}\right) + 0.12 \right) \frac{\varepsilon}{d_o}$$

Eq. (6.4)
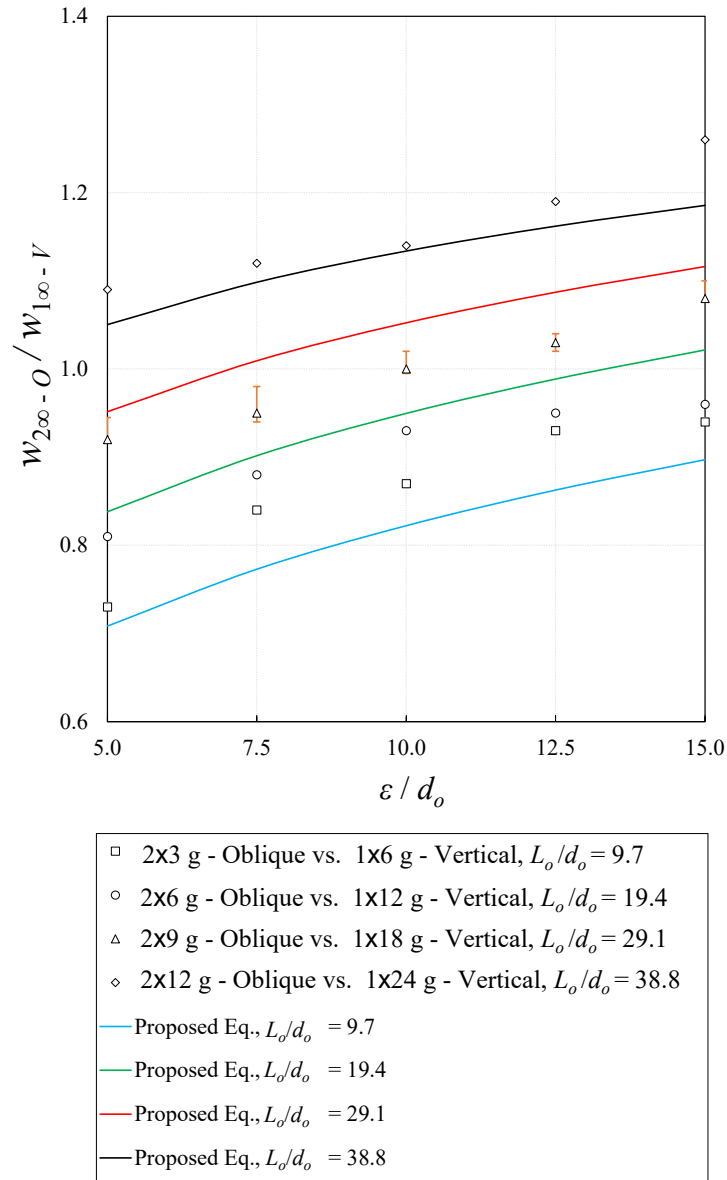
Figure 6.7. Effects of normalized nozzle spacing, ε/d_o, and aspect ratio, L_o/d_o, on the boundary of the swarm regime, $(t/T)^*$. The swarm regime occurs when the total cloud width ratio ($w_{2\text{-}O}/w_{2\text{-}V}$) is time-independent.

By assuming that the vertical particle clouds are symmetrically evolved during the time, the volume and surface area of particle clouds were measured in each frame using image analysis and MATLAB programming. Then entrainment coefficients of particle clouds were calculated based on the equation proposed by Moghadaripour et al., (2017b).

The time variations of maximum vertical velocity, $u_{z(max)}$, in the centerline of twin oblique particle clouds were obtained from the PIV analysis of the images. Figure 6.8 shows the effect of release angle and nozzle spacing, ε/d_o = 5, 7.5, 10, 12.5, and 15 (i.e., Test 9-13) on variations of vertical centerline velocity, $u_{z(max)}$, with time for twin oblique particle clouds with an average aspect ratio of L_o/d_o = 19.4. The PIV velocity profiles on the fixed centerline of the twin clouds were obtained with time and the overall trend shows that $u_{z(max)}$ increases from the beginning of the releasing process to reach the peak in the middle of the test. Then the velocity started to reduce until the cloud reached its settling velocity of 0.075 m/s at the swarm phase.

The red open squares represent the velocity data for twin oblique particle clouds and the solid squares show the velocity data for twin vertical particle clouds from Chapter 5. As can be seen in Figure 6.8a, the velocities of twin vertical particle cloud were approximately 5% higher than the twin oblique particle clouds centerline velocities, particularly in the first two seconds from the beginning of release (i.e., t/T = 1.03). Figure 6.8b-6.8d show the velocity profiles of twin oblique and vertical particle clouds with higher nozzle spacing. As can be seen, by increasing nozzle distances, the maximum centerline velocities of sand particles in twin oblique particle clouds became approximately 10% larger than centerline velocities in twin vertical particle clouds. This indicates that the release angle increases the centerline velocity of sand particles between 5% and 10% depending on the source separation.

The frontal heads of particle clouds severely collided with each other in twin oblique particle clouds and such collisions always occur during the second phase of cloud evolution. Therefore, the interaction between sand particles dictates the motion of twin particle clouds to move vertically downward; so, the merged cloud descends faster than twin vertical particle clouds. As shown in Figure 6.8a, the distance between the nozzles was smaller than the other cases; therefore, twin vertical clouds interacted with each other at the early stages of evolution. However, due to lower ambient entrainment particle velocity did not decrease and consequently, particles descended with higher velocities than the twin oblique particle clouds.

As illustrated in Figure 6.8b to 6.8e, the instantaneous centerline velocities of sand particles in oblique particle clouds during the test, with the same aspect ratios and source separations, are

approximately 7% larger than the corresponding twin vertical ones. It's noteworthy that the maximum differences between twin oblique and vertical particle clouds centerline velocities occur approximately in the midpoint of the test.
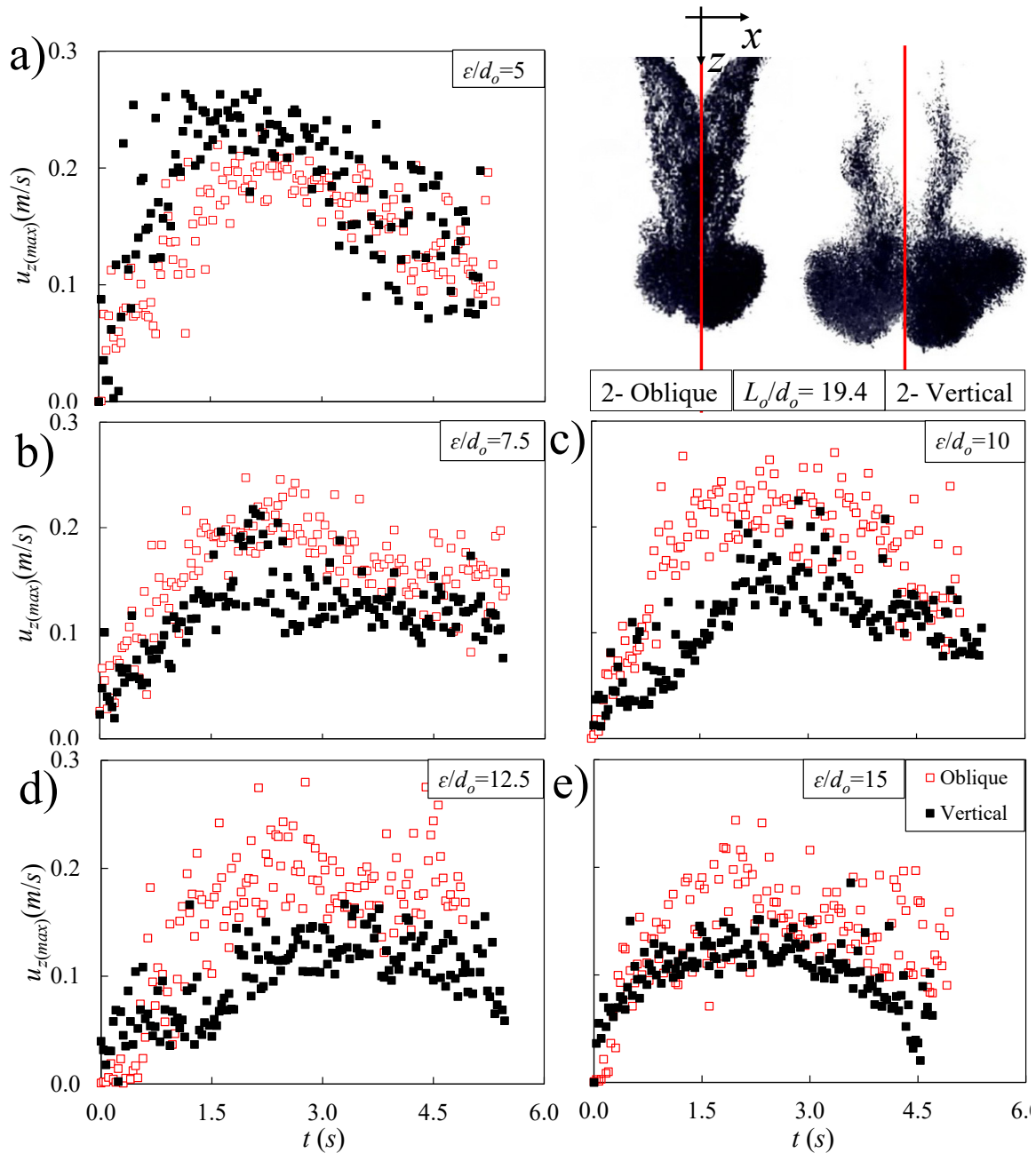
Figure 6.8. Effects of normalized nozzle spacing on the time variations of the maximum centerline velocity, $u_{z(max)}$, inside the cloud for twin oblique and vertical particle clouds with $L_o/d_o = 19.4$: a) Test No. 9, 2x6 grams, and $\varepsilon/d_o = 5$, b) Test No. 10, 2x6 grams, and $\varepsilon/d_o = 7.5$, c) Test No. 11, 2x6

grams, and ε/d_o = 10, d) Test No. 12, 2x6 grams, and ε/d_o = 12.5, e) Test No. 13, 2x6 grams, and ε/d_o = 15.

The total duration of experiments in Figure 6.8e was one second less than the other cases, which are due to the larger distances between two nozzles. Such high nozzle spacing prevented the clouds to move downward with significant particle-particle interactions. The two particle clouds in Figure 6.8e acted as separate single clouds and they had no distinguished interactions since the two nozzles were far from each other to have significant interactions. Therefore, the velocities did not diminish by particle-particle interactions and the clouds reached the bottom of the tank faster than the other cases.

6.3.3. *Effect of particle interactions on evolution of twin oblique particle clouds*

In order to isolate the effect of particle interaction the results of twin oblique particle clouds were compared with the results of single oblique particle clouds with double the mass. Figure 6.9 shows the time evolution images of twin and single photoluminescence oblique particle clouds.

Figure 6.9a shows the three phases of particle cloud formation in a 2x6 grams twin oblique particle clouds with $\alpha = 45°$, $\varepsilon = 120$ mm, and $L_o/d_o = 19.4$. The first image has a non-dimensional time of $t/T = 0.5$. At this time, two particle clouds are drawn toward each other without considerable mixing. Subsequently in $t/T = 0.85$, the frontal heads entangled together, and the interior particles interacted. The breaking of dominant eddies by the collided particles resulted in merging particles that vertically descend without interaction with the ambient water. It should be mentioned that at $t/T = 1.05$ and onward, the green color washed out faster than the red color. This can be partially due to the instability of clouds after the collision. Due to the internal motion and collision of sand particles, the parent clouds were left behind from the frontal heads for $t/T \geq 1.2$. At $t/T = 1.5$, the merged clouds shaped a semi-hemisphere in which the concentration of sand particles around the bottom boundary became higher than the other part of the hemisphere. Figure 6.9b shows the evolution of a single oblique particle cloud with the release angle of $\alpha = 45°$ and an aspect ratio of $L_o/d_o = 19.4$. As can be seen, the first three images with t/T ranged between 0.4 and 1.15 were in the initial acceleration phase until all particles were discharged in water. The particle clouds in the fourth and fifth images ($t/T = 1.4$ and 1.5) were in the thermal phase. At $t/T = 1.7$, the parent cloud left behind from sand particles as the red color began to wash out due to water entrainment and

particle interactions with the ambient. The trailing stem gradually faded and the cloud frontal head expanded throughout the process until all sand particles were deposited.
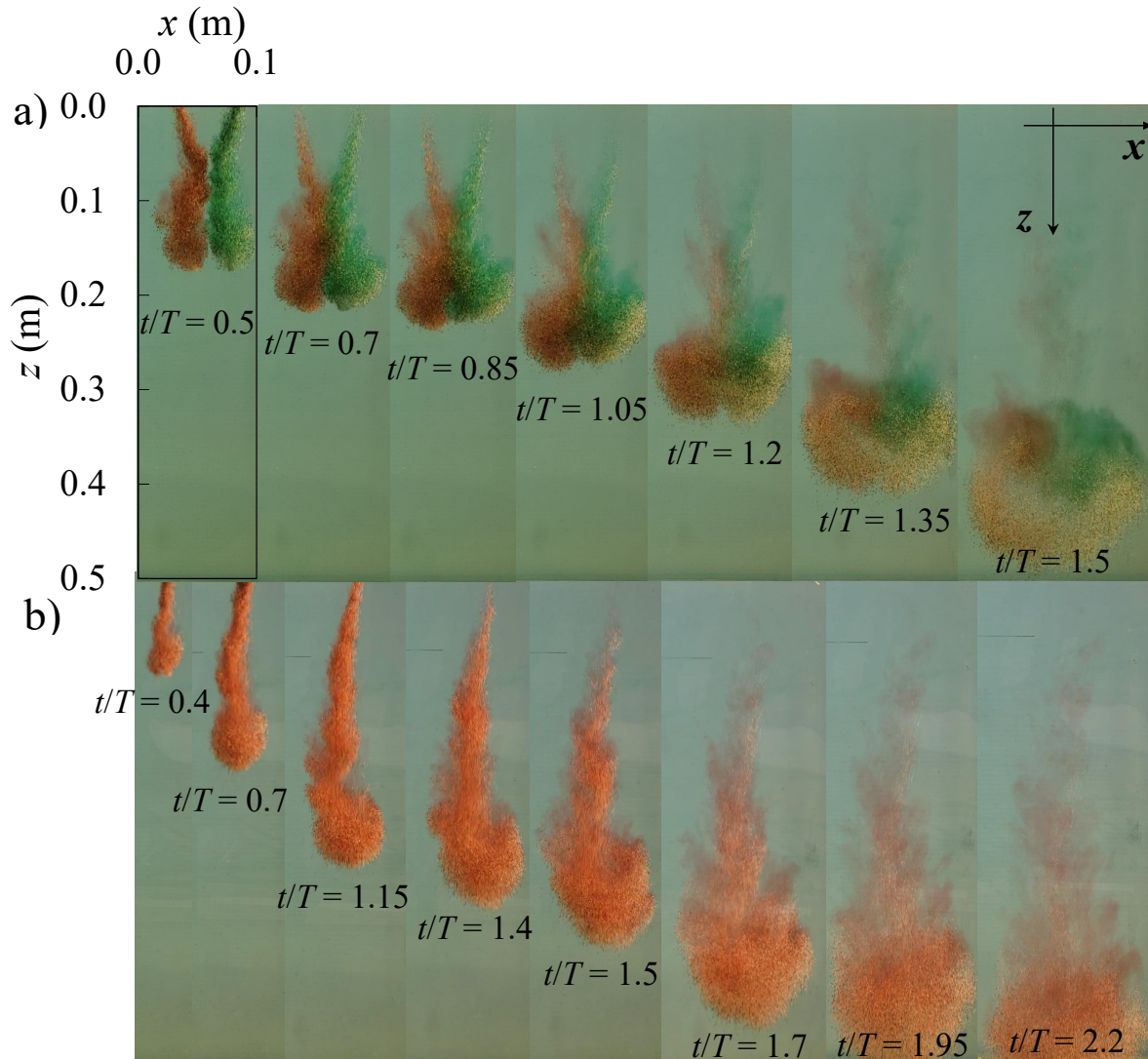
Figure 6.9. Time evolution of twin and single oblique particle clouds. The adjacent particle clouds and the entrained ambient were photoluminescence: a) Test No. 13 (2x6 grams, $\alpha = 45°$, $\varepsilon = 120$ mm, $L_o/d_o = 19.4$); b) Test No. 8 (1x12 gram, $\alpha = 45°$, $L_o/d_o = 19.4$).

Figure 6.10 shows the variations of entrainment coefficients with the normalized frontal position of the twin vertical cloud. As can be seen, overall ambient entrainment coefficients significantly decrease by increasing the aspect ratio of particle clouds. The entrainment coefficients at the beginning of release for all aspect ratios were approximately 0.11, they drastically decreased until they reached $Z_f/d_o = 25$ to 30 depending on their aspect ratios. Moreover, as can be seen in Figure

161

6.10, Lai et al., (2016) presented approximately the same result for the beginning of the releasing process (i.e., $\alpha_e = 0.105$ vol/vol). However, they showed that by falling along the water depth, the entrainment coefficient was drastically reduced until reached $Z_f/d_o = 8$, and after that, it remained constant. The dispersion of polydisperse particles indicated a constant ambient entrainment coefficient of $\alpha_e = 0.07$ (Lai et al., 2013).
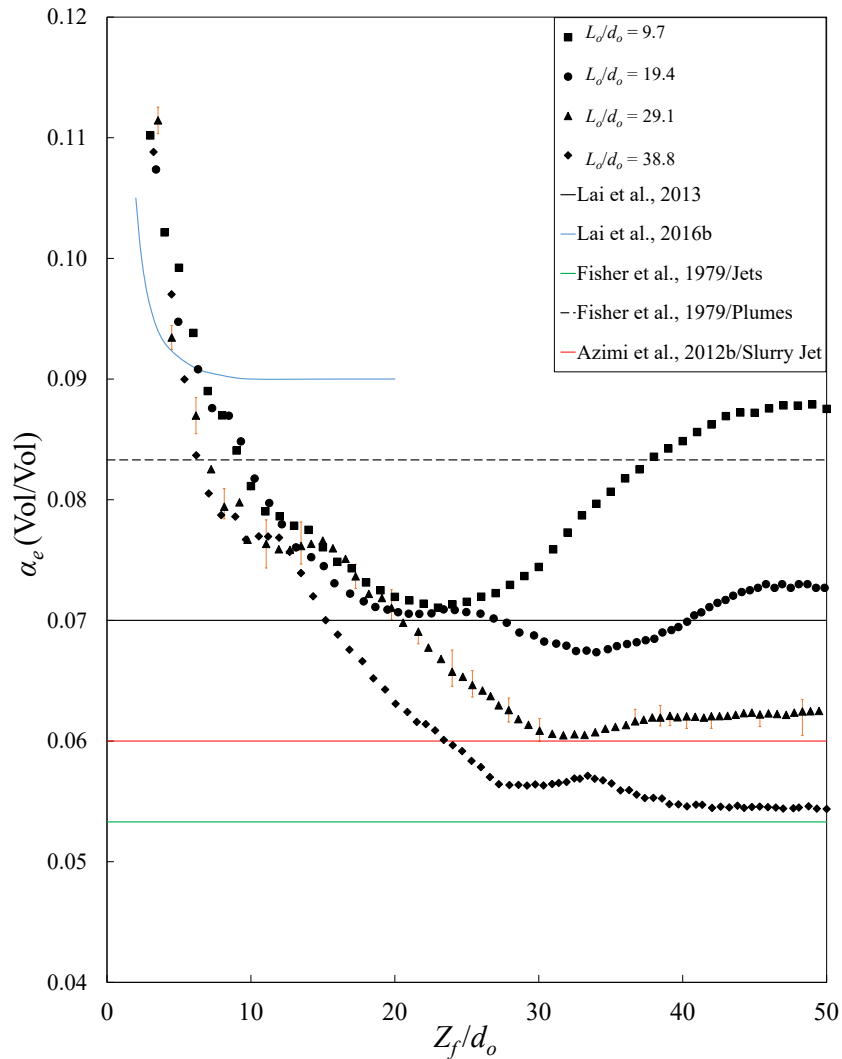
Figure 6.10: Variations of entrainment coefficient, α_e, for turbulent thermals and plumes as a function of the non-dimensional frontal vertical position. Dashed lines and the curve indicate different reported entrainment coefficients of previous studies.

It should be mentioned that Fisher et al. (1979) proposed different values for the entrainment coefficient of jets and plumes with values of 0.0533 and 0.0833, respectively. Azimi et al. (2012b) conducted experimental studies on slurry jets and calculated the entrainment coefficient for slurry

jets ($\alpha_e = 0.06$) which was very close to the proposed coefficient by Fisher et al. (1979). The minimum values of entrainment coefficients occurred in the second phase of cloud formation. The entrainment coefficients begin to grow as the cloud enters into the dispersive regime. Such mixing improvement in the dispersive regime was more pronounced in small aspect ratios (i.e, $L_o/d_o = 9.7$), in which particle clouds had the opportunity to form completely and experience the three stages of evolution. The third stage of evolution was incomplete in the middle aspect ratios (i.e., $L_o/d_o = 19.4, 29.1$), and for $L_o/d_o = 38.8$, the particle cloud acted as a sand jet and the entrainment coefficient became constant with a value similar to the water jets (Fisher et al., 1979). It can be concluded that the entrainment coefficients are not constant during particle cloud evolutions. Considering all aspect ratios, the swarm entrainment coefficients ranged between 0.055 and 0.11.

6.3.4. *Simultaneous effect of release angle and particle interactions*

In order to study the effect of release angle and particle interactions on the evolution of twin particle clouds with time, the effective cloud width of twin oblique particle cloud, w_{2-O}, was normalized with the corresponding effective cloud width of the single vertical particle cloud, w_{1-V}, with the same mass and nozzle spacing. Figure 6.11 shows the effects of aspect ratio and nozzle spacing on variations of twin oblique particle cloud width with non-dimensional time. It should be noted that the data points corresponding to $\varepsilon/d_o = 0$ belong to single oblique particle clouds. Moreover, the overbars in Figure 6.11b indicate the uncertainty of width measurement in this study.

As can be seen in Figures 6.11, the width of twin oblique particle clouds ranged between 1.5 and 4 times the cloud width of corresponding single vertical particle clouds at the beginning of releasing process. The fluctuations in cloud width of twin oblique particle clouds are due to the combination of release angle and particle collision effects. The difference between the cloud width in twin oblique and single vertical particle clouds decreases with time and converges at the end of the test. The simultaneous effect of release angle and particle interaction on cloud evolution can be explained by two mechanisms; the two oblique clouds move toward each other horizontally, which makes the total width of the cloud to be smaller while they merge and make a merged cloud. The width of single vertical cloud starts to grow from the moment that the sand particles are released into the water and gradually becomes wider with time. However, in particle clouds with larger source separation (i.e., $\varepsilon/d_o = 15$), the effect of cloud merging becomes more prominent so

that the slope of the plot takes longer to drop in comparison with other source separations. In a particular moment, the overall ratio of w_{2-O}/w_{1-V} in all source separations and aspect ratios becomes very close to each other. This makes the effect of nozzle spacing insignificant and the differences between the width ratios becomes less than 25%.
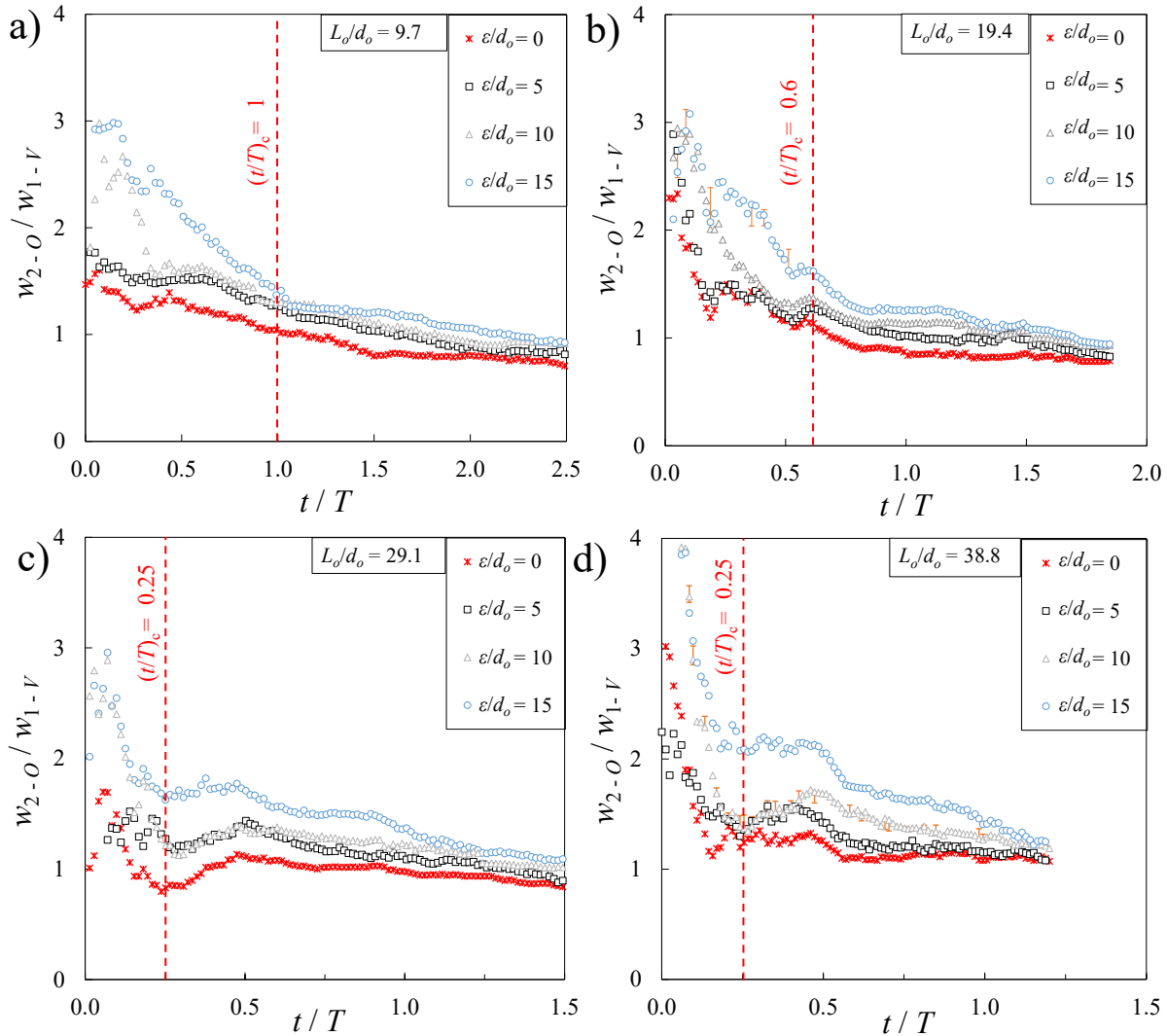
Figure 6.11. Time histories of the total cloud width for oblique twin particle clouds with a release angle of $\alpha = 45°$, and a single vertical particle cloud; a) 2x3 grams oblique versus 1x6 gram vertical; b) 2x6 grams oblique versus 1x12 gram vertical; c) 2x9 grams oblique versus 1x18 gram vertical; d) 2x12 grams oblique versus 1x24 gram vertical.

A critical non-dimensional time is introduced, $(t/T)_C$, in which the width of two oblique particle clouds in all source separations, particularly large nozzle distances, begins to smoothly approach

the cloud width of a single vertical particle cloud far from the release point. The critical non-dimensional times in this study were $(t/T)_C = 1.0$, 0.6, 0.25 and 0.25 for $L_o/d_o = 9.7$, 19.4, 29.1, and 38.8, respectively. As can be seen, the normalized width of twin oblique particle clouds increased with increasing nozzle spacing and the differences were significant before the critical non-dimensional time. For example, the differences between the width ratios in Figure 6.11a, 6.11b, and 6.11c before the critical times are approximately above 50%, but after the critical time, the differences are less than 25%. In all cases, the normalized width of twin oblique particle clouds approached the swarm regime with a swarm width ratio, $w_{2\infty\text{-}O}/w_{1\infty\text{-}V}$, of approximately ±30 percent of the swarm width of single vertical particle clouds. Such variation indicates the importance of nozzle spacing and cloud's aspect ratio on variations of cloud width in swarm regime, which can directly affect the diameter of sediment mound.

In order to illustrate more details on the normalized swarm width ratio, $w_{2\infty\text{-}O}/w_{1\infty\text{-}V}$, the correlations of normalized cloud width in swarm regime, w_∞, with all nozzle spacing and all aspect ratios are shown in Figure 6.12. The width of twin oblique particle cloud in swarm regime, $w_{2\infty\text{-}O}$, was normalized with the cloud width of single vertical particle cloud ($\alpha = 90°$) of the same aspect ratio in swarm regime, $w_{1\infty\text{-}V}$, which was obtained from the study of Janati and Azimi (2021). As can be seen in Figure 6.12, the normalized swarm width ratio varied from 0.73 for lowest aspect ratio and the least nozzle spacing (i.e., $L_o/d_o = 9.7$ and $\varepsilon/d_o = 5$) to 1.26 for the highest aspect ratio and the highest nozzle spacing (i.e., $L_o/d_o = 38.8$ and $\varepsilon/d_o = 15$). As illustrated in Figure 6.12, the settling width of twin oblique particle clouds for $L_o/d_o = 38.8$ in all source separations and for $L_o/d_o = 29.1$ in large source separations (i.e., $\varepsilon/d_o \geq 10$) were larger than the corresponding vertical cloud's settling width (i.e., $w_{2\infty\text{-}O} / w_{1\infty\text{-}V} > 1$). This indicates that by dividing sand mass and releasing it through two adjacent nozzles the cloud width in the swarm regime increases as single vertical clouds with a high aspect ratio act as a sand jet, which has smaller width in comparison with a twin particle cloud of half the mass. Such practice is beneficial in field operations such as in land reclamation projects, where a large area of water should be filled with a uniform layer of sand particles. The required materials can be split by half and released within a particular distance between dredgers.
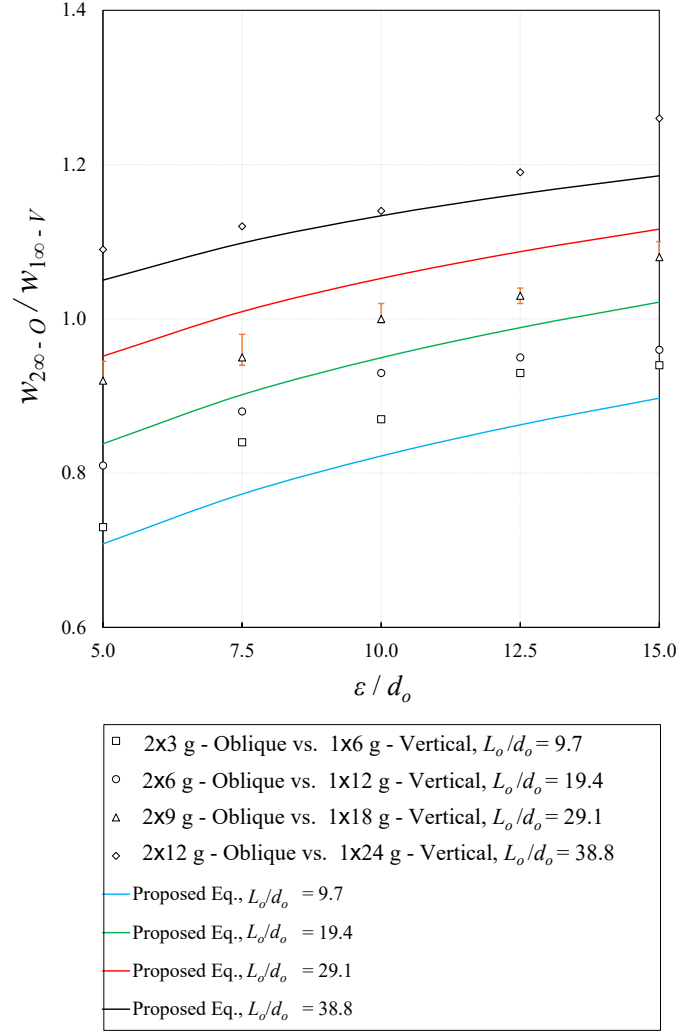
Figure 6.12. Effects of cloud aspect ratio, L_o/d_o, and normalized nozzle spacing, ε/d_o, on variations of non-dimensional swarm width, $w_{2\infty}$, at the settling stage represented by $(t/T)_\infty$.

For twin particle clouds with small aspect ratios (i.e., $L_o/d_o = 9.7$, 19.4), the settling width of a single vertical cloud is approximately 10% to 25% larger than the width of the merged cloud in the swarm phase. This is because in small aspect ratios, the single vertical cloud has the opportunity to form a particle cloud and reaches its swarm regime sooner than the merged cloud. In order to predict the cloud width ratio of twin oblique particle clouds to the single vertical cloud and make a comparison between them in swarm regime, an empirical equation is formulated using the multivariable regression analysis of experimental data with $R^2 = 0.9$ as:

$$\frac{w_{2\infty-O}}{w_{1\infty-V}} = \left(0.013(L_o/d_o) + 0.375\right)(\frac{\varepsilon}{d_o})^{(-0.0036(L_o/d_o)+0.25)} \qquad (5)$$

166

The above equation is valid for aspect ratios ranging between 9.7 and 38.8 and normalized nozzle spacing from 5 to 15. The performance of the proposed formula for different aspect ratios is shown in Figure 6.12. As can be observed in Figure 6.12, the overall range of width increment in one aspect ratio, but different source separations, decreases by increasing the aspect ratios. For example, the total ranges of swarm width ratio, $w_{2\infty\text{-}O}/w_{1\infty\text{-}V}$, in L_o/d_o = 9.7, 19.4, 29.1 and 38.8 are approximately 30%, 20%, 17% and 14 % respectively based on both the experimental data and the proposed equation, which can be beneficial to know in dredging activities.

6.4. Conclusions

The effects of nozzle spacing and aspect ratio on the dynamics of single and twin oblique particle clouds in stagnant water were investigated using a series of laboratory experiments. The variations of cloud's width, frontal position, centerline velocity, and the centroid of oblique particle clouds were studied with time and the results were compared with single and twin vertical particle clouds. The effect of release angle in single oblique particle clouds indicated that the clouds descended slower than the corresponding vertical particle clouds as the release angle pushed the cloud front towards the horizontal direction. It was observed that by reducing the aspect ratio in single oblique particle clouds, the clouds tended to evolve more in the horizontal direction. The ratio of horizontal to vertical centroids, X_{bar}/Z_{bar}, in single oblique particle clouds decreased with time and reached the average value of 0.09 for $t/T \geq 1.5$. Empirical equations were proposed to obtain X_{bar} and Z_{bar} based on the evolution time and aspect ratio, which can be useful for the understanding of the particle cloud's behavior, design, and optimization of the dredging processes.

To study the effect of release angle in single particle clouds, single vertical and oblique particle clouds width were compared and it was found that oblique particle clouds have larger width and smaller frontal distance. A critical non-dimensional time, $(t/T)_C$, was defined to study the effectiveness of oblique release and a practical model was proposed to predict the settling width of twin oblique particle cloud based on the aspect ratio and source separations. It was found that the aspect ratio increased the settling width of twin oblique clouds by 35% to 50%. The oblique release of twin particle clouds initially increased the overall cloud's width by 2 to 6 times of the two vertically released clouds. Once the twin oblique cloud descended further downward, the cloud's width became comparable to the cloud's width of twin vertical particle clouds.

The time evolution of entrainment coefficients for single vertical particle clouds was calculated and the results indicated that the entrainment coefficients decreased during the cloud's evolution

and reached a plateau at $Z_f/d_o = 40$. It was found that the entrainment coefficient varies with the cloud's aspect ratio and it decreases with increasing L_o/d_o. The maximum centerline velocity inside the two oblique particle clouds was higher than the two vertical clouds except for small nozzle spacing of $\varepsilon/d_o = 5$. The higher velocity inside twin oblique particle clouds in comparison to twin vertical clouds indicated the stronger particle-particle interactions and vortex breakup in the oblique release of particles.

Chapter 7

7. Conclusions and Recommendations for Future Research

7.1   Summary and Conclusions

In summary, this thesis examines the water entry of a single disk and a group of small sand particles using high-speed imaging and Particle Image Velocimetry (PIV) techniques. Multiple considerations for improving data from high-speed imaging and PIV are outlined to enhance our understanding of water entry processes. An overview of the major contributions and conclusions with suggestions for future work are given in this chapter.

In chapter 2, the results of an extensive experimental investigation of free-falling thick disks and the subsequent phenomena for hydrophobic disks with different characteristics were presented. Three release conditions including one fully guarded and two partially guarded release systems were used for the first time in the water entry problem. The cavity dynamics and crown formation of solid and annular disks were examined for the first time for disks with different densities that were released in different conditions. Significant phenomena of water entry such as pinch-off depth and time were measured as well as the frontal position of the disk at pinch-off and compared with previous studies. It was found that the pinch-off time and depth in annular disks were found to be shorter due to the formation of a central cavity jet. The fully guarded condition removed the crown and expedited the pinch-off process in comparison to the partially guarded release conditions. The crown characteristics of a solid disk and an annular disk were obtained. The results showed that the crown diameters in the annular disks were between 10% and 20% smaller than that of the crown diameters in solid disks. The crown seal was also classified into Partial Seal (PS), Fully Seal (FS), Partial Seal with a central Jet (PSJ), and Fully Seal with a central Jet (FSJ). The release conditions highly affected the velocity of the free-falling disks. The maximum settling velocity of the disks were obtained in the guarded release condition and it was decreased by increasing the air distance. Using the measurement from the PIV system, the velocity and vorticity field around the disk were investigated and it was found that by increasing the density of the disk both velocity and vorticity became stronger.

Experiments were carried out with one partially released condition with four different release

heights in Chapter 3. The main focus of this chapter was on the impact energy of the disks and energy loss due to the impact. A threshold release height of $h_r = 4d_o$ was obtained where the cavity and crown showed different behavior before and after the pinch-off. It was indicated that in a constant release height increasing the disks' density increased the pinch-off depth accordingly. Moreover, increasing the thickness of the disk enlarged the underwater cavity as well as the air pocket attached to the disk at the pinch-off. The impact energies of the disks were proportional to the release height and if the impact energy became greater than 36% of the initial energy (i.e., $E_i = 0.36E_o$) the crown becomes fully sealed. A correlation was proposed to predict the impact Froude number with the dimensionless moment of inertia (I^*). It was found that the crown characteristics are highly affected by the impact energy in comparison to the density or aspect ratio of disks. Regarding the energy loss of the disks at the impact, the results showed that increasing the release height causes more energy loss at the impact. However, the impact has less effect on the denser and thicker disks, and disks lost less energy at the impact in comparison to other disks. Additionally, the falling velocity of the disks increased by increasing the initial energy of the disks.

In Chapter 4, the wall effect was investigated on the cavity characteristics of the disks with different densities and release heights. Different water tanks were used and it was found that by decreasing the width of the tank, the crown tends to become partially sealed or fully open at the smallest tank. Pinch-off characteristics of the cavity were also examined, and it was found that the cavity takes more time in smaller tanks to pinch-off. Moreover, surface undulations were observed on the cavity formed in the smallest tank. The velocity field, vorticity field, swirling strength, average kinetic energy, and turbulent kinetic energy around the falling disks at pinch-off were investigated by analyzing the PIV data in the smallest and largest water tanks for disks with different densities. The results were compared in tanks with different widths, and it was found that in the smallest tank, Tank 150, the vorticity cannot be fully formed behind the free-falling disk due to the confinement. By increasing the width of the tank, there is enough space for the vortices to be fully formed, therefore more swirling is formed in the larger tank. Consequently, sine average and turbulent kinetic energies are related to the vorticity formations, when the width of the tank increases, enough space is provided for the vortices to be completely formed. Therefore, the magnitude and affected area of the water behind the disk are also increased.

In the second part of this thesis, the dispersion of small sand particles in water was studied. In Chapter 5, the characteristics of particle clouds were measured for two adjacent particle clouds

and the results were compared with a single particle cloud. Different parameters including cloud width, frontal velocity, and frontal position of the cloud were obtained through image processing. For the first time, the effect of source separation distances were investigated and a critical source separation distance $(\varepsilon/d_o)_C = 2.5$ was introduced. In this critical distance, the twin particle cloud reached its maximum frontal velocity because of smaller ambient entrainments and less energy loss due to the interactions between sand particles and ambient water. Moreover, less mass loss in water was observed due to the elimination of the trailing part. It was found that the normalized effective width increased by increasing the source distance of $\varepsilon/d_o = 7.5$ and then decreased by further increasing that and finally reached a plateau. The radial velocity of the particle clouds which was obtained which indicated that the time duration of a single particle loud passing the vortex region was higher than the one in twin particle clouds by 30%. It can be concluded that the tailing of a single cloud could stay longer in the water column compared to the twin particle cloud, therefore greater mass loss could occur which caused serious environmental concerns. The vertical centerline velocity of the cloud was measured, and it was found that the maximum value occurred at a distance ratio of $\varepsilon/d_o = 5$. The results indicated that the entrainment coefficient was inversely proportional to the aspect ratio. In terms of turbulence intensity, the results showed that the velocity fluctuations were greater in larger aspect ratios in closer distances of nozzles, and in smaller aspect ratios they were higher in larger distance ratios. In conclusion, the study showed that diving the total release mass into two equal potions was helpful in reducing aquatic environmental issues by removing the trailing part of the cloud and reducing the mixing time.

In Chapter 6, the effects of nozzle distance and aspect ratio on the dispersion of single and twin oblique particle clouds were studied and compared with their vertical counterparts. Vertical clouds descended faster than oblique ones due to the horizontal component of oblique particle clouds. Decreasing the aspect ratio caused the oblique particle clouds to move further in the horizontal direction. Moreover, oblique particle clouds had a greater width than vertical clouds. The settling width of twin oblique particle clouds can be predicted through a proposed model based on the nozzle distance and aspect ratios. Moreover, the entrainment coefficients of the particle clouds were measured, and it was found that they decreased during the evolution of the particle cloud and reached a plateau at $Z_f = 40d_o$. Also, the entrainment coefficients increased with decreasing the aspect ratio of the particle clouds. The maximum inside vertical velocity of the twin oblique particle clouds was mostly greater than the ones in twin vertical clouds (except for $\varepsilon/d_o = 5$) due to

the higher particle-particle interactions and vortex breakup in the oblique release situation.

7.2. Recommendation for future research

7.2.1. *A single solid object*

In the preceding chapters, extensive experimental results and analyses were presented on the water entry of a single object (a disk) and a group of solid particles (sand particles). Several different areas in this field can be explored to have more information on the entry of solid objects into fluids as follow:

➢   In this thesis, three different densities for the disks were considered, however, in future studies, the effects of a wide range of densities can be considered on the free-falling disks.

➢   Another idea is considering fluid with different properties as a medium. For example, non-Newtonian fluids, or more specifically micellar fluids (see Figure 7.1.) with different concentrations can be used instead of water to investigate the free-fall of solid objects considering all of the variables studied in this research.

➢   In Chapter 2, annular disks were used in the experiments. As can be seen in Figure 7.1. some preliminary studies have been conducted with an annular disk with a hole diameter of 25.4 mm, thickness of 25.4 mm and diameter of 76.2 mm in CTAB/NASAL (5% concentration) solution. A screen with 5 mm x 5 mm holes on the central hole was stuck. Below are the results for the preliminary experiments where the central jet was divided into several jets. Moreover, the shape of splash, underwater cavity and pinch-off should be investigated and compared with the same experiments in water.

$t = 12$ ms $t = 32$ ms $t = 52$ ms $t = 72$ ms $t = 92$ ms $t = 112$ ms $t = 132$ ms $t = 152$ ms
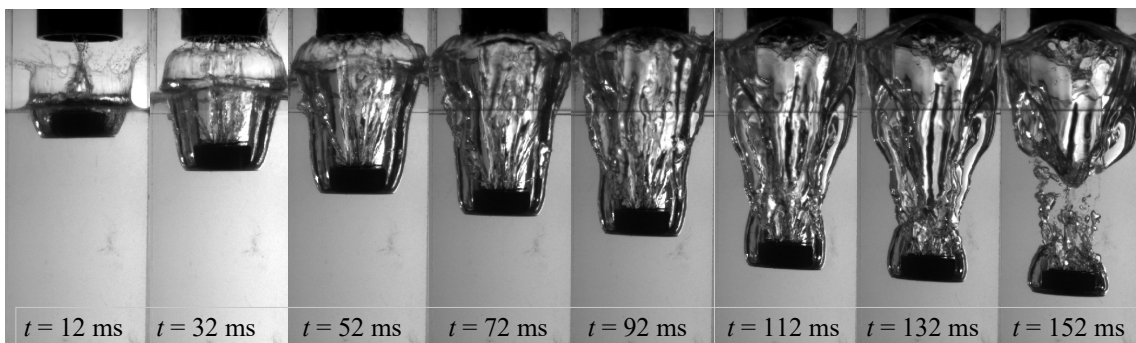
Figure 7.1. A preliminary experiment with an annular disk and CTAB/NASAL micellar fluid.

➢ Following the previous item, the water entry problems using micellar fluids in different temperatures can be also another topic to study.

➢ In Chapter 2 a regime plot was proposed and further completed in chapter four as Figure 7.2.:
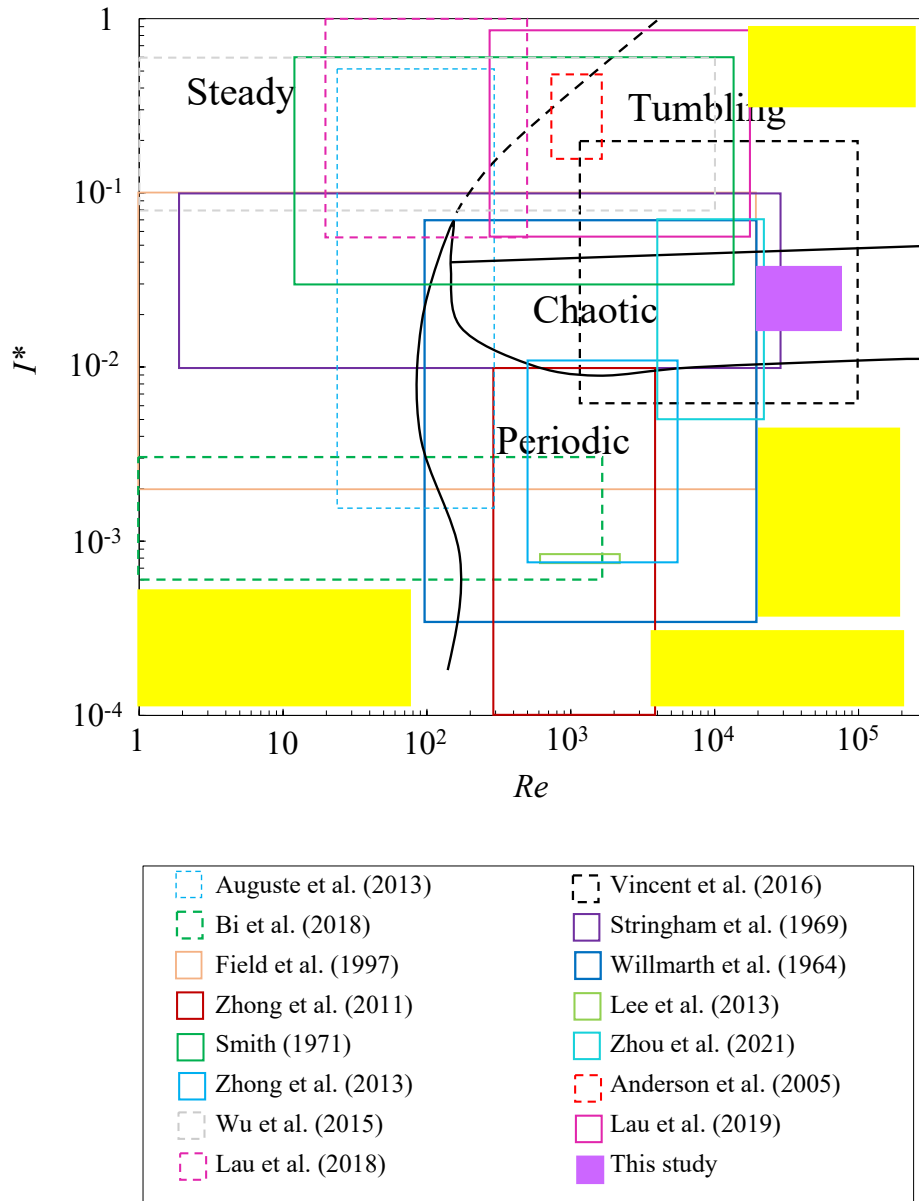
Figure 7.2. A proposed non-dimensional moment of inertia and Reynolds number range for future studies. Falling mode based on Field et al. (1997), dashed curved by Heisinger et al. (2014).

As can be seen in Figure 7.2, in some areas of Reynolds number and non-dimensional moment of

inertia, there are not any studies available. Possible projects for future studies can be designed in the yellow highlighted areas.

➢ The numerical modeling of free-falling disks in water can be beneficial in water entry problems and the results can be compared with the existing data. Moreover, various disk densities, aspect ratios, and different coating can be used in this regard. In addition, various fluids can be substituted with water to investigate the medium effect on the water entry of a solid object.

➢ Considering simultaneous releasing of the same objects with different distances (i.e., Adjacent release) can be considered as a possible research idea. Moreover, free-falling of a disk and a sphere adjacent to each other or any two different solid objects can be interesting in water entry problems.

➢ Releasing two solid disks together in a way that one disk is located beneath the other one without sticking to each other (i.e., Tandem release) can be useful in water entry investigation. Additionally, the same subject with a solid disk and an annular disk can be useful as well.

➢ A force driven solid and annular disk set up can be made to investigate the controlled impact force on the formation of splash curtain and underwater cavity.

➢ The settling location and trajectory pattern of free-falling thick disks with different geometry and aspect ratio can be investigated in water or other Newtonian and non-Newtonian fluids and flow mixtures.

➢ The effects of an immiscible oil layer on the splash and cavity formation by a free-falling can be investigated. Moreover, all the controlling parameters can be included to investigate.

➢ The water entry of solid objects with different geometries can be also investigated. For example, a donut shape object which can be created by a 3D printer with different aspect ratios.

7.2.2. Particle cloud

A series of experiments were conducted in this study to investigate the water entry of a group of small solid particles in Chapters 5 and 6. The sand particles were considered large since the Stokes number was $S_t = 0.55$ (large size particles have the Stokes number of $0.33 \leq S_t < 1$).

➢ A possible study can be the same parameters except with the different particle size. Small or medium particle size can be considered as a future study since the particle clouds dynamics are highly affected by the sand particles diameter.

➢ Another idea can be releasing sand particles through several nozzles at the same time. The nozzles can be linearly distributed or have a circular arrangements with different distances.

➢ Instead of sand particles, small solid steel particles or particles with different densities can be used to investigate the effect of particle density of the dynamics of particle cloud.

➢ In this thesis only a release angle of 45° was considered. Different release angles such as 30°, 60°, can be used for future studies.

➢ Different releasing orientation can be considered for future studies. For example, in this thesis in the twin oblique releasing case, the angled parts are in front of each other. In the future project, they can be back to back of each other as Figure 7.3 with various angles of θ.
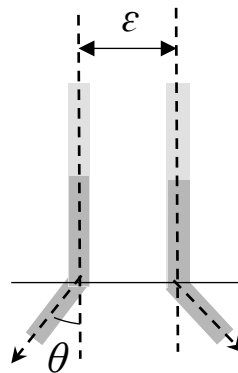
Figure 7.3. A new arrangement of sand releasing nozzles, releasing sand particles obliquely and back to back each other with various angles (θ).

➢ The dispersion pattern of twin particle clouds passing through an immiscible oil layer can be another future project.

➢ Another possible study can be releasing the particle clouds in non-Newtonian fluid, i.e., micellar fluids. Moreover, micellar fluid can be considered with different temperatures.

Appendix I

Dynamic Interaction of Twin Particle Clouds in Stagnant Water

Abstract

A series of laboratory experiments was conducted to investigate the interactions of particles in two adjacent particle clouds vertically released in stagnant water. In order to understand the effects of controlling parameters in particle interactions between two particle clouds, the effects of sand mass and the distance between two nozzles of the adjacent particle clouds (source separation distance) were studied. By diving the mass of sand particles into two equal masses and releasing them through two adjacent nozzles, the overall sand concentration decreased due to the attenuation of the cloud length. The length, width, and frontal velocity of twin particle clouds were measured and the results were compared with the corresponding single particle cloud with the same sand mass and nozzle diameter. The entrainment coefficients of twin particle clouds with different aspect ratios and source separation distances were calculated and the results were compared with the corresponding single particle clouds. The results showed that the maximum cloud aspect ratio in single particle clouds decreased between 20 and 40 percent when the same particles were released through two adjacent nozzles. The reduction of aspect ratio in twin particles decreases the tendency of pollution distribution in aquatic environment. The velocity field inside twin particle clouds during cloud evolution was measured with Particle Image Velocimetry (PIV) technique. The PIV results showed that the ambient water enters the particle cloud from the sides and the space between two adjacent particle clouds.

A1. Introduction

Particle clouds are formed when a finite mass of dense sand particles is released into a quiescent ambient, whereas the continuous disposal of sedimentary materials into a stagnant ambient forms a sand jet. The mixing of particles in ambient water has been observed in different engineering applications, including wastewater disposal, construction of artificial islands, dredging activities, and mining operations (Azimi et al. 2012a, 2012b, 2015). In such activities, the understanding of how sand particles can be placed precisely in designated areas and how sedimentary materials disperse in the ambient are important to either preserve the sand mass for bottom placement or decrease the turbidity in the aquatic environment, which can adversely affect the aquatic ecosystems. The initial condition of releasing dredge materials, the type of dredged materials, and the local conditions determine the level of environmental interferences. The understanding of particle dynamics and their controlling parameters are important for proper design, optimization, and monitoring of the dredging release processes.

Previous experimental studies have investigated the dynamic behavior of sand particles in stagnant water (Bush et al. 2003, Azimi et al. 2011, Lai et al. 2016a, b, Zhao et al. 2014, Sharif and Azimi 2020). A particle cloud is formed when a finite amount of sand particles is released through a nozzle and dumped into the water. The particle cloud descends, and particle evolution can be described by three phases of motion (Rahimipour & Wilkinson 1992). The initial acceleration phase (Phase 1) within which the particle cloud accelerates as a solid body until reaches a turbulent condition, the self-preserving or turbulent thermal phase (Phase 2) where the vortex ring is formed inside the cloud so that the cloud decelerates since the water entrains into the cloud from the edges and the dispersive or particle-settling phase (Phase 3) in which sand particles detached from the entrained fluid and descend individually at their settling velocities ($u\infty$). A cloud number can be defined as the ratio of particle settling velocity of each particle $u\infty$ to the characteristic circulation velocity uc in the particle thermal as: $Nc = u\infty/uc$ where $uc = B^{1/2}/r_o$, B is buoyancy, and r_o is the bulk radius of the cloud (Rahimipour and Wilkinson, 1992). Moghadaripour et al. 2017a rearranged the cloud number equation and stated that particle cloud evolution depends on two main factors including the aspect ratio (L_o/d_o) and the Stokes number (St), where the aspect ratio is the ratio of the length of occupied sand in a pipe with a diameter of d_o as $L_o = 4m/\pi d^2 c_o\rho s$, where c_o is the initial sand volume fraction (i.e., $c_o = 0.6$ volume/volume), ρs is the sand density, and Stokes

number, $St = [(\rho s - \rho w)d^2 u_o]/18\mu d_o$ where d_{50} is the mean particle size and μ is the dynamic viscosity of water. Bond and Johari (2005) found that the effect of L_o/d_o is very remarkable and controls the motion of particle clouds. Moghadaripour et al., 2017a and 2017b conducted a wide range of experiments and found that the aspect ratio has a significant effect on the growth of cloud width; however, it has a small impact on the depth progression of particle clouds.

In recent years various studies were conducted regarding the behavior of particle cloud in the presence of viscous fluid (Mohammadidinani 2017, Manzouri and Azimi 2019a and 2019b). The dynamic of particle clouds in a viscous fluid showed that the motion of particles and the number of frontal heads are correlated with the aspect ratio as well (Azimi 2019). It was found that the width of particle clouds in viscous fluid increased with the aspect ratio, although it never exceeded the growth rate of particle clouds in the water. Mohammadidinani et al., (2017) performed experiments on the dynamics of a sand jet passing through a layer of oil into the water. They observed that the existence of an oil layer decays the initial velocity of particle clouds. Consequently, the initial momentum of sand jets or particle clouds can be controlled with an oil layer which acts as a damper in the system.

The cloud motion characteristics such as cloud length, width, and velocity were evaluated to understand the motion of particle clouds dispersion. The particle grouping and wake formation behind particles increase the velocity of particles and these results in a bulk velocity higher than the individual settling velocity of particles. Azimi et al, 2012a indicated a group settling velocity of $5u_\infty$ for sand jets front (i.e., $L_o/d_o \rightarrow \infty$) and a threshold particle cloud velocity of $1.4u_\infty$ was defined for particle clouds with a limited aspect ratio to categorize the thermal and dispersive phases (Buhler and Papantoniou, 2001). The objective of the current study is to investigate the effect of releasing sand particles in form of twin particle clouds in stagnant water and compare the results with the corresponding single particle cloud.

A2. Experimental setup

Laboratory experiments were conducted in a 1.65 m (length) X 0.85 m (width) X 0.95 m (depth) glass- walled water tank in the Multiphase Flow Research Laboratory (MFRL) at Lakehead University. The water depth was set at 0.85 m in the tank with a temperature of 20° C $\pm 2^O$ C ($\mu =$

9.77x10^{-4} kg/m.s). A schematic front view of the presented setup is shown in Fig. A1. Moreover, Fig. A1 shows a snapshot images of twin particle cloud. Sand particles were released through two nozzles with the inside diameter of $d_o = 8$ mm (Test No. T11). Single and twin particle clouds with a relatively wide range of aspect ratios (i.e., $9.7 \leq L_o/d_o \leq 38.8$) were formed by releasing different mass of sand particles (i.e., $m = 6$ g, 12 g, 18 g, and 24 g) with a density of 2564 kg/m^3 through vertical nozzles into water. It should be noted that the sand particles with a median sand size of $d50 = 0.507$ mm were carefully washed and dried before filling the nozzles. The releasing processes of sand particles with different aspect ratios and source separations were recorded by a high-speed camera (Photron-FASTCAM, 1024PCI-100KC, Japan) with a frequency of 30 Hz (30 frames per second). Particle clouds were illuminated with light sources (Woods L13, 1000-Watt Telescope Work Light, Canada) to eliminate background reflection. In order to minimize bubble formation due to air entrainment from water surface, a 5 mm distance was considered between the nozzles and water surface. In this study, the Stokes number was calculated as $St = 0.55$ which means that sand particles in this study are classified as hydrodynamically large particles (Moghadaripour et al. 2017a).
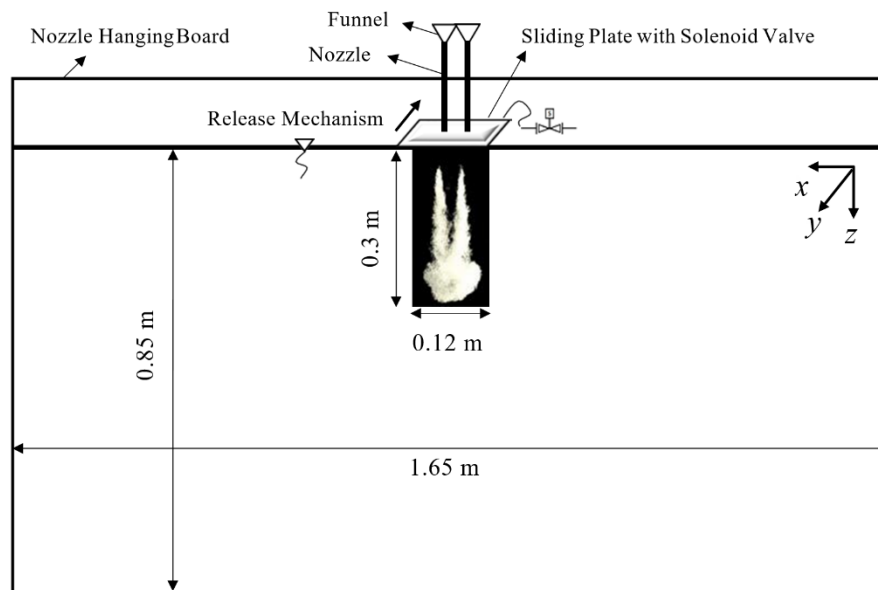
Figure A1. A schematic front view of the experimental setup and coordinate system. The sample image is related to Test No. T11 ($L_o/d_o = 19.4$, $\varepsilon/d_o = 2.5$)

To investigate the evolution of twin particle clouds, four tests (i.e., T1 to T4, see Table A1) were carried out with $\varepsilon/d_o = 0$, which indicates that the two nozzles are completely aligned and represents a single particle cloud. These tests are used as benchmark tests in this study. 24 experiments (i.e., T5 to T28, see Table A2) with various aspect ratios (L_o/d_o) and source separations (ε/d_o), were conducted and the results were compared with the benchmark tests to evaluate the performance of twin particle clouds.

Four main aspect ratios were defined in this study based on sand particles mass and nozzle diameter including L_o/d_o = 9.7, 19.4, 29.1, and 38.8. For twin particle clouds experiments, the total mass was split into two equal portions and particles were released in water through two nozzles which were held by a nozzle board above the tank. In order to investigate the effect of source separation, the two nozzles were distanced from $\varepsilon = 2$ cm to 12 cm and the source separations were normalized with the nozzle diameter, ε/d_o (see Table A1 and Table A2).

Table A1. Experimental details of the benchmark tests (single particle clouds), $\varepsilon/d_o = 0$

Test	*Mass* (g)	L (cm)	L_o/d_o	*Nc*
T1	1x6	7.76	9.7	0.112
T2	1x12	15.52	19.4	0.099
T3	1x18	23.28	29.1	0.093
T4	1x24	31.04	38.8	0.089

In order to analyze the recorded images, the MATLAB image processing toolbox (Math Works, Inc., 2018) was used to detect the cloud's edges, binarize the images, and extract the required data including cloud width, length, and frontal positions. Particle Image Velocimetry toolbox (PIVlab) from MATLAB was employed to extract the velocity data of individual particles inside the cloud along the centerline of particle clouds. The details on image preparation and image thresholding procedures can be found in Janati and Azimi (2021).

Table A2. Experimental details of the twin particle clouds with different source separations, $do =$ 8 mm, $d50 = 0.507$ mm

Test	ε/d_o	Mass per Nozzle (g)	L (cm)	L_o/d_o	Nc
T5	2.5	3	7.76	9.7	0.112
T6	5	3	7.76	9.7	0.112
T7	7.5	3	7.76	9.7	0.112
T8	10	3	7.76	9.7	0.112
T9	12.5	3	7.76	9.7	0.112
T10	15	3	7.76	9.7	0.112
T11	2.5	6	15.52	19.4	0.099
T12	5	6	15.52	19.4	0.099
T13	7.5	6	15.52	19.4	0.099
T14	10	6	15.52	19.4	0.099
T15	12.5	6	15.52	19.4	0.099
T16	15	6	15.52	19.4	0.099
T17	2.5	9	23.28	29.1	0.093
T18	5	9	23.28	29.1	0.093
T19	7.5	9	23.28	29.1	0.093
T20	10	9	23.28	29.1	0.093
T21	12.5	9	23.28	29.1	0.093
T22	15	9	23.28	29.1	0.093
T23	2.5	12	31.04	38.8	0.089
T24	5	12	31.04	38.8	0.089
T25	7.5	12	31.04	38.8	0.089
T26	10	12	31.04	38.8	0.089
T27	12.5	12	31.04	38.8	0.089
T28	15	12	31.04	38.8	0.089

A3. Results

A3.1. Twin Particle Cloud Evolution

Time evolution of single particle cloud and twin particle cloud with nozzle distance of $\varepsilon = 4$ cm in

four different non-dimensional times (t/T), is illustrated in Fig. A2 with photo-illumination techniques. It should be noted that T is a characteristic time scale ($T = B^{0.5}/u_\infty^2$), which is $T = 1.38$ s, 1.95 s, 2.39 s and 2.76 s for $Lo/do = 9.7$, 19.4, 29.1, and 38.8, respectively.
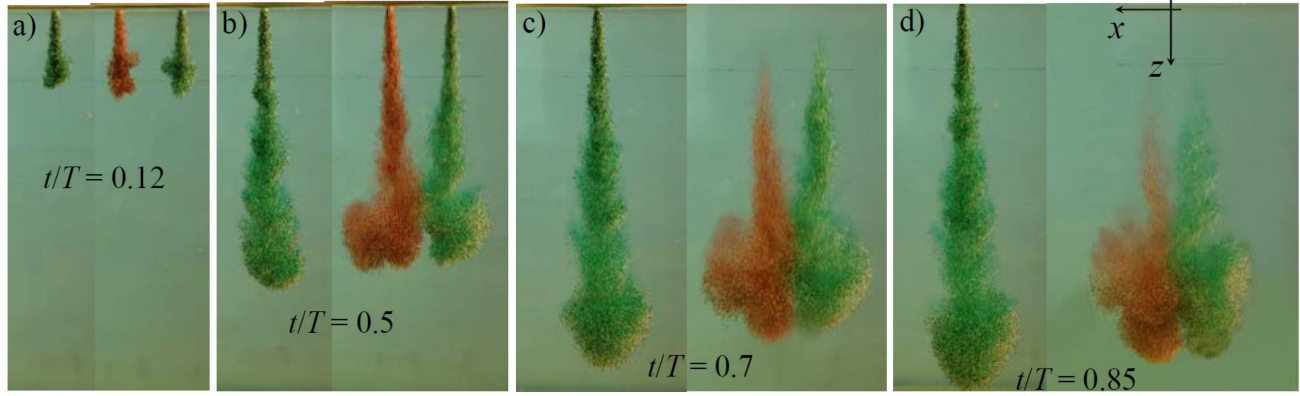
Figure A2. Time evolution of twin and single particle clouds with the aspect ratio of $L_o/d_o = 19.4$ in different non-dimensional times. Test No. T2 ($L_o/d_o = 19.4$, $\varepsilon/d_o = 0$) for the single cloud and Test No. T12 for the twin cloud ($Lo/do = 19.4$, $\varepsilon/do = 5$, $T = 1.95$ s)

The illustrated single and twin particle clouds have the same aspect ratio of $L_o/d_o = 19.4$ so that the effect of dividing sand particles mass into two equal portions can be compared. As can be seen in Fig. A2, the most important effect of dividing the mass into two masses is that the trailing part of the cloud in the water column can be diminished quicker in twin particle clouds. As a result, the risk of turbidity and mass loss, which can cause severe pollution in the water environment, can be reduced. Another benefit of splitting the total mass of sand particle into two parts is mixing enhancement and dilution improvement. As shown in Fig. A2d ($t/T = 0.85$), while the single cloud is still in its first phase of cloud formation and is discharging into the water, the two adjacent clouds are fully developed, entangled with each other, and start to merge so that the dilution process initiates earlier in twin particle clouds than the corresponding single clouds. Such process is helpful in minimizing the duration of discharging process. Fig. A3 shows the evolution of twin particle clouds with $Lo/do = 9.7$ and $\varepsilon/do = 0$, 2.5, 5, 7.5, 10, 12.5, 15 (i.e., test No. T1 and T5 to T10) in four different times of $t = 0.85$ s, 1.5 s, 2 s, and 2.5 s. The effect of increasing the distance between two nozzles on formation of twin particle clouds can be observed. As can be seen, the actual planar cloud areas, which were shaded by sand particles, become larger once two clouds are separated

and distant from each other. Moreover, once the two clouds start to merge, the trailing part of each cloud becomes smaller after the interactions. This phenomenon can be useful in conditions where a vast area of the aquatic environment needs to be nourished with nutritional substances. However, when two clouds are released far from each other (even if they have no interactions), they still have impacts on one another's motion. At the beginning of the turbulent thermal phase, because of the ambient entrainment between two clouds, twin particle clouds with large source separation can force the adjacent cloud to move faster or slower (see Figs. A3b and A3c; $\varepsilon/d_o = 12.5, 15$).
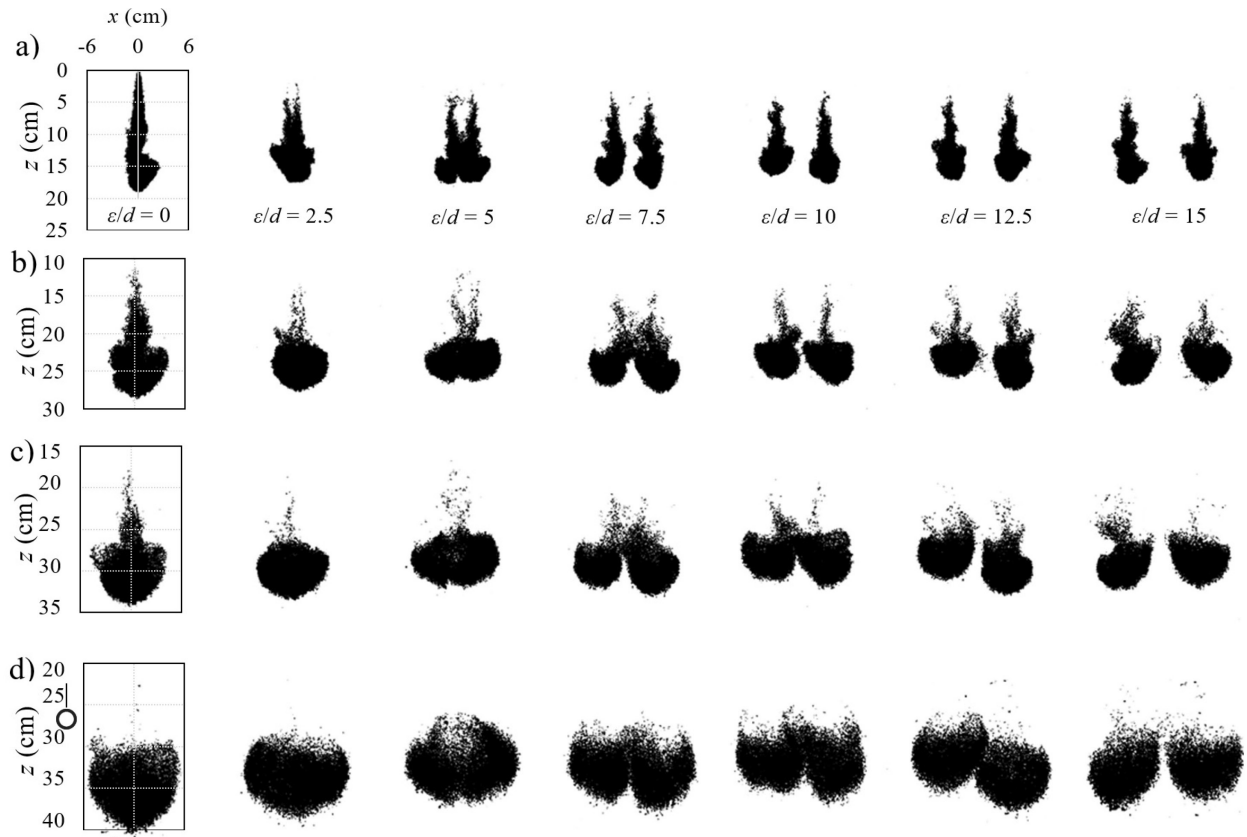
Figure A3. Single and twin particle cloud development in a different phases of motion with Lo/do = 9.7 (1x6 g vs 2x3 g, test No. T1 and T5 to T10): a) initial acceleration phase $t = 0.85$ s, b) turbulent thermal phase $t = 1.5$ s, c) turbulent thermal phase $t = 2$ s and d) dispersive phase $t = 2.5$ s.

Additionally, as shown in Fig. A3, the twin clouds with very close distances (i.e., $\varepsilon/d_o = 2.5, 5$) evolved in a dense and highly symmetric shape that lookalikes a sphere with a sparse trailing

section. However, by increasing the source separation (i.e., $\varepsilon/d_o \geq 12.5, 15$), the two clouds are not fully merged even in the dispersive phase and they only have a very small attraction toward each other (see Fig. A3d). In this condition, the trailing part is wider than the twin particle clouds with smaller source separation.

A3.2. Particle cloud's length

n order to find out the percentage of the length reduction in twin particle clouds, the variations of cloud length in single and twin particle clouds with time are illustrated in Fig. A4. As mentioned before, the overall cloud's length is diminished by dividing the sand mass into two parts. However, the amount of this change is not exactly equal to 50% of a single cloud's length. As can be seen, by increasing the aspect ratio, the percentage differences between single and twin particle clouds' lengths are the same in all aspect ratios except in $L_o/d_o = 38.8$. For example, in Fig. A4a to A4c with $L_o/d_o = 9.7$, 19.4, and 29.1, the maximum length of a single particle cloud is approximately 36% larger than the maximum length of twin particle clouds. However, in $L_o/d_o = 38.8$ due to the limitation of water depth in the tank, the single particle cloud acted as a sand jet (Janati an Azimi, 2021). In high aspect ratios, the particle cloud's length is not fully formed and the particles reached the bottom of the tank due to high aspect ratio compared to the tank depth. In all cases, the cloud's length started to decrease after reaching its maximum as the trailing part fell into the cloud's head. It should be mentioned that the cloud's length is considered from the frontal cloud's head to the back of the cloud's trailing part and calculated through image processing techniques in MATLAB software. Moreover, in twin particle clouds with large source separations (i.e., $\varepsilon/d_o \geq 10$), the length of the twin clouds with the same aspect ratios was not extremely affected by increasing the nozzle distances and the total differences between their lengths are approximately 10%.
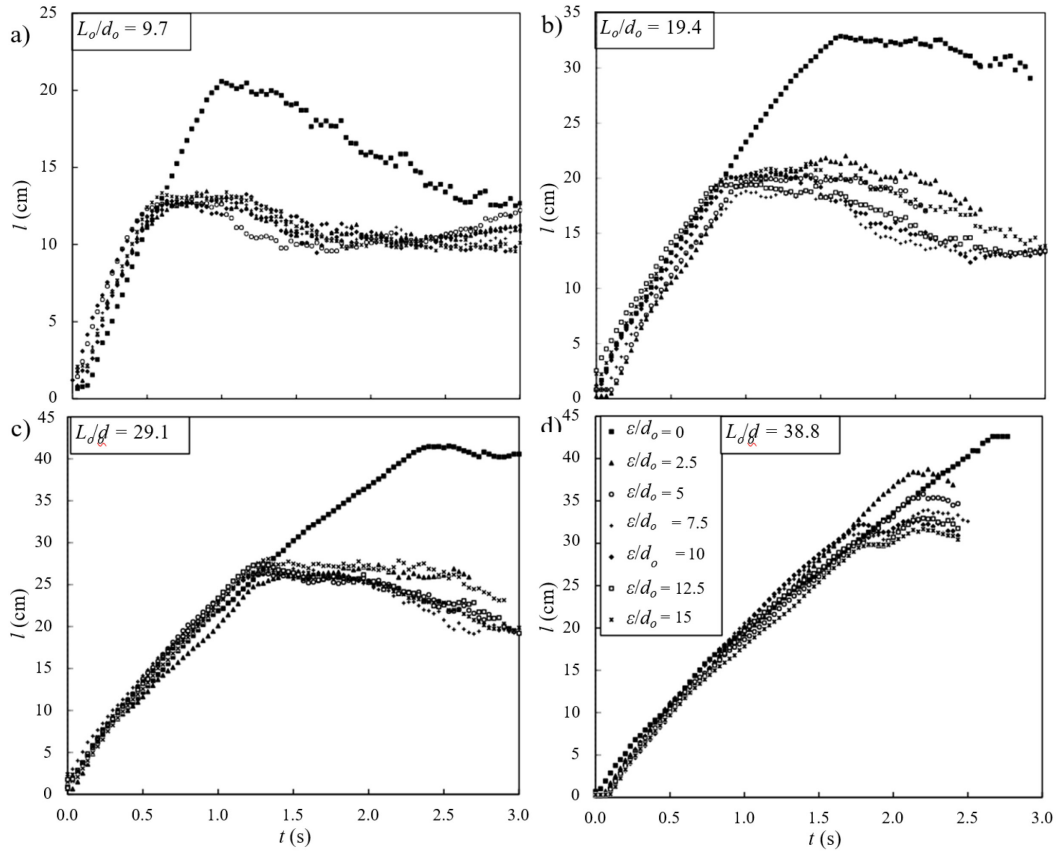
Figure A4. Variations of single and twin particle clouds' length for different source separations and aspect ratios; a) $L_o/d_o = 9.7$, b) $L_o/d_o = 19.4$, c) $L_o/d_o = 29.1$, b) $L_o/d_o = 38.8$. (Test No. T1 to T28)

A3.3. Particle cloud's width

The cloud width was defined as the cloud's maximum horizontal extent (Bush et al., 2003). Fig. A5 shows the effects of source separation and aspect ratio on variations of cloud's width (w) with time. The distance between the adjacent nozzles (ε) was included on calculation of the total cloud width. As can be seen in all four plots, the growth rate of a single particle cloud (i.e., $\varepsilon/d_o = 0$) is lower than other nozzle distances. However, in all other source separations with different aspect ratios, the cloud's width at the beginning of the releasing process remains the same until $t = 1$ s. After $t = 1$ s, the cloud's width begins to deviate from each other with a gradual accelerating slope for twin particle cloud with different source separations. However, for the minimum source separations (i.e., $\varepsilon/d_o = 2.5$), the twin cloud's width after $t = 1$ s started to incline toward the single

cloud's width and even in small aspect ratios (i.e., $L_o/d_o = 9.7$, 19.4), their width in some stages is completely similar to each other. For example, for $L_o/d_o = 19.4$, the cloud's width of a single cloud increased linearly from the start point of the releasing process, but after $t = 1$ s to $t = 1.5$ s, the twin clouds width did not change and had a constant value of approximately $w = 7.5$ cm. However, after crossing $t = 1.5$ s, both cloud's width increased with the same slope. Additionally, in other source separations cases, the cloud's width increased at a slow rate despite increasing the distance between adjacent nozzles. As illustrated in Fig. A5a to A5d, the width of the cloud in medium and large source separations (i.e., $\varepsilon/d_o \geq 7.5$) slightly increased by 15% to 20% as source separation increased.
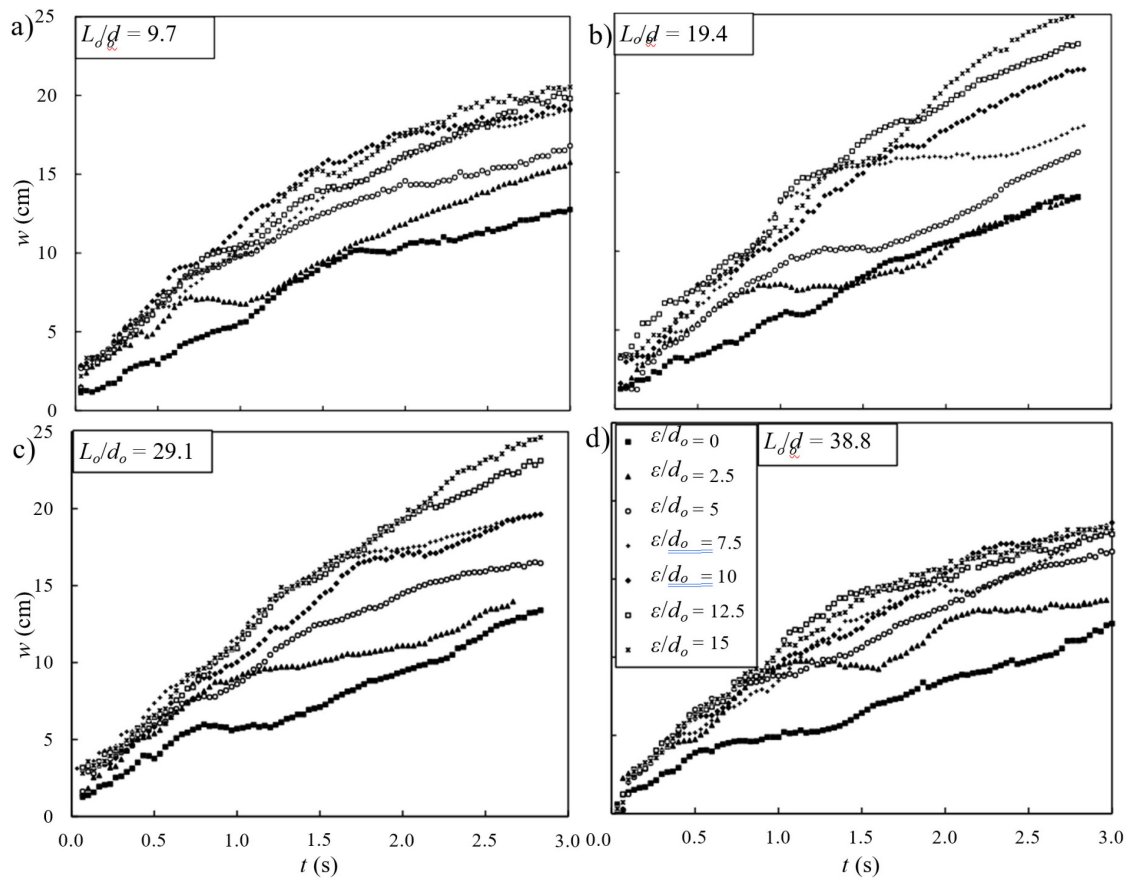
Figure A5. Variations of twin clouds' width in different source separations for different aspect ratios; a) $L_o/d_o = 9.7$, b) $L_o/d_o = 19.4$, c) $L_o/d_o = 29.1$, b) $L_o/d_o = 38.8$. (Test No. T1 to T28)

A3.4. Particle cloud's velocity

The frontal cloud's velocity was calculated based on the foremost position of the particle cloud's frontal head, which was obtained using the MATLAB programming from the recorded images in this study. Fig. A6 illustrates the variations of the twin cloud's frontal speed for $L_o/d_o = 9.7$ and $\varepsilon/d_O = 2.5$ and the results were compared with the proposed equation of Moghadaripour et al. (2017b) for a single particle cloud with the same aspect ratio. The equation for particle clouds with a large particle size is $uf/u\infty = 9.9\ (z/d_o(L_o/d_o)^{-0.4})^{-0.68}$ and this equation was proposed for particle clouds with an aspect ratio (L_o/d_o) between 1.5 and 19.6. As can be seen in Fig. A6, in a very close nozzles distance, (i.e., $\varepsilon/d_o = 2.5$), the results show promising compatibility with Moghadaripour's equation for $z \geq 20$ cm, when the two clouds were completely mixed and sand particles started to descend as a whole merged cloud instead of bursting out. However, from the location where two clouds were released at $z = 20$ cm, some frontal velocity fluctuations can be observed. Fig. A6 shows that as soon as the two clouds are released into water, they tend to expand by the entrainment of the surrounding ambience. However, when two particle clouds are discharged at a very close distance (see Fig. A6), they have a common ambient and each cloud tries to entrain the common water volume into its domain. This may be the main reason why twin particle clouds were drawn toward each other, and they have a tendency to evolve as one single particle cloud. After frontal head merging, the frontal velocity gradually decreased until they reach the settling velocity of $u\infty = 0.075$ m/s at the end of the tank.
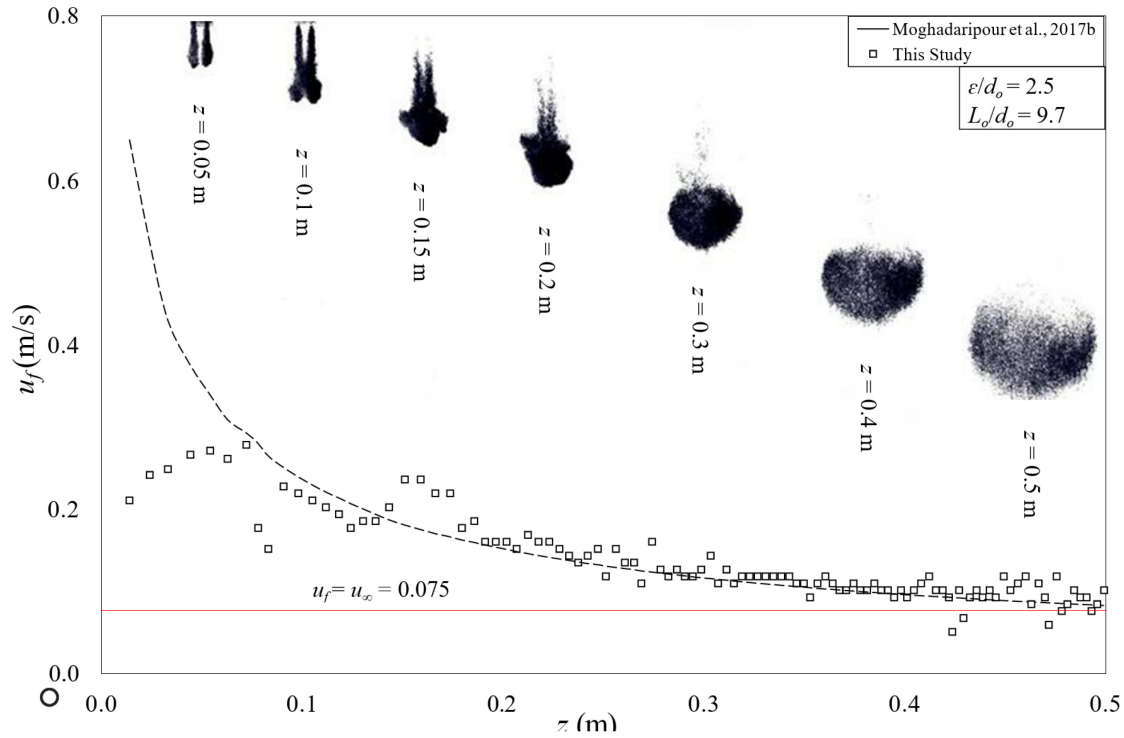
Figure A6. Variations of cloud frontal velocity (u_f) along with the water depth (z) for the test No. T5. The related images of the experiments are added in different positions.

In order to measure the velocity of sand particles inside the cloud (uz), the centerline velocity of the main twin cloud (Fig. A7a1) and from the centerline of left (Fig. A7b1) and right (Fig. A7c1) clouds were measured using the PIVlab toolbox (MATLAB), and the results were plotted for test No. T11 (2x6 g, $\varepsilon/do = 2.5$, $L_o/d_o = 19.4$) in Fig. A7a, A7b, and A7c. Three critical lines were selected and the axial velocity profiles were extracted from images. It should be noted that the PIVlab images on Fig. A7 (i.e., Fig A7a1, A7b1 and A7c1), only show one frame of the test, however, the plots present the whole test duration (i.e., Fig A7a, A7b and A7c). Fig. A7a represents data on the centerline of the main twin cloud where $uz(max)$ started to increase to its maximum value of $uz(max) = 0.26$ m/s in the first 3 seconds of the test and after that, it quickly diminished in the second half of the test. This indicates that the plot has a sharp peak at approximately $t = 3$ s and the velocity fluctuation interval is approximately 0.05 m/s at that time. Fig. A7b and 7c show the maximum vertical velocity on the centerline of the left and right clouds. The peak velocity occurred at $t = 1.7$ s and the peak velocity values were similar in both cases (i.e., $uz(max) = 0.18$ m/s). As can be seen, on the centerline of both individual clouds on the left and right sides, the maximum

centerline velocities increased until they reached the plateau at $u_z(max)$ = 0.18 m/s and remained at this stage for approximately three seconds. The velocity fluctuations were less than 0.007 m/s on the plateau. Velocity fluctuations decreased until the end of the test. Overall, the maximum velocity on the centerline of the main cloud (Fig. A7a) was 30% more than the velocities on the centerline of the single particle clouds (Figs. A7b and A7c). Consequently, once the velocities of the cloud in the middle of the main cloud became more than the velocities in the side clouds, the main cloud had a great tendency to develop from the frontal middle point which is why the particle clouds develop a mushroom-shape frontal head. Moreover, the reason why the velocity of individual particles inside the clouds remained the same for 3 seconds in the middle of the test was that they have smaller velocities therefore less interactions occurred in comparison with the main cloud's centerline. Therefore, it took more time for them to dissipate their kinetic energies in comparison to the case in which the cloud has 30% greater velocities.
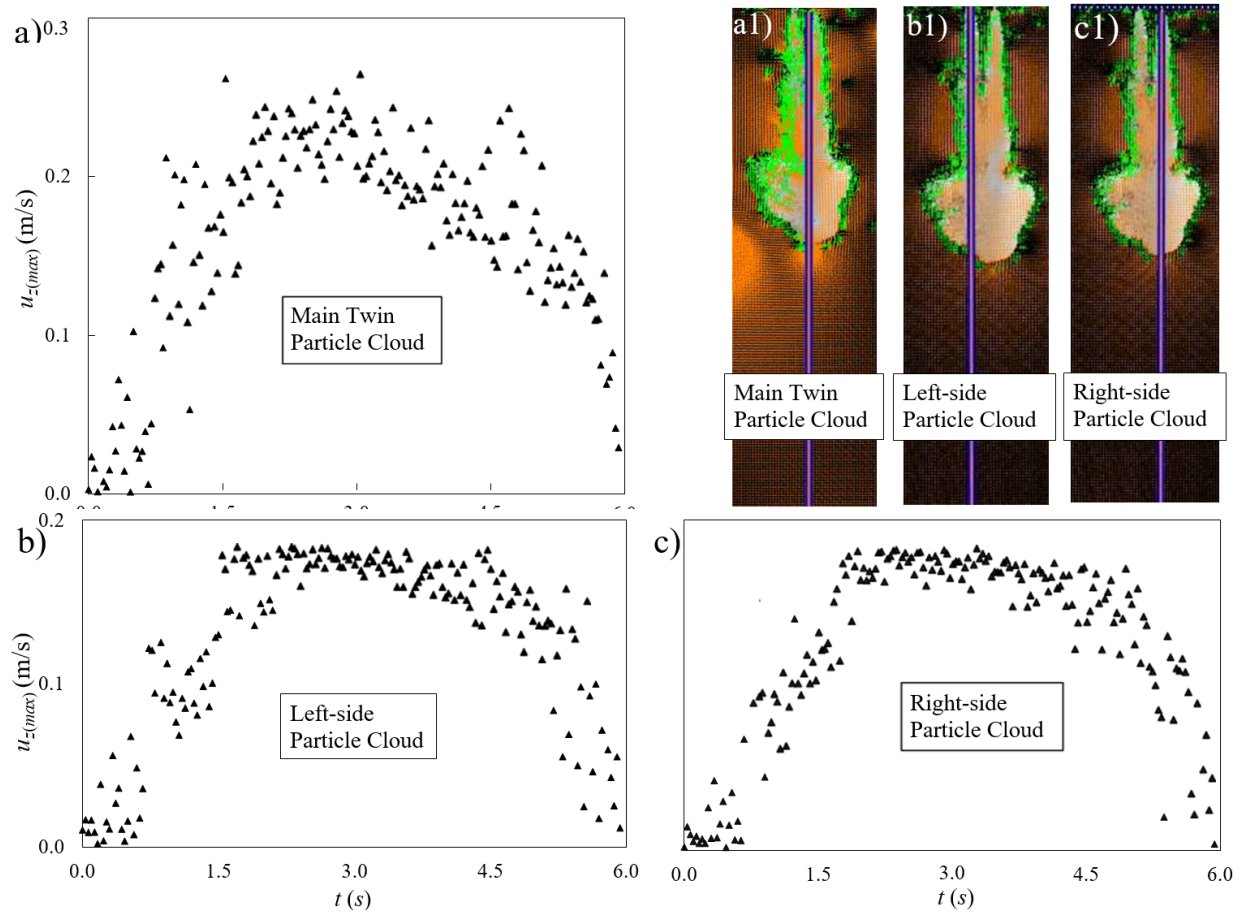
Figure A7. Variations of cloud centerline velocity in a different part of twin particle clouds for

the test No. T11 (2x6 g, ε/d_o = 2.5, L_o/d_o = 19.4). a) Centerline velocity of the twin cloud. b) variations of velocity in the centerline of the left-side cloud. c) variations of velocity in the centerline of the right-side cloud.

A4. Conclusion

The present study shows the results of laboratory investigation on the behavior of twin sand particles in quiescent water. The main physical characteristics of twin particle clouds such as length, width, and velocity of the clouds were obtained through advanced image processing techniques and the effects of source separations and aspect ratio were studied. The results were also compared with the corresponding single particle clouds (ε/d_o = 0). It was found that, although the mass of sand particles in twin particle clouds are divided into two parts and each of which contains 50% of the total mass, their lengths were 64% of the length of the corresponding single particle clouds. This outcome can be beneficial for the aquatic environments since the remaining sand particles in water column can cause more environmental pollution However, this is not applicable for particle clouds with large aspect ratios (i.e., L_o/do = 38.8), since the particle cloud acted as a sand jet due to the limited depth of the tank.

Moreover, twin particle clouds with source separation of ε/d_o = 2.5 have the smallest cloud width among other source separations of twin clouds. Moreover, in small aspect ratios (i.e., L_o/do = 9.7, 19.4) after passing one second from the beginning of the test, the twin clouds' width becomes as small as the cloud width of single particle cloud. For source separations greater than $7.5d_o$, increasing source separations by 50% make the clouds' width larger by approximately 15% to 20%, which may be useful in particular dredging activities, where a designated area is defined to dump dredged materials. For ε/do = 2.5, the cloud's frontal velocity reached the maximum amongst other source separations and this twin particle cloud had the smallest width amongst the twin clouds as well.

The last part of this study focused on the particle cloud velocity at both macro and micro levels. At the macro-level, the frontal velocity (u_f) of the whole cloud was investigated and at the micro-level, the inside clouds' maximum vertical velocities (u_z) were extracted with the PIVlab toolbox. It was found that the frontal velocity of twin particle clouds was compatible with the study of

Moghadaripour et al. (2017b). However, at the beginning of the test, the frontal velocities had fluctuations until they reached a certain position (i.e., for $\varepsilon/d_o = 2.5$, $L_o/d_o = 9.7$; $z = 20$ cm), where the two clouds were completely merged. Moreover, the velocity of particles on the centerlines of the individual clouds reached at most 70% of the ones on the centerline of the main merged cloud, which showed that there were severe particle interactions and collisions exactly on the centerline of the main cloud than the ones on the centerline of the side clouds. In addition, particle velocities inside the individual clouds were uniform with less fluctuation than the ones in the middle of the main cloud.

Appendix B

Experimental Study on the Water Entry of Gravity-Driven Annular Disks

Abstract

The impact of a gravity-driven circular disk on free surface water generates a number of fascinating phenomena such as crown formation, cavity development, radial jet formation, and causes significant air entrainment. A series of laboratory experiments was conducted to investigate the crown formation and cavity development induced by a free-falling disk in stagnant ambient water. Cavity dynamics has many important applications in sports, military, and underwater equipment. The effects of different controlling parameters such as disk aspect ratio and release conditions were investigated in this study. In to evaluate the geometry effects on the dynamics of free-falling disk, the free surface impact of a doughnut-shaped disk was also compared with a solid cylindrical disk to study the effect of central hole with different diameters on the time-history of water surface fluctuations, cavity formation, and air entrainment. Highspeed images were recorded with a speed of 2500 frames per second and an exposure time of 0.1 μs. It was observed that the cavity eventually pinches off at the stagnation point and then two vertical opposite jets are formed moving forward. The results were analyzed with the image analysis toolbox of the MATLAB program . It was observed that the cavity formation, frontal velocity of the disks, pinch off duration, and jet formations are highly affected by the controlling parameters. Detailed information on the energy dissipation of the disks was extracted and it was found out that the energy loss is highly affected by the release height and by increasing the density of the disk the non-dimensional energy loss decreases accordingly.

B1. Introduction

Once a solid object enters water, a series of physical phenomena occur including crown formation, creation of underwater cavity, pinch-off, and upward jet. Many researchers have been studying these phenomena for more than a century (Worthington, 1908; May, 1975; Aristoff & Bush 2009; Mansoor et al., 2014; Sun et al., 2019). The subject of water entry has many

A paper based on the content of this appendix has been accepted in the *IAHR 2023 Annual Conference, May* 2023 as Janati, M., Azimi, A. H., 2023. Experimental Study on the Water Entry of Gravity-Driven Annular Disks.

applications in various fields including military, sports, ship slamming, and naval-oriented studies (Kapsenberg, 2011; May, 1975; Seddon & Moatamedi, 2006; Abrate, 2013; Janati et al., 2022). The geometry, coating materithe waterensity, and the release height of the object are important parameters in water entry process which can affect the above surface crown and underwater cavity formations.

Most of the studies focused on the water entry of spheres and their consecutive phenomena (Marston et al., 2012; Tan et al., 2016; Duclaux et al., 2007). Aristoff and Bush (2009) investigated the free-falling motion of hydrophobic spheres with different diameters and initial velocities in water through a combination of theoretical and experimental studies. Using the Weber number as a variable, four distinct regimes were classified to describe the interaction between solid sphere and water known as a surface seal, shallow seal, deep seal, and quasi-static regimes. Moreover, it was found that the hydrophilic surface properties of solid objects affect consecutive water entry and cavity formation. Truscott et al. (2012) investigated the unsteady forces acting on vertically entered spheres with different materials. They found that high-density spheres had a state of vertical movement after the cavity pinch-off whereas low-density spheres had shown oscillating motions. Mansoor et al. (2014) investigated the water entry of spheres in a guarded release condition and without a surface seal to investigate the water surface impact, deep-seal formation, and descent of a solid sphere in the ambient water. The pinch-off depth and time were extracted from measurements and the results were compared with the surface seal condition. The effects of wall boundaries on cavity formation were studied, surface undulations were observed at the air-water interface, and multiple pinch-off points were formed at the location of undulation crests.

According to previous studies, a disk is classified as a thin or thick disk based on the ratio of the disk diameter, d_o, to thickness, e, with a threshold of $\chi = d_o/e = 10$. The water entry of thin disks and their descent modes in water have been extensively investigated using both experimental and numerical methods (Willmarth et al., 1964; Field et al., 1997; Zhong et al., 2011; Auguste et al., 2013). Different falling patterns were observed due to the instability of thin disks known as steady, fluttering, and tumbling falling modes. All defined modes were correlated with the disks and ambient fluid characteristics (Willmarth et al., 1964; Field et al., 1997). Zhou et al. (2021)

experimentally studied the falling of eccentric annular disks in water and found that large eccentricity stabilizes the movement of the free-falling disk, whereas small eccentricity (i.e., $e' <$ 0.06) leads to chaotic, tumbling, or asymmetric zigzag motions. Accordingly, three falling modes of eccentric disks were identified that are known as fluttering/chaotic/tumbling motions, the transition motion, and the new stable descending motion (Zhou et al., 2021).

In a "Focus on Fluids" letter, Moffatt (2013) reviewed the analysis of Auguste et al. (2013) and suggested studying the effects of disk geometry such as annular disks, surface roughness, and wavy edge on the descent modes of the disks. Moffatt (2013) emphasized the importance of the mentioned parameters on wake formation and disk instability. Based on Moffatt's recommendations, a series of laboratory experiments were carried out by Vincent et al. (2016) to study the falling modes of annular disks and the results were compared with the solid cylindrical disks. It was observed that the central hole in the annular disks effectively stabilized the free-falling motion of the disk in relatively large Reynolds number (Re). This study explores cavity dynamics, crown formation, pinch-off development, and free-falling motion of thick annular disks with different aspect ratios, densities, and release heights. The selected disks have rough edges and have the aspect ratios of $\chi = 1.5$ and 3.

B2. Material and Methods

B2.1. Experimental setup

A series of laboratory experiments were conducted in the Multiphase Flow Research Laboratory (MFRL) at Lakehead University using a glass-walled tank with cross-section dimensions of 1650 mm x 850 mm and with a depth of 800 mm. The water in the tank was at rest and maintained at a constant level with a depth of 650 mm in all experiments. A schematic front view of the experimental setup, the coordinate system, and a sample image of Test No. 12 are shown in Figure B1. The experimental parameters such as the characteristics of the disk, release height, impact velocities, and aspect ratios are listed in Table B1. The impact Froude number, $Fr_0 = V_0/(gd')^{1/2}$, where $d' = d_o - d_i$ is the equivalent diameter of the annular disk, d_o and d_i are the outer and inner diameters of the disk, respectively, and g is the gravitational acceleration. The experimental tank was filled with tap water having a temperature of $T = 20 \pm 0.5$ °C, a density of $\rho_w = 998$ kgm^{-3},

and kinematic viscosity of $v = 1.02 \times 10^{-6}$ m^2/s. Six disks with different densities and aspect ratios were utilized in this study.
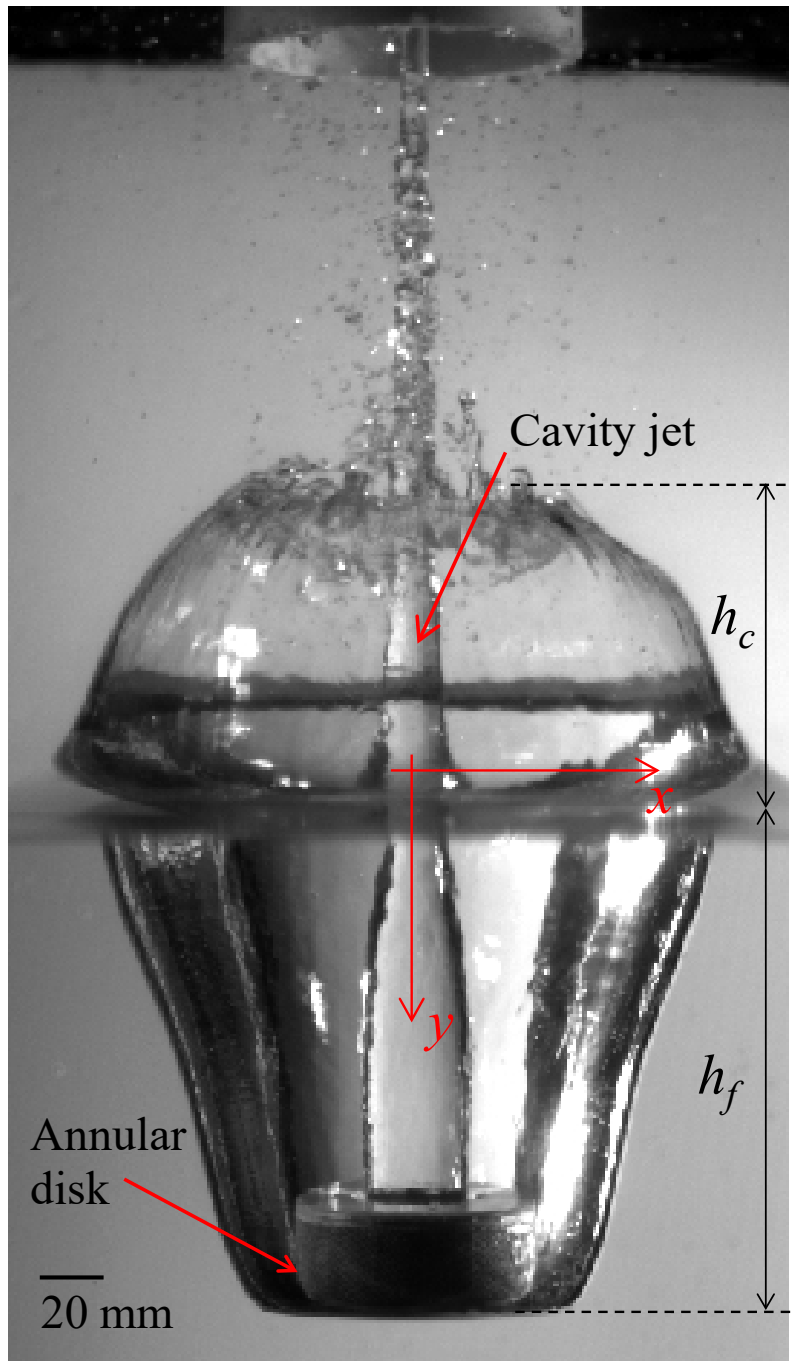
Figure B1. Image showing the water-entry cavity formed by falling a gravity-driven hydrophobic annular disk, Test No. 12; $\chi = 3$, $\rho_d/\rho_w = 2.335$, $d_i = 38.1$ mm, $e = 25.4$ mm, $h_r = 500$ mm.

The disks were made of compressed rubber and were considered to have homogenous densities, which were hydrophobized by treatment with a commercially available super hydrophobic agent, Glaco Mirror Coat' zero' (Soft99 Corp. Co., Ltd., Japan) with the approximate thickness of 1 µm. The water contact angle was measured based on the proposed method by Truscott et al. (2013) which was 123°. Disks with three different densities of disks were selected as $\rho_d = 1,079$ kgm^{-3}, 1,381 kgm^{-3}, and 2,331 kgm^{-3} with the outside diameter of $d_o = 76.2$ mm and the centric hole diameter of $d_i = 38.1$ mm. Two disk thicknesses were selected (i.e., $e = 25.4$ mm and 50.8 mm) in this study to create the aspect ratio of $\chi = 1.5$, and 3. Four release heights were selected as $h_r = 200$ mm, 300 mm, 400 mm, and 500 mm. Disks were released through a pipe that was held 200 mm above the water surface and at the center of the tank and the tank wall boundary did not affect the motion of the disks. Each experiment was repeated three times to ensure the repeatability of tests and exhibited consistent cavity and crown formations over all trials.

Table B1: Experimental details and physical parameters of free-falling thick annular disks in stagnant water, $d_o = 76.2$ mm (3 in), $d_i = 38.1$ mm (1.5 in).

Test No.	h_r	e	M	ρ_d	V_o	χ	Fr_o	Re_o
	(mm)	(mm)	(g)	(kgm^{-3})	(ms^{-1})	(-)	(-)	(-)
1	200	25.4	94	1079	0.84	1.5	1.37	31339
2	300	25.4	94	1079	0.90	1.5	1.47	33636
3	400	25.4	94	1079	1.55	1.5	2.53	57828
4	500	25.4	94	1079	1.69	1.5	2.76	62969
5	200	25.4	120	1381	0.97	1.5	1.59	36338
6	300	25.4	120	1381	1.03	1.5	1.68	38345
7	400	25.4	120	1381	1.65	1.5	2.70	61758
8	500	25.4	120	1381	1.76	1.5	2.88	65831
9	200	25.4	202	2331	1.12	1.5	1.82	41666
10	300	25.4	202	2331	1.17	1.5	1.91	43609

11	400	25.4	202	2331	1.80	1.5	2.94	67166
12	500	25.4	202	2331	2.13	1.5	3.49	79637
13	200	50.8	188	1079	1.02	3	1.67	38105
14	300	50.8	188	1079	1.10	3	1.80	41011
15	400	50.8	188	1079	1.77	3	2.90	66240
16	500	50.8	188	1079	1.93	3	3.16	72229
17	200	50.8	240	1381	0.92	3	1.50	34254
18	300	50.8	240	1381	1.03	3	1.68	38315
19	400	50.8	240	1381	1.84	3	3.01	68846
20	500	50.8	240	1381	2.24	3	3.66	83630
21	200	50.8	404	2331	1.19	3	1.95	44486
22	300	50.8	404	2331	1.36	3	2.23	50831
23	400	50.8	404	2331	2.29	3	3.20	85381
24	500	50.8	404	2331	2.33	3	3.80	86853

High-speed imaging technique and the MatLab object detection algorithm (MatLab version R2018b, MathWorks, Natick, MA, US) were employed to calculate the impact velocity of each disk, V_o and consequently the Froude number for each test. It should be mentioned that the High-speed images with a frequency of 2500 fps and resolution of 1280 x 800 pixels were captured by a high-speed camera (Phantom, Miro Lab 110, New Jersey, Wayne, USA) and a camera lens of AF Nikkor 50 mm, f/1.4D (Nikon, Tokyo, Japan). The water tank and falling disk were illuminated using two light sources (Woods L13, 1,000-W telescope work light, CA) from both sides of the glass tank. A minimum of 10 minutes of relaxation time between each experiment was considered to eliminate the disk-water interactions and water fluctuations. The water surface level was rechecked during the relaxation time to maintain a consistent water level for the next experiment.

B3. Experimental Results

B3.1. Crown and cavity formation

In this section, the experimental observations of the crown formation and underwater cavity characteristics of free-falling thick annular disks are presented. The effect of geometry, disks's density, and release heights are also investigated and the results are plotted accordingly. In Figure B2, the consecutive images of water entry of a thick annular disk related to Test No. 9 with the aspect ratio of $\chi = 3$, are illustrated. The density ratio of the disk is $\rho_d/\rho_w = 1.08$, the diameter of the central hole is $d_i = 38.1$ mm, the release height is $h_r = 400$ mm and the time difference between each frame is 20 ms.
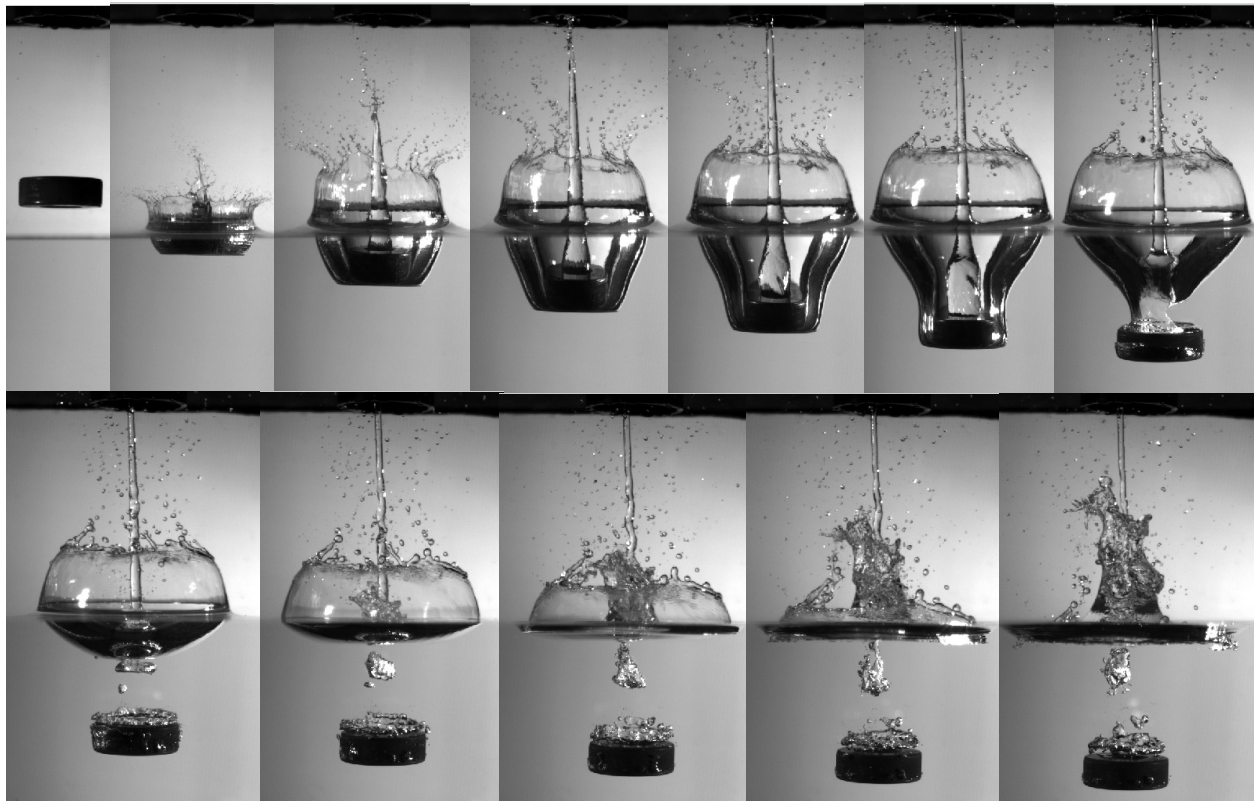
Figure B2. Image showing the water-entry cavity formed by falling a gravity-driven hydrophobic annular disk, Test No. 9; $\chi = 3$, $\rho_d/\rho_w = 1.08$, $d_i = 38.1$ mm, $e = 25.4$ mm, $h_r = 400$ mm. The time between each frame is 20 ms.

As can be seen in Figure B2, the surface crown is formed as soon as the disk impacts water. A

central cavity jet is also formed which moves upward much faster than the crown. Similarly, the underwater cavity is formed and expands while the disk moves downward until the surrounding static pressure becomes greater than the inside pressure. Then the cavity starts to contract until it pinches off. After pinch-off, a large bubble is detached from the jet down to the water and an upward jet moves upward and interacts with the returning cavity jet at the water surface. Then the crown collapse and a cavity ring above the disk which was formed by the downward jet moves upward toward the water surface.

The crown diameter is measured and extracted by employing the boundary detection technique with MatLab programming, then normalized by the disk's diameter (D_c/d_o) and plotted versus Froude numbers (Fr_o) in Figure B3. The results show that the release height of the disks is important in the crown diameter at the threshold limit of $h_r/d_o = 4$. In release heights smaller than four times of disks' diameter, $h_r/d_o \leq 4$, the normalized crown diameter is significantly smaller than the ones with $h_r/d_o > 4$ in all densities and aspect ratios, approximately 40% to 50%. The ranges of normalized crown diameter are $1.45 < D_c/d_o < 1.65$ in $h_r/d_o \leq 4$ and $2.1 < D_c/d_o < 2.4$ in $h_r/d_o > 4$.
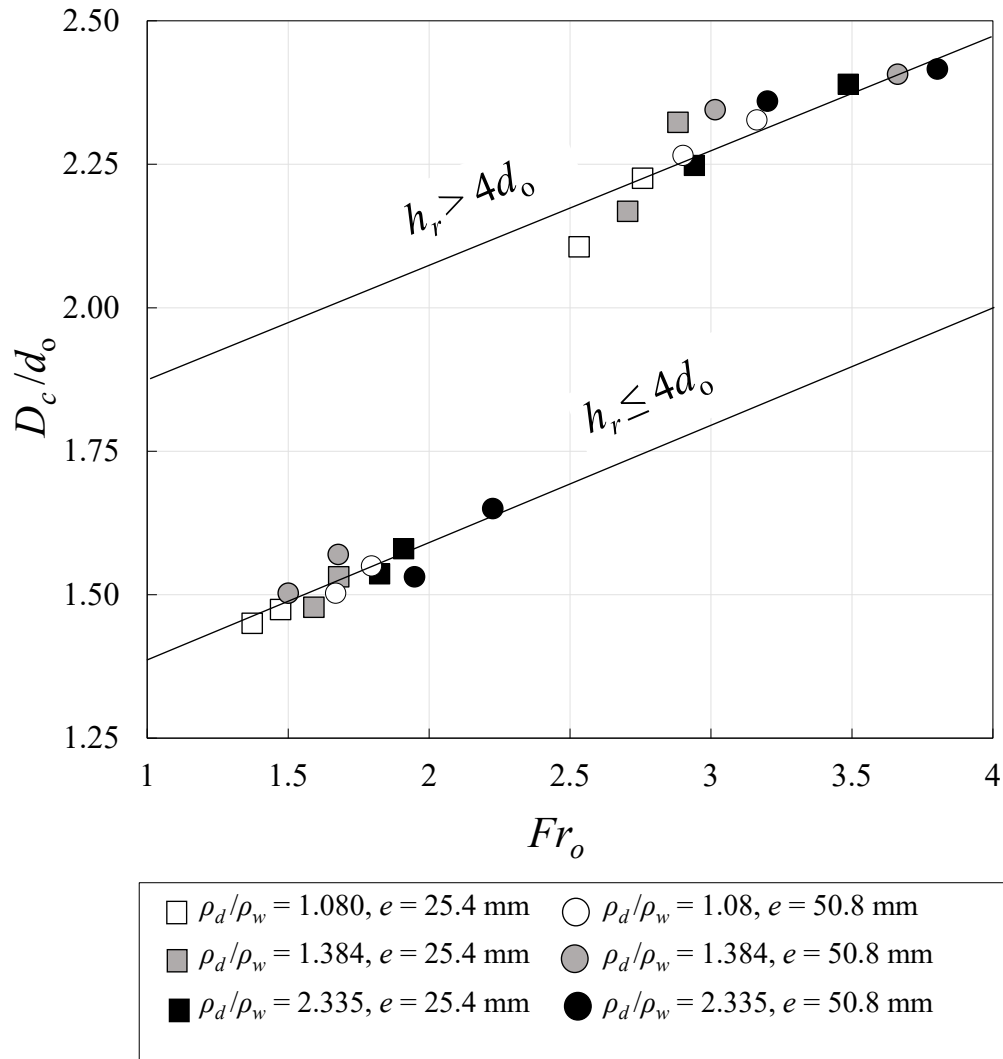
Figure B3. Variations of dimensionless crown diameter, D_c/d_o, with impact Froude number, Fr_o, for different release heights. The solid lines represent the proposed equations.

B3.2. Pinch-off

The pinch-off phenomenon occurs when the underwater cavity reaches a state where the cavity divides into two parts due to the increase in surrounding static pressure. In the annular disks, the pinch-off forms a singularity ring because of the central cavity jet. Several important parameters are measured at the pinch-off and the results are shown in this section. Pinch-off depth is one of those parameters and is measured from the water surface to the depth where pinch-off occurs. The pinch-off frame of free-falling thick annular disks is shown in Figure B4.
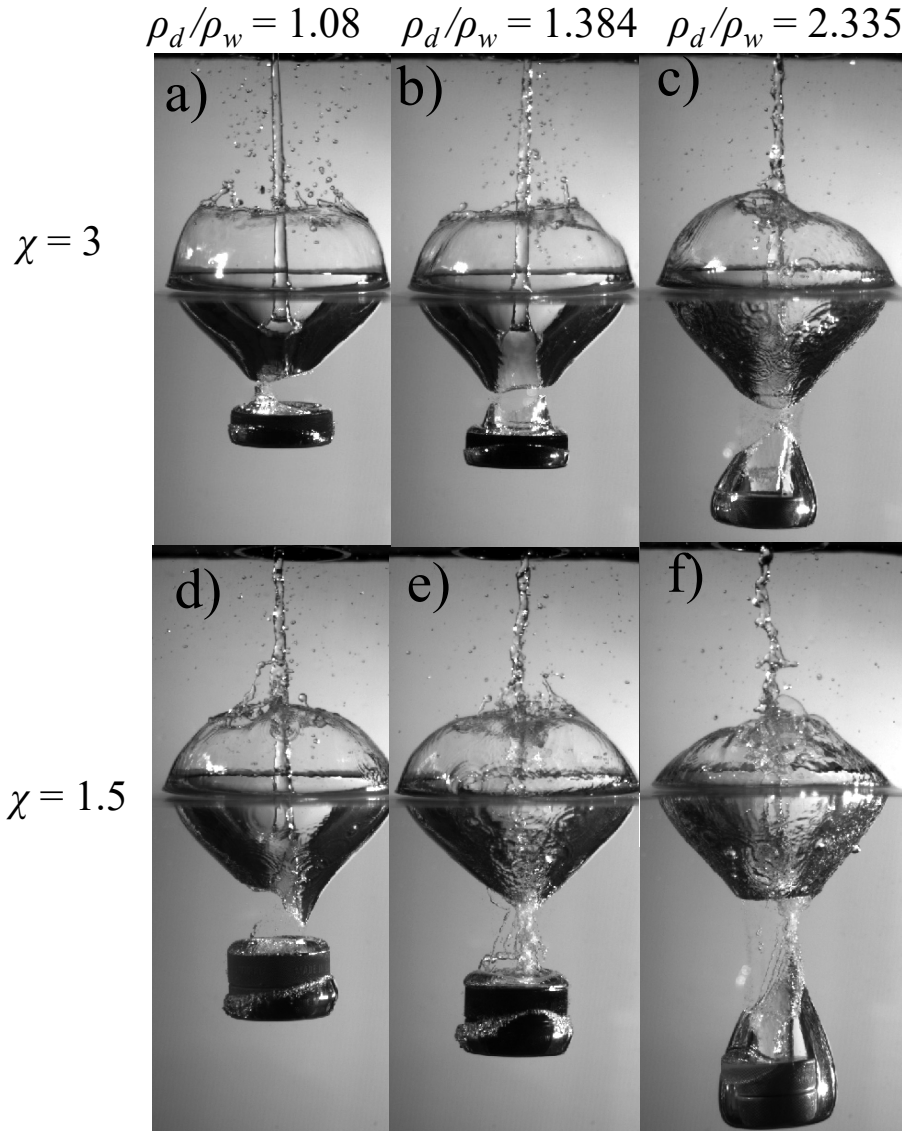
Figure B4. Pinch-off frame of free-falling thick annular disks. Disk density and mass varied and the release height was constant, h_r = 400 mm: a) Test No. 7, χ = 3, ρ_d/ρ_w = 1.080; b) Test No. 8, χ = 3, ρ_d/ρ_w = 1.384; c) Test No. 9, χ = 3, ρ_d/ρ_w = 2.335; d) Test No. 19, χ = 1.5, ρ_d/ρ_w = 1.080; e) Test No. 20, χ = 1.5, ρ_d/ρ_w = 1.384; f) Test No. 21, χ = 1.5, ρ_d/ρ_w = 2.335. Images were taken at the pinch-off time.

In order to compare the results based on the disks' density and aspect ratio in a constant release height which is h_r = 400 mm, all six disks were released into the water and the results showed the pinch-off phenomena in Test No. 7 to 9, and 19 to 21. The first row including Figures B4a to B4c shows the results related to the aspect ratio of χ = 3, and with a different density ratio of ρ_d/ρ_w =

1.080, 1.384, and 2.335 in different columns. The second row illustrates disks with the aspect ratio of $\chi = 1.5$ with the three densities. As can be seen, the shape and appearance of the crown are different based on the disk's aspect ratios and densities. For example, in Figure B4a which shows the lightest disk with the aspect ratio of $\chi = 3$, the crown at pinch-off is not fully sealed. Moreover, the surface of the crown is clear without any distortions and interference with the central cavity jet. The pinch-off depth is smaller than in all other cases and the cavity above the surface of the disk is very small. By increasing the density of the disk, the pinch-off depth slightly increases, however, the cavity pocket which sticks above the surface of the disk gets larger. In addition, the crown is now fully sealed in Figure B4c, and severe distortions can be seen on the cavity surface because of the splash of the crown toward the cavity inside. In Figure B4d, the aspect ratio decreased by half and the crown is sealed due to the increase in thickness of the disk, but the distortion is not observed. By increasing the density of the disks, i.e., Figure B4g, the crown pack becomes smaller, the crown is sealed, and again severe distortion can be observed on the cavity surface.

Due to the importance of the underwater cavity pinch-off, all pinch-off depths were measured from the experiments, normalized by the disk diameter, and plotted in Figure B5. As can be seen the normalized pinch-off depth increases by increasing the Froude number which is directly affected by the release height of the disk.
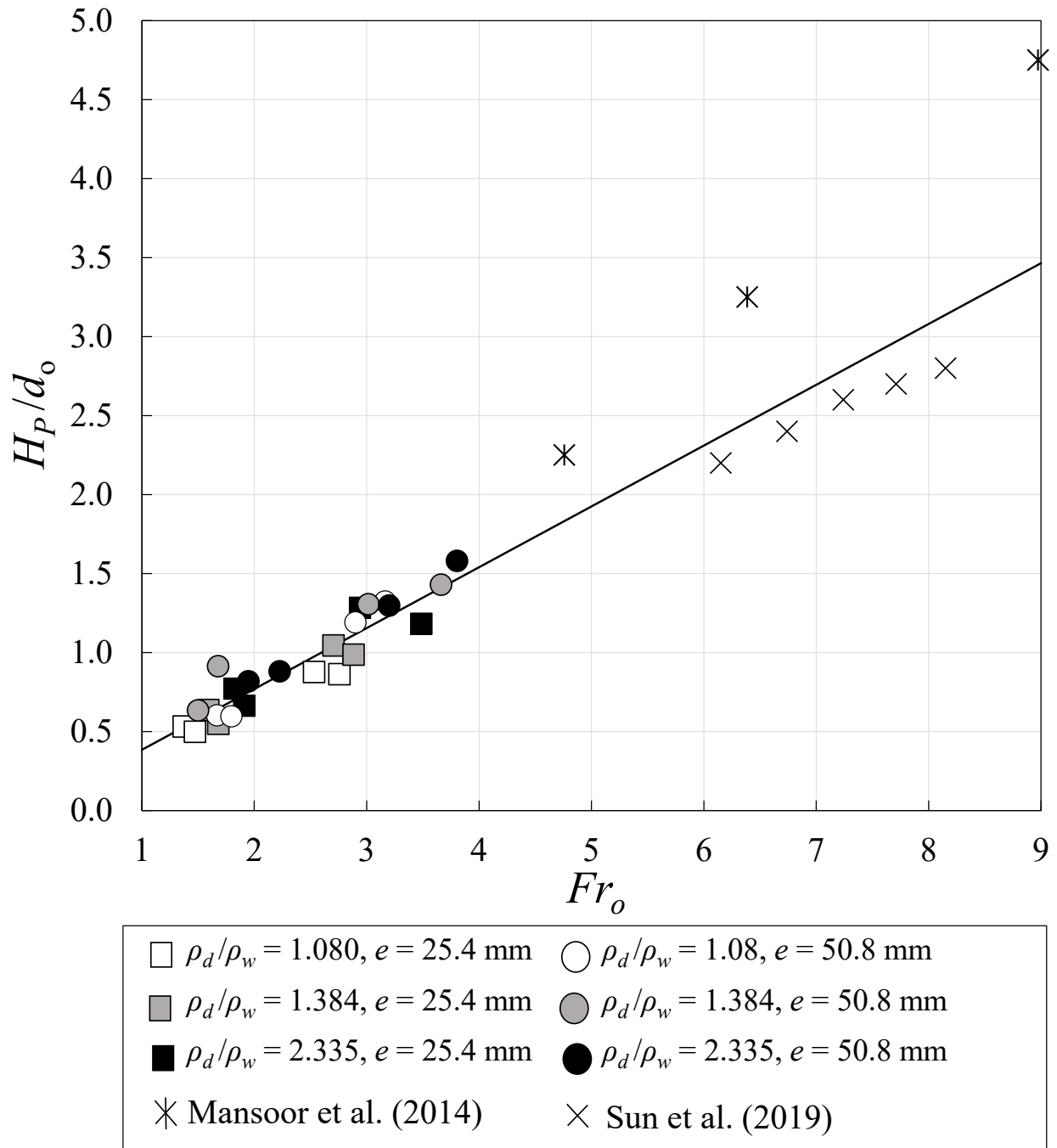
Figure B5. Variations of non-dimensional pinch-off depth with the initial impact and geometrical properties: a) correlations of H_p/d_o as a function of impact Froude number.

As can be seen, a black solid line shows the proposed equation in the current study with the $R^2 = 0.98$ to predict the pinch-off depth based on the impact Froude number as:

$$H_p/d_o = 0.385 Fr_o \qquad \text{Eq. (B1)}$$

The results related to the study of Sun et al. (2019) and Mansoor et al. (2014) related to the water entry of spheres were added to this plot for comparison. In the study of Sun et al. (2019) the diameter of the sphere was 57.2 mm with a density of 1837 kgm^{-3} and Mansoor et al. (2014) used steel spheres with the diameter of 15 mm, 20 mm, and 25 mm and density of 7850 kgm^{-3}. The results related to Sun et al. (2019) have good agreement with the proposed equation in this study, however, the results of Mansoor et al. (2014) are drastically higher than other studies due to the higher density and smaller diameter of the spheres.

The duration in which the disk impacts water till the cavity pinches off is called pinch-off time, t_p, and in the current study, the pinch-off times were measured in all experiments, the results were normalized by the diameter of the disk and gravity acceleration, $t_p/(d_o/g)^{1/2}$ and they are presented in Figure B6 versus the impact Froude number, Fr_o. As can be seen, the solid line shows the average non-dimensional pinch-off time, $t_p/(d_o/g)^{1/2} = 1.37$. The solid red line represents the results of the study of Duclaux et al. (2007) which is 16% higher than this study and is $t_p/(d_o/g)^{1/2} = 1.6$. Overall, the pinch-off time is approximately constant in the previous studies regardless of the density and geometry of the object.
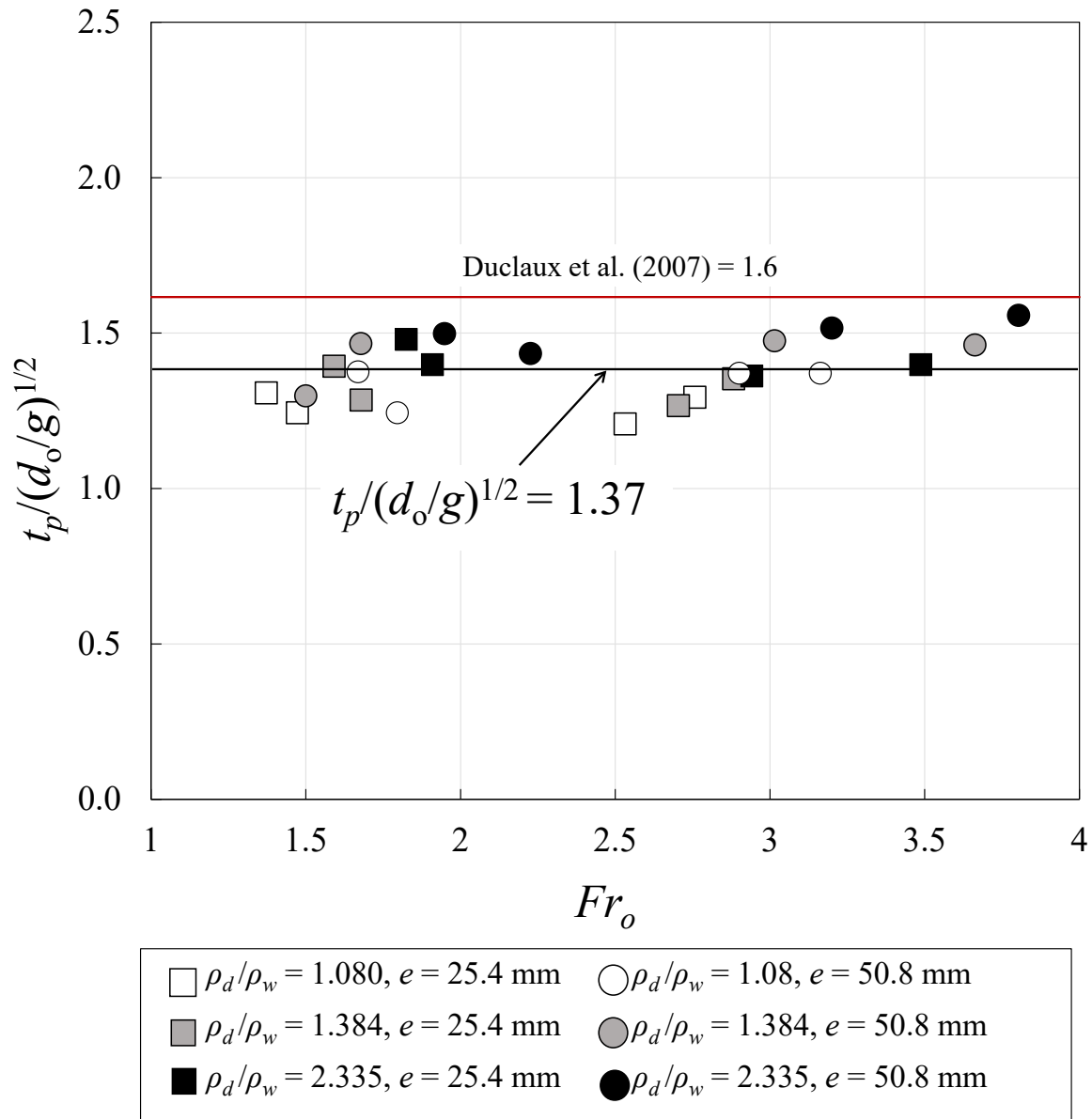
Figure B6. Variations of dimensionless pinch-off time, $t_p/(d_o/g)^{1/2}$, as a function of impact Froude number. The solid black line shows the average value of the current study $t_p/(d_o/g)^{1/2} = 1.37$, and the solid red line is the result of Duclaux et al. (2007) for the study of a sphere.

B3.3. Energy loss

The object entering a water body loses a large amount of energy at the impact moment. In Figure B7, the energy loss of the disks at the impact was calculated, normalized, $\Delta E/E_o$, and plotted versus the impact Froude number, Fr_o. As can be seen in Figure B7, release height is the most

determinative parameter in the energy loss of the object and the non-dimensional energy loss of the disks was linearly correlated with the release heights. Moreover, the energy loss rate decreases by enhancing the release height. In the same release height, the non-dimensional energy loss increases by decreasing the density of the disks. For example, the disk with the density of $\rho_d/\rho_w = 1.080$, and aspect ratio of $\chi = 3$, had the maximum energy losses at the impact and the densest disk with the density of $\rho_d/\rho_w = 2.335$, and aspect ratio of $\chi = 1.5$ has the smallest amount of energy loss. Therefore, by increasing the density of the disk the energy loss rate decreases, and the disk overcomes the impact effect.
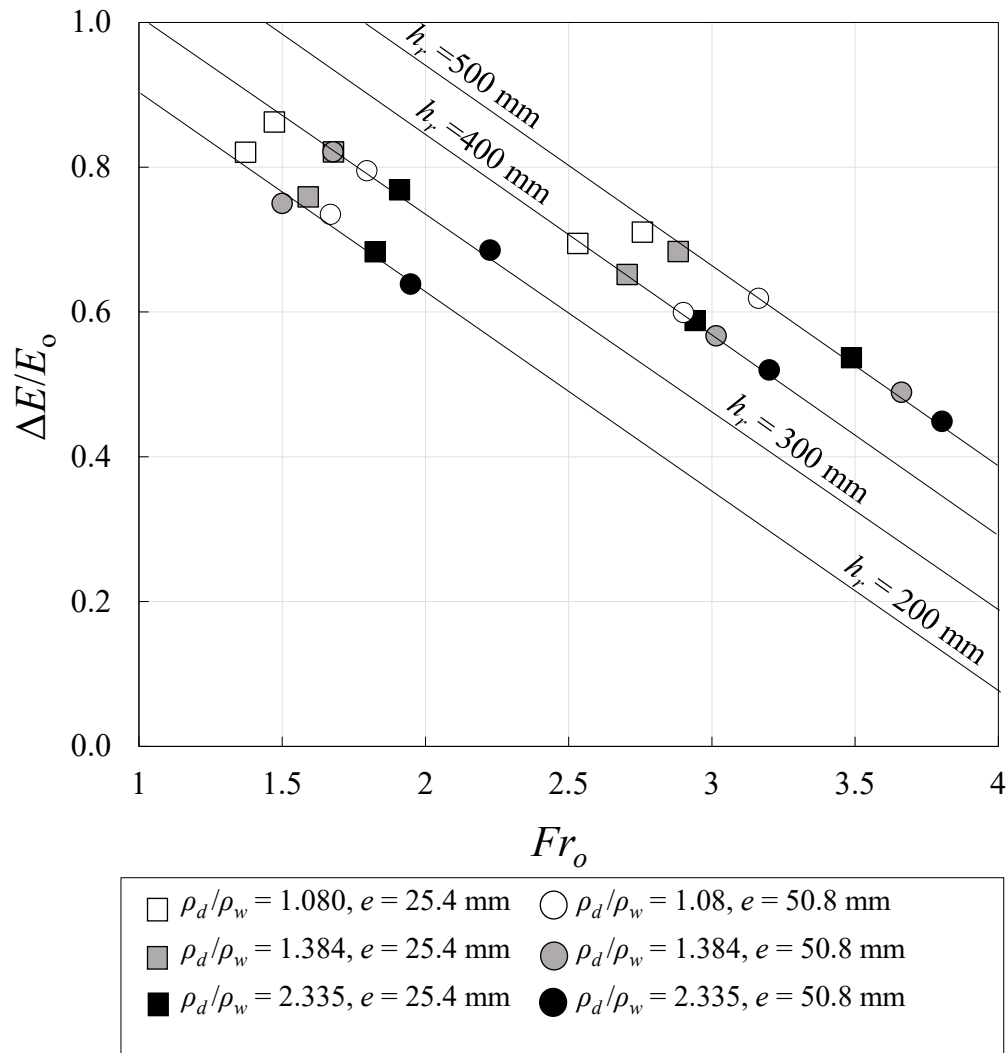
Figure B7. Variations of dimensionless energy loss versus Froude number. Each solid line represents a specific release height including $h_r = 200$ mm, 300 mm, 400 mm, and 500 mm.

B4. Conclusion

The results of the experimental investigation of gravity-driven annular thick disks and the following phenomena including surface crown formation and underwater cavity dynamics were presented in this study. Disks with three different densities, two different aspect ratios, and four different release heights were used in this study. To record the process of water entry and to extract the results from the sequential images, high-speed imaging and MatLab programming were implemented. The subsequent phenomena such as crown diameter, pinch-off depth, and pinch-off depth in annular disks were measured and plotted versus the Froude number. The non-dimensional crown diameter was found to be directly affected by the release height of the disks and a threshold value of $h_r = 4d_o$, where the results suddenly increased beyond that, was obtained through the experiments.

Pinch-off depths were increased by increasing the Froude number and pinch-off times were approximately constant, $t_p/(d_o/g)^{1/2} = 1.37$. The energy loss of the disks was measured at the impact time and the results were normalized by the initial energy of the disk. It was found that the normalized energy loss was correlated with the release height of the disks. Moreover, by increasing the density of the disk, the energy loss decreases. Because when the disk has a smaller density, it is easier to lose energy at the impact in comparison to a disk with high density.

Nomenclature

a = acceleration reduction, m/s^2

A_s = surface area of the cloud m^2;

B = cloud buoyancy m^4/s^2;

B_o = sediment cloud initial buoyancy with the total volume of solid particles m^4/s^2;

c_o = initial sand concentration, volume/volume;

d_o = outside diameter of the disk, mm;

d_o = nozzle inside diameter, mm;

d_{50} = particle median grain size, mm;

D_{50} = particle median grain size, mm;

d_o = outside diameter of the disk, mm;

D_c = crown diameter, mm;

d_i = diameter of the central hole in annular disks, mm;

d' = equivalent diameter, mm;

D_f = frontal position of the disk, mm;

D_p = pinch-off depth, mm;

e = disk thickness, mm;

E_i = impact energy, N.m;

E_o = initial energy, N.m;

Fr_o = impact Froude number;

Fr = Froude number;

Fr_i = initial Froude number;

g = acceleration due to gravity, ms^{-2};

g' = reduced gravity, ms^{-2};

h_{air} = release height in the air, mm:

h_p = release height in the pipe, mm:

h' = equivalent height, mm

h_o = impact head, mm

h_r = release height, mm

h_{pipe} = release height in the pipe, mm;

H_c = crown height, mm;

H = total release height, mm;

H_d = central position of the disk, m;

H_f = frontal depth of the disks, m;

H_p = Pinch-off depth of the disks, m;

$I*$ = dimensionless moment of inertia;

l = length scale, mm;

L_o = length scale, mm;

m = particle total mass, g;

m = disk mass, g;

$\dot{m}$ = mass rate, g/s;

N_C = cloud number;

r_o = initial equivalent radius of a sphere of the particle cloud, mm;

r = Disk radius, mm;

r' = equivalent radius of object, mm;

Ra = Rayleigh number;

Re = Reynolds number;

St = Stokes' number;

t = time, s;

t_o = time when clouds need to reach the *a-a* section, s;

t_p = pinch-off time, s;

T_p = scaled pinch-off time;

T = characteristic time scale, s;

t_s = settling time, s;

t_c = crown time, s;

t_{p2} = second pinch-off time, s;

t_s = settling time, s;

Q_e = entrained flow rate, m^3s^{-1};

u = radial velocity, ms^{-1};

u_{rms} = root mean square velocity of the disk, ms^{-1}

u_o = initial velocity at the nozzle, ms^{-1};

u_e = velocity of entrained water, ms^{-1};

u_x = radial velocity of entrained water, ms^{-1};

$u_z^{'}$ = turbulence intensity, ms^{-1};

u_f = frontal velocity of cloud, ms^{-1};

u_z = vertical centerline velocity inside the cloud, ms^{-1};

u_∞ = particle settling velocity, ms^{-1};

v = axial velocity, ms^{-1};

V_o = impact velocity of the disk, ms^{-1};

V = mean velocity of the disk, ms^{-1};

V_p = pinch-off velocity, ms^{-1};

V_S = settling velocity, ms^{-1};

w = width of single oblique or vertical particle cloud, m;

w_{1-V} = width of single vertical particle cloud, m;

w_{2-O} = width of twin oblique particle cloud, m;

w_{2-V} = width of twin vertical particle cloud minus nozzle distance, m;

W = total width of twin vertical particle cloud, m;

X_{bar} = horizontal centroid component of the cloud, mm;

z = vertical distance, mm;

Z_{bar} = vertical centroid component of the cloud, mm;

Z_b = boundary height, mm;

Z_f = frontal position, mm;

Z_v = virtual origin, mm;

α = angle between nozzle and fluid surface, degrees;

α_e = entrainment coefficient, volume/volume;

ε = distance between nozzles, mm;

ρ_d = density of disks, kgm^{-3};

ρ_w = density of water, kgm^{-3};

ρ_s = density of sand particles, kgm^{-3};

μ = dynamic viscosity (kg/(ms));

ζ, ϕ = coefficients;

χ = disk aspect ratio

ω = vorticity, s^{-1}

μ_w = dynamic viscosity of water, $\mathrm{kgm^{-1}s^{-1}}$

φ_1, φ_2 = coefficients

υ = kinematic viscosity of water, $\mathrm{m^2s^{-1}}$

References

Abramovich, G.N., 1963. "The Theory of Turbulent Jets". *MIT Press*, 671p.

Abrate, S., 2013. "Hull Slamming". *Appl. Mech.* Rev. 64 (6), 060803.

Andersen A., Pesavento U., Wang Z.J., 2005. "Unsteady aerodynamics of fluttering and tumbling plates". *J. Fluid. Mech*. 541:65.

Aristoff, J.M. & Bush, J.W.M., 2009. "Water Entry of Small Hydrophobic Spheres". *J. Fluid Mech.* 619, 45–34.

Aristoff, J.M., Truscott, T.T., Techet, A. H. & Bush, J.W.M., 2010. "The Water Entry of Decelerating Spheres". *Phys. Fluids* 22 (3), 032102.

Auguste, F., Magnaudet, J. & Fabre, D., 2013. "Falling Styles of Disks". *J. Fluid. Mech*. 719, 388–405.

Azimi, A.H., 2019. "Experimental investigation on the motion of particle cloud in viscous fluids". *ASME J. Fluids Eng*. 141 (3), 031202 14 p.

Azimi, A. H., Zhu D. Z., and Rajaratnam, N., 2012a. "Experimental Study of Sand Jet Front in Water". *Int. J. Multiphase Flow* 40: 19–37.

Azimi, A., Zhu, D. Z., and Rajaratnam, N., 2012b. "Computational Investigation on Vertical Slurry Jets". *Int. J. Multiphase Flow* 47: pp. 94–114.

Azimi, A. H., Zhu, D. Z., and Rajaratnam, N., 2011. "Effect of particle size on the characteristics of sand jet in water." *Journal of Engineering Mechanics*, *ASCE*, Vol. 137, No. 12, pp. 822-834.

Azimi, A. H., 2019. "Experimental investigation on the motion of particle cloud in viscous fluids". *Journal of Fluids Engineering* 141(3): 031202(1-14).

Azimi, A. H., Zhu, D. Z., Rajaratnam, N., 2014. "An experimental study of sand deposition from slurry wall jets". *Journal of Engineering Mechanics*, ASCE, Vol. 140, No. 2, pp. 296-314.

Azimi, A. H., Qian, Y., Zhu, D. Z., Rajaratnam, N., 2015. "An experimental study on circular

slurry wall jets". *International Journal of Multiphase Flow* Vol. 74, pp. 34-44.

Bergmann R, Van Der Meer D, Gekle S, Van Der Bos A, Lohse D., 2009. "Controlled Impact of a Disk on a Water Surface: Cavity Dynamics". *J. Fluid Mech*. 381–409.

Bi, D., Wei, Y., Wang, C., 2018. Experimental Study on The Vortex Structure and Path Instability of Freely Falling Annular Disks. *Sci. China Technol. Sci*. 61, 853–866 (2018).

Birkhoff G., Zarantonello, Eh., 1957. Jets, Wakes, and Cavities. *Appl. Math. Mech*. New York: Academic. 353 Pp.

Bond, D., & Johari, H., 2005. "Effects of initial geometry on the development of thermals". *Experiments in Fluids* 39(3), 589–599.

Brennen, C., 2013. Cavitation and Bubble Dynamics. *Oxford University Press*.

Buhler, J., and Papantoniou, D., 2001. "On the motion of suspension thermals and particle swarms". *Journal of Hydraulic Research* 39(6): 643–653.

Bush, John W. M., Thurber B. A., and Blanchette F., 2003. "Particle Clouds in Homogeneous and Stratified Environments". *J. Fluid. Mech*., 489 (489): 29–54.

Cai, J., Hall, N., Elenany, M., Zhu, D.Z., Rajaratnam, N., 2010. "Observations on sand jets in air". *Journal of Engineering Mechanics* 136: 1181–1186.

Cenedese, C., and Linden P. F., 2014. "Entrainment in two coalescing axisymmetric turbulent plumes". *Journal of Fluid Mechanics* 752: R2.

Chan, S. N., Lee, K.W. Y., and Lee, J. H.W., 2014. "Numerical modeling of horizontal sediment-laden jets." *Environ. Fluid Mech.*, 14(1), 173–200.

Chen, J. C., and Rodi W., 1980. "Vertical turbulent buoyant jets: A review of experimental data". *London: Pergamon Press*.

Chin, D. A., 2013. "Water-quality Engineering in Natural Systems: Fate and Transport Processes in the Water Environment". *CLEAN- Soil*, *Air*, *Water* (Vol. 41).

Davies, R.M. and Taylor, G. I., 1950. "The mechanics of large bubbles rising through extended liquids and through liquids in tubes". Proc. Roy. Soc. A, 200, 375–390.

Duclaux, V., Caille, F., Duez, C., Ybert, C., Bocquet, L, and Clanet, C., 2007. "Dynamics of transient cavities". *J. Fluid Mech*. 591,1–19.

Duez, C., Ybert, C., Clanet, C. & Bocquet, L., 2007. Making A Splash with Water Repellency. *Nat. Phys.* 3 (3), 180–183.

Er, J. W., Law, A., Adams, E., and Zhao B., 2016. "Open-Water Disposal of Barged Sediments". *J. Waterway, Port, Coastal, Ocean Engineering* 04016006:1-16.

Eshraghi, J., Jung, S., and Vlachos, P. P., 2020. "To seal or not to seal: The closure dynamics of a splash curtain". *Phys. Rev. Fluids* 5, 104001.

Fernandes, P., Ern, P., Risso, F., & Magnaudet, J., 2008. "Dynamics of axisymmetric bodies rising along a zigzag path". *Journal of Fluid Mechanics*, 606, 209-223.

Field, S. B., Klaus, M. & Moore, M. G., 1997. "Chaotic Dynamics of Falling Disks". *Nature* 388, 252–254.

Fischer, H. B., List, E. J., Koh, R. C. Y., Imberger, J. & Brooks, N. H. (eds), 1979. "Mixing in Inland and Coastal Waters". *San Diego, CA: Academic*.

Gaudet, S., 1998. "Numerical Simulation of Circular Disks Entering the Free Surface of a Fluid". *Phys. Fluids* 10, 2489–2499.

Gekle, S., Gordillo, J. M., Van der Meer, D., and Lohse, D., 2009b. "High-speed jet formation after solid object impact". *Phys. Rev. Lett*., 102:034502.

Gekle, S., Snoeijer, J. H., Lohse, D., and Van der Meer, D., 2009a. "Approach to universality in axisymmetric bubble pinch-off". *Phys. Rev. E*, 80:036305.

Gensheimer, R., Adams, E. and Law, A., 2013. "Dynamics of particle clouds in ambient currents with application to open-water sediment disposal". *Journal of Hydraulic Engineering* 139: 114–123.

Gilbarg, D., Anderson, R.A., 1948. "Influence of atmospheric pressure on the phenomena accompanying the entry of spheres into water", *J. Appl. Phys*. 19 (2) 127–139.

Glasheen, J.W.& McMahon, T. A., 1996b. "Vertical Water Entry of Disks at Low Froude Numbers". *Phys. Fluids* 8, 2078–2083.

Heisinger, L., Newton, P. & Kanso, E., 2014. "Coins Falling in Water". *J. Fluid Mech.* 742, 243–253.

Jackson, B., Jung, S., and Vlachos, P., "Surface seal in the water-entry of hydrophobic spheres" in 64th Annual Meeting of the APS Division of Fluid Dynamics, 2011.

Jalaal, M., Kemper, D., & Lohse, D., 2019. "Viscoplastic water entry". *Journal of Fluid Mechanics,* 864, 596-613.

Janati M, Azimi A. H., 2021a. "Mixing of Twin Particle Clouds in Stagnant Water". *ASCE J Eng Mech* 147(5):04021022.

Janati M, Azimi A. H., 2021b. "On the motion of single and twin oblique particle clouds in stagnant water". *ASME J Fluids Eng* 143(10): 101402.

Janati, M., and Azimi, A.H., 2023. "On the crown formation and cavity dynamics of free-falling thick disks", *Physics of Fluids* 35, 012104.

Janati, M., Manzouri, M., and Azimi, A. H., 2022. "Effects of immiscible interface and particle channelization on particle dynamics of oblique oily sand jets", *Physics of Fluids* 34, 053315.

Kapsenberg, G. K., 2011. "Slamming of Ships: Where Are We Now?" *Phil. Trans. R. Soc*. A 369 (1947), 2892–2919.

Kim, N., & Park, H., 2019. "Water Entry of Rounded Cylindrical Bodies with Different Aspect Ratios and Surface Conditions". *J. Fluid Mech.* 863, 757-788.

Korobkin, A. A. & Pukhnachov, V. V. 1988 Initial stage of water impact. Annu. Rev. Fluid Mech. 20, 159–185.

Lai, A. C. H., Adams, E. E., and Law, A. W. K., 2018. "Mass Loss to the Trailing Stem of a Sediment Cloud". *Journal of Hydraulic Engineering* 144(4): 06018003.

Lai, A. C. H., Chan, S. N., Law, A. W. and Adams, E. E., 2016b. "Spreading Hypothesis of a Particle Plume". *Journal of Hydraulic Engineering* 142(12): 1–12.

Lai, A. C. H., & Lee, J. H. W., 2012. "Dynamic interaction of multiple buoyant jets". *Journal of Fluid Mechanics* 708: 539–575.

Lai, A. C. H., Wang, R. Q., Law, A. W. K. and Adams, E. E., 2016a. "Modeling and experiments of poly-disperse particle clouds". *Environmental Fluid Mechanics* 16(4): 875–898.

Lai, A. C. H., Zhao, B., Law, A. W. K. and Adams, E. E., 2013. "Two-phase modeling of sediment clouds". *Environmental Fluid Mechanics* 13(5): 435–463.

Lai, A. C. H., Zhao, B., Law, A. W. K., & Adams, E. E., 2014. "A numerical and analytical study of the effect of aspect ratio on the behavior of a round thermal". *Environmental Fluid Mechanics* 15(1): 85–108.

Lau E.M., Huang W.X., Xu C.X., 2018. "Progression of heavy plates from stable falling to tumbling flight". *Journal of Fluid Mechanics* 850:1009.

Lau, E.M., Zhang, JD., Jia, YX. *et al.,* 2019. "Vortical structures in the wake of falling plates". *J Vis*. 22, 15–24.

Lee, C., Su, Z., Zhong, H., Chen, S., Zhou, M., & Wu, J., 2013. "Experimental investigation of freely falling thin disks. Part 2. Transition of three-dimensional motion from zigzag to spiral". *Journal of Fluid Mechanics*, 732, 77-104.

Lee, D.G. and Kim, H.Y., 2008. "Impact of a superhydrophobic sphere onto water". *Langmuir*, 24(1), pp.142-145.

Lee, J.H.W., Chu, V.H., 2003. "Turbulent Jets and Plumes: A Lagrangian Approach". *Kluwer Academic Publisher*.

Mansoor, M.M., Marston, J.O., Vakarelski, I.U. & Thoroddsen, S.T., 2014. "Water Entry Without

Surface Seal: Extended Cavity Formation". *J. Fluid Mech.* 743, 295–326.

Manzouri, M., and Azimi, A. H., 2019a. "A study of mound formation by discharging sand particles through oblique pipes in stagnant water". *International Journal of Sediment Research*.

Manzouri, M., and Azimi, A. H., 2019b. "Effects on oily sand jet evolution from impact momentum and channelization of particles through an immiscible interface". *International Journal of Multiphase Flow* Vol. 121, 103124 (18 Pages).

Marston, J.O., Truscott, T.T., Speirs, N.B., Mansoor, M.M. & Thoroddsen, S.T., 2016. "Crown Sealing and Buckling Instability During Water Entry of Spheres". *J. Fluid Mech.* 794, 506–529.

Marston, J.,O., Vakarelski, I., & Thoroddsen, S., 2012. "Cavity Formation by The Impact of Leidenfrost Spheres". *J. Fluid Mech.* 699, 465-488.

MATLAB software (Computer software, Math Works, Inc. 2018), Natick, MA.

May, A., 1951. "Effect of the surface condition of a sphere on its water-entry cavity". Journal of Applied Physics, 22(10):1219–1222.

May, A., 1975. "Water Entry and The Cavity-Running Behavior of Missiles, Final Technical Report", Report No. A924020, *Navsea Hydryballistics Advisory Committee*, Silver Spring, Md.

Mirzaei, M., Taghvaei, H., Golneshan, A.A., 2020b. "Improvement of cavity shape modeling in water-entry of circular cylinders by considering the cavity memory effect". *Appl. Ocean Res*. 97. 1-11.

Moffatt, H. K., 2013. "Three Coins in A Fountain". *J. Fluid. Mech*. 720, 1–4.

Moghadaripour, M., Azimi, A. H. and Elyasi, S., 2017a. "Experimental study of oblique particle clouds in water". *International Journal of Multiphase Flow* 91: 101–119.

Moghadaripour, M., Azimi, A. H. and Elyasi, S., 2017b. "Experimental Study of Particle Clouds in Stagnant Water". *ASCE J. Eng. Mech. 143(9),* p. 04017082.

Mohammadidinani, N., Azimi, A. H., And Elyasi, S., 2017. "Experimental Investigation of Sand

Jets Passing Through Immiscible Fluids". *Asme, Journal of Fluids Engineering*, 139(5), 051303, 13 P.

Morton, B. R., Taylor, G. I. and Turner, J. S., (1956). "Turbulent gravitational convection from maintained and instantaneous sources". *Proc. R. Soc. Lond. A Math. Phys. Eng. Sci.*: 234(1196), 1–23.

Nakatsuji, K., Tamai, M. and Murota, A., 1990. "Dynamic behaviour of sand clouds in water". *International Conference on Physical Modelling of Transport and Dispersion*, MIT, Cambridge, 8C, 1–6.

Noh, Y. and Fernando, H.J.S., 1993. "The Transition in the Sedimentation Pattern of a Particle Cloud". P*hysics of Fluids* A5, 12: 3049-3055.

Rabbi, R., Speirs, N., Kiyama, A., Belden, J., & Truscott, T., 2021. "Impact Force Reduction by Consecutive Water Entry of Spheres". *J. Fluid Mech.* 915, A55.

Rahimipour, H, and Wilkinson, D., 1992. "Dynamic Behaviour of Particle Clouds". *In: Proceedings of the Eleventh Australasian Fluid Mechanics Conference, 1 and 2. University of Tasmania, Hobart, Australia,* pp. 743–746. vols.

Rao, K. K., Nott, P. R. and Sundaresan, S., 2008. "An introduction to granular flow". *Cambridge University Press*, Cambridge, N.Y.

Rooney, G. G., 2015. "Merging of a row of plumes or jets with an application to plume rise in a channel". *Journal of Fluid Mechanics* 771: R11–R112.

Rooney, G. G., 2016. "Merging of two or more plumes arranged around a circle". *Journal of Fluid Mechanics* 796: 712–731.

Ruggaber, G.J., 2000. "The dynamics of particle clouds related to open-water sediment disposal." Ph.D. thesis, Dept. of Civil and Environmental Engineering, Massachusetts Institute of Technology, Cambridge, MA.

Seddon, C. M. & Moatamedi, M., 2006. "Review of Water Entry with Applications to Aerospace

Structures". *Intl J. Impact Engng* 32, 1045–1067.

Sharif, F., Azimi A.H., 2020. "Particle cloud dynamics in stagnant water". *International Journal of Multiphase Flow*. Vol. 125, 103197-1-15.

Sharif, F., Azimi A. H., 2021. "Effects of velocity ratio on dynamics of sand-water coaxial jets". *International Journal of Multiphase Flow*.

Shenoy, A., & Kleinstreuer, C., 2010. "Influence of aspect ratio on the dynamics of a freely moving circular disk". *J. Fluid Mech*. 653, 463-487.

Slack, G.W., 1963. "Sedimentation of a large number of particles as a cluster in air". *Nature* 200: 1306.

Smith E.H., 1971. "Autorotating wings: an experimental investigation". *J Fluid Mech* 50:513.

Speirs, N., Pan, Z., Belden, J., & Truscott, T., 2018. "The water entry of multi-droplet streams and jets". *J. Fluid Mech.* 844, 1084-1111.

Stringham, G. E., Simons, D. B, And Guy, H. P., 1969. "The Behavior of Large Particles Falling in Quiescent Liquids". *U.S. Geol. Surv. Prof.* Pap. 562-C,1.

Sun, T., Wang, H., Zong, Z., Zhang, G., Wang, A., Xu, C., 2019. "Splash Formation and Cavity Dynamics of Sphere Entry Through a Viscous Liquid Resting on The Water". *AIP Adv.* 9, 075211.

Tomkins, C.D. and Adrian R.J., 2003. "Spanwise structure and scale growth in turbulent boundary layers," *J. Fluid Mech*. 490, 37–74.

Tan, B.C.W., Vlaskamp, J.H.A., Denissenko, P., and Thomas,P.J., 2016. "Cavity Formation in The Wake of Falling Spheres Submerging into a Stratified Two-Layer System of Immiscible Liquids". *J. Fluid Mech.* 790, 33–56.

Tchoufag, J., Fabre, D., & Magnaudet, J., 2014. "Global linear stability analysis of the wake and path of buoyancy-driven disks and thin cylinders". *Journal of Fluid Mechanics* 740, 278-311.

Thielicke, W. and Stamhuis, E.J., 2014. PIVlab, Time-Resolved Digital Particle Image

Velocimetry Tool for MATLAB (version: 2.02).

Truscott, T. T., Epps, B. P., & Belden, J., 2013. "Water Entry of Projectiles". *Annual Review of Fluid Mechanics*, 46(1), 355–378.

Truscott, T.T, Epps, B. P., and Techet, A.H., 2012. "Unsteady forces on spheres during free surface water entry". *J. Fluid Mech*, 704:173–210.

Truscott, T.T. & Techet, A.H., 2009. "Water-Entry of Spinning Spheres". *J. Fluid Mech*. 625, 135–165.

Turner, J.S., 1964. "The motion of buoyant elements in turbulent surroundings". *Journal of Fluid Mechanics* 16: Part 1, 1-16.

Turner, J. S., 1969. "Buoyant plumes and thermals". *Annual Revision. Fluid Mechanics* 1 (1): 29–44.

Vakarelski, I., Patankar, N., Marston, J. et al., 2012. "Stabilization of Leidenfrost Vapour Layer by Textured Superhydrophobic Surfaces". *Nature* 489, 274–277.

Vincent, L., Shambaugh, W., & Kanso, E., 2016. "Holes Stabilize Freely Falling Coins". *J. Fluid Mech*. 801, 250-259.

Wang, R., Adams, E. E., Law, A. W. K., and Lai, A. C. H., 2015. "Scaling particle cloud dynamics: From lab to field". *Journal Hydraulic Engineering*.

Wang, X., Kikkert, G. A., 2014. "Behaviour of oblique jets released in a moving ambient". *Journal of Hydraulic Research*.

Wang, Y., Wang, Z., Du, Y., Wang, J., Wang, Y., and Huang, C., 2022. "The mechanism of surface-seal splash during water entry", *Physics of Fluids*, 34, 042110.

Wen, F., and Nacamuli, A., 1996. "The effect of the Rayleigh number on a particle cloud". *Hydrodynamics*: *Theory and Applications* vol. 1 and 2, 1275–1280.

Willmarth, W. W., Hawk, N. E., & Harvey, R. L., 1964. "Steady and Unsteady Motions and Wakes

of Freely Falling Disks". *Phys. Fluids*, 7(2), 197-208.

Witten, I. H., and Frank, E., 2005. "Data Mining-Practical Machine Learning Tools and Techniques". Morgan Kaufmann, San Francisco, Ca, P. 525.

Worthington, A. M., 1908. "A Study of Splashes". *Longmans Green*.

Worthington, A. M., "On impact with a liquid surface," Proc. R. Soc. London 34, 217–230 (1882).

Worthington, A.M. & Cole, R. S., 1897. "Impact with a Liquid Surface, Studied by The Aid of Instantaneous Photography". *Phil. Trans. R. Soc. Lond. A* 189, 137–148.

Worthington, A.M. & Cole, R. S., 1900. "Impact with a Liquid Surface, Studied by The Aid of Instantaneous Photography: Paper 2". *Phil. Trans. R. Soc. Lond. A* 194, 175–1499.

Wu R.J., Lin SY., 2015. "The flow of a falling ellipse: numerical method and classification. *J Mech* 31(06):771.

Wygnanski, I., & Fiedler, H., 1969. "Some measurements in the self-preserving jet". *Journal of Fluid Mechanics* 38(3): 577–612.

Xu, T., Li, J., Li, Z., Liao, S., 2021. "Accurate Predictions of Chaotic Motion of a Free Fall Disk". *Phys. Fluids*, 33, 033325.

Yan, J., Li, S., Kan, X., Zhang, A. and Liu, L., 2021. "Updated Lagrangian particle hydrodynamics (ULPH) modeling of solid object water entry problems". *Computational Mechanics*, 67(6), pp.1685-1703.

Zang, Z.P., Gao, F. P., Cui, J.S., 2013." Physical modeling and swirling strength analysis of vortex shedding from near-bed piggyback pipelines". 40, 50-59.

Zhang, Q., Zong, Z., Li, H. T., and Sun T. Z., 2022. "Experimental study of the impact of splash closure on the cavity evolution behind a sphere entering water". *Physics of Fluids*. 34, 042118.

Zhao, B., Law, A. W. K., Eric Adams, E., Shao, D. and Huang, Z., 2012. "Effect of air release height on the formation of sediment thermals in water". *Journal of Hydraulic Research* 50(5):

532–540.

Zhao, B., Law, A.W.K., Adams, E.E., and Er., J.W., 2014. "Formation of Particle Clouds". *Journal of Fluid Mechanics* 746 (1): 193–213.

Zhao, S., Wei, C., Cong, W., 2016. "Numerical Investigation of Water Entry of Half Hydrophilic and Half Hydrophobic Spheres". *Mathematical Problems in Engineering*, vol. 2016, Article ID 5265818, 15 pages.

Zhong, H. J., Chen, S. Y. & Lee, C. B., 2011. "Experimental Investigation of Freely Falling Thin Disks: Transition from Zigzag to Spiral". *Phys. Fluids* 23, 9–12.

Zhong, H., Lee, C., Su, Z., Chen, S., Zhou, M., & Wu, J. 2013. "Experimental investigation of freely falling thin disks. Part 1. The flow structures and Reynolds number effects on the zigzag motion". *Journal of Fluid Mechanics* 716, 228-250.

Zhou, J., Adrian, R. J., Balachandar, S., and Kendall, T.M., 1999. "Mechanisms for generating coherent packets of hairpin vortices in channel flow," *J. Fluid Mech*. 387(1), 353–396.

Zhou, X., Yuan S., Zhang S., 2021. "Eccentric Disks Falling in Water". *Phys. Fluids* 33, 3, 1-7.